VOLUME 18 NUMBER 2 2025 ISSN 2218-7979
eISSN 2409-370X

# International Journal of Biology and Chemistry

Al-Farabi Kazakh National University

International Journal of Biology and Chemistry is published twice a year by
al-Farabi Kazakh National University, al-Farabi ave., 71, 050040, Almaty, Kazakhstan
website: http://ijbch.kaznu.kz/

Any inquiry for subscriptions should be sent to:
Prof. Mukhambetkali Burkitbayev, al-Farabi Kazakh National University
al-Farabi ave., 71, 050040, Almaty, Kazakhstan
e-mail: Mukhambetkali.Burkitbayev@kaznu.edu.kz

© 2025 al-Farabi Kazakh National University

Int. j. biol. chem. (Online)

# EDITORIAL

The most significant achievements in the field of natural sciences are reached in joint collaboration, where important roles are taken by biology and chemistry. Therefore publication of a Journal, displaying results of current studies in the field of biology and chemistry, facilitates highlighting theoretical and practical issues and distribution of scientific discoveries.

One of the basic goals of the Journal is to promote the extensive exchange of information between the scientists from all over the world. We welcome publishing original papers and materials of biological and chemical conferences, held in different countries (by prior agreement, after the process of their subsequent selection).

Creation of International Journal of Biology and Chemistry is of great importance, since scientists worldwide, including other continents, might publish their articles, which will help to widen the geography of future collaboration.

The Journal aims to publish the results of the experimental and theoretical studies in the field of biology, biotechnology, chemistry and chemical technology. Among the emphasized subjects are: modern issues of technologies for organic synthesis; scientific basis of the production of biologically active preparations; modern issues of technologies for processing of raw materials; production of new materials and technologies; study on chemical and physical properties and structure of oil and coal; theoretical and practical issues in processing of hydrocarbons; modern achievements in the field of nanotechnology; results of studies in various branches of biology, chemistry and related technologies.

We hope to receive papers from the leading scientific centers, which are involved in the application of the scientific principles of biological and chemical sciences on practice and fundamental research, related to production of new materials, technologies well ecological issues.

IRSTI 34.23.15; 34.27.19; 34.15.23 https://doi.org/10.26577/IJBCh20251821

G.A. Bayandy[1, 2], N.B. Baltakhozha[1, 2], Kh.E. Yerkinova[1, 2],
K.B. Nurpeis[2], G.N. Sailauova[2], I.T. Smekenov[1, 2],
A.K. Bissenbaev[1, 2*]

[1]Scientific Research Institute of Biology and Biotechnology Problems,
Al-Farabi Kazakh National University, Almaty, Kazakhstan
[2]Al-Farabi Kazakh National University, Almaty, Kazakhstan
*e-mail: amangeldy.bisenbaev@kaznu.kz

*(Received 12 May 2025; received in revised form 26 December 2025; accepted 29 December 2025)*

# Production of the soluble form of the Rabies virus glycoprotein ectodomain as a subunit vaccine candidate

**Abstract.** Rabies remains a serious global public health concern. The envelope glycoprotein of the rabies virus (RABV-G) is the principal viral antigen and harbors critical neutralizing epitopes, making it a promising target for subunit vaccine development and diagnostic applications. Nevertheless, the efficient production of recombinant RABV-G with preserved antigenic and immunogenic properties remains technically demanding. In this work, we developed an optimized strategy for the expression and purification of recombinant RABV-G and assessed its antigenicity and immunogenicity. The rabies virus glycoprotein ectodomain (rRABV-GE) was successfully expressed in *Escherichia coli* Rosetta2(DE3)pLysS and purified in a biologically relevant form. The rRABV-GE gene was codon-optimized and cloned into the pET-28c(+) expression vector, resulting in recombinant protein expression largely in an insoluble state. Consequently, the protein was subjected to refolding and purification procedures. To improve protein solubility, hydrophobic loop regions were substituted with flexible linker sequences. Protein purification was performed under denaturing conditions using urea, followed by affinity chromatography. The identity and antigenicity of the purified protein were confirmed by Western blot analysis and indirect enzyme-linked immunosorbent assay (ELISA). ELISA testing was performed using rabbit sera collected from animals immunized with the commercial Purified Vero Cell Rabies Vaccine (RHABDOVAC-1). Collectively, these findings indicate that the optimized bacterial expression platform enables the production of biologically relevant rRABV-GE and provides a cost-effective approach for the development of rabies subunit vaccines and diagnostic reagents. In summary, the recombinant rRABV-G protein produced in this study appears to be a suitable diagnostic antigen for ELISA-based and other rabies virus immunodiagnostic uses.

**Keywords:** Rabies virus, glycoprotein ectodomain, antibody, ELISA, Rosetta2(DE3)pLysS, vaccine.

## Introduction

Rabies is considered one of the most lethal viral infections, with an almost 100% fatality rate once clinical symptoms develop. The causative agent, rabies virus (RABV), is an RNA virus belonging to the family Rhabdoviridae and the genus Lyssavirus. RABV causes rabies, an acute infection of the central nervous system that progresses rapidly and is invariably fatal in the absence of timely intervention [1]. As a prototype neurotropic virus, RABV possesses a small, negative-sense single-stranded RNA genome of approximately 12 kb, which encodes five structural proteins: nucleoprotein (N), phosphoprotein (P), matrix protein (M), glycoprotein (G), and RNA-dependent RNA polymerase (L). Among these, the viral glycoprotein (RABV-G) plays a pivotal role in pathogenesis by mediating viral attachment and entry through interaction with host cell receptors [2].

The G protein, with a molecular weight ranging from 62 to 67 kDa, is a type I transmembrane glycoprotein composed of 505 amino acids. It contains two to four potential N-glycosylation sites, although only one or two are glycosylated depending on the viral strain [3]. Structurally, the protein is divided into three domains: an ectodomain, a transmembrane region, and a cytoplasmic domain. The ectodomain consists of 439 amino acid residues and assembles

© 2025 al-Farabi Kazakh National University

into a homotrimeric structure. The transmembrane domain spans approximately 20 amino acids (residues 460–480), while the cytoplasmic domain comprises 44 amino acids that extend into the cytoplasm of infected cells and interact with the matrix protein during viral assembly [4]. Importantly, the ectodomain is exposed on the surface of the virion and represents the only viral component involved in host cell receptor recognition, underscoring its essential role in viral infectivity and its significance as the primary target of virus-neutralizing antibodies [5].

Antibodies interact with RABV-G primarily through their heavy chain and bind to a bipartite conformational epitope on the viral protein to achieve neutralization. These structures provide valuable insights for vaccine and therapeutic development. The purified ectodomain of RABV-G (RABV-GE), produced in eukaryotic cells, has demonstrated effectiveness as a subunit vaccine in animal models [6]. Currently available rabies vaccines are costly, technically demanding to manufacture, and require intensive immunization schedules and boosters to induce and sustain protective immunity. Given that RABV-GE is the most immunologically relevant component of rabies vaccines, a system was established for the production of a subunit vaccine based on a soluble form of RABV-GE obtained from *Escherichia coli* [7].

In the present work, expression conditions for the recombinant ectodomain of the rabies virus G protein were optimized in *Escherichia coli* strain Rosetta2(DE3)pLysS. Additionally, a purification protocol was optimized for isolating the protein from the insoluble fraction using urea-based denaturation and affinity chromatography on a HisTrap column [8].

## Materials and methods

### *Plasmid Construction*

The nucleotide sequence of the ectodomain of the rabies virus glycoprotein (RABV-GE; NCBI accession number GQ918139.1) was synthesized with the substitution of two fusion loops by flexible linkers (GGSGG) and the addition of a C-terminal c-Myc epitope. Prior to synthesis, the gene sequence was optimized in terms of codon usage and GC content for efficient expression in *Escherichia coli* using the GenSmart Codon Optimization tool (https://www.genscript.com/tools/gensmart-codon-optimization). The optimized gene was synthesized by GeneCust (Dudelange, Luxembourg) and cloned into the pBluescript II SK(+) vector.

The sequence of the G protein ectodomain (1357 bp, rRABV-GE) was subcloned from the pBluescript II SK(+) vector into the pET-28c(+) expression vector using the *Nco*I and *Xho*I restriction sites, thereby introducing a sequence encoding a C-terminal 6×His tag to the gene (resulting in C-terminal 6×His-tagged proteins). Plasmid DNA was extracted using the GeneJET Plasmid Miniprep Kit (Thermo Scientific, #K0503) according to the manufacturer's instructions. *E. coli* DH5α (Promega, USA) was used as the cloning host for propagation of the expression constructs. Plasmids from positive colonies were analyzed using polymerase chain reaction (PCR) with gene-specific primers Dir_NcoI_G-ecto (ACCGACCATGGGGAAATTTCCCATATATACG) and Rev_XhoI_G-ecto (ATTACCTCGA GCAGGTCCTCTTCAGAGATC), synthesized by Macrogen (South Korea), as well as by restriction digestion with *Nco*I and *Xho*I enzymes (Thermo Fisher Scientific, USA). PCR amplification was performed on a thermocycler (Eppendorf, model AG 22331, Germany) under the following conditions: initial denaturation at 94 °C for 5 min; 30 cycles of denaturation at 94 °C for 30 s, annealing at 55 °C for 30 s, and extension at 72 °C for 90 s; followed by a final extension at 72 °C for 5 min.

### *Expression of the rRABV-GE protein in bacterial cells and its chromatographic purification*

The constructed expression plasmid, pET-28c/rRABV-GE, produces the corresponding protein carrying C-terminal 6×His and c-Myc tags. The expression strain *E. coli* Rosetta2(DE3)pLysS (Invitrogen, Thermo Fisher Scientific, USA) was prepared and transformed according to the standard protocol [9].

The rRABV-GE protein was obtained through heterologous expression in *E. coli* Rosetta2(DE3)pLysS cells carrying the expression plasmid encoding the rRABV-GE gene. After transformation, bacterial cultures were grown at 37 °C until reaching a mid-logarithmic phase (OD600 ≈ 0.6). To optimize protein expression and folding, the incubation temperature was subsequently reduced to 4, 16, or 30 °C and maintained for 30 min prior to induction. Protein expression was then initiated by the addition of IPTG (isopropyl β-D-1-thiogalactopyranoside; Thermo Fisher Scientific, USA) at final concentrations ranging from 0.05 to 0.5 mM, followed by continued cultivation for 16 h. As additional components, 1% glucose (Applichem, Germany) and 3% $C_2H_5OH$ (Applichem, Germany) were added prior to induction.

All protein purification procedures were performed at 4 °C. To obtain the recombinant rRABV-

GE protein under native (non-denaturing) conditions, bacterial cells were harvested by centrifugation at 6000 rpm for 7 min at 4 °C using a centrifuge (Eppendorf, model 5417 R, Germany). The resulting cell pellets were disrupted by ultrasonication using an OmniRuptor 4000 (Omni International, USA) in lysis buffer composed of 50 mM sodium phosphate (pH 7.6; Sigma-Aldrich, USA), 100 mM NaCl (Applichem, Germany), 20 mM imidazole (Applichem, Germany), 5% glycerol (Applichem, Germany), 1 mM EDTA (pH 8.0; Applichem, Germany), 10 mM β-mercaptoethanol (Sigma-Aldrich, USA), 1 mM DTT (Sigma-Aldrich, USA), and 2% Triton X-100 (Sigma-Aldrich, USA), supplemented with a complete protease inhibitor cocktail (Roche, Switzerland). EDTA was included to suppress proteolytic activity, while DTT and β-mercaptoethanol were used to maintain reducing conditions. The non-ionic detergent Triton X-100 facilitated efficient solubilization of membrane-associated and cytoplasmic proteins while preserving their native conformation [10,11].

Following cell disruption, the lysates were clarified by centrifugation at 11,000 × g for 60 min at 4 °C using a centrifuge (Eppendorf, model 5804 R, Germany). The supernatant was subsequently loaded onto a 1 mL HisTrap HP affinity column (Cytiva, USA) pre-charged with $Ni^{2+}$ ions (Sigma-Aldrich, USA). Protein elution was carried out using a linear imidazole (Applichem, Germany) gradient ranging from 20 to 500 mM.

For purification of inclusion bodies, cell pellets obtained from 1 L of bacterial culture were resuspended in 20 mL of 50 mM sodium phosphate buffer (pH 7.6) containing 20 mM NaCl and lysed by ultrasonic homogenization at 40% amplitude. The lysate was centrifuged at 14,000 rpm for 20 min at 4 °C using a centrifuge (Eppendorf, model 5417 R, Germany), and the resulting pellet was resuspended in 20 mL of buffer containing 1 M urea (Applichem, Germany) and 1% Triton X-100, followed by centrifugation. This washing step was repeated three times to remove contaminating soluble proteins.

For denaturation and reduction, the purified inclusion body pellets were dissolved in 100 mL of 50 mM sodium phosphate buffer (pH 7.6) containing 8 M urea, 500 mM NaCl, 20 mM imidazole, and 5 mM β-mercaptoethanol. The suspension was incubated for 16 h at room temperature under constant agitation to ensure complete denaturation and reduction. Insoluble material was removed by centrifugation at 12,000 rpm for 20 min using a centrifuge (Eppendorf, model 5417 R, Germany), and the clarified supernatant was applied to a $Ni^{2+}$-charged HisTrap HP column. Bound proteins were eluted in a single step using 500 mM imidazole.

Protein purification and fraction collection were performed using an ÄKTA Start FPLC system (Cytiva, USA). The column was equilibrated for 5 min, protein sample (20 mL) was loaded, washed for 15 min, and eluted in 7 mL fractions, collecting 500 µL per fraction. The overall flow rate during purification was 0.5 mL/min. The purity and homogeneity of the recombinant protein were assessed by SDS-PAGE. Purified protein samples were stored at −20 °C in a buffer containing 50% glycerol.

*Refolding of rRABV-GE expressed in E. coli* Rosetta2(DE3)pLysS

For refolding of the denatured purified rRABV-GE protein, gradient dialysis was performed using a Cellu Sep cellulose membrane (Membrane Filtration Products, USA) with a molecular weight cut-off of 14 kDa at 4°C. The dialysis buffer, containing 100 mM NaCl, 50 mM sodium phosphate buffer (pH 7.6), 0.5 M arginine (Applichem, Germany), 20% glycerol, and urea, was gradually reduced from 6M to 0M in a stepwise manner, with the buffer changed every 3 hours. After overnight incubation, the protein was collected into a 1.5 mL Eppendorf tube and stored on ice [12,13].

*Western Blot Analysis of Purified Proteins*

Two micrograms of each purified protein were resolved by SDS–PAGE on a 10% polyacrylamide gel and subsequently transferred onto a PVDF membrane using a Bio-Rad Mini Trans-Blot Cell (Bio-Rad, USA), in accordance with the manufacturer's instructions. Membranes were blocked for 1.5 h at room temperature in 1× TBS (50 mM Tris–HCl (Applichem, Germany), pH 7.5, 20 mM NaCl) containing 5% non-fat dry milk and 0.1% Tween-20 (Sigma-Aldrich, USA), with gentle agitation using a shaker (Biosan, OS-20, Latvia).

Following blocking, the membranes were incubated overnight at 4 °C with anti-Myc monoclonal antibody (Abcam, UK) diluted 1:5000 in blocking buffer supplemented with 0.1% Tween-20. The membranes were then washed five times for 5 min each with 1× TBS containing 0.1% Tween-20 and subsequently incubated for 1 h at room temperature with the appropriate horseradish peroxidase–conjugated anti-mouse IgG secondary antibody (Abcam, UK). After a second series of five 5-minute washes, the membrane was treated with the chemiluminescent substrate for 60–120 seconds in the dark and the signal was captured on Kodak X-Omat film (Kodak, USA).

*Preparation of Anti-RABV-G Polyclonal Antibody*

Polyclonal antibodies were produced in rabbits by subcutaneous injection of the RHABDOVAC 1 vaccine (Antigen, Almaty, Kazakhstan), emulsified in an equal volume of complete Freund's adjuvant (Invitrogen, Thermo Fisher Scientific, USA). Subsequent booster injections were performed at two-week intervals using the same dose emulsified in incomplete Freund's adjuvant (Invitrogen, Thermo Fisher Scientific, USA). A pre-immune serum sample was collected prior to the first injection to serve as a negative control. One week after the final (fourth) injection, blood was collected for isolation of the immune serum. The animal study protocol was approved by the Local Ethics Committee of the LLP Scientific and Production Enterprise «Antigen», Almaty, Kazakhstan (protocol code #14, 25 November 2024).

The antibody was raised against the RABV vaccine. For primary immunization, rabbits were subcutaneously injected with 1 mL of RHABDOVAC-1 vaccine at five sites on the dorsal surface. Booster immunizations were administered three times at 14-day intervals, with each dose consisting of 1 mL of the vaccine. One week after the final booster, blood samples were collected, and 3 mL of the resulting antiserum was subjected to ammonium sulfate (Applichem, Germany) precipitation at 50% saturation. The precipitated proteins were recovered by centrifugation, dissolved in purified water, and dialyzed against 10 mM potassium phosphate buffer (pH 7.0; Applichem, Germany).

The dialyzed immunoglobulin fraction was subsequently loaded onto a Protein A–agarose affinity column (Pierce, Thermo Fisher Scientific, USA) pre-equilibrated with the same buffer. After thorough washing, bound antibodies were eluted using 100 mM glycine buffer (pH 3.0). Fractions containing IgG were pooled, and the pH was immediately adjusted to 7.0 with 1.0 M Tris base (Applichem, Germany). The purified antibody preparation was stored at 4 °C until further use. To generate a high-specificity immune response, a polyclonal antibody was raised in rabbits against the ectodomain of the rabies virus glycoprotein (RABV-G), which is a critical viral antigen involved in host cell recognition and membrane fusion. This domain was selected due to its surface exposure and immunogenicity, making it an ideal target for antibody development.

*Determination of Antiserum Titer by ELISA*

The production of antigen-specific antibodies was confirmed using an indirect enzyme-linked immunosorbent assay (ELISA) performed according to standard immunological procedures. Microtiter plates were coated with viral antigens and blocked with bovine serum albumin (BSA; Sigma-Aldrich, USA) to minimize non-specific binding. Detection was achieved using horseradish peroxidase (HRP)–conjugated goat anti-rabbit secondary antibodies (Abcam, USA). All measurements were carried out in triplicate to ensure reproducibility.

Antiserum titers were determined by indirect ELISA using 96-well polystyrene microplates (Thermo Fisher Scientific, USA). Each well was coated with 1 μg of whole RABV diluted in 100 μL of 1× phosphate-buffered saline (PBS, pH 7.4; Thermo Fisher Scientific, USA) and incubated overnight at 4 °C. Plates were washed three times with 1× PBS containing 0.05% Tween-20 (PBST) and then blocked with 100 μL of 3% BSA in PBST for 1 h at 37 °C, followed by two additional washing steps.

Serial dilutions of antiserum (anti-RABV-G and anti-rRABV-GE), ranging from 1:500 to 1:128,000, were added to the antigen-coated wells (100 μL per well) and incubated for 2 h at room temperature. After four washes with PBST, 100 μL of HRP-conjugated goat anti-rabbit IgG antibody (1:30,000) was added to each well and incubated for 1 h at 37 °C.

Following extensive washing, 100 μL of freshly prepared tetramethylbenzidine (TMB; Thermo Fisher Scientific, USA) substrate was added and allowed to react at room temperature. The enzymatic reaction was terminated by the addition of 1 M sulfuric acid (Sigma-Aldrich, USA), and absorbance was measured at 450 nm using a microplate reader (DAS, Italy). Each assay included both positive and negative control sera, and all samples were analyzed in triplicate.

## Results and discussion

*Construction of a Recombinant Design for Expression of the G Protein Ectodomain*

The production of a soluble, homogeneous, and properly folded extracellular domain of the rabies virus glycoprotein (RABV-G) is a critical prerequisite for its downstream application in diagnostics and immunological studies. Previous studies by Yang et al. demonstrated that the predicted fusion loops within the extracellular domain of RABV-G, located between amino acid residues 73–79 and 117–125, are enriched in hydrophobic amino acids, which significantly contributes to protein aggregation and heterogeneity when expressed recombinantly in *E. coli* [14,15].

In agreement with these findings, the relatively short length of these fusion loops (17–19 amino acids) allows substitution of hydrophobic residues without disturbing the overall folding or antigenicity of the protein [15]. Based on this rationale, we substituted the hydrophobic amino acids in the fusion loop regions with the Gly-Gly-Ser-Gly-Gly linker prior to gene synthesis (Figure 1). This strategy has been previously reported to enhance solubility and promote proper folding of RABV-GE [15], and thus was expected to improve the biochemical properties of the recombinant protein in our system.

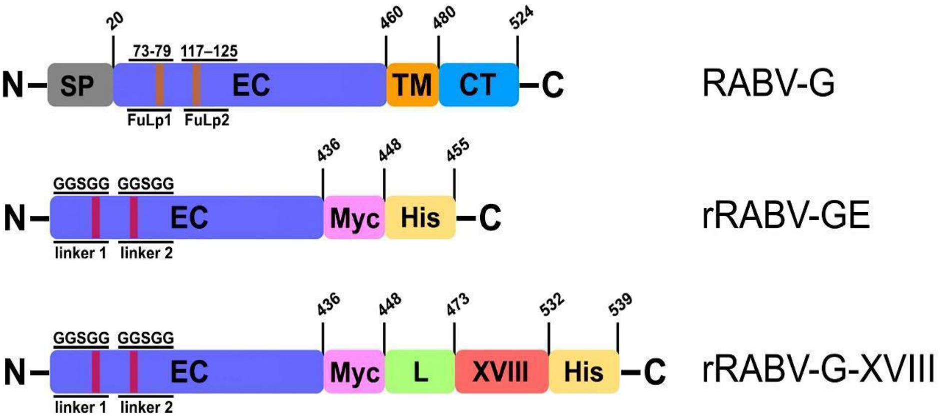

**Figure 1** – Recombinant construct of the RABV-GE gene. Full sequence of RABV-G: SP = signal peptide, EC = ectodomain, TM = transmembrane domain, CT = cytosolic domain. In rRABV-GE, the hydrophobic residues at positions 73–79 and 117–125 were replaced with the Gly-Gly-Ser-Gly-Gly linker

Following codon optimization for *E. coli*, the redesigned rRABV-GE gene was successfully synthesized and cloned into the pET-28c(+) expression vector, yielding the pET-28c-rRABV-GE construct containing a C-terminal 6×His tag and c-Myc epitope (Figure 2). Restriction digestion and PCR analysis confirmed correct insertion of the target gene, indicating successful construction of the expression plasmid. These results demonstrate the feasibility of generating a genetically stable construct suitable for high-level expression in bacterial systems.

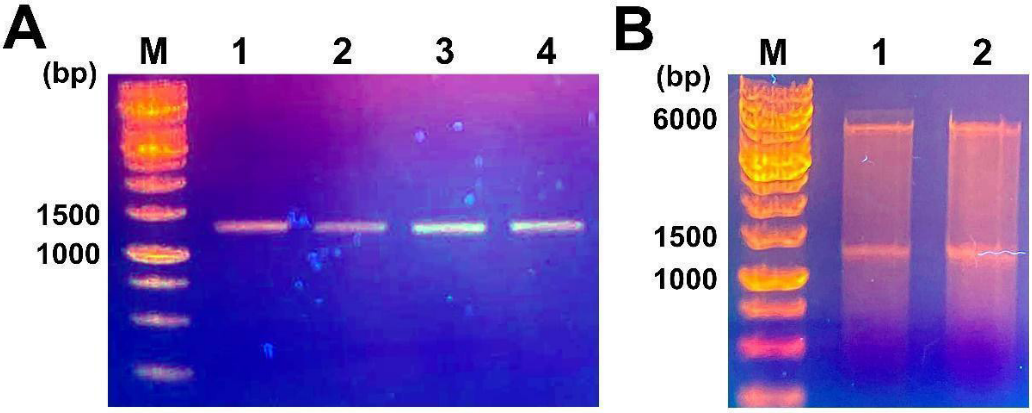

**Figure 2** – Analysis of constructed recombinant plasmids pET-28c-rRABV-GE in *E. coli* strain DH5α. A) PCR analysis; B) Restriction analysis. M – 1 kb GeneRuler marker; 1–4 – recombinant plasmid clones

*Expression of the Recombinant rRABV-GE Protein in the E. coli Expression Strain*

The recombinant rRABV-GE protein was expressed using a T7 RNA polymerase–based expression system in *E. coli* Rosetta2(DE3)PLysS cells. This strain was selected due to its ability to supply tRNAs for codons rarely used in *E. coli*, thereby enhancing the expression efficiency of heterologous eukaryotic proteins. The presence of the pLysS element further minimized basal expression, reducing potential toxicity and proteolytic degradation prior to induction [16].

To improve the solubility and yield of rRABV-GE, expression conditions were systematically optimized by varying IPTG concentration and induction temperature, parameters known to critically influence recombinant protein folding in *E. coli*. Lower induction temperatures (16 °C and 4 °C) are frequently employed to reduce the rate of translation, thereby allowing nascent polypeptide chains more time to fold correctly and decreasing the likelihood of aggregation into inclusion bodies [17,18]. Similarly, reducing IPTG concentration can moderate transcriptional strength and alleviate metabolic burden on host cells, often resulting in improved solubility of heterologous proteins [19]. In the present study, IPTG concentrations ranging from 0.05 to 0.5 mM and induction temperatures of 4 °C, 16 °C, and 30 °C were evaluated. SDS-PAGE analysis demonstrated robust expression of a protein with an apparent molecular mass of approximately 50 kDa, consistent with the predicted size of rRABV-GE (50.8 kDa). The absence of this band in non-induced samples confirmed tight regulation of expression and IPTG-dependent induction (Figure 3). These results indicate that codon optimization and host strain selection were sufficient to achieve high-level expression of rRABV-GE.

Despite these modifications, rRABV-GE remained predominantly localized in the insoluble fraction, with no significant increase in soluble protein yield observed. This outcome suggests that aggregation of rRABV-GE is not primarily driven by excessive expression rates, but rather by intrinsic structural features of the protein (Figure 3).

Rabies virus glycoprotein is a highly structured viral envelope protein that requires correct disulfide bond formation and glycosylation for native folding and stability [20]. The reducing environment of the *E. coli* cytoplasm is unfavorable for disulfide bond formation, and the absence of eukaryotic post-translational modifications further compromises proper folding. Similar observations have been reported for other viral glycoproteins expressed in bacterial systems, where temperature and IPTG optimization alone was insufficient to prevent inclusion body formation [15,21]. Thus, although modulation of induction parameters is a widely applied strategy for enhancing soluble expression, our results indicate that such approaches are insufficient for rRABV-GE, reinforcing the necessity of downstream refolding strategies or alternative expression platforms for producing functionally folded protein.

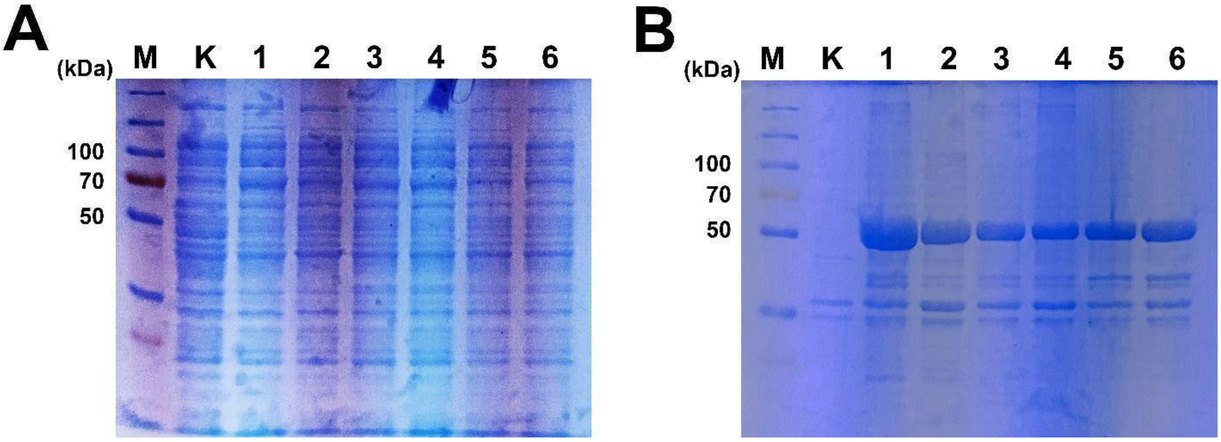

**Figure 3** – Optimization of rRABV-GE protein induction in *E. coli* Rosetta2(DE3)PLysS cells.
A) Proteins from cell extract; B) Proteins from membrane fraction. M – Marker PageRuler™ Plus Prestained Protein Ladder, 10 to 250 kDa; K – Control, untransformed cells; 1 – Induction with 0.5 mM IPTG at 30°C, overnight (ON); 2 – Induction with 0.5 mM IPTG at 16°C, overnight (ON); 3 – Induction with 0.5 mM IPTG at 4°C, overnight (ON); 4 – Induction with 0.05 mM IPTG, 1% glucose, and 3% ethanol at 30°C, overnight (ON); 5 – Induction with 0.1 mM IPTG, 1% glucose, and 3% ethanol at 30°C, overnight (ON); 6 – Induction with 0.5 mM IPTG, 1% glucose, and 3% ethanol at 30°C, overnight (ON)

*Purification, Refolding, and Immunoreactivity of rRABV-GE*

Recombinant rRABV-GE was purified from inclusion bodies under denaturing conditions using 8 M urea, followed by nickel affinity chromatography. The use of urea effectively disrupted aggregated protein structures, enabling solubilization and purification of the target protein [13,22]. Subsequent refolding via stepwise dialysis with decreasing urea concentrations allowed gradual restoration of native-like conformation while minimizing aggregation.

The inclusion of arginine and glycerol in the refolding buffer proved essential for stabilizing the protein during renaturation, consistent with previous studies demonstrating their protective effects against misfolding and precipitation [23,24]. SDS-PAGE analysis confirmed high purity of the refolded protein (Figure 4), and the stability of rRABV-GE during storage further supports successful refolding.

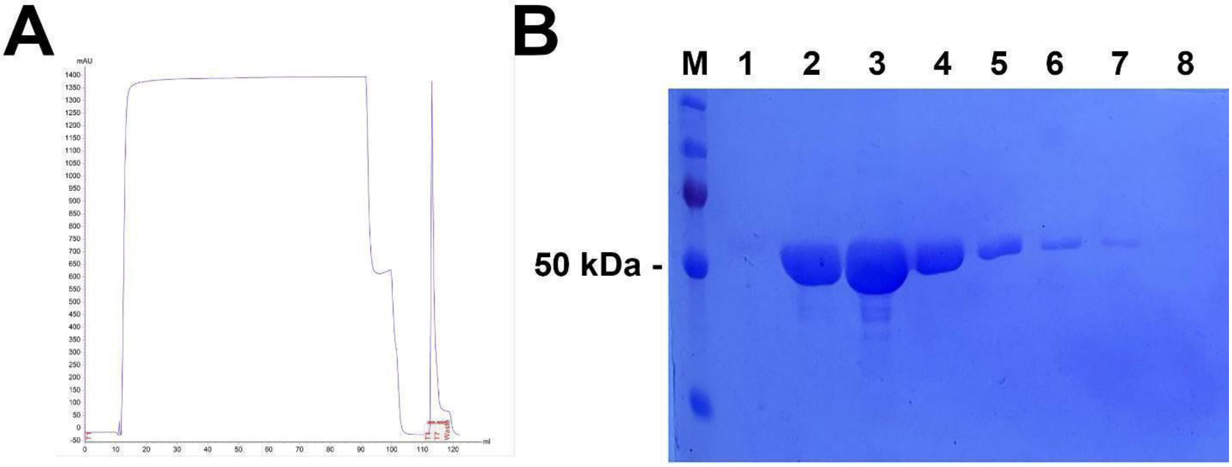

**Figure 4** – Chromatographic purification of the G protein ectodomain.
A) Chromatographic purification histogram; B) SDS-PAGE analysis of purified protein fractions.
M – PageRuler™ Plus Prestained Protein Ladder, 10 to 250 kDa;
1–8 – purified protein fractions corresponding to tubes 4 through 11

Western blot analysis using serum from rabbits immunized with inactivated rabies virus provided critical insight into the antigenic integrity of the recombinant rRABV-GE protein (Figure 5). The observed specific recognition of rRABV-GE by anti-rabies virus antibodies indicates that key antigenic determinants present in native viral glycoprotein G are preserved in the recombinant protein, despite its bacterial origin and the substitution of hydrophobic residues within the fusion loop regions.

Importantly, this finding demonstrates that the Gly-Gly-Ser-Gly-Gly linker substitutions at positions 73–79 and 117–125 do not disrupt major linear or conformational epitopes recognized by polyclonal immune sera. This observation is consistent with previous reports showing that the antigenic sites of RABV-G are distributed across multiple regions of the ectodomain and are relatively tolerant to localized sequence modifications, particularly within fusion-associated regions [14,15]. The ability of polyclonal serum to recognize rRABV-GE also suggests that at least a subset of conformational epitopes is retained following denaturation and refolding, highlighting the effectiveness of the applied refolding protocol. Given that Western blot analysis involves protein denaturation, the observed immunoreactivity further implies preservation of linear epitopes, which are crucial for diagnostic applications such as ELISA-based assays [25].

Taken together, the Western blot results provide strong evidence that rRABV-GE maintains immunological relevance and supports its suitability as a recombinant antigen for serological detection of rabies virus–specific antibodies. These findings validate the design strategy and justify further development of rRABV-GE for diagnostic and potentially immunotechnological applications.

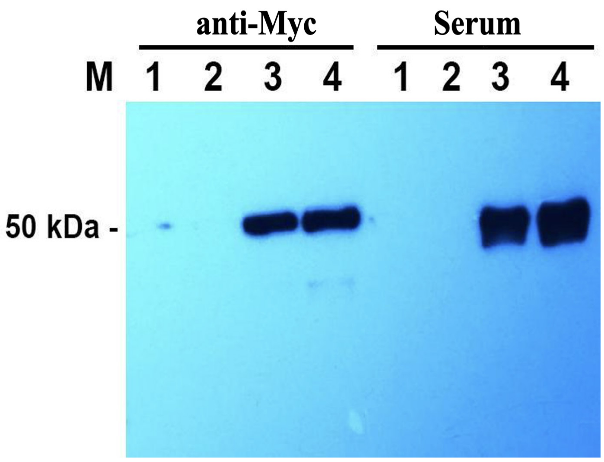

**Figure 5 –** Western blot analysis of the rRABV-GE protein. 1–2 – Cell lysate: proteins induced with 0.5 mM IPTG at 30 °C, overnight (ON); 3–4 – Pellet: proteins induced with 0.5 mM IPTG at 30 °C, overnight (ON)

Functionally, the refolded rRABV-GE protein demonstrated strong immunoreactivity in an indirect ELISA format. When used as a capture antigen, it reliably detected rabies virus–specific antibodies in sera from rabbits immunized with a commercial Vero cell–derived vaccine, while sera from non-immunized animals showed minimal reactivity (Table 1). The clear correlation between optical density values and serum antibody titers indicates that the recombinant protein retains conformational epitopes relevant for antibody recognition.

Overall, these results demonstrate that although rRABV-GE is expressed in *E. coli* predominantly as an insoluble protein, it can be efficiently purified, refolded, and retain strong antigenic properties. This highlights its potential utility as a cost-effective recombinant antigen for diagnostic applications and supports further development toward improved expression strategies or fusion-based designs aimed at enhancing solubility and structural stability.

**Table 1** – List of anti-Rabies virus antibodies OD450 values measured by ELISA in rabbits' serum samples

| Sample | OD450 value* | Rabies vaccine inoculation |
|---|---|---|
| ^1:500 | 0.605 ± 0.032 | + |
| ^1:1000 | 0.347 ± 0.019 | + |
| ^1:2000 | 0.207 ± 0.015 | + |
| ^1:4000 | 0.131 ± 0.009 | + |
| ^1:8000 | 0.095 ± 0.007 | + |
| ^1:16000 | 0.088 ± 0.009 | + |
| ^1:32000 | 0.075 ± 0.008 | + |
| ^1:64000 | 0.074 ± 0.008 | + |
| ^1:128000 | 0.069 ± 0.010 | + |
| #1 | 0.055 ± 0.008 | - |
| #2 | 0.063 ± 0.009 | - |
| #3 | 0.049 ± 0.006 | - |

^ Samples titer: serum sample from rabbits immunized with rRABV-GE.

# Sample 1-3: serum sample from rabbits who did not undergo rRABV-GE inoculation.

* The antibody titer is determined as the maximum dilution of the serum at which the ratio of A450 (A450 of the serum after immunization / A450 of the serum before immunization) exceeds 2:1. Data are presented as the mean ± standard deviation (SD).

## Conclusion

The production of a soluble form of the rabies virus glycoprotein ectodomain (rRABV-GE) has long been challenged by the intrinsic structural complexity, hydrophobic regions, and conformational instability of this viral protein, which collectively complicate its heterologous expression and purification. In the present study, these limitations were successfully addressed through the development of a robust and reproducible strategy for the expression, purification, and refolding of rRABV-GE in a bacterial expression system. Codon optimization, targeted substitution of hydrophobic fusion loop residues with flexible linker sequences, and carefully controlled purification and refolding conditions enabled the production of a highly pure and stable recombinant protein. Immunological characterization demonstrated that the purified rRABV-GE retains antigenic determinants relevant to rabies virus–specific immune responses. A strong correlation between serum neutralizing antibody titers and ELISA optical density values confirmed the suitability of rRABV-GE as a sensitive and specific diagnostic antigen. These findings indicate that the truncated ectodomain preserves key neutralizing epitopes, supporting its applicability in immunodiagnostic assays and underscoring its potential relevance for subunit-based vaccine research. Importantly, the optimized production workflow allowed consistent recovery of rRABV-GE at milligram-scale yields with high purity and stability, highlighting the scalability and practicality of the approach for both laboratory and applied use. This overcomes major obstacles previously associated with insolubility and aggregation of RABV-G–derived recombinant proteins in prokaryotic systems.

In summary, this study establishes an efficient and reproducible platform for the production of soluble, immunoreactive rRABV-GE. The availability of such a recombinant antigen provides a valuable foundation for the development of improved ELISA-based diagnostic tools and supports further exploration of rRABV-GE as a component of next-generation rabies vaccines.

## Acknowledgments

This project was supported by the Ministry of Science and Higher Education of the Republic of Kazakhstan (grant number AP14870256).

## Conflict of interest

All authors are aware of the article’s content and declare no conflict of interest.

## References

1. Yousaf M., Qasim M., Zia S., Rehman Khan M., Ur Ashfaq U., Khan S. (2012) Rabies molecular virology, diagnosis, prevention and treatment. *Virology Journal*, vol. 9, no. 1, pp. 1–5. https://doi.org/10.1186/1743-422X-9-50
2. Fooks A.R., Banyard A.C., Ertl H.J. (2019) New human rabies vaccines in the pipeline. *Vaccine*, vol. 37, pp. 140–145. https://doi.org/10.1016/j.vaccine.2018.08.039
3. Fisher C.R., Streicker D.G., Schnell M.J. (2018) The spread and evolution of rabies virus: Conquering new frontiers. *Nature Reviews Microbiology*, vol. 16, no. 4, pp. 241–255. https://doi.org/10.1038/nrmicro.2018.11
4. Dhulipala S., Uversky V. (2022) Looking at the pathogenesis of the rabies lyssavirus strain Pasteur Vaccins through a prism of the disorder-based bioinformatics. *Biomolecules*, vol. 12, no. 10, p. 1436. https://doi.org/10.3390/biom12101436
5. Charlton K.M., Casey G.A. (1981) Experimental rabies in skunks: Persistence of virus in denervated muscle at the inoculation site. *Canadian Journal of Comparative Medicine*, vol. 45, pp. 357. PMID: 7337867; PMCID: PMC1320163
6. Dietzschold B., Wunner W., Smith C. (1988) The molecular biology of rabies virus. *Clinical Infectious Diseases*, vol. 10, no. 4, pp. 771–784. https://doi.org/10.1093/clinids/10.supplement _4.s771
7. Targovnik A.M., Ferrari A., Mc Callum G.J., Arregui M.B., Smith I., Bracco L.F., Alfonso V., López M.G., Martínez-Solís M., Herrero S., Miranda M.V. (2019) Highly efficient production of rabies virus glycoprotein G ectodomain in Sf9 insect cells. *Biotech.*, vol 9, article number 385. https://doi.org/10.1007/s13205-019-1920-4
8. Li X., Luo J., Wang S., Shen Y., Qiu Y., Wang X., Deng X., Liu X., Bao W., Liu P., Zhou J., Ding C., Ma Z. (2010) Engineering, expression, and immuno-characterization of recombinant protein comprising multi-neutralization sites of rabies virus glycoprotein. *Protein Expression and Purification*, vol. 70, no. 2, pp. pp. 179-183. https://doi.org/10.1016/j.pep.2009.09.005
9. Das A., Bysack A., Raghuraman H. (2021) Effectiveness of dual-detergent strategy using Triton X-100 in membrane protein purification. *Biochemical and Biophysical Research Communications*, vol. 578, pp. 122–128. https://doi.org/10.1016/j.bbrc.2021.09.031
10. Geiger T., Clarke S. (1987) Deamidation, isomerization, and racemization at asparaginyl and aspartyl residues in peptides. Succinimide-linked reactions that contribute to protein degradation. *Journal of Biological Chemistry,* vol. 262, no. 2, pp. 785–794. https://doi.org/10.1016/S0021-9258(19)75855-4
11. Gaudin Y. (2000) Rabies virus-induced membrane fusion pathway. *Journal of Cell Biology*, vol. 150, no. 3, pp. 601–612. https://doi.org/10.1083/jcb.150.3.601
12. Pan L.Q., Xie Z.M., Tang X.J., M. Wu, Wang F.R., Naranmandura H., Chen S.Q. (2013) Engineering and refolding of a novel trimeric fusion protein TRAIL-collagen XVIII NC1. *Appl Microbiol Biotechnol.*, vol. 97, no 16, pp. 7253-7264. https://doi.org/10.1007/s00253-012-4604-0
13. Singh S.M., Panda A.K. (2005) Solubilization and refolding of bacterial inclusion body proteins. *Journal of Bioscience and Bioengineering*, vol. 99, no. 4, pp. 303–310. https://doi.org/10.1263/jbb.99.303

14. Yang F., Lin S., Ye F., Yang J., Qi J., Chen Z., et al. (2020) Structural analysis of rabies virus glycoprotein reveals pH-dependent conformational changes and interactions with a neutralizing antibody. *Cell Host & Microbe*, vol. 27, no. 3, pp. 441–453. https://doi.org/10.1016/j.chom. 2019.12.012

15. Berkmen M. (2012) Production of disulfide-bonded proteins in Escherichia coli. *Protein Expression and Purification*, vol. 82, no. 1, pp. 240–251. https://doi.org/10.1016/j.pep.2011.10.009

16. Lipinszki Z., Vernyik V., Farago N., Sari T., Puskas L.G., Blattner F.R., Posfai G., Gyorfy Z. (2018) Enhancing the Translational Capacity of E. coli by Resolving the Codon Bias. *ACS Synthetic Biology*, vol. 7, no 11, pp. 2656-2664. https://doi.org/10.1021/acssynbio.8b00332

17. Bhatwa A., Wang W., Hassan Y.I., Abraham N., Li X.-Z.,Zhou T. (2021) Challenges associated with the formation of recombinant protein inclusion bodies in *Escherichia coli* and strategies to address them for industrial applications. *Front. Bioeng. Biotechnol*., vol 9, article 630551. https://doi.org/10.3389/fbioe.2021.630551

18. Hemamalini N., Ezhilmathi S., Mercy Angela A. (2019). Recombinant protein expression optimization in Escherichia coli: A review. *Indian Journal of Animal Research*, vol 54, no 6, pp. 653-660. doi: 10.18805/ijar.B-3808

19. Baneyx F., Mujacic M. (2004) Recombinant protein folding and misfolding in Escherichia coli. *Nature Biotechnology*, vol. 22, no. 11, pp. 1399–1408. https://doi.org/10.1038/nbt1029

20. Sahdev S., Khattar S.K., Saini K.S. (2008) Production of active eukaryotic proteins through bacterial expression systems: a review of the existing biotechnology strategies. *Microbial Cell Factories*, vol. 7, no 1-2, pp. 249-264. https://doi.org/10.1007/s11010-007-9603-6

21. Chen R. (2012) Bacterial expression systems for recombinant protein production: E. coli and beyond. *Protein & Cell*, vol. 3, no. 12, pp. 934–947. https://doi.org/10.1016/j.biotechadv.2011.09.013

22. Arakawa T., Ejima D., Tsumoto K., Obeyama N., Tanaka Y., Kita Y., Timasheff S.N. (2007) Suppression of protein interactions by arginine: A proposed mechanism of the arginine effects. *Biophysical Chemistry*, vol. 127, no. 1–2, pp. 1–8. https://doi.org/10.1016/j.bpc.2006.12.007

23. Golovanov A.P., Hautbergue G.M., Wilson S.A., Lian L.-Y. (2004) A simple method for improving protein solubility and long-term stability. *Journal of the American Chemical Society*, vol. 126, no. 29, pp. 8933–8939. https://doi.org/10.1021/ja049297h

24. Maeda Y., Idehara M., Imoto T. (1995) Effective renaturation of reduced lysozyme by gentle removal of urea. *Protein Engineering, Design and Selection*, vol. 8, no. 2, pp. 201–205. https://doi.org/10.1093/protein/8.2.201

25. De-Simone S.G.; Gomes L.R.; Napoleão-Pêgo P.; LechugaG.C.; de Pina J.S.; da Silva F.R. (2021) epitope mapping of the diphtheria toxin and development of an ELISA-specific diagnostic assay. *Vaccines*, vol 9, no 4, Article 313. https://doi.org/10.3390/vaccines9040313

***Information about authors:***

*Gulshat A. Bayandy – M.Sc., PhD Student, Department of Molecular Biology and Genetics, Faculty of Biology and Biotechnology, Al-Farabi Kazakh National University (Almaty, Kazakhstan, e-mail: bayandy.gulshat92@gmail.com).*

*Nuraiym B. Baltakhozha – M.Sc., PhD Student, Department of Molecular Biology and Genetics, Faculty of Biology and Biotechnology, Al-Farabi Kazakh National University (Almaty, Kazakhstan, e-mail: baltakhozhanuraiym@mail.ru).*

*Khamida E. Yerkin – M.Sc., Research Intern, Scientific Research Institute of Biology and Biotechnology Problems, Al-Farabi Kazakh National University (Almaty, Kazakhstan, e-mail: e-mail: khamida.yerkin@gmail.com).*

*Kuralai B. Nurpeis – Bachelor's Student, Department of Molecular Biology and Genetics, Faculty of Biology and Biotechnology, Al-Farabi Kazakh National University (Almaty, Kazakhstan, e-mail: kukalai2004@gmail.com).*

*Gulzat N. Sailauova – Bachelor's Student, Department of Molecular Biology and Genetics, Faculty of Biology and Biotechnology, Al-Farabi Kazakh National University (Almaty, Kazakhstan, e-mail: saylauova04@mail.ru).*

*Izat T. Smekenov – PhD, Senior Lecturer, Department of Molecular Biology and Genetics, Faculty of Biology and Biotechnology, Al-Farabi Kazakh National University (Almaty, Kazakhstan, e-mail: smekenovizat@gmail.com).*

*Amangeldy A. Bissenbaev – Doctor of Biological Sciences, Professor, Department of Molecular Biology and Genetics, Faculty of Biology and Biotechnology, Al-Farabi Kazakh National University (Almaty, Kazakhstan, e-mail: amangeldy.bisenbaev@kaznu.kz).*

IRSTI 62.09.39; 62.01.73 https://doi.org/10.26577/IJBCh20251823

**T. Maryyam**[1], **S. Rahayu**[2], **D. Sukmawati**[2], **A.H. Anvar**[3],
**H.A. Shakir**[4], **M. Khan**[4], **J. Ul-Haq**[1], **M. Irfan**[1*]

[1] University of Sargodha, Sargodha, Pakistan
[2] State University of Jakarta, Jakarta, Indonesia
[3] Khazar University, Baku, Azerbaijan
[4] University of the Punjab, Lahore, Pakistan
*e-mail: Irfan.ashraf@uos.edu.pk

*(Received 01 December 2025; received in revised form 22 December 2025; accepted 26 December 2025)*

# Bibliometric and co-occurrence study of the production of cellulase from Bacillus (2000–2025)

**Abstract:** Cellulase refers to a group of enzymes that can break down cellulose, the most widespread organic polymer on Earth. It is one of the most important industrial enzymes due to its application in the production of valuable products such as biofuels, papers and textiles. Many microorganisms naturally produce cellulase, including *Bacillus* species. This study presents detailed bibliometric analysis of *Bacillus* cellulase. The core objective of this study is to provide global research trends related to *Bacillus* cellulase. It highlights leading authors, institutions, countries and sources that have major contributions in this area of research. The Scopus Dataset of 2212 documents was included for analysis. VOSviewer and Biblioshiny software were employed for bibliometric analysis and visualization. The most prolific author was Zhang Y. with highest number of publications (45) and citations. China ranked first among top contributing countries, followed by India with second position. This study will help researchers in understanding global research trends on *Bacillus* cellulase.

**Keywords:** *Bacillus*, cellulase, Bibliometric study, VOSviewer, Biblioshiny.

## Introduction

Enzymes are special proteins that catalyze metabolic processes in living organisms. Hence, enzymes are very essential for sustaining life [1]. Their applications extend beyond biological systems to various industrial processes. Enzymes are utilized in medical diagnostics, waste treatments, food production, and chemical synthesis [2]. Cellulases are a group of enzymes which are produced by many living organisms such as fungi, bacteria and algae [3]. They degrade cellulose which is the most abundant biological mass on earth [4]. Cellulase is known to be one of the most valuable enzymes that is used in textile, paper , detergent, food and feed industries [5]. One of the key industrial uses of cellulase enzymes is in the production of biofuels [6].

Cellulose is considered as the most abundant natural biopolymer on Earth. It is found as a key structural element of plant cell wall in the form of lignocellulose [7, 8]. Cellulases are enzymes that can degrade cellulose in lignocellulosic biomass. Thus, it plays a crucial role in conversion of plant waste into useful products like sugars and biofuels [9, 10]. As lignocellulosic biomass is the alternative of fossil fuels and can be used in the production of Biofuels. Microorganisms including bacteria, fungi, and actinomycetes are capable of producing cellulases that can be utilized in the degradation of biomass. Bacterial Cellulases are reported to have higher growth rate and versatility in genetic composition which makes them advantageous [11].

As majority of microorganisms have been reported for their cellulolytic potential. Among them *Bacillus* species have higher growth rate and can be easily genetically engineered [13, 14]. Furthermore, cellulases produced from *Bacillus* species are stable and can withstand a broad range of temperatures (30 to 100 °C) and pH levels (pH 8-10) [15]. Furthermore, enzyme production in *Bacillus* species can be improved as they are amenable to genetic engineering. These species can also survive in varying environmental conditions [16]. *Bacillus* strains are identified as good sources of cellulase enzymes. These strains have been isolated from many sources including compost and soil. *Bacillus* species, along with other bacteria like *Pseudomonas* and *Klebsiella* produce cellulases and play role in biodegradation of organic materials in compost [17]. Thus, *Bacillus* species hold significant importance as promising sources of cellulases and hemicellulases, enzymes

© 2025 al-Farabi Kazakh National University

crucial for lignocellulosic biomass degradation. In comparison with fungi, these bacteria are more efficient in productivity ~~[18].~~ In 2019, Manzum and Mamun have demonstrated the potential of *Bacillus* isolates from soil to produce cellulase. In their study, *Bacillus* bacteria were isolated from 24 soil samples and some isolates showed enzyme activity up to 0.17 U/ml. One isolate, 1RW, showed the highest cellulase activity and was identified as likely being *Bacillus licheniformis* or *Bacillus subtilis* [5] .

Research on Bacillus cellulase has made significant strides. Various studies have been conducted focusing on optimizing fermentation conditions for cellulase enzyme production from *Bacillus sp.* [19-21]. Islam et al.[22] reported that maximum cellulase production occurred at pH 3.5, 35°C, and 150-rpm agitation after 24 hours. Due to optimized conditions, enzyme yield was increased. While, highest enzyme activity was observed at pH 5.5 and 50°C. Hence, they are suitable for industrial uses in biomass conversion. Research efforts have also been made to improve Bacillus strains. Ega et al [23]. improved cellulase production in *Bacillus subtilis* VS15 through genome shuffling. They created mutant strains of *Bacillus subtilis* VS15 by mutagenesis and then combined them through protoplast fusion.

To the best of our knowledge, there is no bibliometric analysis has been done specifically on *Bacillus* cellulase research. Although, many scientific studies have been published on cellulase and *Bacillus* species. However, there is no complete summary that shows how this research has developed over time and which countries and authors have made major contributions in this field. In addition, the collaboration pattern between countries and authors is important to be identified. The purpose of this study is to fill this gap by performing a detailed bibliometric analysis on *Bacillus* cellulase from the year 2000 to 2025. This study will provide an overview of global research trends, prolific authors and countries, top journals and most frequent keywords in the field of *Bacillus* cellulase. Moreover, this analysis will develop a roadmap to assist future researchers.

## Materials and methods

The first stage in the bibliometric analysis was data collection. For this purpose, the Scopus database (www.scopus.com) was used, as it is the comprehensive and internationally recognized source of scientific literature. To retrieve relevant publications specific keywords related to the research topic were used. These keywords included "cellulase", "bacteria", "bacterial cellulase", "microbial cellulase". In the Scopus search bar, these keywords were entered using appropriate Boolean operators such as AND and OR to combine terms and refine results (e.g., "cellulose" AND "bacteria"). Data was retrieved on 20 June 2025, spanning publications from 2000 to 2025. Data was refined to narrow down the search results and select the most relevant articles for the study. Only research publications and review studies were included in the analysis. The following final query was entered into the main search bar of the Scopus database:

TITLE-ABS-KEY ("*Bacillus*" AND "cellulase") AND PUYEAR > 1999 AND PUBYEAR < 2026 AND (LIMIT-TO (SRCTYPE , "j")) AND (LIMIT-TO (PUBSTAGE , "final")) AND (EXCLUDE (SUBJAREA , "PHYS") OR EXCLUDE (SUBJAREA , "COMP") OR EXCLUDE (SUBJAREA , "EART") OR EXCLUDE (SUBJAREA , "ECON") OR EXCLUDE (SUBJAREA , "NURS") OR EXCLUDE (SUBJAREA , "MATH") OR EXCLUDE (SUBJAREA , "SOCI") OR EXCLUDE (SUBJAREA , "HEAL") OR EXCLUDE (SUBJAREA , "BUSI") OR EXCLUDE (SUBJAREA , "ARTS") OR EXCLUDE (SUBJAREA , "DECI")) AND (LIMIT-TO (DOCTYPE, "ar") OR LIMIT-TO (DOCTYPE , "re")) AND (LIMIT-TO (LANGUAGE , "English"))

After refining the dataset, the entire list of resulting 2256 documents was downloaded in three different formats: BibTeX (.bib), CSV (.csv) and plain Text (.txt). These formats were used in different softwares for analysis.

In the next step, preliminary dataset was imported into EndNote to perform duplicate check. EndNote identified and removed duplicates based on author, year and title. Duplicate records were found. Then, the titles and keywords of the documents were reviewed to assess relevance. This step was important for eliminating articles that were irrelevant to the research topic. Out of 2256 documents, 44 were excluded. The resulting dataset was then used for further analysis. This study used MS Excel, R studio, Biblioshiney and VOSviewer software to conduct bibliometric analysis and data visualization.

The dataset was analyzed using version 1.6.20 VOSviewer by uploading *.csv* format of the data. VOSviewer can be used to generate co-authorship network between authors and countries that collaborate in the specific research area. It can also establish networks of scientific publications, SCIENTIFIC journals, keywords, or terms. This study also employed R studio for conducting bibliometric analysis and visualization. R studio in an open-source software. The bibliometric analysis was undertaken through utilizing packages in R studio which are "bibliometrix" and "bibliometrixData". These packages enabled the execution of Biblioshiney software, wich was used in order to analyze and visualize the data.

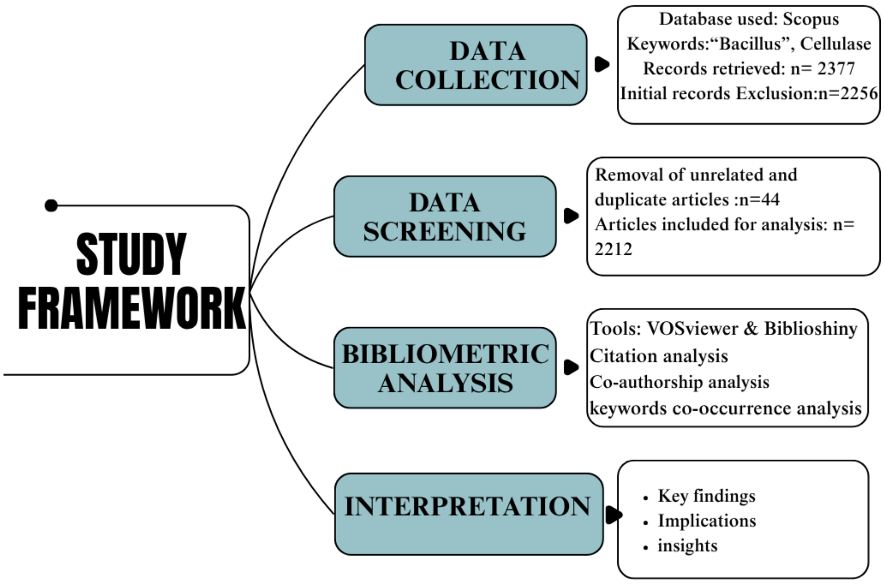

**Figure 1 –** Flow diagram of methodology of bibliometric and co-occurance study of the production of cellulose from Bacillus (2000-2025

## Results and discussion

Results of bibliometric analysis include publication trends, productive authors and countries, and Potential journals. Moreover, co-authorship networks among authors and countries have also been discussed. The descriptive analysis of the chosen data is given in Table 1. The analysis was conducted using the Meta data of 2212 articles from the period 2001-2025. The number of publications is increasing every year, with an annual growth rate of 7.16%. This shows the ongoing interest in this research field.

**Table 1 –** Main information about the Scopus dataset regarding cellulase production by Bacillus species (2000-2025)

| Description | Results |
|---|---|
| Timespan | 2000-2025 |
| Sources | 651 |
| Documents | 2212 |
| Annual Growth Rate | 7.16% |
| **Document Types** | |
| Research Articles | 2106 |
| Review Articles | 106 |
| **Authors** | |
| Total | 7913 |
| Authors of single-authored docs | 35 |
| **Authors Collaboration** | |
| Average no. of authors (Each Doc.) | 5.57 |
| International co-authorships, % | 22.06 |

### *1.1. Analysis of annual scientific production (2000–2025)*

By analyzing publication trends in topic of Bacillus cellulase, it was observed that number of documents were increased over the years, which indicates a growing interest in research. Figure 2 shows the annual scientific production from 2000 to 2025. It can be observed that scientific activity was quite low in the early 2000s, with fewer than 40 articles published each year. This phase represents the early developmental stage. It was also observed that scientific production increased between 2010 and 2018, from 40 to 118 publications. This steady growth indicates that more researchers were getting involved in the topic. A notable acceleration in publications output was observed after 2019. The most productive years were observed between 2020 and 2024. In 2021 and 2023, 216 publications were recorded, while 2022 – 199 documents. Production reached its peak in 2024, where 258 articles were published in a single year. This sharp rise in recent years indicates that cellulase enzyme research has become very important and active. The plot shows decline in 2025 with 107 articles. This is likely not because interest in the topic has increased. It is more likely that the data for 2025 is not yet complete in the database, as the year is still ongoing at the time of analysis

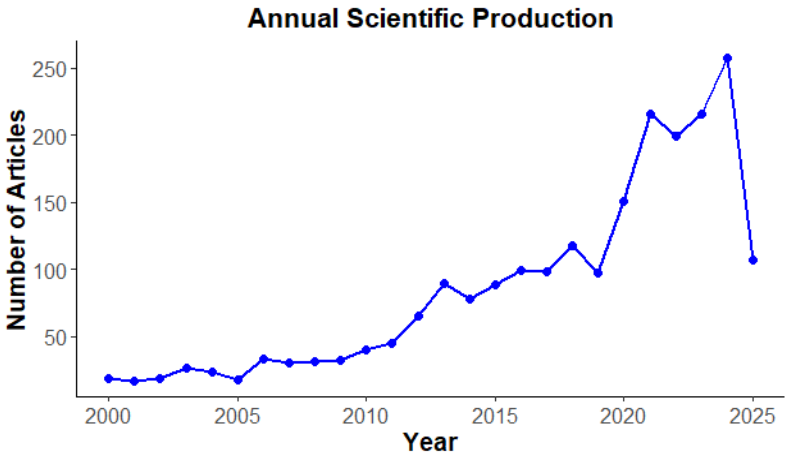

**Figure 2** – Number of articles published per year on the Bacillus cellulase by Scopus database (2000-2025)

### *1.2. Most prolific authors*

Figure 3 presents the leading authors who have published the most articles in the field of Bacillus cellulase. Among them Zhang Y. is the top contributing author with 45 publications. Whang Y. contributed 41 articles and stands at the second.

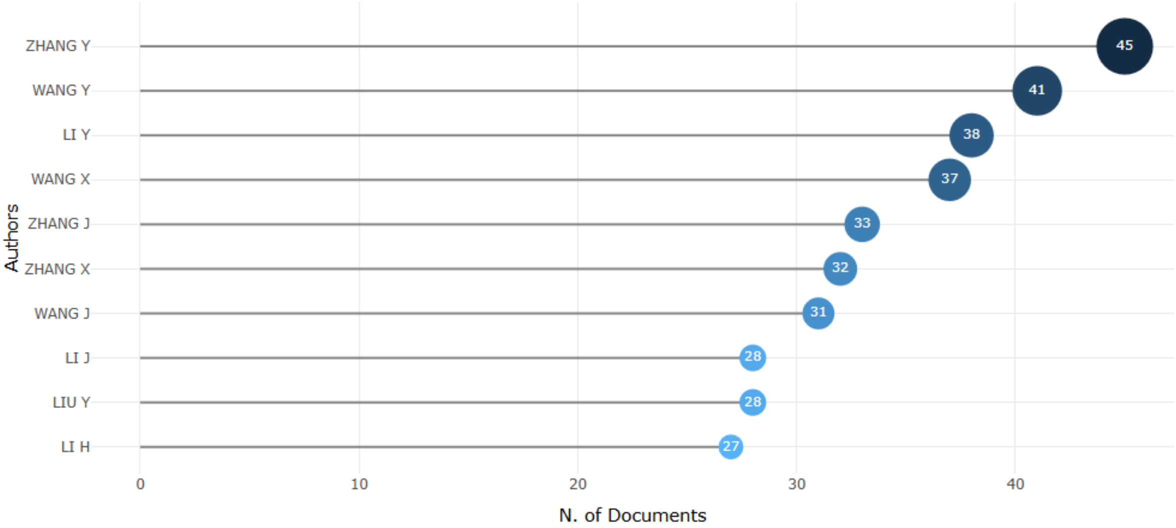

**Figure 3** – Most productive authors on basis of publications number about Bacillus cellulase by Scopus database (2000–2025)

Table 2 includes the additional measures in deciding the top 10 most productive authors who actively participated in research area of Bacillus cellulase. A total of 7913 authors have contributed to the research in this domain. The top authors were determined based on key indicators such as number of publications, h-index, and total citations. These measures are essential to understand both the productivity and the scientific impact of each author

**Table 2** – Impact metrics of top contributing authors in field of Bacillus cellulase by Scopus database (2000–2025)

| Authors | Number of publications | Articles fractionalized | h index | Total citations |
|---|---|---|---|---|
| Zhang Y. | 45 | 6.67 | 17 | 958 |
| Wang Y. | 41 | 6.57 | 17 | 958 |
| Li Y. | 38 | 5.47 | 17 | 699 |
| Wang X. | 37 | 5.16 | 15 | 802 |
| Zhang J. | 33 | 4.77 | 14 | 420 |
| Wang J. | 31 | 4.51 | 10 | 716 |
| Kumar V. | 18 | 4.30 | 13 | 428 |
| Zhang X. | 32 | 4.28 | 12 | 671 |
| Li J. | 28 | 4.20 | 14 | 714 |
| Liu Y. | 28 | 3.59 | 12 | 375 |

Zhang Y. is ranked first among the top 10 most prolific authors in the field of *Bacillus* cellulase research. He has the highest number of publications (45) and his work has been widely cited. h-index has reached 17, which shows his research is both productive and well recognized. The second author, Wang Y. follows closely with 41 publications and an h-index as 17, similar to Zhang Y. It means both authors have similar level of citation impact. Li Y is the third most productive author, with 38 publications and an h-index of 17, which is the same as the top two authors. This suggests that his work is equally impactful. Wang X. ranks fourth with 37 publications and an h-index of 15, which also indicates a strong citation impact. Interestingly, Wang X. has received 802 total citations, which is higher than Li Y, despite having one fewer publication and a slightly lower h-index. This means X. Wang's individual papers may have received more citations on average, highlighting the relevance and impact of their research. The subsequent authors include Zhang J., Wang J., Kumar V., Zhang X., Li J., Liu Y. They have also made significant contributions in the field and appear among the top 10. Overall, Zhang Y. is the main contributor in this research area.

### *1.3. Potential journals*

Analysis of academic journals can be useful for scholars and researchers to find the most active and latest sources. The potential journals that published the most articles on Bacillus celulase have been illustrated here. To identify the most influential journals in the research area, Bradford's Law was applied. Bradford's Law used in bibliometric analysis helps identify core journals by dividing journals into 3 zones: A core zone with few but highly productive sources; a second zone with moderately producing sources, and a third zone with many sources that produce relatively few relevant journals.

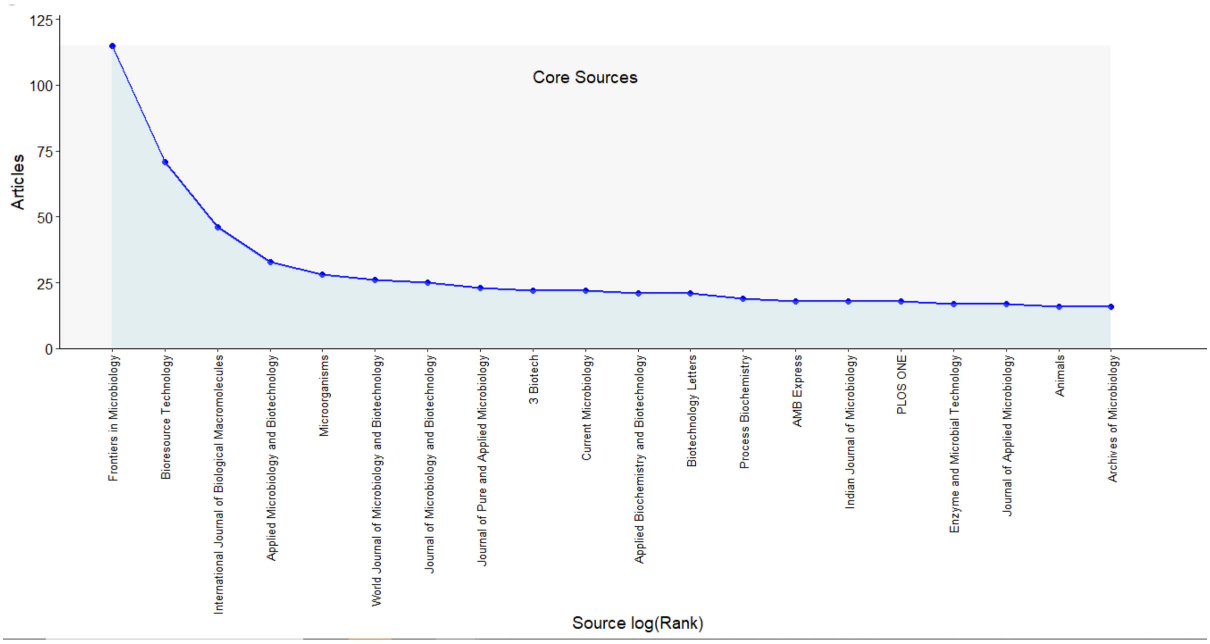

**Figure 4** – Distribution of Core Sources (zone 1) about Bacillus cellulase by Scopus database (2000–2025) according to Bradford's Law

There is total 651 sources in the dataset. The statistical data reveals that not all sources are equally significant. In this study only the topmost productive sources have been presented, who have the most data published in Bacillus cellulase domain. As per Bradford's law, zone 1 represents the core sources that are most productive and have the highest number of publications on Bacillus cellulase. Many other journals have relatively fewer publications and come under subsequent zones such as zone 1 and zone 2. Figure 4 shows the core sources that come under zone 1 in accordance with Bradford's law. Zone 1 contains 20 sources from the dataset. The "Frontiers in Microbiology" holds the record of highest productive journal.

**Table 3** – Journal ranking based on Bradford's Law with publications about Bacillus cellulase by Scopus database (2000–2025) according to Bradford's Law

| **Source** | Rank | Frequency | Cumulative frequency | Zone |
|---|---|---|---|---|
| Frontiers in Microbiology | 1 | 115 | 115 | 1 |
| Bioresource Technology | 2 | 71 | 186 | 1 |
| International Journal of Biological Macromolecules | 3 | 46 | 232 | 1 |
| Applied Microbiology and Biotechnology | 4 | 33 | 265 | 1 |
| Microorganisms | 5 | 28 | 293 | 1 |
| World Journal of Microbiology and Biotechnology | 6 | 26 | 319 | 1 |
| Journal of Microbiology and Biotechnology | 7 | 25 | 344 | 1 |
| Journal of pure and applied Microbiology | 8 | 23 | 367 | 1 |
| BioTech | 9 | 22 | 389 | 1 |
| Current Microbiology | 10 | 22 | 411 | 1 |

### *1.4. Top contributing countries and institutions*

Figure 6 illustrates the top 10 countries who have produced maximum number of articles on research area of Bacillus cellulase, spanning the duration from 2000 to 2025. Based on publications count, the China stands at the top of list with the highest number of publications (1484). followed by India with 1039 publications. Among the top ten productive countries, Only CHINA and INDIA has published more than 1000 articles. This suggests the significant contribution of these countries in the research. South Korea secured the third position with 313 papers. This distribution indicates that Asian countries, especially China and India, are at the forefront of research in this area. Overall, this analysis was performed to highlight global interest in the field.

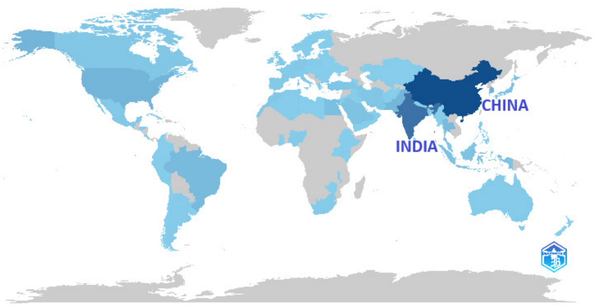

**Figure 5** – Country wise scientific production on Bacillus cellulase by Scopus database (2000–2025), where darker colors represent higher scientific output, notably India and China

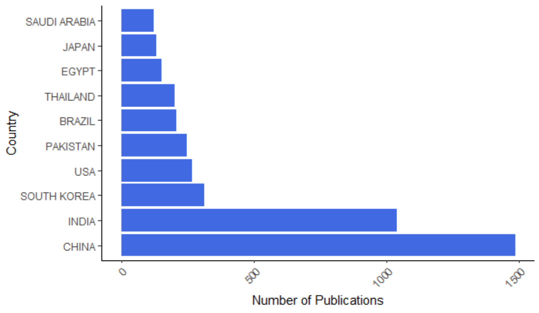

**Figure 6** – Country-wise distribution of scientific publications on *Bacillus* cellulase by Scopus database (2000–2025)

This study highlights the most productive affiliations as well. Analyzing the most influential institution shows where the key research developments have taken place. In Figure 7 are shown the top most influential institutions having significant contribution in the topic. Institutions were arranged based on total number of publications and were identified 10 leaders. These top institutions with the most publications included three Universities from China and two from Pakistan. King Saud University (Saudi Arabia) and University of Karachi (Pakistan) lead with 33 publications each, followed closely by Kurukshetra University (India) and Chiang Mai University (Thailand) with 29 each.

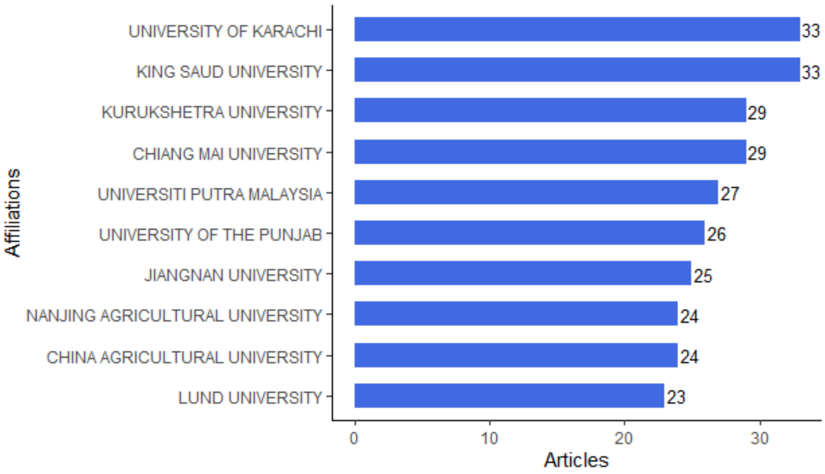

**Figure 7** – Top 10 prominent institutions having publications on Bacillus cellulase by Scopus database (2000–2025)

To avoid confusion, it is important to explain that scientific production by country and by institution are two separate aspects in bibliometric analysis. Country-level data shows how many publications come from each country overall, while institution-level data highlights the contributions of specific universities or research centers. For example, a country may have many institutions publishing moderately, or a few publishing heavily. Therefore, both types of analysis are included to provide a complete view of research output.

### *1.5. Highly cited documents*

Among the total of 2212 documents, top 10 most cited publications were collected using Biblioshiney software. This analysis is important as it emphasizes the most impactful research in the field. The most cited article in data set with 1027 citations was "Silage review: Recent advances and future uses of silage additives", published in Journal of dairy science in the year 2018 by .

### *1.6. Most Frequent Keywords*

The word cloud (Figure 8) of the most frequently used words in the topic of Bacillus cellualse was obtained from Biblioshiney. During the data analysis prominent keywords were identified. The keyword analysis identifies research trends and maps the focus areas. Keywords map also guide future researchers to focus on specific areas. In the Figure 8, it can be observed that the keyword "cellulase" emerged as the most frequently used word with the highest frequency of 1308. As it is central to the research field. The next terms are "article" and nonhuman" which are more general metadata terms, but they reflect the nature of the literature as most studies are based on nonhuman organisms. Among the discovered keywords, "Bacillus" and "*Bacillus subtilis*" are also prominent. These bacteria are the primary subjects and important sources of cellulase production. Overall, "Cellulase" and "Bacillus" are the core focus of the research topic's discourse.

**Table 4 –** Top 10 most cited publications related to the field of Bacillus cellulase by Scopus database (2000–2025)

| Title | First author | Year | Journal | Total citations | Refrence |
|---|---|---|---|---|---|
| Silage review: Recent advances and future uses of silage additives | Muck Re | 2018 | Journal of dairy science | 1027 | [24] |
| Biofilms in the Food Industry: Health Aspects and Control Methods | Galié S | 2018 | Frontiers in Microbiology | 1026 | [25] |
| Microbial hemicellulases | Shallom D | 2003 | Current opinion in microbiology | 1012 | [26] |
| Biotechnology of Microbial Xylanases: Enzymology, Molecular Biology, and Application | Subramaniyan S | 2002 | Critical reviews in biotechnology | 1004 | [27] |
| *Bacillus*: A Biological Tool for Crop Improvement through Bio-Molecular Changes in Adverse Environments | Radhakrishnan R | 2017 | Frontiers in physiology | 749 | [28] |
| Extremophiles as a source for novel enzymes | Van Den Burg B | 2003 | Current opinion in microbiology | 851 | [29] |
| The prospects of cellulase-producing bacteria for the bioconversion of lignocellulosic biomass | Maki M | 2009 | International journal of biological sciences | 843 | [30] |
| *Bacillus subtilis* as cell factory for pharmaceutical proteins: a biotechnological approach to optimize the host organism | Westers L | 2004 | Biochimica et Biophysica Acta (BBA)- Molecular Cell Research | 695 | [31] |
| Purification and characterization of cellulase produced by *Bacillus amyoliquefaciens* DL-3 utilizing rice hull | Lee Yj | 2008 | Biosource Technology | 525 | [32] |
| Improved lignocellulose conversion to biofuels with thermophilic bacteria and thermostable enzymes | Bhalla A | 2013 | Biosource Technology | 406 | [33] |

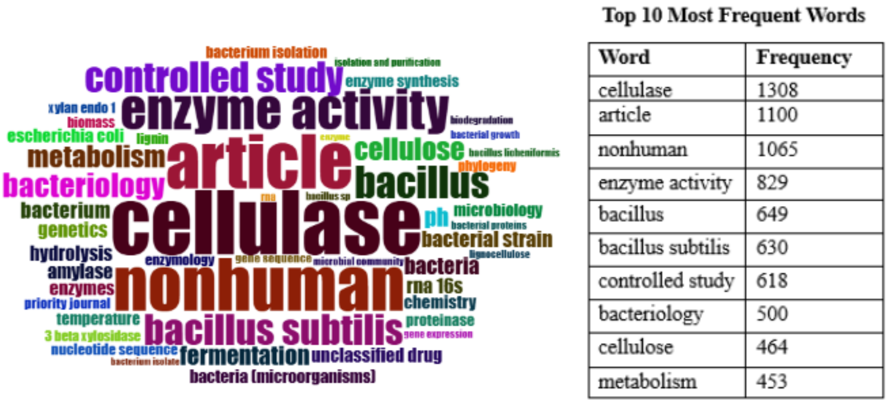

**Top 10 Most Frequent Words**

| Word | Frequency |
|---|---|
| cellulase | 1308 |
| article | 1100 |
| nonhuman | 1065 |
| enzyme activity | 829 |
| bacillus | 649 |
| bacillus subtilis | 630 |
| controlled study | 618 |
| bacteriology | 500 |
| cellulose | 464 |
| metabolism | 453 |

**Figure 8** – Word cloud of most frequently used author's keywords of publications related to the field of Bacillus cellulase in Scopus database (2000–2025)

### *1.7. Keywords co-occurrence analysis*

Co-occurrence of various keywords (Figure 9) shows how different topics are connected to each other. It is important part of bibliometric analysis and helps researchers to identify main topics in research field. The network on keywords reveals how different topics are related to each other. Researchers can also find research gaps in knowledge or areas that need more explanation.

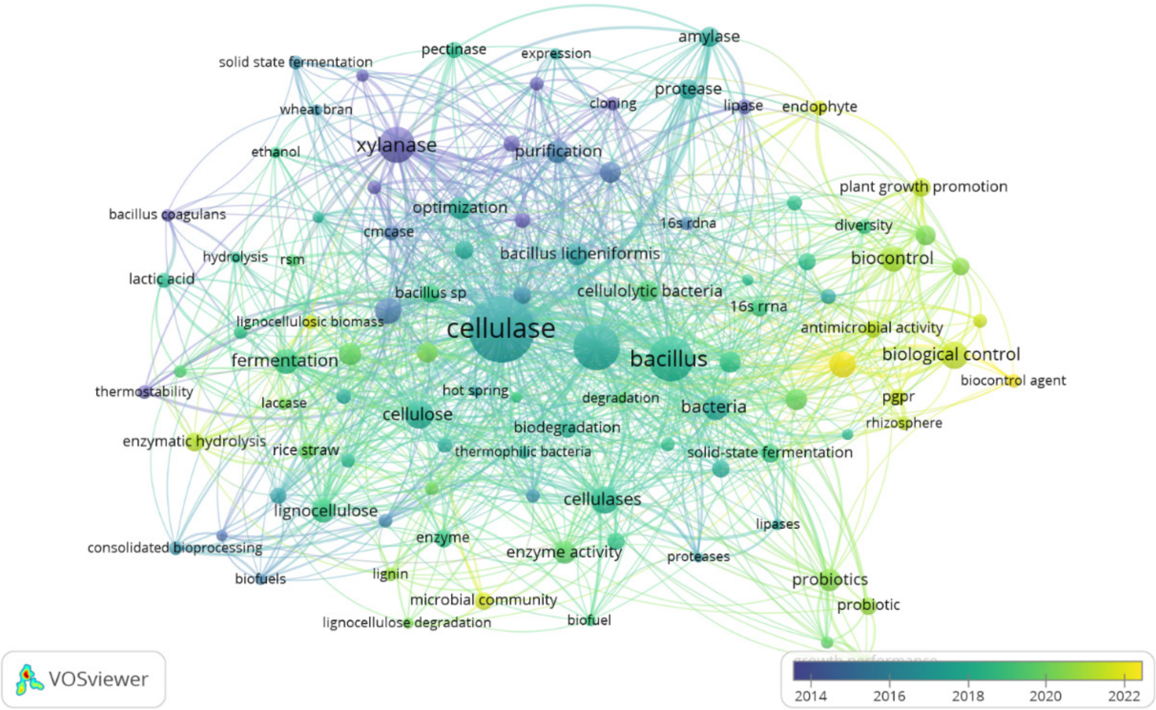

**Figure 9** – The Overlay visualization map of most frequently used author's keywords of publications related to the field of Bacillus cellulase in Scopus database (2000–2025)

## 4. Collaboration Analysis

Co-authorship analysis is an important part of bibliometric studies. It helps to understand how authors collaborate in a specific research field. A co-authorship network was constructed using VOS-viewer. In the network, authors who had published at least three documents were included. As a result, total of 424 authors met the threshold and were included in the visualization. Each circle (node) in the network represents an author and the size of the circle indicates the number of publications by that author. Larger node depicts the more publications of relevant author. The links between the circles indicate collaboration among authors. A cluster in a network is a group of authors with strong collaboration.

In the network visualization shown in Fig.10, there are six clusters of authors that relate to each other on Bacillus cellulase research. The green cluster is the largest, led by Qin Wensheng, who is strongly connected with authors such as Guo Haipeng, Chen Yuantong, and Chio Chonglong. This green cluster is linked with other clusters shown in purple and red clusters. These inter group connections suggest collaboration between different research groups. Two groups that are linked can have joint research projects.

Zhang Ying and Wang Xin are the main authors in the red cluster which shows that these two researchers play a key role in the collaborative work within this group. Other researchers in this cluster include Guo Wei, Wang Kui, and Liu Yun. A yellow cluster includes Yang Yuxin and Liu Gongwei, also working closely with each other. The blue cluster is led by Muhammad Sohail, showing intensive cooperation with authors such as Samy F. Mahmoud, Wang Li. Another light blue cluster, led by Afsheen Aman, is relatively small but showing significant collaboration.

Collaboration network is a visual map that depicts how countries work together in research field. This network is important because it shows global connections in research. In Figure 11, each Node (circle) represents a country. While connecting lines depict strength of co-authorship between countries. The size of node accounts for collaboration level. In the network, it can be observed that China has the largest node which shows its strong global collaborations. China and India are the top collaborating countries with strong collaboration

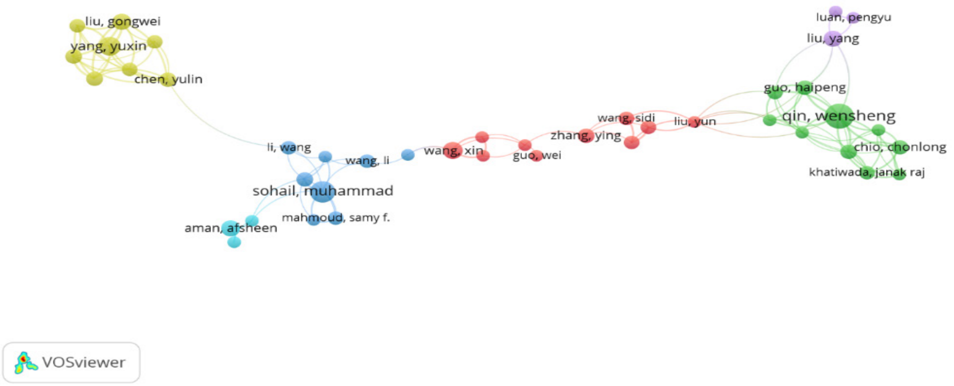

**Figure 10** – Co-authorship network among authors of publications related to the field of Bacillus cellulase in Scopus database (2000–2025)

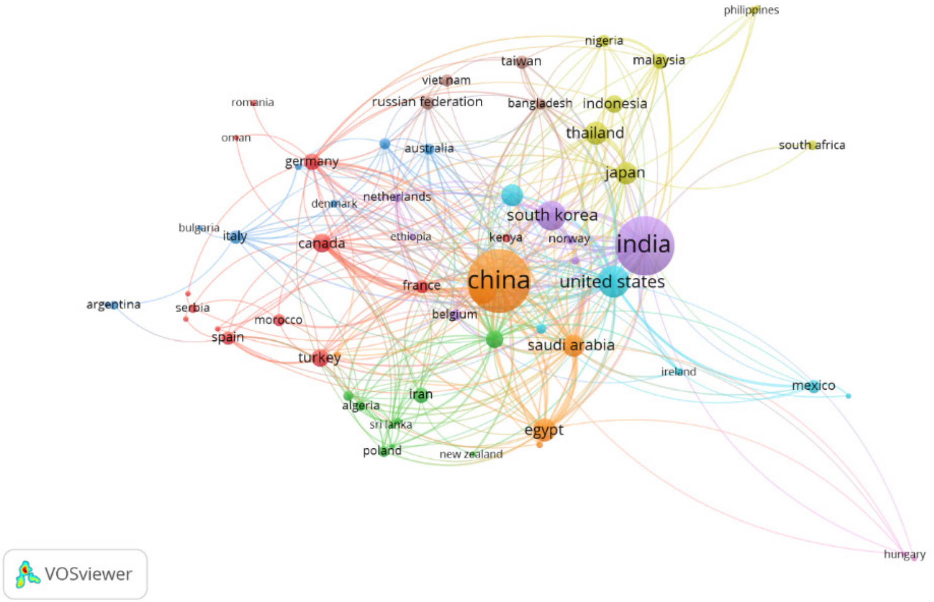

**Figure 11** – Collaboration network among countries of publications related to the field of Bacillus cellulase in Scopus database (2000–2025)

Clusters in the collaboration network represent groups of countries that have strong research collaboration. As China, Saudi Arabia and Egypt are in the same color cluster showing close connections. Out of 104 countries, only 63 were included in the network.

## 5. Limitations of the study

There are certain limitations related to this study which need to be mentioned. Firstly, the study utilized only one database (Scoupus) for data collection. Although Scopus is trusted and well recognized database. But there is a likelihood that some relevant publications indexed in other renowned databases such as Web of Science or Google Scholar might be missing in the dataset. This sampling bias may cause gaps in the analysis. Despite these limitations, this study provides a useful overview of global research trends on Bacillus cellulase.

## Conclusion

This study has provided the current status of research on Bacillus cellulase. The collaboration networks among authors and countries have also been presented. It was observed that research on this subject is continuously growing with every passing year. The duration of most recent years from 2020 and 2024 was the most active phase in conducting research. Bibliometric and co-occurrence analysis have identified trends in research and research gaps that need to be addressed. The global research interest in the topic was revealed by identifying contributions of researchers and countries in the field. This study acknowledged the impact of prominent authors, countries, affiliations in progressing the field of Bacillus cellulase. Overall, this analysis contributed to the existing knowledge and will assist scholars and future scholars.

Moreover, the results of this bibliometric analysis offer a systematic basis for future research endeavors to focus on more application-based and interdisciplinary research. Greater collaboration between the academic and industrial communities could help expedite technological development and subsequent applications of Bacillus cellulase in the biofuel industry, waste treatment, agriculture, and biotechnology. Future research endeavors should aim to experimentally verify and scale up research, as well as combine it with current biotechnological advances to fill the research gaps. The observation of publication trends and collaboration patterns will continue to be important for monitoring scientific developments. In this manner, bibliometric analyses, such as the current study, not only act as analytical tools but also as guides for the advancement of the field.

## Conflict of Interest

All authors are aware of the article's content and declare no conflict of interest.

## References

1. Lewis T., Stone W.L. (2023) Biochemistry, proteins enzymes. *StatPearls Publishing*. Available at: https://www.ncbi.nlm.nih.gov/sites/books/NBK554481/
2. Engel P.C. (2020) *Enzymes: A very short introduction*. Oxford University Press, vol. 661. https://doi.org/10.1093/actrade/9780198824985.001.0001
3. Patel K., Amaresan N. (2022) Mass multiplication, production cost analysis, and marketing of cellulase. In: *Industrial Microbiology Based Entrepreneurship: Making Money from Microbes*. Springer, pp. 37–50. https://doi.org/10.1007/978-981-19-6664-4_4
4. Atreya M.E. (2015) Engineering cellulase enzymes for bioenergy. *University of California, Berkeley*.
5. Manzum A.A., Mamun M.A.A. (2019) Isolation of *Bacillus* spp. bacteria from soil for production of cellulase. *Nepal Journal of Biotechnology*, vol. 6, no. 1, pp. 57–61. https://doi.org/10.3126/njb.v6i1.22338
6. Sachdeva D.V. (Year not specified) An insight into microbial cellulases.
7. Marinho E. (2025) Cellulose: A comprehensive review of its properties and applications. *Sustainable Chemistry and Environment*, vol. 11, article 100283. https://doi.org/10.1016/j.scenv.2025.100283
8. Dupree P., Cresswell R., Deralia P., et al. (2024) New insights into the structure of cellulose in plant cell walls. *Research Square* (Preprint). https://doi.org/10.21203/rs.3.rs-4970084/v1
9. Ilić N., Milić M., Beluhan S., et al. (2025) Cellulases: From lignocellulosic biomass to improved production. *Energies*, vol. 18, article 1002. https://doi.org/10.3390/en18021002
10. Srivastava S., Bhargava A. (2026) Application of cellulases in the enzymatic hydrolysis of lignocellulosic biomass. In: *Bioproducts from Lignocellulosic Biomass*, vol. 1, Woodhead Series in Bioenergy, pp. 77–95. https://doi.org/10.1016/B978-0-443-21604-6.00002-4
11. Chavda N.R., Panchal K.S., Chaudhary R.K., et al. (2021) Bacterial cellulases and its applications: A review. *Biochemical Analysis and Biochemistry*, vol. 10, no. 8, article 400.
12. Amer A., Bibi A. (2018) Fungal cellulase: Production and applications: A minireview. *LIFE: International Journal of Health and Life Sciences*, vol. 4, no. 1, pp. 19–36. https://hdl.handle.net/11573/1227140
13. Mohapatra S., Maity S., Dash H.R., et al. (2017) *Bacillus* and biopolymer: Prospects and challenges. *Biochemistry and Biophysics Reports*, vol. 12, pp. 206–213. https://doi.org/10.1016/j.bbrep.2017.10.001
14. Akinsemolu A.A., Onyeaka H., Odion S., et al. (2024) Exploring *Bacillus subtilis*: Ecology, biotechnological applications, and future prospects. *Journal of Basic Microbiology*. https://doi.org/10.1002/jobm.202300614
15. Bajaj B.K., et al. (2009) Partial purification and characterization of a highly thermostable and pH stable endoglucanase from a newly isolated *Bacillus* strain M-9. *Indian Journal of Chemical Technology*, vol. 16, pp. 382–387.
16. Zhou C., Zhou H., Li D., et al. (2020) Optimized expression and enhanced production of alkaline protease by genetically modified *Bacillus licheniformis* 2709. *Microbial Cell Factories*, vol. 19, pp. 1–13. https://doi.org/10.1186/s12934-020-01307-2
17. Amore A., Pepe O., Ventorino V., et al. (2020) Cellulolytic *Bacillus* strains from natural habitats: A review.
18. Kumari A., Kumar M., Bhoi B. (2024) Role of bacterial degradation in lignocellulosic biomass for biofuel production. In: *Valorization of Biomass Wastes for Environmental Sustainability*. Springer, pp. 303–315. https://doi.org/10.1007/978-3-031-52485-1_17

19. Singh J., Kaur P. (2012) Optimization of process parameters for cellulase production from *Bacillus* sp. JS14 using response surface methodology. *Brazilian Archives of Biology and Technology*, vol. 55, pp. 505–512. https://doi.org/10.1590/S1516-89132012000400004

20. Acharya S., Chaudhary A. (2012) Optimization of fermentation conditions for cellulase production by *Bacillus licheniformis* MVS1 and *Bacillus* sp. MVS3. *Brazilian Archives of Biology and Technology*, vol. 55, pp. 497–503. https://doi.org/10.1590/S1516-89132012000400003

21. Gozan M., Harahap A.F., Bakti C.P., et al. (2018) Optimization of cellulase production by *Bacillus* sp. BPPT CC RK2 using response surface methodology. *E3S Web of Conferences*. https://doi.org/10.1051/e3sconf/20186702051

22. Islam M., Sarkar P.K., Mohiuddin A.K.M., et al. (2019) Optimization of fermentation condition for cellulase enzyme production from *Bacillus* sp. *Malaysian Journal of Halal Research*, vol. 2, no. 2, pp. 19–24. https://doi.org/10.2478/mjhr-2019-0009

23. Ega S.L., Drendel G., Petrovski S., et al. (2020) Comparative analysis of structural variations due to genome shuffling of *Bacillus subtilis* VS15. *International Journal of Molecular Sciences*, vol. 21, no. 4, article 1299. https://doi.org/10.3390/ijms21041299

24. Muck R.E., Nadeau E.M.G., McAllister T.A., et al. (2018) Silage review: Recent advances and future uses of silage additives. *Journal of Dairy Science*, vol. 101, no. 5, pp. 3980–4000. https://doi.org/10.3168/jds.2017-13839

25. Galié S., García-Gutiérrez C., Miguélez E.M., et al. (2018) Biofilms in the food industry: Health aspects and control methods. *Frontiers in Microbiology*, vol. 9, article 898. https://doi.org/10.3389/fmicb.2018.00898

26. Shallom D., Shoham Y. (2003) Microbial hemicellulases. *Current Opinion in Microbiology*, vol. 6, no. 3, pp. 219–228. https://doi.org/10.1016/S1369-5274(03)00056-0

27. Subramaniyan S., Prema P. (2002) Biotechnology of microbial xylanases: Enzymology, molecular biology, and application. *Critical Reviews in Biotechnology*, vol. 22, no. 1, pp. 33–64. https://doi.org/10.1080/07388550290789450

28. Radhakrishnan R., Hashem A., Abd_Allah E.F. (2017) *Bacillus*: A biological tool for crop improvement. *Frontiers in Physiology*, vol. 8, article 667. https://doi.org/10.3389/fphys.2017.00667

29. Van den Burg B. (2003) Extremophiles as a source for novel enzymes. *Current Opinion in Microbiology*, vol. 6, no. 3, pp. 213–218. https://doi.org/10.1016/S1369-5274(03)00060-2

30. Maki M., Leung K.T., Qin W. (2009) Prospects of cellulase-producing bacteria for lignocellulosic bioconversion. *International Journal of Biological Sciences*, vol. 5, no. 5, pp. 500–516. https://doi.org/10.7150/ijbs.5.500

31. Westers L., Westers H., Quax W.J. (2004) *Bacillus subtilis* as a cell factory for pharmaceutical proteins. *Biochimica et Biophysica Acta*, vol. 1694, nos. 1–3, pp. 299–310. https://doi.org/10.1016/j.bbamcr.2004.02.011

32. Lee Y.-J., Kim B.-K., Lee B.-H., et al. (2008) Purification and characterization of cellulase from *Bacillus amyoliquefaciens* DL-3. *Bioresource Technology*, vol. 99, no. 2, pp. 378–386. https://doi.org/10.1016/j.biortech.2006.12.013

33. Bhalla A., Bansal N., Kumar S., Bischoff K.M., et al. (2013) Improved lignocellulose conversion with thermophilic bacteria. *Bioresource Technology*, vol. 128, pp. 751–759. https://doi.org/10.1016/j.biortech.2012.10.145

***Information about authors:***

*Tehreem Maryyam – Master Student, Department of Biotechnology, University of Sargodha, (Sargodha, Punjab, Pakistan, e-mail: maryyamtehreem@gmail.com)*

*Sri Rahayu – Associate Professor, Department of Biology, Faculty of Mathematics and Natural Sciences, State University of Jakarta (Jakarta, Indonesia, e-mail: sri.rahayu@unj.ac.id)*

*Dalia Sukmawati – Professor, Department of Biology, Faculty of Mathematics and Natural Sciences, State University of Jakarta (Jakarta, Indonesia, e-mail: dalia-sukmawati@unj.ac.id)*

*Afsana Huseynova Anvar – Lecturer, Department of Life Science, Khazar University (Baku, Azerbaijan, e-mail: afsanalab212@gmail.com)*

*Hafiz Abdullah Shakir – Associate Professor, Institute of Zoology, University of the Punjab (Lahore, Pakistan, e-mail: hashakir@yahoo.com)*

*Muhammad Khan – Associate Professor, Institute of Zoology, University of the Punjab (Lahore, Pakistan, e-mail: khan_zoologist@ymail.com)*

*Jabbar Ul-Haq – PhD, Assistant Professor, Department of Economics, University of Sargodha, (Sargodha, Punjab, Pakistan, e-mail: jabbar.ulhaq@uos.edu.pk)*

*Muhammad Irfan – Associate Professor, Master Student, Department of Biotechnology, University of Sargodha (Sargodha, Punjab, Pakistan, e-mail: Irfan.ashraf@uos.edu.pk)*

International Journal of Biology and Chemistry 18, № 2 (2025)

IRSTI 34.29.35 https://doi.org/10.26577/IJBCh20251824

M. Mussina[1], B. Tynybekov[1], G. Öz[2], A. Ydyrys[1, 3],
M. Nurtayeva[4], M. Imanaliyeva[3, 5*]

[1]Al-Farabi Kazakh National University, Almaty, Kazakhstan
[2]İstanbul Üniversitesi, İstanbul, Türkiye
[3]Biomedical Research Centre, Al-Farabi Kazakh National University, Almaty, Kazakhstan
[4]Communal Government Agency "Specialized Lyceum № 126", Almaty, Kazakhstan
[5]Kazakh Women's Teacher Training University, Almaty, Kazakhstan
*e-mail: moldirimanalieva19@gmail.com

*(Received 20 August 2025; received in revised form 08 December 2025; accepted 26 December 2025)*

# Environmental influence on the phytochemical composition of *Calligonum leucocladum* populations in Kazakhstan

**Abstract.** *Calligonum leucocladum (*Polygonaceae) is a characteristic shrub of arid and semi-arid regions of Central Asia, where plant survival is limited by scarce water and extreme temperature fluctuations. This study investigated the phytochemical profiles of three spatially separated populations of *C. leucocladum* collected from natural habitats in Kazakhstan. The results demonstrated the presence of various phenolic compounds, organic acids, and amino acids. Among them, artepillin C and caffeic acid phenethyl ester (CAPE) were detected in this species for the first time. Distinct differences in metabolite accumulation between populations were recorded. In particular, individuals from population P3, located in semi-arid mountainous terrain at an altitude of about 800 m above sea level, were characterised by increased concentrations of phenolic compounds, soluble carbohydrates and the osmoprotective amino acid proline. These population – specific metabolic features probably reflect biochemical adaptations to contrasting environmental influenc s. These results indicate that *C. leucocladum* is a valuable source of biologically active compounds, and variations in the composition of its metabolites are closely related to habitat conditions.

**Keywords:** *Calligonum leucocladum,* phenolic compounds, artepillin C, proline, pharmacological potential, metabolic adaptation.

## Introduction

*Calligonum leucocladum* is a perennial shrub of the Polygonaceae family, naturally distributed in arid and semi-arid areas of southern Kazakhstan and adjacent regions of Central Asia. This species is adapted to an environment characterised by low rainfall and high heat stress, and is known to accumulate a number of biologically active compounds of ecological and potential medical interest [1].

Within its natural range, *C. leucocladum* contributes to the functioning of desert ecosystems in several ways. Its well-developed root system stabilises loose sandy substrates and reduces wind and water erosion, which is a major factor in land degradation in these regions. By influencing soil structure and moisture retention in the rhizosphere, the plant can locally mitigate microclimatic conditions, including extreme surface temperatures. In addition, *C. leucocladum* supports elements of local biodiversity by providing habitat and food resources for insects, birds, and other fauna species [1]. Furthermore, it is important for the restoration of degraded landscapes, making it a key component of environmental rehabilitation programmes. The species' resistance to high temperatures and low humidity demonstrates its adaptive capabilities in addressing climate change issues. Successful examples of its use in ecosystem rehabilitation can be seen in the sandy regions of southern Kazakhstan, where plantations have significantly reduced land degradation [2].

The uniqueness of the species *C. leucocladum* from a pharmacognostic perspective is determined not only by the standard set of polyphenols and organic acids but also by the presence of specific secondary metabolites. Study reports the successful identification of previously undescribed structures in this plant, particularly derivatives of phenylethyl acid and catechol [3]. Preliminary data indicate that the isolated compounds exhibit pronounced biological activity, opening avenues for their study in the context of developing antioxidant, anti-inflammat -

© 2025 al-Farabi Kazakh National University

ry, and cytotoxic drugs. Other important compounds have also been found in the plant, including rutin, quercetin and chlorogenic acid, which are known for their medicinal properties [3]. In addition, the plant contains sugars and amino acids, which play an important role in metabolism. Quantitative studies have shown that the content of polymethoxyflavones in the leaves can be 20–30% higher than in the flowers. This chemical composition makes *C. leucocladum* a promising source of raw materials for the production of pharmaceuticals and functional foods [4]. It is also important to note that the chemical composition of the plant varies depending on the geographical location of the population, which highlights the need to study different populations [5].

Research on this plant opens unique perspectives for science and medicine. It is of great interest as a research object due to rich chemical composition, adaptation mechanisms, and broad spectrum of biological activity [6].

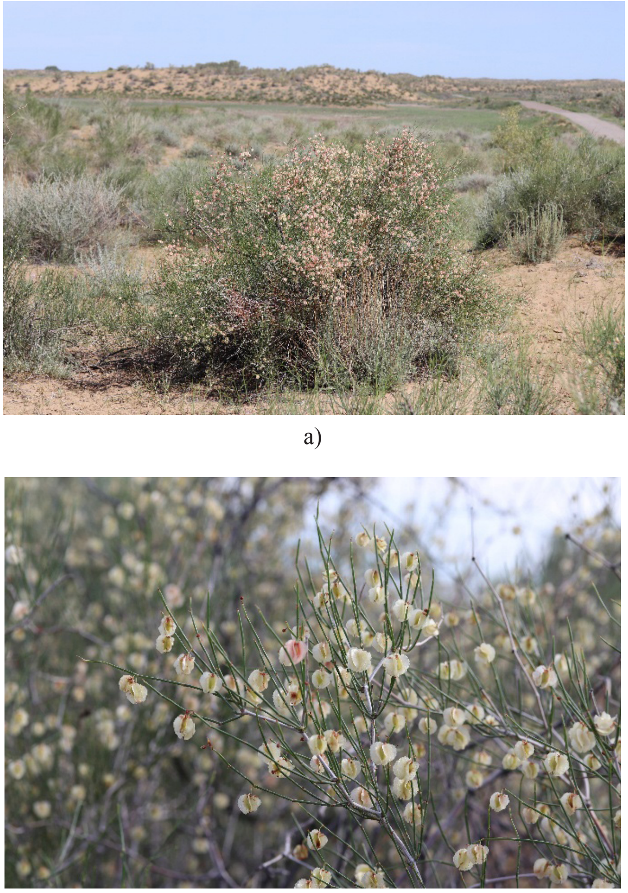
a)

b)

**Figure 1** – Morphological features of *C. leucocladum* general habit of the plant in its natural habitat; b) close-up view of branches and flowers

Future studies could focus on exploring the biosynthetic pathways of the plant's key compounds and investigating the interactions of its components with biological systems. Genetic analysis of various populations of this plant can shed light on intraspecific variability and mechanisms of adaptation to extreme environmental conditions [7]. The study of the pharmacological activity of *C. leucocladum* extracts on disease models will lay the foundation for the development of new drugs, which is particularly relevant for the medicine of the future [8-9].

Furthermore, attention should be given to developing sustainable cultivation methods for this plant, especially in degraded ecosystems. This will not only help preserve natural populations but also enable the use of this species for bioremediation, soil restoration, and maintaining ecological balance. Simultaneously, research into how climatic factors influence the plant's chemical composition is vital. Identifying these relationships will allow for the determination of optimal cultivation conditions, a prerequisite for its effective application in agriculture and pharmacology [10].

The plant we selected stands out among other species of the genus *Calligonum* due to its unique ability to survive under extreme conditions of low humidity and high temperatures. Its advantage lies in its high content of polyphenols and flavonoids, which give it pronounced antioxidant and anti-inflammatory properties. For example, compared to *Calligonum caput-medusae*, which also grows in Central Asia and is known for its ecological functions, *C. leucocladum* has greater therapeutic potential and a richer chemical composition [7]. *C. leucocladum* populations are threatened by intense human impact. The main issues include the destruction of natural habitats due to farming, construction, and landscape changes. An additional factor contributing to population decline is climate change, which leads to ecosystem degradation and species decline [11]. The decline in populations of this plant could lead to the loss of its ecological functions and pharmacological potential. Comprehensive measures are needed to preserve this species, including the creation of protected areas, population monitoring, and the implementation of restoration programs. In addition, the use of cultivation methods under controlled conditions can ensure stable production of biologically active substances without harvesting plants in the wild [12]. The decline in populations creates a risk of losing its key ecological functions, such as preventing soil erosion and maintaining biodiversity, as well as its pharmacological potential [13]. Comprehensive measures are needed to conserve and restore this species. One step could be the creation of protected natural areas and regular monitoring of the population status. It is also important to develop population restoration programs, including the use of cultivation methods under controlled conditions. This approach will help to preserve natural populations and ensure stable production of biologically active compounds without harming ecosystems [13-15].

*C. leucocladum* possesses a rich and complex phytochemical profile, underpinning its considerable promise for the development of novel therapeutic agents [16]. Among its bioactive constituents, compounds with demonstrable anti-inflammatory effects show potential for managing conditions such as rheumatoid arthritis, inflammatory bowel disease, and asthma. Furthermore, its antioxidant properties are of significant interest for the prevention and therapeutic mitigation of neurodegenerative pathologies, including Alzheimer's and Parkinson's diseases [17]. The plant also has significant anticancer potential, as it inhibits the growth of cancer cells and reduces their proliferation. Its antibacterial and antifungal properties make it suitable for combating skin infections, respiratory infections, and infections of the genitourinary system [18]. In addition, it can regulate blood glucose levels, making it useful for the prevention and management of diabetes. Its wound-healing and antioxidant properties allow it to be used in dermatology to treat skin diseases and accelerate wound healing [19]. The plant's immunomodulatory properties open up possibilities for its use in immunodeficiency or autoimmune diseases. These properties may also be useful in cardiovascular diseases, including atherosclerosis, and as an adjunctive therapy in chronic inflammatory conditions [20].

To fully unlock its potential, large-scale research, including clinical trials, is needed. This will not only confirm the plant's effectiveness in treating various diseases but also help determine the best ways to use it, safe dosages, and possible side effects. Only through a comprehensive approach can the full potential of this unique plant for science, medicine, and ecology be realised [21-23].

The aim of this study is to investigate chemical composition of three populations of *C. leucocladum* from different natural areas of Kazakhstan.

## Materials and methods

### *Collection and preparation of plant samples*

Plant samples of *C. leucocladum* were collected from three natural populations in July 2024. Population 1 was located in the Taukum sands, Balkhash district, Almaty region. Population 2 was sampled in the Saryesik-Atyrau sands, near Bakanas, in the same district and region. Population 3 was collected from the Miyaly area within the Saryesik-Atyrau sands, Balkhash district, Almaty region (Figure 2).

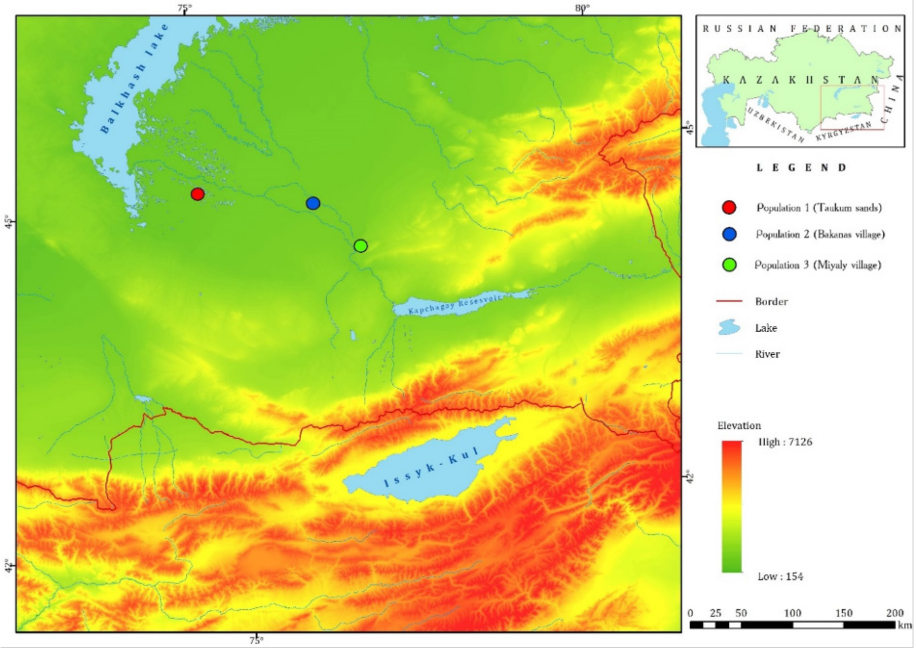

**Figure 2** – Map of the Balkhash district (Almaty region, Kazakhstan) indicating the sampling locations of the three *C. leucocladum* populations

For each location, geographical coordinates were recorded, as well as key environmental indicators such as altitude, ambient temperature and precipitation levels. Species identification was confirmed by a qualified taxonomist, and reference samples were transferred to the Herbarium of the Institute of Botany and Phytointroduction (Almaty, Kazakhstan; Index Herbariorum code: ALTB; specimen number 2200). The plant material was manually separated into morphological parts (flowers, leaves, and stems) and then dried naturally under stable conditions (25 °C, 40% relative humidity) in a shaded, well-ventilated environment for two weeks. The dried samples were ground into a fine powder using a grinder ZM200 (Retsch, Germany) and stored at −20 °C in sealed containers to preserve their integrity until analysis.

*Extraction of biologically active compounds*

A total of 1.5 g of powdered plant material was extracted using ultrasonic extraction (UAE) with an Transsonic T570 ultrasonic water bath (Elma, Germany) at a constant frequency of 40 kHz and a temperature of 40 °C. The extraction solvent consisted of 25 ml of 80% methanol (MeOH) acidified with 0.1% hydrochloric acid. The extraction process lasted 50 minutes, after which centrifugation was performed at 10,000 rpm for 10 minutes at 4 °C using a Beckman Coulter Allegra X-30R centrifuge (C0650 rotor, Beckman Coulter, USA). The supernatant was filtered through a 0.22 µm PTFE membrane filter (Millipore, USA) and stored at -80 °C for further analysis.

*Determination of total phenolic content.* Total phenolic content (TPC) was determined by colorimetric analysis using the Folin-Ciocalteu method in accordance with a standardised protocol [24]. In brief, 20 µl of extract was mixed with 100 µl of Folin-Ciocalteu reagent (Sigma-Aldrich, USA) and incubated at room temperature in the dark for 5 minutes. Then, 80 µl of 7.5% sodium carbonate was added and the reaction was allowed to proceed for 60 minutes. Absorbance was measured at 760 nm using a BioTek Epoch microplate reader (BioTek Instruments, VT, USA). A calibration curve was constructed using gallic acid (Sigma-Aldrich, USA) as a standard within a concentration range of 0.01–0.1 mg/mL. The total phenolic content was expressed as milligrams of gallic acid equivalents (GAE) per gram of dry weight (mg GAE/g DW).

*Determination of total flavonoid content (TFC).* The total flavonoid content was quantified using an aluminium chloride-based colorimetric assay [25]. 100 µl of extract was mixed with 100 µl of 2% $AlCl_3$ in methanol. After incubation at room temperature for 10 minutes, the absorbance was measured at 510 nm using a BioTek Epoch microplate reader (Agilent Technologies, USA). Quercetin (Sigma-Aldrich, USA) was used as the reference standard, and the results were expressed in mg of quercetin equivalent (QUE) per g of dry sample.

*Determination of total proanthocyanidin content.* Total proanthocyanidin content was determined using the vanillin-HCl method [26]. 100 µl of extract was mixed with 500 µl of 4% vanillin (Sigma-Aldrich, USA) in methanol and 250 µl of concentrated hydrochloric acıd HCl 37%. Following a 15-minute incubation at room temperature, the absorbance of the reaction mixture was measured at 500 nm using a microplate reader (BioTek Epoch, Agilent Technologies, USA). The proanthocyanidin content was quantified by comparison with a catechin calibration curve (Sigma-Aldrich, USA), with results expressed as milligrams of catechin equivalents per gram of dry weight (mg CE/g DW).

*Determination of total carotenoid content.* Carotenoids were extracted using a hexane : acetone solvent system (7:3 by volume) [27]. 1 g of plant powder sample was homogenised and subjected to ultrasonic treatment (Elma, Germany) at 40 °C for 20 minutes. After centrifugation at 5000 rpm (C0650 rotor, Beckman Coulter, USA) for 5 minutes, the supernatant was collected and the absorbance was measured at 450 nm using a BioTek Epoch microplate reader (Agilent, USA). The total carotenoid content was expressed in mg of β-carotene per g of sample.

Moisture content determination. The moisture content of the dried plant samples was determined gravimetrically by drying 1 g of powdered material in an oven at 105 °C to constant weight. The moisture content was calculated as the percentage of weight loss relative to the initial sample mass.

*Determination of protein and ash content.* The total protein content was quantified using the Bradford method [28] with bovine serum albumin (BSA) as a standard. For protein extraction, plant tissues were first homogenized in phosphate buffer (0.1 M, pH 7.0) and centrifuged at 12,000 × g for 15 min at 4°C; the supernatant was used for protein content determination. The ash content was determined gravimetrically by incinerating 1 g of dry, powdered sample in a muffle furnace at 550°C for 4–6 hours until a constant weight was obtained.

*Antioxidant activity analysis*

CUPRAC assay. The cupric ion reducing antioxidant capacity (CUPRAC) assay was performed by mixing 10 µL of plant extract with 90 µL of CU-

PRAC reagent (neocuproine, copper(II) chloride, and ammonium acetate; Sigma-Aldrich, USA) [29]. After incubation in the dark (30 min), the absorbance was read at 450 nm using a BioTek Epoch microplate reader (Agilent Technologies, USA). Antioxidant activity was expressed as mg of Trolox equivalents (TE) per g of dry sample.

DPPH assay. The free radical scavenging activity was measured using the 2,2-diphenyl-1-picrylhydrazyl (DPPH) method adapted from [30]. A 0.1 mM DPPH (Sigma-Aldrich, USA) solution in methanol was prepared. Then, 100 µl of the methanolic extract was mixed with 100 µl of the DPPH solution and incubated for 30 minutes in the dark at room temperature. The absorbance was recorded at 510 nm using a BioTek Epoch microplate reader (Agilent, USA), and the results were expressed in milligrams of Trolox equivalents (TE) per gram of dry sample.

*LC-MS/MS analysis of polyphenols*

*Extraction of polyphenols.* Polyphenols were extracted by homogenising 100 mg of plant material in 1 ml of methanol : water : formic acid (80:19:1 by volume). The mixture was subjected to ultrasonic treatment Transsonic T570 ultrasonic bath (Elma, Germany) and centrifuged Beckman Coulter Allegra X-30R centrifuge (Beckman Coulter, USA) at 13,500 rpm for 5 minutes at 4 °C. The supernatant liquids were collected for LC-MS/MS analysis.

*LC-MS/MS conditions.* Polyphenols were identified and quantified using a Thermo TSQ Quantis LC-MS/MS system with an electrospray ionisation (ESI) source (Thermo Fisher Scientific, USA). Analyses were conducted on a Phenomenex C18 column (150 × 2.1 mm, 2.6 µm; 40 °C). The mobile phase, a mixture of 0.1% formic acid in water (A) and acetonitrile (B), was eluted under a gradient program (5–95% B in 20 min) at 0.3 mL/min. The injection volume was set to 5 µL. Compound quantification relied on external calibration curves generated from high-purity (≥95%) reference standards (Sigma-Aldrich, USA).

*Extraction and LC-MS/MS analysis of free amino acids.* For the extraction of free amino acids, a methanol : water : formic acid mixture (80:20:1, v/v/v) was employed following an adapted protocol [31]. In brief, 100 mg of powdered plant material was homogenized with 1 mL of this solvent. The homogenate was subsequently centrifuged at 14,000 rpm for 30 minutes at 4 °C in a Beckman Coulter Allegra X-30R centrifuge (Beckman Coulter, USA). The resulting supernatant was carefully collected, passed through a 0.22 µm PTFE membrane filter, and prepared for chromatographic analysis.

The quantitative profiling of amino acids was conducted using the same Thermo Scientific TSQ Quantis LC-MS/MS instrument applied for polyphenols, albeit with a modified chromatographic method optimized for amino acid separation. Definitive identification and quantification were accomplished by matching the retention times and specific mass-to-charge (m/z) transitions of the analytes to those of pure amino acid standards (Sigma-Aldrich, USA). A series of external calibration curves, spanning a concentration range from 0.1 to 100 µg/mL, were established for each target compound to enable precise quantification.

*Determination of soluble sugars*. The concentrations of glucose, fructose, and sucrose were quantified using high-performance liquid chromatography with refractive index detection (HPLC-RID) [32]. Briefly, 100 mg of dry plant powder was extracted with 5 ml of 80% (v/v) aqueous ethanol at 80°C for 30 minutes. The extract was centrifuged at 10,000 rpm for 10 minutes, filtered through a 0.22 µm PTFE syringe filter, and analyzed. Chromatographic separation was performed on a Rezex™ ROA-Organic Acid H+ (8%) column (300 × 7.8 mm; Phenomenex, USA) maintained at 60 °C. An isocratic mobile phase of 5 mM sulfuric acid was used at a flow rate of 0.6 mL/min. Detection was carried out using a Refractive Index Detector (RID) (model, e.g., Waters 2414 or equivalent). Quantification was achieved by comparison with external calibration curves constructed from authentic standards of glucose, fructose, and sucrose (Sigma-Aldrich, USA).

*Statistical analysis.* All measurements were conducted in three independent replicates (n = 3). The data are expressed as the mean ± standard deviation (SD). To assess the significance of differences between the studied groups, a one-way analysis of variance (ANOVA) was applied, followed by Tukey's honest significant difference (HSD) post hoc test for pairwise comparisons. A p-value of less than 0.05 was considered statistically significant. All statistical computations were performed using GraphPad Prism software (version 9).

## Results and discussion

### *Biochemical composition and population variability*

The high content of polyphenols in various populations of *C. leucocladum* is associated with the plant's adaptation mechanisms to changing climatic conditions. The P3 population, collected in a semi-arid high-altitude region (about 800 m above sea level), showed the greatest accumulation of polyphenols, probably due to the combined effects of environmental factors such as increased ultraviolet radiation, lower temperatures and moderate drought. In such conditions, polyphenols act as antioxidants, protecting cells from oxidative damage. The P1 population located in an arid lowland area (about 300 m above sea level) demonstrated moderate levels of polyphenols, which may reflect adaptation to chronic heat and aridity. The lowest accumulation of polyphenols was observed in the P2 population, which taken in a more humid environment at an average altitude (≈500 m above sea level), which indicates a decrease in the synthesis of secondary metabolites with a decrease in abiotic stress. Thus, the metabolic profile of *C. leucocladum* is formed as a phenotypic reaction to environmental conditions, while populations from more stressful habitats show distinct phytochemical signs.

This pattern is further confirmed by the analysis of floral tissues, in which the concentrations of the main biologically active compounds varied significantly depending on the population (Table 1). Phenolic compounds, which play a key role in plant protection and can be potentially beneficial to human health, reached the highest levels in flowers of P3 (2.13± 0.14 mg GAE/g), which indicates a strong antioxidant potential. Flowers P1 and P2 contained lower levels of phenol (1.31 ± 0.03 and 1.34 ± 0.03 mg GE/g, respectively), although these concentrations can still provide biological activity. Flavonoids, which also contribute to antioxidant protection, are most abundant in P3 (40.24 ± 1.23 mg QE/g), which indicates an increased ability of this population to neutralize free radicals. The flavonoid content in P1 and P2 was about half that in P3. Analyses of antioxidant activity (CUPRAC and DPPH) confirmed these data, while P3 extracts demonstrated the greatest ability to remove radicals. Proanthocyanidins, known for their antioxidant and anti-inflammatory properties, prevailed in P3 (24.32± 0.65 mg CE/g), which was twice the levels in other samples. Carotenoids, important for plant photoprotection and used in the cosmetics and food industries, reached their maximum concentration in P2 (3909.11 ± 298.50 micrograms of β-carotene/g), while P1 and P3 contained significantly lower amounts.

The interpopulation differences were also evident in protein accumulation: in P1 (0.71 ± 0.06%), the protein content was significantly higher than in P2 (0.46 ± 0.02%). This variability may reflect differences in nitrogen metabolism or biosynthetic activity. On the contrary, the ash content in different populations varied minimally, stabilizing at about 3.6%, which indicates the constant assimilation and precipitation of minerals regardless of local growing conditions.

Each studied population has different biochemical characteristics: P3 has a high content of antioxidants, P2 has a high content of carotenoids, and P1 has a high protein content. These characteristics point to various potential applications, from pharmacology to the food and cosmetics industry.

**Table 1 –** Biochemical composition of *C. leucocladum* flowers from three populations grown under different environmental conditions

| Populations | Total Phenols, mg GAE/g | Total Flavonoids, mg QUE/g | CUPRAC, mg TE/g | DDPPH, mg TE/g | Proanthocyanidin, mg CE/g) | Total Carotenoids, mg β-carotene/g | Total Protein, % | Ash, % |
|---|---|---|---|---|---|---|---|---|
| P1 flower | 1.31 ± 0.03 | 22.47 ± 2.34 | 4.03 ± 0.14 | 7.49 ± 0.34 | 12.69 ± 0.36 | 2.71 ± 0.11 | 0.71 ± 0.06 | 3.59 ± 0.27 |
| P2 flower | 1.34 ± 0.03 | 23.96 ± 1.10 | 3.66 ± 0.06 | 6.42 ± 0.55 | 10.61 ± 0.35 | 3.91 ± 0.30 | 0.46 ± 0.02 | 3.69 ± 0.35 |
| P3 flower | 2.13 ± 0.14 | 40.24 ± 1.23 | 5.70 ± 0.36 | 7.02 ± 0.43 | 24.32 ± 0.65 | 2.07 ± 0.11 | 0.64 ± 0.01 | 3.59 ± 0.36 |

Note: P1: arid region, slightly alkaline soils; P2: moderately humid region, neutral soils; P3: semi-arid highland region, slightly acidic soils. Values are presented as mean ± standard deviation (n = 3) on a dry weight basis

Analysis of leaf tissues revealed significant differences in the content of protective phytochemicals, which may also be beneficial to human health (Table 2). Phenolic compounds known for their antioxidant properties were present in the highest concentration in the leaves of Population P3 (3.60 ± 0.14 mg GAE/g), which indicates a high protective ability. The levels of P2 (3.01 ± 0.20 mg GAE/g) and P1 (2.77 ± 0.10 mg GAE/g) were moderately lower, but remained significant. Flavonoids, which support plant resistance to stress and exhibit bioactive potential, showed a similar trend: the largest amount accumulated in P3 (59.48 ± 3.32 mg units/g), followed by P2 (44.63 ± 3.89 mg units/g) and P1 (38.77 ± 0.95 mg units/g).

Analyses of antioxidant activity confirmed these observations. CUPRAC values were highest in leaves of P3 (10.49 ± 0.26 mg TE/g), exceeding the values of P2 (8.76 ± 0.33 mg TE/g) and P1 (7.86 ± 0.29 mg TE/g). Similarly, DPPH radical scavenging activity was most pronounced in P3 (12.54 ± 1.03 mg TE/g), while P1 (10.42 ± 0.90 mg TE/g) and P2 (9.73 ± 0.46 mg TE/g) showed lower but significant activity. Proanthocyanidins, which are valued for their antioxidant and anti-inflammatory properties, were also most abundant in P3 (48.53 ± 1.07 mg CE/g), while P2 (35.95 ± 2.37 mg CE/g) and P1 (27.44 ± 0.45 mg CE/g) were found in lower amounts.

On the contrary, carotenoids, the key compounds for photoprotection, reached their maximum concentration in the leaves of P1 (22 178.24 ± 963.96 micrograms of β-carotene/g). The beta-carotene content in leaves P2 and P3 was relatively low (18,269.13 ± 298.50 and 16,753.35 ± 390.83 micrograms/g, respectively), although it still remained significant. The protein content, indicating metabolic activity, was highest in the P1 group (1.43 ± 0.11%), followed by P3 (0.95 ± 0.07%) and P2 (0.71 ± 0.07%). Conversely, the ash content reflecting the mineral fraction remained relatively the same in different populations, ranging from 10.24 ± 0.72% (P3) to 10.92 ± 0.96% (P2), indicating stable absorption of minerals regardless of differences in habitat.

Collectively, the metabolic profiles of the leaves indicate different functional capabilities: P3 is characterized by pronounced antioxidant and anti-inflammatory properties, P1 is characterized by an increased content of carotenoids and protein, and P2 is characterized by intermediate but noticeable levels of several classes of biologically active substances. These differences in composition highlight the variety of applications of *C. leucocladum* leaf extracts in pharmaceutical, nutraceutical, and cosmetic products.

A comparative analysis of metabolites in the tissues of flowers and leaves revealed pronounced organ-specific accumulation patterns. In all populations, the leaves consistently contained significantly higher concentrations of the main antioxidant compounds. For example, in a population with high stress levels of P3, the total phenol content in leaves was about 70% higher (3.60 mg GAE/g) compared to flowers (2.13 mg GAE/g). Similar differences were observed in the total amount of flavonoids and proanthocyanidins, which confirms the role of leaves as the main site of biosynthesis of these protective secondary metabolites. Accordingly, the *in vitro* antioxidant capacity, measured by CUPRAC and DPPH assays, was significantly higher in extracts obtained from the leaves.

In contrast, the tissues of the flowers show a distinct metabolic effect, expressed in selective enrichment with certain specialized flavonoids. For example, the concentration of hyperoside in P3 flowers exceeds the concentration in leaves by more than ten times. This differential separation implies a potential ecological function – such as attracting pollinators or protecting gametophytes – in reproductive structures. Taking together, these results highlight the crucial influence of tissue type on phytochemical composition, which directly influences the targeted collection of plant raw materials in various fields of application, from pharmacology to the development of functional ingredients.

**Table 2 –** Biochemical analysis of *C. leucocladum* leaves from three populations grown under different environmental conditions

| Populations | Total Phenols, mg GAE/g | Total Flavonoids, mg QUE/g | CUPRAC, mg TE/g | DDPPH, mg TE/g | Proanthocyanidin, mg CE/g) | Total Carotenoids, mg β-carotene/g | Total Protein, % | Ash, % |
|---|---|---|---|---|---|---|---|---|
| P1 leaf | 2.77 ± 0.10 | 38.77 ± 0.95 | 7.86 ± 0.29 | 10.42 ± 0.90 | 27.44 ± 0.45 | 22.17 ± 0.96 | 1.43 ± 0.11 | 10.41 ± 0.38 |
| P2 leaf | 3.01 ± 0.20 | 44.63 ± 3.89 | 8.76 ± 0.33 | 9.73 ± 0.46 | 35.95 ± 2.37 | 18.27 ± 0.30 | 0.71 ± 0.07 | 10.92 ± 0.96 |
| P3 leaf | 3.60 ± 0.14 | 59.48 ± 3.32 | 10.49 ± 0.26 | 12.54 ± 1.03 | 48.53 ± 1.07 | 16.75 ± 0.39 | 0.95 ± 0.07 | 10.24 ± 0.72 |

Note: P1: arid region, slightly alkaline soils; P2: moderately humid region, neutral soils; P3: semi-arid highland region, slightly acidic soils. Values are presented as mean ± standard deviation (n = 3) on a dry weight basis

*Identification of phenolic compounds*

A total of 23 phenolic compounds representing a wide range of biologically active components with documented pharmacological activity were identified in the analyzed samples of *C. leucocladum.* These include antioxidants such as epicatechin [33], apigenin [34], and quercetin [35], as well as compounds with pronounced anti-inflammatory (for example, gallic acid [36], hyperoside [37]), cardioprotective (chlorogenic acid [38]), and potential antitumor properties (chrysin [39]). Of particular importance was the discovery of artepillin C, a rare compound with anti-inflammatory and antimicrobial effects [40].

Significant qualitative and quantitative differences in the content of polyphenols were observed both in plant organs and in populations (Table 3). A constant trend was a noticeably higher accumulation of most phenolic compounds in leaf tissues compared to parts of the flower, which makes the foliage the main site of biosynthesis of these pharmacologically significant metabolites.

As a result of the analysis, clear signs characteristic of a particular population were identified. The P3 population demonstrated the highest concentrations of epicatechin, especially in flowers (2322.67 ± 170.68 mg/kg) and leaves (1874.59 ± 137.75 mg/kg), indicating its potential as a rich source of this powerful antioxidant. On the contrary, the leaves of P2 were characterized by an increased content of chlorogenic acid (5.56 ± 0.33 mg/kg), which indicates differences in the metabolism of phenolic acids. The P1 population was characterized by a pronounced accumulation of anti-inflammatory compounds with particularly high concentrations of gallic acid (39.19 ± 1.41 mg/kg) and chrysin (82.20 ± 5.57 mg/kg). Of particular phytochemical interest was the detection of hesperidin exclusively in P1 leaves (12.88 ± 0.40 mg/kg) and trace amounts of artepillin C exclusively in P2 leaves (0.04 ± 0.0004 mg/kg), indicating unique biosynthetic capabilities or strictly regulated metabolic pathways characteristic of these populations.

The results confirm that each *C. leucocladum* population has special phenolic properties: P3 is characterized by high antioxidant activity, P1 by anti-inflammatory action, and P2 by a more balanced distribution of key metabolites. These chemical characteristics specific to a particular population highlight the significant potential of this species as a source of naturally occurring bioactive substances for pharmaceutical and biotechnological applications.

**Table 3 –** Phenolic Compounds in flowers and leaves of *C. leucocladum* from three populations (mg/kg, on dry base)

| № | Phenolic compound | Formula | Population 1 | | Population 2 | | Population 3 | |
|---|---|---|---|---|---|---|---|---|
| | | | flower | leaf | flower | leaf | flower | leaf |
| 1 | (-)-Epicatechin | $C_{15}H_{14}O_6$ | 1099.72 ± 80.81 | 1697.06 ± 124.71 | 861.36 ± 63.30 | 2021.26 ± 148.53 | 2322.67 ± 170.68 | 1874.59 ± 137.75 |
| 2 | Apigenin | $C_{15}H_{10}O_5$ | 3.44 ± 0.18 | 4.19 ± 0.22 | 3.23 ± 0.17 | 3.17 ± 0.17 | 3.85 ± 0.20 | 3.58 ± 0.19 |
| 3 | Artepillin C | $C_{19}H_{24}O_3$ | nd | 0.07 ± 0.001 | 0.04± 0.001 | nd | 0.04 ± 0.001 | nd |
| 4 | Caffeic acid phenethyl ester | $C_{17}H_{16}O_4$ | 0.25 ± 0.002 | 0.31 ± 0.003 | 0.25± 0.002 | 0.26±0.002 | 0.25 ± 0.002 | 0.27 ± 0.002 |
| 5 | Catechol | $C_6H_6O_2$ | 0.06 ± 0.001 | 0.02 ± 0.002 | 0.13± 0.001 | 0.09±0.001 | 0.10 ± 0.001 | 0.12 ± 0.001 |
| 6 | Chlorogenic acid | $C_{16}H_{18}O_9$ | 1.98 ± 0.12 | 2.01 ± 0.12 | 2.46 ± 0.14 | 5.56 ± 0.33 | 1.48 ± 0.09 | 1.36 ± 0.08 |
| 7 | Chrysin | $C_{15}H_{10}O_4$ | 67.65 ± 4.58 | 82.20 ± 5.57 | 62.25±4.22 | 68.57±4.65 | 69.10 ± 4.68 | 63.63 ± 4.31 |
| 8 | Galangin | $C_{15}H_{10}O_5$ | 57.90 ± 2.65 | 71.56 ± 3.27 | 57.75±2.64 | 65.29±2.99 | 58.35± 2.67 | 59.64 ± 2.73 |
| 9 | Gallic acid | $C_7H_6O_5$ | 16.41 ± 0.59 | 39.19 ± 1.41 | 21.03± 0.76 | 12.84±0.46 | 23.32 ± 0.84 | 14.99 ± 0.54 |
| 10 | Hesperidin | $C_{28}H_{34}O_{15}$ | 12.88 ± 0.40 | nd | nd | nd | nd | nd |
| 11 | Hyperosid | $C_{21}H_{20}O_{12}$ | 883.26±56.97 | 125.64 ± 8.10 | 562.24± 36.27 | 98.68±6.37 | 1055.85±68.11 | 90.54 ± 5.84 |
| 12 | Kaempherol | $C_{15}H_{10}O_6$ | 6.89 ± 0.36 | 13.62 ± 0.71 | 7.82 ± 0.41 | 12.39±0.65 | 5.33 ± 0.28 | 8.80 ± 0.46 |
| 13 | Luteolin | $C_{15}H_{10}O_6$ | 1.05 ± 0.02 | 3.91 ± 0.07 | 1.45 ± 0.02 | 2.11 ± 0.04 | 0.98 ± 0.02 | 1.32 ± 0.02 |
| 14 | Myricetin | $C_{15}H_{10}O_8$ | 0.41 ± 0.01 | 1.18 ± 0.03 | 0.34 ± 0.01 | 0.73 ± 0.02 | 0.71 ± 0.02 | 0.82 ± 0.02 |
| 15 | Naringenin | $C_{15}H_{12}O_5$ | 2.98 ± 0.21 | 3.50 ± 0.24 | 3.04 ± 0.21 | 3.15 ± 0.22 | 3.55 ± 0.25 | 3.18 ± 0.22 |

*Continuation of the table*

| № | Phenolic compound | Formula | Population 1 | | Population 2 | | Population 3 | |
|---|---|---|---|---|---|---|---|---|
| | | | flower | leaf | flower | leaf | flower | leaf |
| 16 | Neochlorogenic acid | $C_{16}H_{18}O_9$ | 2.10 ± 0.17 | 1.84 ± 0.15 | 2.33 ± 0.18 | 5.15 ± 0.41 | 1.65 ± 0.13 | 1.22 ± 0.10 |
| 17 | Protocatechuic acid | $C_7H_6O_4$ | 4.78 ± 0.22 | 4.43 ± 0.20 | 3.60 ± 0.16 | 3.68 ± 0.17 | 4.54 ± 0.21 | 3.78 ± 0.17 |
| 18 | Pinocembrin | $C_{15}H_{12}O_4$ | 47.50 ± 2.60 | 54.74 ± 2.99 | 51.57± 2.82 | 47.73±2.61 | 48.14 ± 2.63 | 52.80 ± 2.89 |
| 19 | Quercitrin | $C_{21}H_{20}O_{11}$ | 51.06 ± 1.13 | 1.66 ± 0.04 | 0.10± 0.002 | 0.09±0.002 | 0.10 ± 0.002 | 0.14 ± 0.003 |
| 20 | Rutin | $C_{27}H_{30}O_{16}$ | 14.93 ± 0.23 | 2.70 ± 0.04 | 5.31 ± 0.08 | 0.72 ± 0.01 | 5.04 ± 0.08 | 0.87 ± 0.01 |
| 21 | t-Cinnamic acid | $C_9H_8O_2$ | 1.23 ± 0.06 | 2.58 ± 0.12 | 1.04 ± 0.05 | 2.08 ± 0.10 | 3.68 ± 0.18 | 1.83 ± 0.09 |
| 22 | t-Caffeic acid | $C_9H_8O_4$ | nd | nd | 43.46 ±2.56 | nd | nd | nd |
| 23 | t-Ferulic acid | $C_{10}H_{10}O_4$ | 2.40 ± 0.09 | 12.58 ± 0.48 | 2.08 ± 0.08 | 5.68 ± 0.22 | 3.18 ± 0.12 | 10.18 ± 0.39 |

Note: nd – not detected.
P1: arid region, slightly alkaline soils; P2: moderately humid region, neutral soils; P3: semi-arid highland region, slightly acidic soils. Values are presented as mean ± standard deviation (n = 3) on a dry weight basis

The novelty of the study results is highlighted by the identification of several specialized metabolites that had not previously been reported in the genera Calligonum. The key discovery was the discovery of artepillin C, a compound not previously described in *C. leucocladum* or its relatives. Artepillin C, the main biologically active component of Brazilian propolis, is known for its powerful anti-inflammatory, antitumor, and antioxidant properties [41]. His presence in S. The results, confirmed by mass spectrometry and chromatographic analysis, indicate the existence of unexplored biosynthetic pathways in this species, which opens up new opportunities for studying the chemical adaptation of plants. This discovery positions *C. leucocladum* as a potential source of artepatillin C for the development of pharmaceutical drugs, especially in oncology and for anti-inflammatory therapy [42].

Equally notable was the discovery of caffeic acid phenethyl ether (CAPE), a compound commonly associated with bee products (such as propolis) and rarely found in higher plants. CAPE exhibits strong antioxidant and anti-inflammatory activity, mitigating oxidative stress at the cellular level [43]. Its presence in *C. leucocladum* means that this species can serve as an alternative source of this valuable plant-based metabolite, which contributes to research into its biosynthesis and sustainable production for therapeutic purposes.

In addition, catechol was first discovered in *C. leucocladum.* This phenolic compound plays a crucial role in the biosynthesis of lignin and tannin and helps protect plants from abiotic stressors such as drought and ultraviolet radiation, as well as from pathogens [44]. Its accumulation may reflect an adaptive response to extreme environmental conditions of the species. Catechol is promising as an object of fundamental research in the field of plant stress physiology, as well as a leading compound for the development of antioxidant agents and biochemical markers.

In addition to these new findings, the exceptionally high concentrations of hyperoside and rutin observed, in particular, in the P3 population, deserve special attention. Both flavonoids are well-established antioxidants with proven cardioprotective, neuroprotective, and anti-inflammatory activities [45]. Their significant accumulation once again highlights the pharmacological potential of *C. leucocladum,* especially for use in vascular integrity disorders and chronic inflammatory diseases.

Another notable discovery was the identification of transferulic acid, a compound not previously described in the scientific literature for this species. It has powerful antioxidant activity, contributing to the protection of plant cells from oxidative stress. This biological activity indicates its potential use in dermatological and pharmaceutical preparations designed to counteract photoaging and mitigate skin damage caused by ultraviolet radiation. The study of its biosynthetic pathway, metabolic function, and therapeutic potential is justified, since transferulic acid can serve as a valuable component in new antioxidant and anti-inflammatory drugs [46].

*Amino acid profile and adaptive metabolic responses*

The analysis extended to the profile of free amino acids, determining the number of 36 compounds in the tissues of flowers and leaves of three populations (Table 4). Amino acids play an important role not only as fundamental building blocks for proteins necessary for human health – they play an important role in collagen synthesis (proline, hydroxyproline), neurotransmission (tryptophan as a precursor to serotonin), and tissue repair [47] -but also play a central role in plant physiology and stress adaptation.

A clear pattern specific to the organ was revealed: leaves constantly have a higher concentration of most amino acids compared to flowers. This is consistent with the role of leaves as the main site of photosynthesis and the associated intensive metabolism. It is noteworthy that proline, a key osmoprotector, accumulates in exceptionally high concentrations in P3 leaves (21,128.47 ± 1,116.16 µmol/g DW), which underlines the importance of the osmotic regulation mechanism in response to drought or salinity stress.

The P3 population demonstrated the most pronounced accumulation of amino acids in general, which indicates increased biosynthetic activity as an adaptive strategy to its more extreme semi-arid high-altitude habitat conditions. This is evidenced by the maximum levels of serine (involved in the synthesis of proteins and metabolites) and taurine (a membrane stabilizer and antioxidant). A significant accumulation of conditionally essential stress-sensitive amino acids was especially noticeable: gamma-aminobutyric acid (GABA) in P3 leaves (4358.80 ± 181.51 µmol/g DW) emphasizes its role in ionic homeostasis and signaling, while the increased content of beta-alanine and taurine indicates enhanced antioxidant protection.

Essential amino acids (leucine, isoleucine, threonine, valine) also reached peak concentrations in P3 leaves, supporting the need for stress-related protein synthesis. In addition, a noticeable accumulation of less common metabolites, such as beta-aminoisobutyric acid (2399.01 ± 154.74 µmol/g DW in P3 leaves), indicates special protective functions. In contrast, amino acids that play a key metabolic role, such as glutamic acid and methionine, maintained stable concentrations in all populations, reflecting their main functions in the household.

Populations P1 and P2 exhibit a more moderate amino acid profile, which corresponds to growth under conditions of less severe environmental stress. The pronounced amino acid composition of P3, especially in leaves, demonstrates coordinated metabolic reprogramming towards the biosynthesis of protective compounds. These data not only reveal the biochemical basis of *C. leucocladum* adaptation, but also indicate the potential of P3 as a source of osmoprotectors and stress-related metabolites for the development of biostimulants that increase crop resistance.

**Table 4** – Free amino acid composition in flowers and leaves of three *C. leucocladum* populations with functional classification (µmol/g, on dry base)

| № | Compound | Molecular weight | Population 1 | | Population 2 | | Population 3 | |
|---|---|---|---|---|---|---|---|---|
| | | | flower | leaf | flower | leaf | flower | leaf |
| 1 | 1-Methylhistidine | 169.18 | 43.75 ± 1.18 | 53.66 ± 1.45 | 46.69 ± 1.26 | 60.27 ± 1.62 | 33.62 ± 0.91 | 76.07 ± 2.05 |
| 2 | 3-Methylhistidine | 169.18 | nd | 3.27 ± 0.03 | 3.61 ± 0.03 | 1.66 ± 0.01 | nd | 0.73 ± 0.01 |
| 3 | alpha-Aminoadipic acid | 161.16 | 114.5 ± 6.0 | 193.2 ± 10.1 | 80.78 ± 4.22 | 293.7 ± 154 | 96.97 ± 5.07 | 379.9 ± 19.9 |
| 4 | alpha-Aminobutyric acid | 103.12 | nd | 73.11 ± 3.04 | nd | 42.96 ± 1.79 | 53.70 ± 2.24 | nd |
| 5 | Anserine | 240.26 | 0.59 ± 0.01 | 1.25 ± 0.01 | 0.52 ± 0.01 | 0.38 ± 0.01 | nd | 0.51 ± 0.01 |
| 6 | Arginine | 174.20 | nd | 3.99 ± 0.07 | 0.87 ± 0.02 | 3.25 ± 0.06 | 0.73 ± 0.01 | 3.73 ± 0.07 |
| 7 | Asparagine | 132.12 | 4,400 ±313 | 2,178 ± 155 | 3,700 ± 263 | 2,811 ± 200 | 922.8 ± 65.6 | 2,623 ± 186 |
| 8 | Aspartic Acid | 133.10 | 1,209 ± 42 | 872.4 ± 30.6 | 1,403 ± 49 | 999.3 ± 35.1 | 1069.4 ± 37.6 | 1067.9 ± 37.5 |
| 9 | beta-Alanine | 89.09 | 232.9 ± 16.4 | 217.2 ± 15.3 | 119.0 ± 8.4 | 614.0 ± 43.1 | 96.06 ± 6.74 | 744.3 ± 52.3 |

*Continuation of the table*

| № | Compound | Molecular weight | Population 1 | | Population 2 | | Population 3 | |
|---|---|---|---|---|---|---|---|---|
| | | | flower | leaf | flower | leaf | flower | leaf |
| 10 | beta-Aminoisobutyric acid | 103.12 | 827.4 ± 53.4 | 18,787 ± 121 | 383.8 ± 24.8 | 2,285 ± 147 | 545.6 ± 35.2 | 2,399 ± 155 |
| 11 | Carnosine | 226.23 | 1.04 ± 0.01 | 1.09 ± 0.01 | 0.79 ± 0.01 | 3.10 ± 0.04 | 0.61 ± 0.01 | 1.64 ± 0.02 |
| 12 | Cystathionine | 222.26 | 0.55 ± 0.00 | 0.36 ± 0.00 | 0.06 ± 0.00 | 0.12 ± 0.00 | 0.08 ± 0.00 | 0.56 ± 0.00 |
| 13 | Cystine | 240.30 | nd | nd | nd | 8.27 ± 0.22 | 8.78 ± 0.23 | nd |
| 14 | Citrulline | 175.19 | 10.70 ± 0.40 | 36.59 ± 1.37 | 4.49 ± 0.17 | 84.86 ± 3.19 | 10.51 ± 0.39 | 45.58 ± 1.71 |
| 15 | Ethanolamine | 61.08 | 1,043 ± 78 | 1,441 ± 108 | 1,044 ± 78 | 2,033 ± 153 | 698.3 ± 52.5 | 2,340 ± 176 |
| 16 | gamma-Aminobutyric acid | 103.12 | 1,590 ± 66 | 3,460 ± 144 | 721.0 ± 30.0 | 4,109 ± 171 | 1,052 ± 44 | 4,359 ± 182 |
| 17 | Glutamic Acid | 147.13 | 782.3 ± 48.3 | 1,791 ± 111 | 1,525 ± 94 | 1,561 ± 96 | 1,068 ± 66 | 1,625 ± 100 |
| 18 | Homocystine | 268.40 | 37.17 ± 0.82 | 137.81 ± 3.04 | 23.40 ± 0.52 | 99.00 ± 2.18 | 41.39 ± 0.91 | 112.41 ± 2.48 |
| 19 | Hydroxylysine | 162.19 | 1,972 ± 136 | 1,972 ± 136 | nd | 1,971 ± 136 | 1,971 ± 136 | nd |
| 20 | Hydroxyproline | 131.13 | 128.4 ± 7.7 | 239.1 ± 14.4 | 135.2 ± 8.1 | 459.5 ± 27.7 | 198.3 ± 12.0 | 542.8 ± 32.7 |
| 21 | Histidine | 155.15 | nd | 11.07 ± 0.16 | 5.36 ± 0.08 | 10.35 ± 0.15 | 9.33 ± 0.14 | 10.11 ± 0.15 |
| 22 | Isoleucine | 131.17 | 173.8 ± 8.7 | 345.3 ± 17.2 | 192.2 ± 9.6 | 587.5 ± 29.3 | 280.1 ± 14.0 | 740.0 ± 36.9 |
| 23 | Leucine | 131.17 | 128.5 ± 9.2 | 232.7 ± 16.7 | 137.0 ± 9.8 | 437.6 ± 31.4 | 185.2 ± 13.3 | 546.0 ± 39.2 |
| 24 | Lysine | 146.19 | 1,668 ± 78 | 6,186 ± 288 | 907.2 ± 42.2 | 6,862 ± 319 | 1,400 ± 65 | 8,184 ± 381 |
| 25 | Methionine | 149.21 | 1,542 ± 50 | 1,737 ± 56 | 1,548 ± 50 | 1,677 ± 54 | 1,537 ± 50 | 1,774 ± 57 |
| 26 | Ornithine | 132.16 | 1,557 ± 107 | 1,564 ± 107 | 1,556 ± 107 | 1,562 ± 107 | 1,563 ± 107 | 1,563 ± 107 |
| 27 | Phenylalanine | 165.19 | 1,860 ± 27 | 2,415 ± 36 | 1,822 ± 27 | 2,544 ± 37 | 1,747 ± 26 | 2,005 ± 29 |
| 28 | Phosphoethanolamine | 141.06 | 14.00 ± 0.18 | 4.10 ± 0.05 | 3.06 ± 0.04 | 4.31 ± 0.06 | 13.38 ± 0.17 | 3.83 ± 0.05 |
| 29 | Phosphoserine | 185.07 | 2.33 ± 0.02 | 5.42 ± 0.05 | 5.45 ± 0.06 | 2.76 ± 0.03 | nd | 8.74 ± 0.09 |
| 30 | Proline | 115.13 | 1,348 ± 71 | 13,1366 ± 693 | 1,126 ± 59 | 12,819 ± 677 | 1,146 ± 61 | 21,128 ± 116 |
| 31 | Serine | 105.09 | 1,335 ± 81 | 6,591 ± 402 | 1,557 ± 95 | 8,331 ± 508 | 1,170± 71 | 8,634 ± 526 |
| 32 | Taurine | 125.15 | 4,635 ± 370 | 8,127 ± 649 | 5,247 ± 419 | 7,042± 562 | 2,5323 ± 202 | 10,683 ± 853 |
| 33 | Threonine | 119.12 | 949.0 ± 66.8 | 2,208 ± 155 | 1,375 ± 97 | 2,776 ± 195 | 855.2 ± 60.2 | 2809 ± 197 |
| 34 | Tryptophan | 204.22 | 530.1 ± 16.2 | 2,431 ± 74 | 552.9 ± 16.9 | 1,773 ± 54 | 230.5 ± 7.1 | 1,715 ± 53 |
| 35 | Tyrosine | 181.19 | 661.1 ± 15.3 | 1,396 ± 32 | 487.8 ± 11.3 | 1,444 ± 33 | 929.6 ± 21.6 | 1,329 ± 31 |
| 36 | Valine | 117.15 | 634.1±27.5 | 1412.6 ± 61.4 | 501.1 ± 21.8 | 2349.5 ± 102.1 | 515.5 ± 22.4 | 3,012 ± 131 |

Note: nd – not detected.
P1: arid region, slightly alkaline soils; P2: moderately humid region, neutral soils; P3: semi-arid highland region, slightly acidic soils.
Values are presented as mean ± standard deviation (n = 3) on a dry weight basis

The correlation matrix demonstrates a strong positive relationship between amino acid concentrations in flowers and leaves within each population, indicating that the distribution of amino acids in different parts of the plant depends on general metabolic processes (Figure 3). For example, in population P1, the correlation between flowers and leaves is 0.55, in population P2 it is 0.52, and in population P3 it is 0.56. Leaves from different populations show a high correlation, indicating similar amino acid synthesis processes in this part of the plant. For example, the correlation between leaves from populations P1 and P2 is 0.99, and between P2 and P3 it is 0.98. Similarly, flowers from different populations also show high correlation: between flowers P1 and P2 it is 0.96, and between P2 and P3 it is 0.83. This may reflect the conservative nature of the amino acid composition of flowers, which perform important reproductive functions.

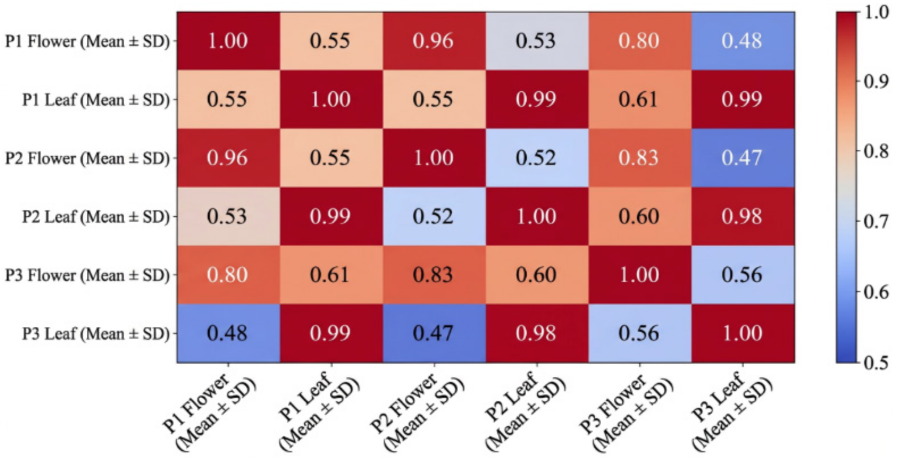

|  | P1 Flower (Mean ± SD) | P1 Leaf (Mean ± SD) | P2 Flower (Mean ± SD) | P2 Leaf (Mean ± SD) | P3 Flower (Mean ± SD) | P3 Leaf (Mean ± SD) |
|---|---|---|---|---|---|---|
| P1 Flower (Mean ± SD) | 1.00 | 0.55 | 0.96 | 0.53 | 0.80 | 0.48 |
| P1 Leaf (Mean ± SD) | 0.55 | 1.00 | 0.55 | 0.99 | 0.61 | 0.99 |
| P2 Flower (Mean ± SD) | 0.96 | 0.55 | 1.00 | 0.52 | 0.83 | 0.47 |
| P2 Leaf (Mean ± SD) | 0.53 | 0.99 | 0.52 | 1.00 | 0.60 | 0.98 |
| P3 Flower (Mean ± SD) | 0.80 | 0.61 | 0.83 | 0.60 | 1.00 | 0.56 |
| P3 Leaf (Mean ± SD) | 0.48 | 0.99 | 0.47 | 0.98 | 0.56 | 1.00 |

**Figure 3** – Correlation matrix of mean amino acid concentrations across *C. leucocladum* populations (P1, P2, P3) and plant organs (flowers and leaves) Pearson correlation coefficients (r): higher positive correlation values (closer to +1) are displayed in brighter colors (e.g., yellow), indicating strong similarity in amino acid composition; lower or negative values (closer to -1 or 0) are shown in darker colors (e.g., blue), indicating weak or inverse relationships. P1: arid region, slightly alkaline soils; P2: moderately humid region, neutral soils; P3: semi-arid highland region, slightly acidic soils.

The correlation between amino acid concentrations in the leaves of one population and the flowers of another is relatively lower. For example, the correlation between the leaves of population P1 and the flowers of population P3 is 0.48, and between the leaves of P2 and the flowers of P3, it is 0.47. This is probably due to differences in the functions of leaves and flowers, as well as specific metabolic processes in these organs. Population P3 shows a moderate correlation between leaves and flowers (0.56), which may be related to its adaptation to specific environmental conditions. At the same time, the leaves of this population have a high correlation with the leaves of other populations, which may indicate similarities in habitat conditions. The results emphasise the conservative nature of the amino acid composition of flowers and leaves, as well as their connection with general metabolic and ecological characteristics. The lower correlation between plant parts from different populations may be the result of adaptation to different habitat conditions. These results are important for further studies of the ecological and metabolic characteristics of *C. leucocladum* and for the development of biotechnological and pharmacological applications.

Population P3 is distinguished by high biosynthetic activity. Its leaves have the highest concentrations of amino acids such as proline, lysine and gamma-aminobutyric acid (GABA). This indicates the presence of specific adaptation mechanisms in this population that stimulate increased metabolism and the accumulation of key metabolites. Population P1 demonstrates a more balanced distribution of amino acids between leaves and flowers. At the same time, the leaves of this population show elevated levels of amino acids such as threonine and phenylalanine, indicating their importance for supporting physiological processes such as protein synthesis and photosynthesis. However, for some amino acids, such as 1-methylhistidine and carnosine, concentrations in flowers exceed those in leaves. This may indicate a special role for these compounds in protective and reproductive processes. Some amino acids, such as glutamic and aspartic acids, exhibit similar concentration levels in different populations and plant parts. This indicates their conservative role in key metabolic processes, such as protein synthesis, nitrogen metabolism, and energy metabolism.

The study of the biological functions of amino acids presented in this work allows us to draw several important conclusions about plant metabolism and their adaptive abilities. Amino acids play an important role in numerous metabolic processes such as building blocks of proteins: they participate in the synthesis of secondary metabolites, regulate stress responses, promote nitrogen transport and accumulation, and support energy metabolism. 1-methylhistidine and 3-methylhistidine are involved in nitrogen metabolism and can serve as markers of stress and protein degradation. Their role in plants remains poorly understood, but their detection in this study highlights their potential as indicators of plant physiological status. Alpha-aminoadipic acid is an intermediate product of lysine catabolism, which highlights its importance in energy metabolism. Alpha-aminobutyric acid is associated with osmoregulation and stress tolerance, for example, to drought, making it important for studying plant adaptation mechanisms. Anserine and carnosine are powerful antioxidants that protect cells from oxidative stress [48]. These compounds also act as pH buffers, helping to maintain metabolic stability under extreme conditions. Arginine and ornithine play a key role in nitrogen metabolism, serving as precursors to nitric oxide and polyamines, which regulate cell growth and stress protection. These amino acids are also involved in nitrogen recycling pathways in plants. Asparagine and aspartic acid are involved in nitrogen transport and storage. They are precursors of other amino acids and nucleotides, making them central components of plant metabolism. Ethanolamine and phosphoethanolamine are involved in the formation of phospholipids, key components of cell membranes. They play an important role in maintaining membrane integrity and allow plants to adapt to external stresses such as drought and high soil salinity. High concentrations of these compounds highlight their importance in plant responses to adverse environmental conditions. Gamma-aminobutyric acid (GABA) is found in significant amounts, especially in leaves. This compound performs important regulatory functions, including ion transport and stress adaptation. High levels of GABA in leaves may be related to its role in protecting plants from abiotic factors such as drought and soil salinity. Glutamic acid is one of the central molecules in nitrogen metabolism [49]. It serves as a precursor for the synthesis of other amino acids and is actively involved in nitrogen-related metabolic processes. Homocysteine and cystathionine play an important role in sulphur metabolism by supporting the synthesis of key compounds such as methionine and cysteine. These amino acids are crucial for protein synthesis and the formation of antioxidant defence systems. Hydroxylysine and hydroxyproline are amino acids necessary for strengthening plant cell walls. They provide mechanical strength to tissues and help plants resist physical stress and infections. Histidine plays an important role in metal binding and antioxidant protection of cells. Its function is especially important for plants deficient in micronutrients such as iron and zinc [50].

*Organic acids in C. leucocladum*

The study of *C. leucocladum* composition reveals that organic acids play a significant role in the plant's central metabolism and adaptation to environmental stress. Malic acid, a key intermediate in the TCA cycle and stomatal regulation, was the dominant organic acid across all samples, with notably high concentrations in P1 tissues, indicating intense metabolic activity. Citric acid, another crucial TCA cycle component involved in metal chelation and stress response, reached its peak concentration in the leaves of population P3, suggesting its active role in adaptive mechanisms under semi-arid highland conditions. Fumaric and tartaric acids also showed elevated levels in P1 leaves, reinforcing the picture of active energy metabolism in this population from arid lowlands. In contrast, acetic, butyric, and propionic acids–often associated with secondary fermentation pathways–were present in lower and more variable concentrations, with localized accumulations (e.g., acetic acid in P2 leaves) that may reflect specific metabolic adjustments. The presence of trace amounts of 3-methylhistidine, particularly in P1 leaves, merits further investigation for its potential role in stress adaptation. Overall, the distinct profiles of organic acids (Table 5) reflect population-specific metabolic strategies, with P1 exhibiting a signature of high primary metabolic flux, while P3 accumulates specific acids like citrate likely involved in stress tolerance.

The analysis results show that malic acid is the dominant component in all plant samples (leaves and flowers). Its concentration is particularly high in sample P1, which may be linked to the plant's high metabolic activity. Malic acid plays a critical role in respiratory processes and may indicate favorable growing conditions or an active growth phase of the plants. Citric acid, the second most abundant acid, is especially prominent in the leaves of sample P3. This could be related to its role in metal detoxification or adaptation to environmental stress factors.

**Table 5** – Concentration of organic acids in flowers and leaves of three *C. leucocladum* populations (µg/g, on dry base)

| № | Compound | Population 1 | | Population 2 | | Population 3 | |
|---|---|---|---|---|---|---|---|
| | | flower | leaf | flower | leaf | flower | leaf |
| 1 | Acetic acid | 5.85 ± 0.98 | 6.54 ± 0.32 | 7.68 ± 0.24 | 18.08 ± 0.19 | 6.0 ± 1.05 | 2.78 ± 0.43 |
| 2 | 3-Methylhistidine | 1.18 ± 0.14 | 19.64 ± 0.67 | 3.61 ± 0.40 | 5.70 ± 0.60 | 3.92 ± 0.18 | 2.60 ± 0.03 |
| 3 | Propionic acid | 1.59 ± 0.26 | 13.63 ± 1.36 | 4.18 ± 0.04 | 1.50 ± 0.17 | 2.74 ± 0.16 | 1.60 ± 0.01 |
| 4 | Butyric acid | 18.24 ± 0.40 | 55.99 ± 2.97 | 7.32 ± 0.28 | 44.7 ± 0.52 | 16.34 ± 0.14 | 31.76 ± 0.33 |
| 5 | Lactic acid | 12.53 ± 0.22 | 6.05 ± 0.34 | 1.38 ± 0.27 | 3.64 ± 0.01 | 2.51 ± 0.41 | 7.48 ± 0.71 |
| 6 | Fumaric acid | 9.90 ± 1.40 | 63.64 ± 6.79 | 7.71 ± 1.21 | 11.12 ± 0.97 | 7.40 ± 1.06 | 18.18 ± 1.05 |
| 7 | Malic acid | 356.64 ± 3.74 | 27.87 ± 0.96 | 54.39 ± 1.09 | 98.96 ± 0.41 | 72.64 ± 1.92 | 181.98 ± 4.45 |
| 8 | Tartaric acid | 76.07 ± 4.02 | 78.92 ± 5.65 | 12.84 ± 0.92 | 30.88 ± 3.58 | 26.62 ± 2.03 | 33.12 ± 1.84 |
| 9 | Citric acid | 170.25 ± 0.50 | 106.88 ± 14.36 | 38.7 ± 0.23 | 95.23 ± 1.20 | 118.48 ± 3.03 | 225.64 ± 4.35 |

Note: nd – not detected.
P1: arid region, slightly alkaline soils; P2: moderately humid region, neutral soils; P3: semi-arid highland region, slightly acidic soils.
Values are presented as mean ± standard deviation (n = 3) on a dry weight basis.
*3-Methylhistidine is an amino acid derivative included here due to its analysis within the organic acid profile.

A comparison of leaves and flowers revealed that leaves contain higher concentrations of acids, which is expected given their primary function in photosynthesis and metabolism. In contrast, flowers show lower acid concentrations, as their role is more focused on reproductive processes and attracting pollinators.

Plants of population P1 stand out with the highest acid concentration, likely due to favorable environmental conditions or the physiological state of the plant. Samples P2 and P3 exhibit more uniform acid distribution, which may result from adaptations to various stresses or genetic traits. These differences in acid concentrations between samples could be attributed to environmental conditions, genetic characteristics of the plants, or growth stages. This data is valuable for further studies on plant adaptation mechanisms and their metabolic activity.

Analysis of soluble carbohydrate composition revealed distinct accumulation patterns between plant organs and among the studied populations (Figure 5). Glucose and fructose were the dominant sugars, showing nearly parallel concentration profiles and significantly higher levels in leaf tissues compared to flowers across all populations. This trend is consistent with the role of leaves as the primary site of photosynthesis and carbon storage. The maximum concentrations of both hexoses were recorded in the leaves of population P3, indicating particularly active carbohydrate metabolism or storage under its semi-arid highland growth conditions. Conversely, floral tissues exhibited the lowest sugar levels, with minimal glucose and fructose content found in P1 and P2 flowers, reflecting the high metabolic demand of reproductive development.

Sucrose distribution contrasted sharply with that of the hexoses, displaying substantially lower concentrations overall. Its highest levels were detected in the leaves of populations P2 and P3, though they remained an order of magnitude lower than glucose or fructose. The notably low sucrose-to-hexose ratio, especially in flowers, suggests that sucrose may be rapidly hydrolyzed in these tissues or efficiently allocated for phloem transport rather than stored. These results underscore a fundamental metabolic division: leaves accumulate hexoses as a stable carbon reserve linked to environmental adaptation, while flowers prioritize sugar utilization for growth and development, with sucrose serving a more transient, transport-related role.

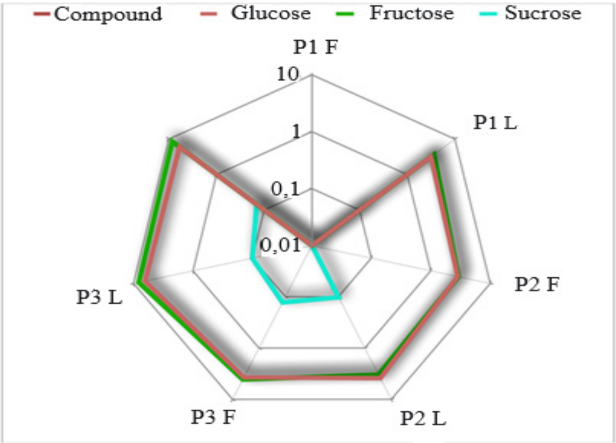

**Figure 5 –** Comparative radar chart of soluble sugar concentrations (glucose, fructose, sucrose) in flowers ("F") and leaves ("L") of three *C. leucocladum* populations (P1: arid region, slightly alkaline soils; P2: moderately humid region, neutral soils; P3: semi-arid highland region, slightly acidic soils). Concentrations are presented on a logarithmic scale (ppm). The chart visualizes the pronounced accumulation of hexoses in leaves versus flowers and the overall low abundance of sucrose.

*Environmental stress and bioactive compound accumulation*

Quantitative phytochemical analysis revealed a clear gradient in the accumulation of bioactive compounds among the three *C. leucocladum* populations, which corresponds directly to the measured environmental parameters of their habitats (Figure 6).

Population 3, collected from a high-altitude semi-arid site (800 ± 40 m a.s.l., 15 ± 2 °C, 100 ± 15 mm rainfall) with increased UV exposure, exhibited the most pronounced metabolic response. It showed the highest concentrations of total phenolics (3.60 ± 0.14 mg GAE $g^{-1}$), flavonoids (59.48 ± 3.32 mg QUE $g^{-1}$), and proanthocyanidins, along with the strongest in vitro antioxidant activity (CUPRAC, DPPH). In contrast, population 1, originating from a warmer arid lowland (300 ± 20 m a.s.l., 25 ± 1 °C, 50 ± 5 mm rainfall), displayed the lowest values for these parameters. Population 2, from a moderately humid mid-altitude region (500 ± 30 m a.s.l., 20 ± 1.5 °C, 75 ± 10 mm rainfall), presented an intermediate profile.

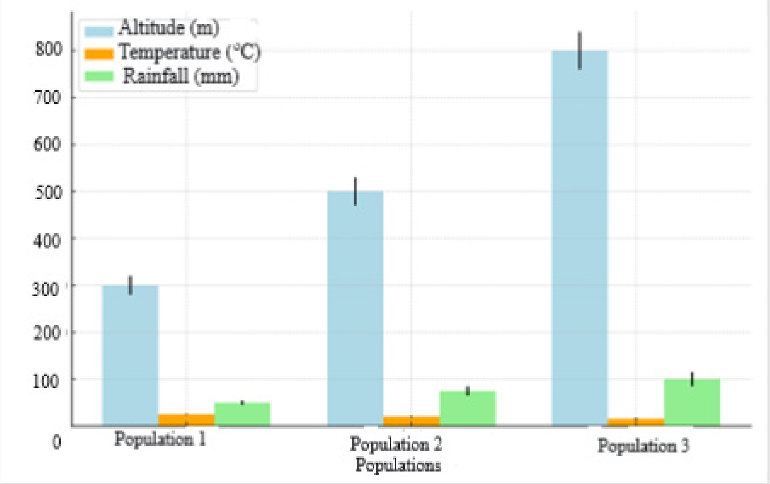

**Figure 6 –** Environmental factors by of three *C. leucocladum* populations (P1: arid region, slightly alkaline soils; P2: moderately humid region, neutral soils; P3: semi-arid highland region, slightly acidic soils)

This gradient demonstrates that the phytochemical composition of *C. leucocladum* is tightly coupled to abiotic stress intensity. The harsher conditions of the P3 habitat characterized by lower temperatures, higher solar radiation, and specific water availability act as a key driver, redirecting carbon flux toward the biosynthesis of protective secondary metabolites such as phenolics and flavonoids [51]. This stress-induced investment in chemical defense appears reduced under the more favorable growth conditions of the P1 site, where resources are likely prioritized for primary metabolism and biomass production.

Rainfall represents an additional key environmental factor influencing secondary metabolite accumulation by regulating water availability for biosynthetic processes. In the present study, P3 was collected from a site with comparatively higher annual precipitation (100 ± 15 mm), which likely ensured sufficient hydration to sustain active metabolite synthesis under concurrent abiotic stress (e.g., lower temperature, higher UV). This combination of adequate water supply and environmental stress appears critical for maximizing phytochemical production. In contrast, the limited rainfall at the P1 site (50 ± 5 mm) may constrain overall metabolic activity, contributing to its lower phenolic and flavonoid content (Tables 1, 2).

Soil properties and nutrient availability, while not directly assessed here, may further modulate the observed metabolic profiles. Future studies integrating soil chemistry data would provide a more complete understanding of the edaphic influences on *C. leucocladum* phytochemistry. Beyond immediate environmental effects, long-term genetic adaptation may also contribute to population-specific metabolic differences. Recurrent exposure to harsh conditions could select for genotypes with enhanced secondary metabolite biosynthesis, potentially explaining the robust metabolic phenotype of P3. Confirming this requires complementary genetic and transcriptomic analyses [7].

The strong environment–metabolism association has direct practical relevance. Our findings suggest that moderate, controlled abiotic stress simulating conditions of higher altitudes (cooler temperatures, increased radiation) or regulated water deficit could be employed in cultivation to enhance the yield of valuable antioxidants (phenolics, flavonoids) in *C. leucocladum*. Concurrently, these results underscore the importance of conserving natural populations and their habitats, as environmental degradation could diminish the species' inherent biochemical potential.

The diverse biochemical profile of *C. leucocladum*, particularly in population P3, reflects an integrated adaptive strategy for arid ecosystems. Elevated levels of polyphenols, flavonoids, and proanthocyanidins mitigate oxidative stress, while specific organic acids (e.g., malic, citric acid) support energy metabolism and detoxification. The discovery of rare compounds (artepillin C, CAPE, catechol) indicates a previously unrecognized biosynthetic capacity that is likely activated under stress [52]. Furthermore, the extreme accumulation of proline and elevated levels of GABA provide direct biochemical evidence of osmotic adjustment and stress signaling, solidifying the classification of P3 as a stress-adapted phenotype [53].

## Conclusions

In summary, this study establishes that *C. leucocladum* harbors a rich and diverse phytochemical profile, with marked variation observed across different populations and plant organs. Notably, the P3 population, originating from a semi-arid highland habitat (≈800 m a.s.l.), exhibited the most pronounced accumulation of bioactive compounds. This finding supports the hypothesis that abiotic stress acts as a key driver, stimulating the biosynthesis of antioxidant and protective metabolites as an adaptive response. The identification of rare specialized metabolites, including artepillin C, caffeic acid phenethyl ester (CAPE), and catechol, underscores the significant and underexplored pharmacological potential of this species and broadens the known chemodiversity of the genus Calligonum. Collectively, these results advance our understanding of biochemical adaptation in plants to environmental stress. Furthermore, they provide a robust scientific foundation for leveraging *C. leucocladum* extracts in applied sectors such as medicine, cosmetology, and the functional food industry. To translate this potential into tangible applications, future research should focus on: (1) elucidating the genetic and regulatory architecture underlying key biosynthetic pathways; (2) rigorously validating the bioactivity and safety profiles through targeted pharmacological models; and (3) developing sustainable, scalable agronomic practices for the commercial cultivation and production of these valuable phytochemicals.

## Acknowledgments

This work was supported by grant project AP26100259 from the Scientific Committee of the Ministry of Science and Higher Education of the Republic of Kazakhstan. The authors also acknowledge the institutional support provided by the Faculty of Biology and Biotechnology at Al-Farabi Kazakh National University.

## Conflict of interest

The authors declare no competing interests.

### References

1. Mussina M., Tynybekov B., Raimbekova B., Ilesbek M., Osmonali B., Issabayeva S., ... & Imanaliyeva M. (2025) Assessment of vegetation and soil characteristics of *Calligonum leucocladum* populations in the Balkhash region, Kazakhstan. *ES Energy and Environment*, vol. 30, p. 1809. https://doi.org/10.30919/ee1809

2. Mirzabaev A., Oskenbayev Y., & Sansyzbayev A. (2025) The role of land restoration for climate change mitigation and biodiversity conservation in Kazakhstan. *Central Asian Journal of Sustainability and Climate Research*, vol. 4, no. 1, pp. 13–30. https://doi.org/10.29258/CAJSCR/2025-R1.v4-1/13-30.eng

3. Yahia Y., Bagues M., Zaghdoud C., Al-Amri S. M., Nagaz K., & Guerfel M. (2019) Phenolic profile, antioxidant capacity and antimicrobial activity of *Calligonum arich* L., desert endemic plant in Tunisia. *South African Journal of Botany*, vol. 124, pp. 414–419. https://doi.org/10.1016/j.sajb.2019.06.005

4. Pervaiz I., Saleem H., Sarfraz M., Tousif M. I., Khurshid U., Ahmad S., ... & Ahemad N. (2020) Multidirectional insights into the phytochemical, biological, and multivariate analysis of the famine food plant (*Calligonum polygonoides* L.): A novel source of bioactive phytocompounds. *Food Research International*, vol. 137, p. 109606. https://doi.org/10.1016/j.foodres.2020.109606

5. Liu N., Guan K., Li W., & Feng Y. (2017) Geographical distribution and eco-adaptability of *Calligonum* L. in the Tarim Basin. *Pakistan Journal of Botany*, vol. 49, no. 3, pp. 1001–1007. https://pakbs.org/pjbot/papers/1497350019.pdf

6. Al-Otaibi M. (2015) Aspects of the autecology of Arta (*Calligonum comosum* L. Her) a medical plant from arid region of Saudi Arabia. *J Biodivers Environ Sci*, vol. 6, no. 3, pp.248-55. https://www.innspub.net/wp-content/uploads/2022/12/JBES-V6-No3-p248-255.pdf

7. Feng Y., Wen Z., Li Y., & Li W. (2021) Climatic factors influencing geographical replacement in the desert genus *Calligonum* Sect. *Medusa* (Polygonaceae) in Xinjiang, China. *Pakistan Journal of Botany*, vol. 53, no. 4, pp. 1339–1342. https://doi.org/10.30848/PJB2021-4(4)

8. Jakupov I. T., Yeszhanova G. T., & Mamytbekova G. K. (2023) Biological activity and pharmaco-therapeutic efficiency of *Calligonum leucocladum* B. dosage forms in the treatment of endometritis of cows. *Advances in Animal and Veterinary Sciences*, vol. 11, no. 7, pp. 1200–1208. https://doi.org/10.17582/journal.aavs/2023/11.7.1200.1208

9. Ydyrys A., Mukhitdinov N., Ivashchenko A., Ashirova Z., Massimzhan M., Imanova E., ... & Kaparbay R. (2024) Methodological guide for geobotanical research on rare, endemic, and medicinal plants: A case study of the Ranunculaceae family. *ES Food & Agroforestry*, vol. 18, p. 1340. https://doi.org/10.30919/esfaf1340

10. Mussina M., Kyrbassova E., Tynybekov B., Hou W., Bozhbanov A., Imanova E., ... & Imanaliyeva M. (2025) Comparative chloroplast genomics of *Calligonum leucocladum* from Kazakhstan: Genetic basis for arid adaptation and agroforestry applications. *ES Food and Agroforestry*, vol. 22, p. 1893. https://doi.org/10.30919/faf1893

11. Li X., Zhang D. (2016) Role of sugar signaling in plant abiotic stress responses. *International Journal of Molecular Sciences*, vol. 17, no. 12, p. 2066. https://doi.org/10.3390/ijms17122066

12. Ibragimov T. S., Tlegenova K., Shilimbet S., Mambetova L., Begenov A. B., Nazarbekova S. T., ... & Tynybekov B. M. (2014) Introduction of *Calligonum* sorts in Southern Kazakhstan. *World Applied Sciences Journal*, vol. 30, no. 8, pp. 955–957. https://doi.org/10.5829/idosi.wasj.2014.30.08.14106

13. Imanaliyeva M., Kurmanbay U., Mamytova N., Kilybayeva T., Toktar M., Adenova B., ... & Childibayeva A. (2025) The soils of natural populations of *Gentiana tianschanica* Rupr. (Gentianaceae) in Ile Alatau, Kazakhstan. *EQA – International Journal of Environmental Quality*, vol. 69, pp. 62–72. https://doi.org/10.6092/issn.2281-4485/20950

14. Imanaliyeva M.T., Tynybekov B.M., Parmanbekova M.K., Imanova E.M., Kyrbasova E.A., Kabylbek K., Kurmanbay U.K. (2024) Anatomical studies of vegetative organs in two *Gentiana* species (Gentianaceae). *Eurasian Journal of Ecology*. vol. 80, no. 3. https://doi.org/10.26577/eje.2024.v80.i3-09

15. Ydyrys A., Myrzabekov B., Murat T., & Muratzhan M. (2025) Flora and ecological conditions of the pastoral arid lands of the Caspian Sea. *Science and Education*, vol. 4, no. 3 (80), pp. 45–60. https://doi.org/10.52578/2305-9397-2025-3-4-45-60

16. Yeszhanova G. T., Bekseitova K. S., & Rakhimzhanova D. T. (2022) Phytochemical analysis of *Calligonum leucocladum* Bunge raw material. *News of Kazakhstan Science (Novosti nauki Kazakhstana)*, no. 1, p. 16. https://doi.org/10.53939/15605655/2023.1.16

17. Nakadate K., Ito N., Kawakami K., & Yamazaki N. (2025) Anti-inflammatory actions of plant-derived compounds and prevention of chronic diseases: From molecular mechanisms to applications. *International Journal of Molecular Sciences*, vol. 26, no. 11, p. 5206. https://doi.org/10.3390/ijms26115206

18. Alghamdi S. S., Alshafi R. A., Huwaizi S., Suliman R. S., Mohammed A. E., Alehaideb Z. I., ... & Rahman I. (2023) Exploring in vitro and in silico biological activities of *Calligonum comosum* and *Rumex vesicarius*: Implications on anticancer and antibacterial therapeutics. *Saudi Pharmaceutical Journal*, vol. 31, no. 11, p. 101794. https://doi.org/10.1016/j.jsps.2023.101794

19. Zhang W., Chen L., Xiong Y., Panayi A. C., Abududilibaier A., Hu Y., ... & Liu G. (2021) Antioxidant therapy and antioxidant-related bionanomaterials in diabetic wound healing. *Frontiers in Bioengineering and Biotechnology*, vol. 9, p. 707479. https://doi.org/10.3389/fbioe.2021.707479

20. Zhang Y., Cai P., Cheng G., & Zhang Y. (2022) A brief review of phenolic compounds identified from plants: Their extraction, analysis, and biological activity. *Natural Product Communications*, vol. 17, no. 1, p. 1934578X211069721. https://doi.org/10.1177/1934578X211069721

21. Hasnat H., Shompa S. A., Islam M. M., Alam S., Richi F. T., Emon N. U., ... & Ahmed F. (2024) Flavonoids: A treasure house of prospective pharmacological potentials. *Heliyon*, vol. 10, no. 6, p. e27533. https://doi.org/10.1016/j.heliyon.2024.e27533

22. Strack D., Fester T. (2006) Isoprenoid metabolites with antioxidant and other properties. *Journal of Plant Physiology*, vol. 163, no. 2, pp. 165–181. https://doi.org/10.1016/j.jplph.2005.05.010

23. Ahmed H., Moawad A., Owis A., AbouZid S., & Ahmed, O. (2016) Flavonoids of *Calligonum polygonoides* and their cytotoxicity. *Pharmaceutical Biology*, vol. 54, no. 10, pp. 2119-2126. https://doi.org/10.3109/13880209.2016.1146778

24. Lucas B. N., Dalla N., Boeira C. P., Verruck S., & Rosa C. S. D. (2022) Determination of total phenolic compounds in plant extracts via Folin–Ciocalteu's method adapted to the usage of digital images. *Food Science and Technology*, vol. 42, p. e35122. https://doi.org/10.1590/fst.35122

25. Shraim A. M., Ahmed T. A., Rahman M. M., & Hijji Y. M. (2021) Determination of total flavonoid content by aluminum chloride assay: A critical evaluation. *LWT – Food Science and Technology*, vol. 150, p. 111932. https://doi.org/10.1016/j.lwt.2021.111932

26. Mitra K., & Uddin N. (2014) Total phenolics, flavonoids, proanthocyanidins, and ascorbic acid contents and in-vitro antioxidant activities of newly developed isolated soy protein. *CAB Digital Library*. https://www.cabidigitallibrary.org/doi/pdf/10.5555/20143242640

27. de Carvalho L. M. J., Gomes P. B., de Oliveira Godoy R. L., Pacheco S., do Monte P. H. F., de Carvalho J. L. V., ... & Ramos S.R. R. (2012) Total carotenoid content, α-carotene and β-carotene, of landrace pumpkins (*Cucurbita moschata* Duch.): A preliminary study. *Food Research International*, vol. 47, no. 2, pp. 337–340. https://doi.org/10.1016/j.foodres.2011.07.040

28. Kielkopf C. L., Bauer W., & Urbatsch I. L. (2020) Bradford assay for determining protein concentration. *Cold Spring Harbor Protocols*, 2020, no. 4, pdb-prot102269. https://doi.org/10.1101/pdb.prot102269

29. Apak R., Güçlü K., Özyürek M., & Karademir S. E. (2004) Novel total antioxidant capacity index for dietary polyphenols and vitamins C and E, using their cupric ion reducing capability in the presence of neocuproine: CUPRAC method. *Journal of Agricultural and Food Chemistry*, vol. 52, no. 26, pp. 7970–7981. https://doi.org/10.1021/jf048741x

30. Kedare S. B., & Singh R. P. (2011) Genesis and development of DPPH method of antioxidant assay. *Journal of Food Science and Technology*, vol. 48, no. 4, pp. 412–422. https://doi.org/10.1007/s13197-011-0251-1

31. Stănilă A., Diaconeasa Z., Sima R., Stănilă S., & Sima N. (2018) Effects of extraction solvents on the quantification of free amino acids in lyophilised brewer's yeast. *Bulletin UASVM Food Science and Technology*, vol. 75, no. 1, pp. 53–60. https://doi.org/10.15835/buasvmcn-fst:2017.0037

32. Xu W., Liang L., & Zhu M. (2015) Determination of sugars in molasses by HPLC following solid-phase extraction. *International Journal of Food Properties*, vol. 18, no. 3, pp. 547–557. https://doi.org/10.1080/10942912.2013.837064

33. Qu Z., Liu A., Li P., Liu C., Xiao W., Huang J., ... & Zhang S. (2021) Advances in physiological functions and mechanisms of (−)-epicatechin. *Critical Reviews in Food Science and Nutrition*, vol. 61, no. 2, pp. 211–233. https://doi.org/10.1080/10408398.2020.1723057

34. Madunić J., Madunić I. V., Gajski G., Popić J., & Garaj-Vrhovac V. (2018) Apigenin: A dietary flavonoid with diverse anticancer properties. *Cancer Letters*, vol. 413, pp. 11–22. https://doi.org/10.1016/j.canlet.2017.10.041

35. Rather R. A., & Bhagat M. (2020) Quercetin as an innovative therapeutic tool for cancer chemoprevention: Molecular mechanisms and implications in human health. *Cancer Medicine*, vol. 9, no. 24, pp. 9181–9192. https://doi.org/10.1002/cam4.1411

36. Bai J., Zhang Y., Tang C., Hou Y., Ai X., Chen X., ... & Meng X. (2021) Gallic acid: Pharmacological activities and molecular mechanisms involved in inflammation-related diseases. *Biomedicine & Pharmacotherapy*, vol. 133, p. 110985. https://doi.org/10.1016/j.biopha.2020.110985

37. Wang Q., Wei H. C., Zhou S. J., Li Y., Zheng T. T., Zhou C. Z., & Wan X. H. (2022) Hyperoside: A review on its sources, biological activities, and molecular mechanisms. *Phytotherapy Research*, vol. 36, no.7, pp. 2779-2802. https://doi.org/10.1002/ptr.7478

38. Yu Y., Zhang Z., & Chang C. (2022) Chlorogenic acid intake guidance: Sources, health benefits, and safety. *Asia Pacific Journal of Clinical Nutrition*, vol. 31, no. 4, pp. 602–610. https://doi.org/10.6133/apjcn.202212_31(4).0003

39. Salari N., Faraji F., Jafarpour S., Faraji F., Rasoulpoor S., Dokaneheifard S., & Mohammadi M. (2022) Anti-cancer activity of chrysin in cancer therapy: A systematic review. *Indian Journal of Surgical Oncology*, vol. 13, no. 4, pp. 681–690. https://doi.org/10.1007/s13193-022-01550-6

40. Sowmya S., Swamy K. R., Alla R. K., Doddawad V. G., Patil K., Sanjay C., & Konakanchi A. (2025) Exploring the integration of Artepillin C, a bioactive constituent of propolis, in dental materials: A review. *Oriental Journal of Chemistry*, vol. 41, no. 4. https://doi.org/10.13005/ojc/410402

41. Szliszka E., Mertas A., Czuba Z. P., & Król W. (2013) Inhibition of inflammatory response by artepillin C in activated RAW264.7 macrophages. *Evidence-Based Complementary and Alternative Medicine*, 2013, p. 735176. https://doi.org/10.1155/2013/735176

42. Shahinozzaman M., Basak B., Emran R., Rozario P., & Obanda D. N. (2020) Artepillin C: A comprehensive review of its chemistry, bioavailability, and pharmacological properties. *Fitoterapia*, vol. 147, p. 104775. https://doi.org/10.1016/j.fitote.2020.104775

43. Yordanov Y. (2019) Caffeic acid phenethyl ester (CAPE): Cornerstone pharmacological studies and drug delivery systems. *Pharmacia*, vol. 66, pp. 223–231. https://doi.org/10.3897/pharmacia.66.e38571

44. Wang A.Y., Gu S.B., Ji X.Q., Bai H.B., Liu C.Y., Guo Q.F., Xu Z.P., Zhao Y., Shen T., Xiang L. (2025) Catechol tetrahydroisoquinolines: synthesis, biological activity, and natural occurrence in portulaca oleracea as analyzed by UPLC-Q-TOF-ESI-MS/MS. *ACS omega*, vol. 10, no. 43, 51620-51635. https://pubs.acs.org/doi/10.1021/acsomega.5c07408

45. Enogieru A. B., Haylett W., Hiss D. C., Bardien S., & Ekpo O. E. (2018) Rutin as a potent antioxidant: Implications for neurodegenerative disorders. *Oxidative Medicine and Cellular Longevity*, 2018, p. 6241017. https://doi.org/10.1155/2018/6241017

46. Milutinov J., Pavlović N., Ćirin D., Atanacković Krstonošić M., & Krstonošić V. (2024) The potential of natural compounds in UV protection products. *Molecules*, vol. 29, no. 22, p. 5409. https://doi.org/10.3390/molecules29225409

47. Wu G. (2010) Functional amino acids in growth, reproduction, and health. *Advances in Nutrition*, vol. 1, no. 1, pp. 31–37. https://doi.org/10.3945/an.110.1008

48. Petkova D., Stoyanova S., Dinkov G., & Bogdanov M. G. (2025) Beyond Protein Building Blocks: A Review of Biological Roles and Therapeutic Potential of Free Amino Acids. *International Journal of Molecular Sciences*, vol. 26, no. 23, 11264. https://doi.org/10.3390/ijms262311264

49. Guo Z., Gong J., Luo S., Zuo Y., & Shen Y. (2023) Role of gamma-aminobutyric acid in plant defense response. *Metabolites*, vol. 13, no. 6, p. 741. https://doi.org/10.3390/metabo13060741

50. Kavi Kishor P. B., Hima Kumari P., Sunita M. S. L., & Sreenivasulu N. (2015) Role of proline in cell wall synthesis and plant development and its implications in plant ontogeny. *Frontiers in Plant Science,* vol. 6, p. 544. https://doi.org/10.3389/fpls.2015.00544

51. Yang F., & Lv G. (2025) Responses of *Calligonum leucocladum* to prolonged drought stress through antioxidant system activation, soluble sugar accumulation, and maintaining photosynthetic homeostasis. *International Journal of Molecular Sciences*, vol. 26, p. 4403. https://doi: 10.3390/ijms26094403

52. Beserra F. P., Gushiken L. F. S., Hussni M. F., Ribeiro V. P., Bonamin F., Jackson C. J., … & Bastos J. K. (2021) Artepillin C as an outstanding phenolic compound of Brazilian green propolis for disease treatment: A review on pharmacological aspects. *Phytotherapy Research*, vol. 35, p. 2274–2286. https://doi.org/10.1002/ptr.6875

53. Hayat S., Hayat Q., Alyemeni M. N., Wani A. S., Pichtel J. & Ahmad A. (2012). Role of proline under changing environments: a review. *Plant Signaling & Behavior*, vol. 7, p. 1456–1466. https://doi.org/10.4161/psb.21949

**_Information about authors:_**

*Maral E. Musina – Postgraduate student, Department of Biodiversity and Bioresources, Al-Farabi Kazakh National University (Almaty, Kazakhstan, e-mail: maral.musina@mail.ru).*

*Bekzat M. Tynybekov – Doctor of Biological Sciences, Professor, Department of Biodiversity and Bioresources, Faculty of Biology and Biotechnology, Al-Farabi Kazakh National University (Almaty, Kazakhstan, e-mail: Bekzat.Tynybekov@kaznu.edu.kz).*

*Gul Öz – Professor, Department of Botany, Faculty of Natural Sciences (Istanbul University, Istanbul, Turkey, e-mail: cevahirg@istanbul.edu.tr).*

*Alibek Ydyrys – PhD, Researcher, Center for Biomedical Research (Al-Farabi Kazakh National University, Almaty, Kazakhstan, e-mail: ydyrys.alibek@gmail.com).*

*Makpal A. Nurtayeva – Biology Teacher, Municipal State Institution "Specialized Lyceum No. 126" (Almaty, Kazakhstan, e-mail: makpal_asil@mail.ru).*

*Moldir T. Imanaliyeva – PhD, Senior Lecturer, Department of Biology, Institute of Natural Sciences, Kazakh National Women's Pedagogical University (Almaty, Kazakhstan, e-mail: moldirimanalieva19@gmail.com).*

*Akmaral S. Nurmahanova – PhD, Researcher, Department of Biodiversity and Bioresources, Faculty of Biology and Biotechnology, Al-Farabi Kazakh National University (Almaty, Kazakhstan, e-mail: Akmaral.Nurmahanova @kaznu.edu.kz).*

IRSTI 34.27.23; 34.27.19 https://doi.org/10.26577/IJBCh20251825

**K. Nokhaiz[1*], S.M. Bukhari[1], K.U. Rehman[2],**
**H.U.R. Chohan[3], A.A. Shahzad[4], S. Andleeb[2], W. Ali[1]**

[1]University of Veterinary and Animal Sciences, Lahore, Pakistan
[2]GC Woman University, Sialkot, Pakistan
[3]King Abdullah University of Science and Technology, Jeddah, Saudi Arabia
[4]University of Education, Lahore, Pakistan
*e-mail: kshf1249@gmail.com

*(Received 30 May 2025; received in revised form 04 December 2025; accepted 26 December 2025)*

# In vitro assessment of potential probiotic lactic acid bacteria isolated from the gastrointestinal tract of chickens

**Abstract.** The global prohibition on antibiotics as growth promoters in poultry has prompted a shift toward probiotics as viable substitutes. Lactic acid bacteria (LAB) offer various benefits, including modulation of gut microbiota, maintenance of intestinal equilibrium, and enhancement of immune function. This study isolated and identified *Lactobacillus* strains from chicken small intestines, evaluating their in vitro survival and gastrointestinal (GI) colonization capabilities. LAB was cultured on de Man Rogosa Sharpe (MRS) agar for 24-48 hours, with species-specific strains identified through biochemical tests and 16S rRNA gene sequencing. Sequence analysis identified the species as *Lactobacillus plantarum*, *Lactobacillus acidophilus*, and *Lactobacillus casei*. Their resilience to simulated gastric conditions and antibiotic susceptibility assessed via the agar well diffusion method, indicated robust tolerance to pH 3.5 and 0.3% bile salts, alongside notable resistance (90%) to tetracycline. Growth kinetics at varying temperatures and NaCl concentrations revealed optimal conditions at 37°C and 4% NaCl, respectively, with growth diminishing at higher concentrations. In conclusion, *Lactobacillus* species exhibit significant resilience to harsh GI conditions, underscoring their potential as effective antibiotic alternatives in poultry production.

**Keywords:** antibiotic alternatives, gut microbiota, lactic acid bacteria, microbial ecology, poultry production, gastrointestinal tract.

## Introduction

The productivity and nutrition of poultry are heavily influenced by the gastrointestinal (GI) health. The GI microbiota and their metabolic byproducts are essential for nutrition, digestion, absorption, and metabolism, ultimately promoting the health and development of poultry [1]. The composition of GI microflor in animals holds significant importance as it has the potential to safeguard hosts from pathogens [2].

The utilization of antibiotics in broilers serves to boost economic growth, protect against infectious diseases, and maintain overall health [3]. The frequent use of antibiotics in chicken diets can lead to significant problems, including the development of antibiotic resistance in pathogens, accumulation of antibiotic residues in animal products, and disruption and depletion of valuable intestinal microflora [4].

The European Union (EU) has officially outlawed the use of all antibiotics as feed additives, except for coccidiostats and histomonostats, under Regulation (EC) No 1831/2003 [5]. Other countries, including South Korea, Canada, Mexico, Japan, New Zealand, and the United States, have either embraced the EU's strategy or formulated their ow standards and recommendations to restrict the use of antibiotics for promoting growth in animals [6]. This situation has prompted researchers to explore alternatives to antibiotics in poultry farming.

Direct-fed microbials, the probiotics, are live microorganisms that, when given in sufficient amounts, are believed to provide health benefits [7]. Within the GI tract, probiotics can inhibit the proliferation of harmful bacteria like *Escherichia coli* and *Salmonella* species. The administration of probiotics has been shown to reduce the likelihood of GI colonization by foodborne pathogens, including *Campylobacter Clostridium* and *Salmonella* [8,9,10].

A promising probiotic, lactic acid bacteria (LAB) can metabolize sugar to make lactic acid.

© 2025 al-Farabi Kazakh National University

It performs a wide range of probiotic activities, including the regulation of gut microbiota composition, conserving host-intestinal equilibrium, and enhancing immune control. An efficient strategy for combating multiple viral infections is to use LAB as potential probiotic candidates [11]. The addition of a *Lactobacillus* species-based probiotic to chicken feed enhances both nutrient absorption and digestion. Furthermore, probiotics administration improves immunological responses, promotes growth, and mitigates the effects of various enterotoxins in animals [12].

Over the past few years, the usage of different probiotic bacteria and organic acids as a substitute for antibiotics in feeds has garnered a lot of attention [13]. For a lactic acid bacterial strain to be used as a probiotic, it must attach to the intestinal epithelium of the host; should tolerate acid and bile salts, exhibits an antagonistic activity towards infectious bacteria; and can survive throughout handling and storage [14].

The probiotic bacteria that are employed the most belong to the genus *Lactobacillus,* including species *Lactobacillus helvecticus*, *Lactobacillus salivarius*, *Lactobacillus plantarum* and *Lactobacillus acidophilus*[15]. The immunity, intestinal regeneration process, and gut microbial balance of pigs can be enhanced by feeding them with probiotics such as *Pediococcus pentosaceus* and *Lactobacillus reuteri* [16].

Based on research, the therapeutic benefits of probiotics can vary from strain to strain. Therefore, it might be more advantageous to combine multiple probiotic strains, each with its own specific activities, rather than relying on a single strain [17]. Given the increasing need for alternatives to antibiotics in poultry, the current research aims to isolate and evaluate lactic acid bacteria (LAB) from the gastrointestinal tract of chickens. The core objective is to identify LAB species with potential as effective probiotics to enhance poultry health and performance.

## Materials and methods

*Research field.* The proposed research was carried out in district Kasur. Kasur has a longitude 74$^{o}$ 27′0″ E and latitude 31$^{o}$ 70 N and is situated in the east of Punjab, Pakistan (Figure 1). It is bordered on the east and south-east by India, on the south-west by district Okara, on the north by district Lahore, and on the north-west by district Nankana Sahib. The district has a total area of 3, 995 square kilometers divided into four Tehsils: Chunian, Kot Radha Kishan Kasur, and Pattoki [18].

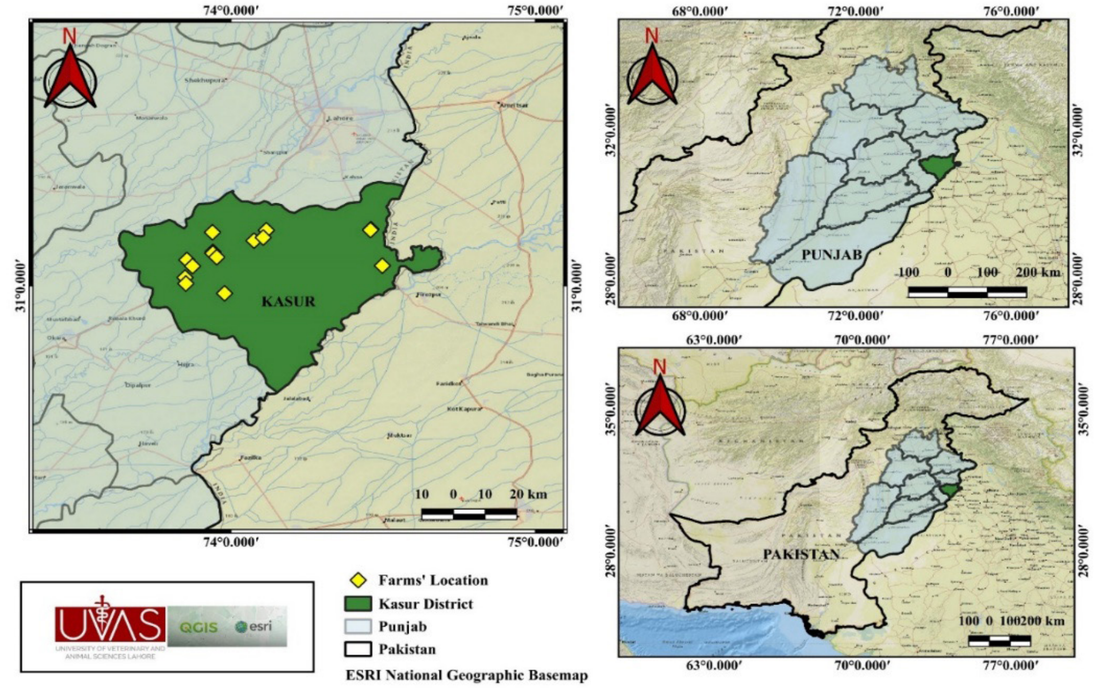

**Figure 1 –** Research field map of district Kasur has a longitude 74$^{o}$ 27′0″ E and latitude 31$^{o}$ 70 N and is situated in the east of Punjab, Pakistan

*Sample collection.* A total of 50 samples were gathered from the small intestines of apparently healthy chickens across 15 poultry farms in Kasur district. Sterile cotton swabs were utilized to collect the samples, and were placed in sterilized vials having phosphate-buffered saline (PBS) of pH 6.8 for additional analysis. All GI tract samples that are obtained were aseptically transported to the laboratory for further microbial examination [19].

*Isolation and preliminary screening of the isolates*

*Isolation of Lactic Acid Bacteria.* Under sterile environment, each sample from the small intestine was streaked onto *Lactobacillus*-specific acidified MRS agar (Oxoid, Basingstoke, UK) and incubated for a duration of 48 hours at 37°C. After initial isolation on MRS agar, presumptive LAB colonies were purified by repeated streaking onto Tryptic Soy Agar (TSA; Oxoid, UK) a non-selective medium commonly used for obtaining pure bacterial cultures. Plates were incubated at 37°C for 24-48 hours [20]. The suspected *Lactobacillus* colonies were Gram stained and further confirmed through biochemical characterizations, including the motility, catalase, and oxidase test [20].

*Characterization of LAB to species level.* The bacterial strains that successfully underwent the *Lactobacillus* confirmation tests were chosen for molecular characterization. Following the manufacturer's guidelines, the DNA was extracted from overnight-grown *Lactobacillus* cells using Bacterial Genomic DNA Extraction Kit (Himedia, India). For the amplification of 16S rRNA gene, two of the universal primers (Sigma-Aldrich, St. Louis. USA) 27 F (5' AGAGTTTGATCCTGGCTCAG 3') and 1492 R (5' TACGGCTACCTTGTTAGGACTT 3') were employed.

The PCR amplification using MyCycler Thermal Cycler (Bio-Rad, USA) was accomplished by using a total volume of 40 µL PCR mix, prepared by adding 8 µL FIREPol master mix (kit number, manufacturer, country of origin) mix, 0.4 µL of each of the reverse and forward primer (Sigma-Aldrich, St. Louis. USA), 2 µL DNA, and 29.2 µL of nuclease-free water. The following protocol was used to do PCR amplifications: pre-denaturation at 95°C for 10 minutes, followed by 30 cycles of denaturation at 95°C for 30 seconds, annealing for 1 minute, and extension at 72°C for 1.5 minutes. After the final cycle, there was a 7-minute extension at 72°C [22].

The amplified ethidium bromide-stained PCR products were electrophoresed into 1% agarose gel and visualized under Gel doc/UV trans-illuminator (Alpha Innotech, USA) with DNA Marker (Thermo Fisher Scientific, USA) All the *Lactobacillus* strains were evaluated for probiotic characteristics after being recognized by 16S rRNA sequencing [23].

*Screening for probiotic properties*

*In vitro assay for acid tolerance.* The resistance of the observed strains to acidic environment was evaluated as described [24] with adjustments. Isolated bacteria were cultured in de Man Rogosa Sharpe (MRS) broth (Oxoid, Basingstoke, UK) at 37°C for 18 hours, then subcultured in fresh MRS broth for 24 hours. After centrifugation at 4000 × g for 5 minutes and two PBS (Merck, Germany) washes, the isolates were resuspended in PBS. A 1/100 dilution of each strain in PBS with pH levels of 2.0, 2.5, 3.0, and 3.5 was incubated for 4 hours. Then bacteria were cultured on MRS agar, under anaerobic conditions (Oxoid jar with AnaeroGen 2.5 L) at 37°C overnight, followed by cell counting on MRS agar.

*Quantification of LAB.* Bacterial colonies grown on selective media were enumerated as colony-forming units per milliliter (CFU/ml). Plates containing colonies within the range of 30-300 were used to calculate CFU.

$$\text{Number of Colonies/mL} = \frac{\text{No of Colonies Counted} \times \text{Dilution Factor}}{\text{Volume of Sample Plated}}$$

*In vitro assay for bile tolerance.* Bile tolerance was examined by using the methodology of [23] with modifications. The isolates were cultured in MRS broth for 18 hours at 37°C, then subcultured in fresh MRS broth and incubated for an additional 24 hours. The subcultured strains were introduced to MRS broth containing 0.3% or 1.0% oxgall (Sigma-Aldrich, St. Louis, MO, USA) and incubated at 37°C. Each sample was streaked on MRS agar plates and further incubated at 37°C for 24 hours. Colonies were subsequently counted and enumerated as CFU/mL. Bile tolerance was assessed by comparing viable cell counts on MRS agar with and without bile (Oxgall). The assay was performed in triplicates.

*Antibiotic susceptibility test.* The method used [20] was employed to assess the antibiotic resistance of the selected *Lactobacillus* species by utilizing commercially available antibiotic discs (Himedia, India). The whole surface of petri plates containing the Muller Hinton agar (Himedia, India) were covered by 100 µL of cell suspensions. The plates were then covered with a paper disc holding antibiotics for chicken: chloramphenicol, ciprofloxacin, erythromycin, ampicillin, tetracycline, and gentamicin. The results were recorded on the basis of Clinical and Laboratory Standards Institute (CLSI) breakpoints [24]. The plates were then incubated anaerobically at 37°C for 24 hours. The diameter of the clear region surrounding the antibiotic discs was used to gauge the antibiotic susceptibility of the isolates.

*Survival and growth kinetics*

*Temperature tolerance.* Freshly cultured isolates were incubated in MRS broth at temperatures ranging from 25°C to 45°C for 24-48 hours to assess their growth. Plate count method was used for this evaluation, with three replicates for each temperature.

*NaCl tolerance.* Using a fresh overnight culture of bacterial isolates, MRS broth was inoculated with various concentrations (4%, 6%, and 8%) of sodium chloride (Merck, Germany). This test was performed as defined by Shakoor et al. [27].

*Statistical analyses.* Three replications were employed for each experiment. Following that, an analysis of variance was performed using statistical analysis system (SAS) software version 9.1 (SAS Institute Inc., USA), and Tukey's test was applied to compare the average scores between the different treatment groups. The significance level was defined as $p < 0.05$.

## Results and discussion

*Sample collection and isolation of Lactic Acid Bacteria.* A total of 50 chicken small intestinal samples were collected from District Kasur for the isolation of Lactic Acid Bacteria (LAB). The isolated colonies exhibited a creamy, off-white appearance and showed a uniform round configuration. After isolating LAB, the specific colonies, identified through Gram staining analysis were further purified by subculturing on supplemented MRS agar. This was followed by pure culturing on Tryptic Soy Agar (TSA). Biochemical test results for selected lactic acid bacterial (LAB) colonies are given in Table 1.

**Table 1** – Biochemical profiling of the isolated lactic acid bacteria

| No. | Biochemical test | Results | Observations |
|---|---|---|---|
| 01. | Oxidase test | Negative | No violet color was observed |
| 02. | Catalase Test | Negative | No bubble liberation |
| 03. | Indole Test | Negative | No color change |
| 04. | Motility assay | Negative | Non-motile (Hanging Drop Method) |
| 05. | Methyl Red Test | Negative | No color change |
| 06. | Vogues Proskauer Test | Negative | No color change |
| 07. | Triple Sugar Iron Test | Negative | No Hydrogen Sulfide gas production was observed |
| 08. | Urease Test | Negative | No color change was observed |
| 09. | Citrate Utilization Test | Negative | No color change |

*Molecular characterization by amplification of targeted gene 16S rRNA of the isolates.* The analysis revealed the 16S rRNA gene extracted from the genome of *Lactobacillus* isolates. Arrows indicate the band of the 16S rRNA gene (585 base pairs) amplified by PCR. Lane M shows the 5000 bp DNA ladder, whereas lanes 1, 2, and 3 represent the 16S rRNA gene amplicons of L. casei, L. acidophilus, and L. plantarum, respectively (Figure 2).

*Screening for Probiotic Properties*

*Tolerance to acidic pH.* Descriptive statistics revealed that as pH levels increased from 2.0 to 3.5, there was a noticeable trend of higher cell counts. The mean cell count at pH 3.5 (166.67) was notably higher as compared to pH 2.0 (70.69) as shown in Table 2, suggesting increased tolerance and growth of LAB as pH levels becomes less acidic. Specifically, species like *L. acidophilus*, *L. plantarum*, and *L. casei* exhibit such behavior when exposed to different acidic conditions.

The one-way analysis of variance (ANOVA) showed that pH has a statistically significant effect on the CFU/mL of LAB species, as the associated p value is 0.001 ($p < 0.05$).

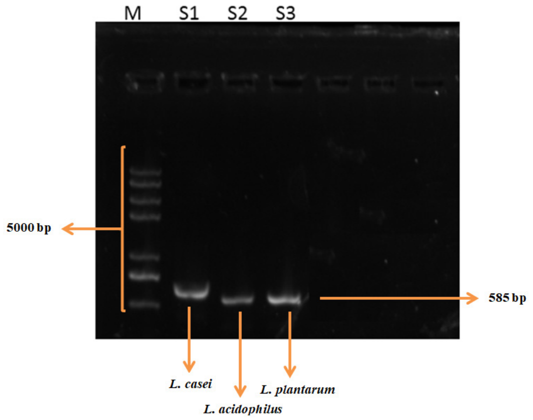

**Figure 2** – PCR analysis of 16S rRNA gene from the genome of *Lactobacillus* isolates.

**Table 2** – Effect of different pH levels on cell count of *Lactobacillus* isolates isolated from the chicken GIT

| pH levels | N | Mean ± Std. Deviation, CFU/mL |
|---|---|---|
| 2.00 | 13 | 70.69 ± 29.50$^a$ |
| 2.50 | 13 | 121.30 ± 54.02$^b$ |
| 3.00 | 12 | 125.08 ± 55.77$^b$ |
| 3.50 | 12 | 166.66 ± 74.14$^c$ |

Note: Superscript letters indicate significant differences between groups ($p < 0.05$), determined using one-way ANOVA followed by Tukey's test.

*Tolerance to bile salts.* The descriptive statistical analysis revealed significant differences in *Lactobacillus* growth between the two oxgall concentrations, as presented in Table 3. At 0.3% oxgall, the mean CFU/mL for *Lactobacillus* was 114.93, with a 95% confidence interval of 88.37 to 141.50 and a range from 100.00 to 288.00. In contrast, at 1.0% oxgall, the mean CFU/mL for *Lactobacillus* was 71.60, with a 95% confidence interval of 57.83 to 85.37 and a range from 33.00 to 102.00. These results indicate higher and more variable bacterial growth at the lower oxgall concentration (0.3%) compared to the higher concentration (1.0%), emphasizing the impact of oxgall concentration on *Lactobacillus* viability.

The ANOVA analysis revealed a noteworthy contrast in the effects of 0.3% and 1% bile salt concentrations on the CFU/mL of *Lactobacillus* species. With an F-value of 9.649, coupled with a p-value of 0.004 ($p < 0.05$), validates a statistically significant correlation. These findings underscore the influence that varying bile salt concentrations have on the behavior or characteristics of *Lactobacillus* species.

**Table 3** – Effect of bile concentration on cell count of *Lactobacillus* isolates from chicken GIT

| Bile Conc. | N | Mean ± Std. Deviation , CFU/mL |
|---|---|---|
| 0.3% | 15 | 114.93 ± 47.964 |
| 1.0% | 15 | 71.60 ± 24.870 |

*Note:* Means are statistically significant ($p < 0.05$).

*Antibiotic susceptibility assay.* The isolates were tested against 6 antibiotics, gentamicin (10 µg), ciprofloxacin (30 µg), ampicillin (10 µg), erythromycin (30 µg), chloramphenicol (30 µg), and tetracycline (30 µg). All the tested isolates showed highest resistance percentage to tetracycline (95%), and least resistance to chloramphenicol (40%), as revealed by the area of inhibition. 45% to 60% of the isolates were resistant to erythromycin and ampicillin, respectively. Around 50% of the tested isolates were intermediately susceptible to all the applied antibiotics as shown in Figure 3.

*Temperature tolerance.* The study identified the optimal temperature range for the growth of various *Lactobacillus* strains, highlighting their thermal adaptability. At 25°C, no growth was detected, indicating this temperature is below the survival threshold for *Lactobacillus plantarum*, which is sensitive to low temperatures. Significant growth was recorded between 35°C and 40°C, with optimal temperature at 37°C, where CFU/mL counts ranged from 278 to 299. Strains such as *L. casei* and *L. acidophilus* thrived within this range. Beyond 40°C, growth began to decline, with CFU/mL counts at 42°C ranging from 110 to 140 and further decreasing to 36 to 66 at 45°C (Figure 4).

*NaCl tolerance.* The growth of *Lactobacillus* species was assessed across different concentrations of sodium chloride (NaCl). Descriptive statistics showed that at 4% NaCl, the mean CFU/mL count was recorded as 104.56, decreasing to 51.13 and 41.13 CFU/mL at 6% and 8% NaCl, respectively. Overall, the mean CFU count across all concentrations was 67.16 CFU/mL, as shown in Table 4.

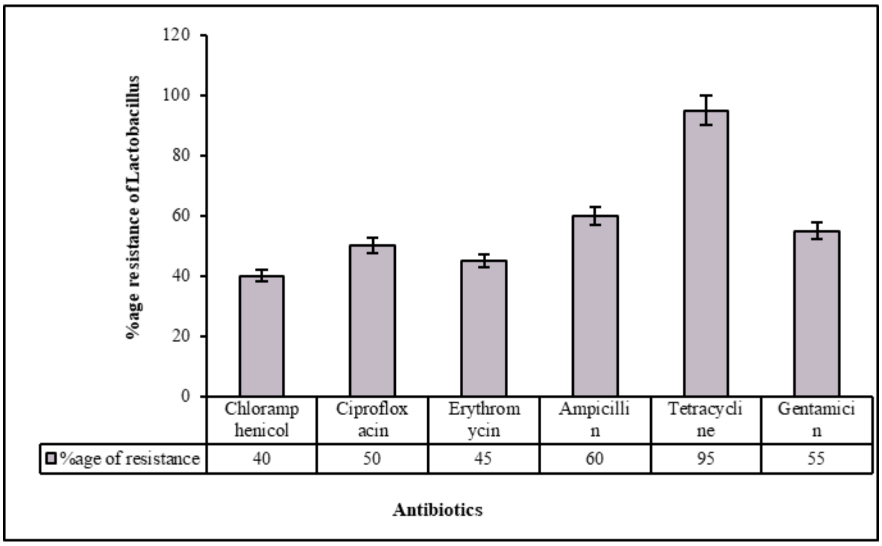

**Figure 3** – Percentage of sensitive, medium and high resistance of isolated *Lactobacillus* species

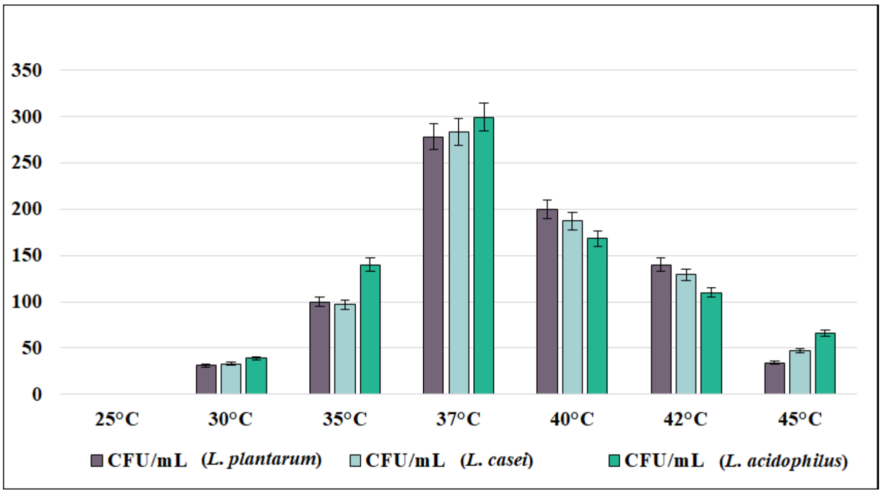

**Figure 4** – Temperature effect on cell count of *Lactobacillus* isolates from chicken GIT

**Table 4** – Effect of different NaCl concentrations on cell count of *Lactobacillus* species isolated from chicken GIT

| NaCl Conc. | N | Mean ± Std. Deviation , CFU/mL |
|---|---|---|
| 4% | 18 | 104.5556 ± 34.622$^{a}$ |
| 6% | 16 | 51.1250 ± 13.210$^{b}$ |
| 8% | 16 | 41.1250 ± 12.268$^{c}$ |

*Note:* Superscript letters indicate statistically significant differences among groups ($p < 0.05$) determined using one-way ANOVA followed by Tukey's test.

The ANOVA results highlighted significant differences in mean CFU/mL among various NaCl concentrations for *Lactobacillus* strains. It was revealed that there is a statistically significant relation between *Lactobacillus* species growth and concentration of NaCl, as shown by the low p value (0.009) ($p < 0.05$).

The present study focused on assessing the probiotic potential of *Lactobacillus* species isolated from the gastrointestinal tract (GIT) of chicken from different farms in district Kasur, through in vitro analysis. Lactic acid bacteria is a potential probiotic candidate as it has the ability to inhibit the intestinal development of pathogenic bacteria, regulate the gut microbiota and improve the overall wellbeing of the host [27].

A total of 50 small intestinal samples were collected and streaked on *Lactobacillus* specific agar. The cell morphologies of the isolates, as observed under light microscope, showed that they were Gram-positive rods. These rods varied in length from 1.1 to 5.7 µm and ranged in shape from crescent to straight. They were arranged in pairs or in long and short chains.

A strong probiotic *Lactobacillus* candidate should be tolerant to high acidic, bile, and salt conditions. Out of the total 50 isolates, 13 isolates showed highest tolerance to maximum pH level (3.0), and 12 showed least growth at pH 2.0. Overall, the strains > 60% of the tested isolates were able to proliferate at high pH levels. [28] studied 8 strains, including *L. paracasei*, *L. salivarius*, and *L. fermentum* which exhibited survival rates of 90% at pH 3. [29]discovered that not a single tested *Lactobacillus*-based probiotic strain could survive for 3 hours at pH 1.5. Our findings can relate with these results as the tested strains were able to withstand high acidic conditions.

According [30], the total bile salt concentrations in the chicken GIT are 0.175 and 0.008% in the cecum and duodenum, respectively. Nevertheless, numerous studies have taken into account the typical level of 0.3% bile salt while assessing the bile salt tolerance of possible probiotic LAB [31]. In our investigations, after six hours of incubation, all of the LAB strains were able to withstand 0.3% bile salt. [32] reported notable differences between the bile salt tolerance of several *Lactobacillus* species.

According to our findings, the tested isolated were able to grow at low NaCl concentration (4%). As the concentration increased from 4% to 6% and then to 8% there was a notable decline in the calculated CFU/mL of the isolates. In contrast, findings of the study conducted [33], except for *L. paracasei*, and *L. johnsonii*, all strains were tolerant to 2% (0.34 mol/L) and 4% (0.68 mol/L). On comparison, the outcomes of the current research suggest that the isolates did not belong to either of the above two species. *L. plantarum* showed the highest resistance to NaCl concentrations.

Antibiotic susceptibility test was performed using the agar well diffusion method. All the tested isolates showed highest resistance percentage to tetracycline (95%), and least resistance to chloramphenicol (40%), as revealed by the zone of inhibition. 45% to 60% of the isolates were resistant to erythromycin and ampicillin, respectively. Around 50% of the tested isolates were intermediately susceptible to all the applied antibiotics. The antibiotic resistance assay revealed that none of the isolates were completely resistant to the tested antibiotics, but each isolate did at least display an intermediate level of resistance to one antibiotic.

If gene transfer is involved, antibiotic resistance can become a concern [34]. However, overall there is no reason for alarm, as it might not be transmissible in nature and is not a particular trait of the microbial genus or species. Therefore, these resistance mechanisms may be inherent to the strain, as demonstrated by [35], who reported on vancomycin-resistant *Lactobacillus* spp.

To check the sensitivity of the isolates, a temperature tolerance test was conducted which revealed that at 25°C, no bacterial growth was observed, indicating that this temperature was below the minimum threshold for the survival of the tested *Lactobacillus* strain, *L. plantarum* as it is sensitive to low temperatures. Significant growth occurred from temperature range 35°C to 40°C. The optimal temperature for growth was found to be 37°C, with CFU/mL counts ranging from 278 to 299. *L. plantarum*, and *L. casei* could grow well at these temperature ranges.

## Conclusion

In conclusion, the current research demonstrates the probiotic potential of *Lactobacillus* species, isolated from the gastrointestinal tracts of chickens in Kasur district. The isolates showed significant tolerance to acidic (pH 3.0) and bile conditions (0.3% bile salt). They can also show resilience to NaCl concentrations up to 4%, and high resistance to tetracycline. Optimal bacterial growth was observed at 37°C, indicating this temperature as the most favorable for metabolic activity and proliferation. However, substantial growth was also recorded within a slightly broader temperature range of 35°C to 40°C, suggesting that the isolates possess moderate thermal adaptability and can maintain stable growth under varying environmental conditions. These findings suggest that *Lactobacillus* strains from chicken GIT are robust probiotic candidates for use as antibiotic alternatives in poultry production.

The use of naturally occurring probiotic strains derived from the host gut microbiota offers a promising alternative to antibiotic growth promoters. Such probiotics may help improve gut microbial balance, enhance nutrient utilization, support immune function, and ultimately promote better growth performance and productivity in poultry. This approach aligns with global efforts to develop sustainable and safe livestock production practices while reducing reliance on antibiotics.

Overall, the results provide valuable preliminary evidence supporting the potential application of indigenous *Lactobacillus* strains as probiotic supplements in poultry farming. However, further in vivo studies, safety assessments, and large-scale trials are necessary to confirm their effectiveness under commercial farming conditions. Future research focusing on formulation, stability, and field application could facilitate their practical use and contribute to improved poultry health, productivity, and food safety.

## Conflict of interest

All authors are aware of the article's content and declare no conflict of interest.

## References

1. Śliżewska K., Markowiak-Kopeć P., Żbikowski A., Szeleszczuk, P. (2020) The effect of synbiotic preparations on the intestinal microbiota and her metabolism in broiler chickens. *Sci Rep*., vol. 10, no. 1, pp. 4281-4294. https://doi.org/10.1038/s41598-020-61256-z.

2. Ciurescu G., Dumitru M., Gheorghe A., Untea A.E. et al. (2020) Effect of *Bacillus subtilis* on growth performance, bone mineralization, and bacterial population of broilers fed with different protein sources. *Poult Sci*., vol. 99, no. 11, pp. 5960-5971. https://doi.org/10.1016/j.psj.2020.08.075.

3. Wealleans A.L., Li W., Romero L.F., Mathis G., et al. (2018) Performance and cost-benefit improvements following supplementation with a combination of direct-fed microbials and enzymes to broiler chickens raised with or without ionophores. *J Appl Poult Res*., vol. 27, no. 1, pp. 23-32. https://doi.org/10.3382/japr/pfx036.

4. Sen S., Ingale S.L., Kim Y.W., Kim J.S., et al. (2012) Effect of supplementation of *Bacillus subtilis* LS 1-2 to broiler diets on growth performance, nutrient retention, caecal microbiology and small intestinal morphology. *Res Vet Sci*., vol. 93, no. 1, pp. 264-268. https://doi.org/10.1016/j.rvsc.2011.05.021.

5. Butaye P., Devriese L.A., Haesebrouck F. (2003) Antimicrobial growth promoters used in animal feed: effects of less well-known antibiotics on gram-positive bacteria. *Clin Microbiol Rev*., vol. 16, no. 2, pp. 175-188. https://doi.org/10.1128/CMR.16.2.175-188.2003.

6. Brown K., Uwiera R.R.E., Kalmokoff M.L., Brooks S.P.J., et al. (2017) Antimicrobial growth promoter use in livestock: a requirement to understand their modes of action to develop effective alternatives. *Int J Antimicrob Agents*., vol. 49, no. 1, pp. 12-24. https://doi.org10.1016/j.ijantimicag.2016.08.006.

7. Pineiro M., Stanton C. (2007) Probiotic bacteria: legislative framework–requirements to evidence Basis. *J Nutr*., vol. 137, no. 3, pp. 850-853. https://doi.org/10.1093/jn/137.3.850S.

8. Khan M., Anjum A.A., Nawaz M., Awan A.R., et al. (2019). Effect of newly characterized probiotic *Lactobacilli* on weight gain, immunomodulation and gut microbiota of *Campylobacter jejuni* challenged broiler chicken. *Pak Vet J*., 39(4), 473-478. https://doi.org/10.29261/pakvetj/2019.051.

9. Dumitru M., Habeanu M., Lefter N.A., Gheorghe A. (2020) The effect of *Bacillus licheniformis* as direct-fed microbial product on growth performance, gastrointestinal disorders and microflora population in weaning piglets. *Rom Biotechnol Lett*., vol. 25, no. 6, pp. 2060-2069. https://doi.org/10.25083/rbl/25.6/2060.2069.

10. Kowalska J.D., Nowak A., Śliżewska K., Stańczyk M., et al. (2020) Anti-Salmonella potential of new Lactobacillus strains with the application in the poultry industry. *Pol J Microbiol*., vol. 69 no. 1, pp. 5-18. https://doi.org/10.33073/pjm-2020-001.

11. Mohsin M., Abbas R.Z., Yin G., Sindhu Z.U.D., et al. (2021) Probiotics as therapeutic, antioxidant and immunomodulatory agents against poultry coccidiosis. *World's Poult Sci J*., vol. 77, no. 2, pp. 331-345. https://doi.org/10.1080/00439339.2021.1883412.

12. Al-Khalaifa H., Al-Nasser A., Al-Surayee T., Al-Kandari S., et al. (2019) Effect of dietary probiotics and prebiotics on the performance of broiler chickens. *Poult Sci*., vol. 98, no. 10, pp. 4465-4479. https://doi.org/10.3382/ps/pez282.

13. GuerraN.P., Bernárdez P.F., Méndez J., Cachaldora P., et al. (2007) Production of four potentially probiotic lactic acid bacteria and their evaluation as feed additives for weaned piglets. *Anim Feed Sci Technol*., vol. 134, no. (1-2), pp. 89-107. https://doi.org/10.1016/j.anifeedsci.2006.05.010.

14. Musikasang H., Tani A., H-kittikun A., Maneerat S. (2009) Probiotic potential of lactic acid bacteria isolated from chicken gastrointestinal digestive tract. *World J Microbiol Biotechnol*., vol. 25, pp. 1337-1345. https://doi.org/10.1007/s11274-009-0020-8.

15. Hyronimus B., Le Marrec C., Sassi A.H., Deschamps A. (2000) Acid and bile tolerance of spore-forming lactic acid bacteria. *Int J Food Microbiol*., vol. 61, no. (2-3), pp. 193-197. https://doi.org/10.1016/S0168-1605(00)00366-4.

16. Valdovska A., Jemeljanovs A., Pilmane M., Zitare I., et al. (2014) Alternative for improving gut microbiota: use of Jerusalem artichoke and probiotics in diet of weaned piglets. *Pol J Vet Sci*., vol. 17, no. 1, pp. 61-69. https://doi.org/10.2478/pjvs-2014-0008.

17. Timmerman H.M., Koning C.J., Mulder L., Rombouts F. M., et al. (2004) Monostrain, multistrain and multispecies probiotics–A comparison of functionality and efficacy. *Int J Food Microbiol*, vol. 96, no. 3, pp. 219-233. https://doi.org/10.1016/j.ijfoodmicro.2004.05.012.

18. 1998 District Census report of Kasur. 2000. Census publication no. 112. Population census organization statistics division, Government of Pakistan. www.pbs.gov.pk.

19.Tsega K.T., Maina K.J., Tesema N.B. (2023) Characterization of potential probiotics *Lactobacillus* species isolated from the gastrointestinal tract of Rhode Island Red (RIR) chicken in Ethiopia. *Heliyon*., vol. 9, no. 7, pp. 1-12. https://doi.org/10.1016/j.heliyon.2023.e17453.

20. Ruangpan Lila., Eleonor A.T. (2004) Bacterial isolation, identification and storage. Laboratory manual of standardized methods for antimicrobial sensitivity tests for bacteria isolated from aquatic animals and environment. http://hdl.handle.net/10862/1616.

21. Jannah S.N., Dinoto A., Wiryawan K.G., Rusmana I. (2014) Characteristics of lactic acid bacteria isolated from gastrointestinal tract of Cemani chicken and their potential use as probiotics. *J Anim Sci Technol*., vol. 37, no. 3, pp. 182-189. https://doi.org/10.5398/medpet.v37i3.7969.

22. Hou Q., Bai X., Li W., Gao X., et al. (2018) Design of primers for evaluation of lactic acid bacteria populations in complex biological samples. *Front Microbiol*., vol. 9, pp. 2045-2055. https://doi.org/10.3389/fmicb.2018.02045.

23. Dowarah R., Verma A.K., Agarwal N., Singh P., et al. (2018) Selection and characterization of probiotic lactic acid bacteria and its impact on growth, nutrient digestibility, health and antioxidant status in weaned piglets. *PloS One*., vol. 13, no. 3, pp. 1-24. https://doi.org/10.1371/journal.pone.0192978.

24. Heravi R.M., Kermanshahi H., Sankian M., Nassiri M.R., et al. (2011) Screening of *Lactobacilli* bacteria isolated from gastrointestinal tract of broiler chickens for their use as probiotic. *Afr J Microbiol Res*., vol. 5, no. 14, pp. 1858-1868. https://doi.org 10.5897/AJMR11.416.

25. Walker D.K., Gilliland S.E. (1993) Relationships among bile tolerance, bile salt deconjugation, and assimilation of cholesterol by *Lactobacillus acidophilus*. *J Dairy Sci*., vol. 76, no. 4, pp. 956-961. https://doi.org/10.3168/jds.S0022-0302(93)77422-6.

26. Wayne P.A. (2020) Performance Standards for Antimicrobial Susceptibility Testing. 30th ed. CLSI supplement M100. Clinical and Laboratory Standards Institute. ISBN 978-1-68440-066-9.

27. Shakoor G., Akbar A., Samad A., Khan S.A., et al. (2017) Isolation of lactic acid bacteria from chicken gut and its probiotic potential characterization. *Int J Biosci*., vol. 11, no. 3, pp. 1-9. http://dx.doi.org/10.12692/ijb/11.3.1-9.

28. Brownlie E.J., Chaharlangi D., Wong E.O.Y., Kim D., et al. (2022) Acids produced by *Lactobacilli* inhibit the growth of commensal *Lachnospiraceae* and S24-7 bacteria. *Gut Microbes*., vol. 14, no. 1, pp. 1-19. https://doi.org/10.1080/19490976.2022.2046452.

29. Ehrmann M.A., Kurzak P., Bauer J., Vogel, R.F. (2002) Characterization of *lactobacilli* towards their use as probiotic adjuncts in poultry. *J Appl Microbiol*., vol. 92, no. 5, pp. 966-975. https://doi.org/10.1046/j.1365-2672.2002.01608.x.

30. Sahadeva R.P.K., Leong S.F., Chua K.H., Tan C.H., et al. (2011) Survival of commercial probiotic strains to pH and bile. *Int Food Res J*., vol. 18, no. 4, pp. 1515-1522. https://api.semanticscholar.org/CorpusID:35409345.

31. Lin J., Sahin O., Michel L.O., Zhang Q. (2003) Critical role of multidrug efflux pump CmeABC in bile resistance and in vivo colonization of *Campylobacter jejuni*. *Infect Immun*., vol. 71, no. 8, pp. 4250-4259. https://doi.org/10.1128/IAI.71.8.4250-4259.2003.

32. García-Hernández Y., Pérez-Sánchez T., Boucourt R., Balcázar J.L., et al. (2016) Isolation, characterization and evaluation of probiotic lactic acid bacteria for potential use in animal production. *Res Vet Sci*., vol. 108, pp. 125-132. https://doi.org/10.1016/j.rvsc.2016.08.009.

33. Zheng Y., Lu Y., Wang J., Yang L., et al. (2013) Probiotic properties of *Lactobacillus* strains isolated from Tibetan kefir grains. *PloS One*., vol. 8, no. 7, pp. 1-18. https://doi.org/10.1371/journal.pone.0069868.

34. Shokryazdan P., Kalavathy R., Sieo C.C., Alitheen N.B., et al. (2014) Isolation and characterization of *Lactobacillus* strains as potential probiotics for chickens. *J Trop Agric Sci*., vol. 37, no. 1, pp. 141-157. http://psasir.upm.edu.my/id/eprint/41782.

35. Gueimonde M., Sánchez B., G. de los Reyes-Gavilán C., Margolles A. (2013) Antibiotic resistance in probiotic bacteria. *Front Microbiol*., vol. 4, pp. 202-208. https://doi.org/10.3389/fmicb.2013.00202.

36. Handwerger S., Pucci M.J., Volk K.J., Liu J., et al. (1994) Vancomycin-resistant *Leuconostoc mesenteroides* and *Lactobacillus casei* synthesize cytoplasmic peptidoglycan precursors that terminate in lactate. *J Bacteriol*., vol. 176, no. 1, pp. 260-264. https://doi.org/10.1128/jb.176.1.260-264.1994.

***Information about authors:***

*Kashaf Nokhaiz – M.Phil Scholar, Department of Wildlife and Ecology, University of Veterinary and Animal Sciences (Lahore, Punjab, Pakistan, e-mail: kshf1249@gmail.com)*

*Syed M. Bukhari – PhD, Assistant Professor, Department of Wildlife and Ecology, University of Veterinary and Animal Sciences (Lahore, Punjab, Pakistan, e-mail: mohsin.bukhari@uvas.edu.pk)*

*Khalil Ur Rehman – PhD, Assistant Professor, GC Woman University, (Sialkot, Punjab, Pakistan, e-mail: khalil.lastnamerehman@yahoo.com)*

*Hafeez Ur Rehman Chohan –Researcher, King Abdullah University of Science and Technology (Jeddah, Saudi Arabia, e-mail: kshf1249@gmail.com)*

*Areej A. Shahzad –PhD Scholar, University of Education, Lahore, Pakistan (Lahore, Punjab, Pakistan, e-mail: areejayeshashahzad@gmail.com)*

*Shahla Andleeb – PhD, Assistant Professor, GC Woman University (Sialkot, Punjab, Pakistan, e-mail: shahla.andleeb@yahoo.com)*

*Waqas Ali – PhD, Assistant Professor, Department of Wildlife and Ecology, University of Veterinary and Animal Sciences (Lahore, Punjab, Pakistan, e-mail: waqas.ali@uvas.edu.pk)*

IRSTI 31.21.25; 34.27.17 https://doi.org/10.26577/IJBCh20251826

T.V. Polyudova[1*], T.A. Akentieva[2], M.V. Antipeva[1, 2],
A.L. Esaev[1], L.P. Yunnikova[1]

[1]Institute of Ecology and Genetics of Microorganisms, Perm Federal Research Center,
Ural Branch of the Russian Academy of Sciences, Perm, Russia
[2]Perm State Agro-Technological University named after academician D.N. Prianishnikov, Perm, Russia
*e-mail: polyudova@iegm.ru

*(Received 30 June 2025; received in revised form 22 December 2025; accepted 26 December 2025)*

# Toxicity and antimicrobial activity of tropylated aniline and its derivatives

**Abstract.** This study investigated the biological activity of tropylated aniline 4-(7-cyclohepta-1,3,5-trienyl) aniline and its derivatives belonging to the group of secondary aromatic amines – *N*-2-hydroxyphenylmethyl-4$^1$-(7-cyclohepta-1,3,5-trienyl)aniline and the group of azomethines – *N*-2-hydroxyphenylmethylene-4$^1$-(7-cyclohepta-1,3,5-trienyl)aniline. Tropylated aniline was synthesized by mixing tropyllium tetrafluoroborate and aniline in ethanol. *N*-2-hydroxyphenylmethyl-4$^1$-(7-cyclohepta-1,3,5-trienyl)aniline and *N*-2-hydroxyphenylmethylene-4$^1$-(7-cyclohepta-1,3,5-trienyl)aniline were obtained via a one-pot multicomponent synthesis. Tropylated aniline and its derivatives showed no toxic effects on Galleria mellonella larvae upon invasive administration of 10 µL solutions at a concentration of 1 mg/mL (10 µg/larva). In vitro experiments demonstrated that Gram-negative bacteria and Gram-positive bacteria with hydrophilic cell walls exhibit low susceptibility to tropylated aniline and are resistant to its derivatives. The minimum inhibitory concentration (MIC) and minimum bactericidal concentration (MBC) of the studied compounds were determined. The MBC/MIC ratio for all susceptible bacteria was ≤4, indicating their bactericidal activity. A dependence of bacterial susceptibility to tropylated aniline and its derivatives on the level of bacterial cell hydrophobicity was demonstrated. High susceptibility to the studied compounds was revealed in mycomembrane bacteria of the Mycobacterium genus, whose cell walls contain mycolic acids and exhibit a high level of hydrophobicity. The obtained compounds are of practical relevance as potential anti-tuberculosis agents.

**Keywords:** antibacterial activity, hydrophobicity, tropylidene cycle, mycomembrane, toxicity, *Galleria mellonella.*

## Introduction

The rapid spread of multidrug resistance (MDR) among bacteria and micromycetes motivates researchers to continuously search for and develop new safe antibacterial compounds [1]. Globally, a vast number of promising compounds are actively being synthesized or isolated from natural sources; however, many have yet to gain widespread recognition due to limited knowledge of their bioactive potential. Substances exhibiting high antibacterial activity combined with practical applicability are relatively uncommon. Most antibiotics are developed based on existing and known molecular scaffolds, whose functional activity is enhanced through modification of peripheral groups [2]. Nevertheless, the emergence of resistance in contemporary bacteria necessitates the search for novel compounds founded on fundamentally new chemical structures.

Modern organic synthesis strategies demand the production of complex, highly functionalized structures from readily available and simple starting materials in a minimal number of steps. One such key starting compound is 1,3,5-cycloheptatriene (tropilidene), a precursor to a wide range of derivatives [3]. Furthermore, the 1,3,5-cycloheptatriene moiety itself is a biologically active pharmacophore. Its structure is integral to natural products such as thujic acid and thujaplicins, which exhibit a dual spectrum of action–demonstrating both antifungal and antibacterial activity [4].

The phase transition capabilities of molecules can be leveraged in drug design, including for creating agents capable of overcoming transdermal barriers.

© 2025 al-Farabi Kazakh National University

Effective antitumor agents, decovine and decocine, have been developed based on alkaloids containing the tropilidene cycle [5].

Tropylation of aniline yields a compound with significantly reduced phytotoxicity, as demonstrated in tests using wheat seeds. Moreover, seed treatment with tropylated aniline substantially enhanced their germination energy [6]. It has also been shown that the low-toxicity compound 4-(7-cyclohepta-1,3,5-trienyl)aniline inhibits the growth of Staphylococcus bacteria and the micromycete Candida albicans. Antifungal and bacteriostatic activity has also been demonstrated for its ditropylated secondary amine derivative, 4-(7-cyclohepta-1,3,5-triehyl)-N-(1-cyclohepta-2,4,6-trienyl)aniline [7].

Consequently, compounds incorporating the tropilidene cycle hold significant interest as potential antibiotic drugs. The absence of toxicity to humans and animals is corroborated by the long-term clinical use of tropilium-containing drugs such as desipramine, peritol (cyproheptadine). It should be noted that the tropylated azomethine – *N*-2-hydroxyphenylmethylene-$4^1$-(7-cyclohepta-1,3,5-trienyl)aniline and the tropylated secondary amine – *N*-2-hydroxyphenylmethyl-$4^1$-(7-cyclohepta-1,3,5-trienyl)aniline are classified as low-toxicity compounds [8].

New insights into the biological activity of tropilidene-containing compounds could significantly broaden the prospects for their practical application.

The aim of this work is to study tropylated aniline and its derivatives, obtained via a simple and safe synthetic method, assessing their toxicity using the *Galleria mellonella* larvae model and evaluating their spectrum of antibacterial activity.

## Materials and methods

*Objects of Study.* Compounds: 4-(7-cyclohepta-1,3,5-trienyl)aniline (Compound 1), *N*-2-hydroxyphenylmethylene-$4^1$-(7-cyclohepta-1,3,5-trienyl) aniline (Compound 2), *N*-2-hydroxyphenylmethyl-$4^1$-(7-cyclohepta-1,3,5-trienyl)aniline (Compound 3). Stock solutions of the test compounds (10 mg/mL) were prepared by dissolving weighted samples in a 1:1 mixture of ethanol:dimethyl sulfoxide (DMSO).

*Synthesis of Compounds*. Compound 1 was synthesized by tropylation of aniline with tropylium tetrafluoroborate in ethanol at room temperature [9]. Compound 2 was obtained via a one-step reaction of salicylaldehyde, aniline, and tropylium tetrafluoroborate at room temperature, using ethanol as the solvent [10]. Compound 3 was prepared in a single step by reacting salicylaldehyde, aniline, sodium tetrahydroborate, and tropylium tetrafluoroborate in ethanol at room temperature [11].

*Toxicity assessment.* Larvae of G. *mellonella* were used [12]. Larvae were obtained from the Educational and Scientific Center for Honeybee Biology at Perm State Agro-Technological University. For each experiment, 30 healthy larvae weighing 0.2 ± 0.02 g were selected, placed in sterile 90-mm Petri dishes, and immobilized by incubation at 4oC for 3 h. Stock solutions of the compounds in the ethanol : DMSO (1:1) solvent mixture (10 mg/mL), diluted 10-fold with sterile deionized water (1 mg/mL), were injected (10 µL) into the hemocoel of G. *mellonella* larvae through the last left proleg using a 30G syringe (BD Micro-FineTM Plus, USA). The larvae were incubated at 37°C for 72 h without feeding. A group of larvae injected with 10 µl of water served as a control. Larval viability was assessed by gentle probing with a blunt needle; larvae that showed no reaction were considered dead.

*Bacterial strains.* Nineteen bacterial strains from different collections were used (Table 1). Strains were pre-cultured for 20-24 h in liquid nutrient media at their optimal temperatures (Table 1). Cultures were adjusted to a suspension of 106 CFU/mL in sterile nutrient medium for the antibacterial activity (ABA) test for inoculation into plates (10 µL per well).

*Antibacterial Activity* (ABA). The stock solution (10 mg/mL) was diluted 10-fold with sterile deionized water for ABA testing. The ABA of the 10-fold diluted ethanol:DMSO solvent mixture was also assessed. ABA was determined using the broth microdilution method in Mueller-Hinton Broth (MHB) or Middlebrook 7H9 medium (Table 1) in 96-well microtiter plates [13]. After bacterial inoculation, plates were incubated at the optimal temperature for each strain for 24 h. Growth visualization was performed by adding 10 µL of a 1% solution of 2,3,5-triphenyltetrazolium chloride to each well and incubating for 30 min. Assessment was based on the red coloration of metabolically active cells. The minimum inhibitory concentration (MIC) of the test compounds was defined as the lowest concentration that prevented visible microbial growth. Minimum bactericidal concentrations (MBC) were determined by removing the contents from wells showing no growth, adding 100 µL of sterile nutrient medium to these wells, and incubating the plates for at least 48 h. Bacteria remaining viable after removal of the antibacterial agent resumed growth. The concentration of the compound solution from which no bacterial growth resumed after removal was recorded as the MBC.

**Table 1 –** Microorganisms used for testing antibacterial activity and their cultivation conditions.

| | Species | Strain | Medium for cultivation | Antibacterial test medium | Opt t°C |
|---|---|---|---|---|---|
| 1 | *Bacillus licheniformis* | VKM B-1711D | LB | MHB | 37 |
| 2 | *Corinebacterium ammoniagenes* | IEGM 1862 | TSB | MHB | 30 |
| 3 | *Enterococcus faecalis* | NCIMB 13280 | TSB | MHB | 37 |
| 4 | *Escherichia coli* | ATCC 25922 | LB | MHB | 37 |
| 5 | *Escherichia coli* | M-17 | LB | MHB | 37 |
| 6 | *Listeria innocua* | M-2 | BHI | MHB | 37 |
| 7 | *Mycobacterium avium* | GISK 168 | Middlbrook 7H9 | Middlbrook 7H9 | 37 |
| 8 | *Mycolicibacterium smegmatis* | GISK 107 | Middlbrook 7H9 | Middlbrook 7H9 | 37 |
| 9 | *Mycolicibacterium smegmatis* | mc$^2$ 155 | Middlbrook 7H9 | Middlbrook 7H9 | 37 |
| 10 | *Proteus vulgaris* | NCIMB 1475 | LB | MHB | 37 |
| 11 | *Pseudomonas fluorescens* | ATCC 948 | LB | MHB | 37 |
| 12 | *Rhodococcus erythropolis* | IEGM 10 | LB | MHB | 30 |
| 13 | *Rhodococcus equi* | NCIMB 10027 | LB | MHB | 30 |
| 14 | *Staphylococcus aureus* | ATCC 25923 | LB | MHB | 37 |
| 15 | *Staphylococcus cohnii* | VKM 3165 | LB | MHB | 37 |
| 16 | *Staphylococcus epidermidis* | ATCC 12228 | LB | MHB | 37 |
| 17 | *Staphylococcus epidermidis* | ATCC 29887 | LB | MHB | 37 |
| 18 | *Streptococcus pyogenes* | ATCC 8668 | TSB | MHB | 37 |
| 19 | *Streptococcus pyogenes* | NCIMB 8884 | TSB | MHB | 37 |

*Determination of Hydrophobicity.* The hydrophobicity of microbial cells was determined using the Microbial Adhesion To Hydrocarbons (MATH) test with n-hexadecane and bacterial suspensions in 10 mM phosphate buffer (pH 7.2), according to the method described by Nachtigall et al. [14].

*Statistical Analysis.* All experiments were performed in at least three independent trials. Statistical analysis was conducted using StatSoft Statistica 12 software (applying the Mann-Whitney U test) and MS Excel 2010 (calculating mean values and confidence intervals at $\alpha$=0.05).

## Results and discussion

Compound 1 was prepared in one step as shown in Figure 1. The implementation of this synthesis method for 4-(7-cyclohepta-1,3,5-trienyl)aniline (tropylated aniline) enabled the use of non-explosive tropylium tetrafluoroborate instead of tropylium perchlorate, and ethanol as the solvent instead of tetrahydrofuran. The reaction mixture was maintained at room temperature for 3 h. The proposed synthesis method is safer compared to the method described in [15], as it eliminates the use of explosive tropylium perchlorate and employs the less toxic solvent ethanol [9].

Compound 2 was obtained by reacting salicylaldehyde, aniline, and tropylium tetrafluoroborate in ethanol, maintaining the reaction mixture at room temperature for 1 h. The reaction proceeded according to the scheme presented in Figure 2.

Compound 3 was prepared by reacting salicylaldehyde, aniline, sodium tetrahydroborate, and tropylium tetrafluoroborate in ethanol, maintaining the reaction mixture at room temperature for 2 hours. The reaction proceeded according to the scheme presented in Figure 3.

The obtained compounds are hydrophobic, insoluble in water, but readily soluble in the ethanol:DMSO solvent mixture.

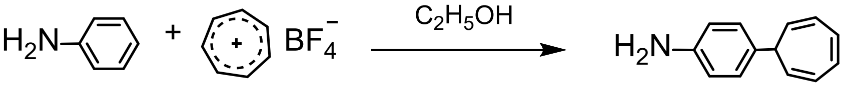

1

**Figure 1** – Scheme for obtaining compound 1 – 4-(7-cyclohepta-1,3,5-trienyl)aniline (tropylated aniline)

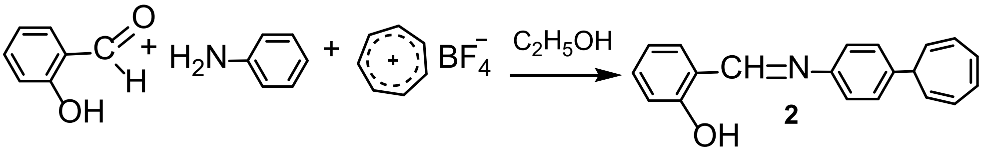

2

**Figure 2** – Scheme for obtaining compound 2 – N-2-hydroxyphenylmethylene-4$^1$-(7-cyclohept-1,3,5-trienyl)aniline

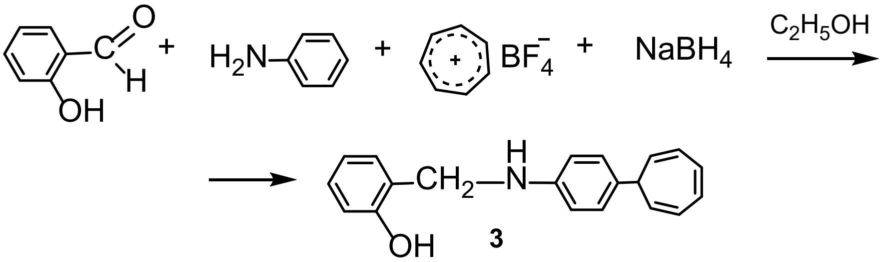

3

**Figure 3** – Scheme for obtaining compound 3 – N-2-hydroxyphenylmethyl-4$^1$-(7-cyclohept-1,3,5-trienyl)aniline

Toxicity of tropylated aniline and its derivatives was assessed using *G. mellonella* larvae. *Galleria* larvae provide a rapid and convenient in vivo model for toxicity evaluation, the results of which correlate with mammalian models [12]. The 100% ethanol:DMSO solvent mixture exhibited toxic effects on *G. mellonella* larvae, with only about 40% survival after 3 days. Diluting the solvent mixture 10-fold with water (10%) eliminated any detectable negative effects on the larvae. Tropylated aniline and its derivatives at a concentration of 1 mg/mL in the 10% solvent mixture also caused no toxic effects in the larvae for 3 days following injection into the hemocoel (10 µg/larvae) (Figure 4).

Investigation of the ABA of tropylated aniline and its derivatives revealed inhibitory effects against a broad spectrum of bacteria. Bactericidal activity was also observed for the compounds (Table 2). The Gram-negative bacteria investigated (*E. coli*, *P. fluorescens*, and *P. vulgaris*) exhibited moderate susceptibility (MIC ≥62.5 µg/ml) only to Compound 1 – 4-(cyclohepta-1,3,5-trien-7-yl)aniline, and were resistant to its modified forms. Bactericidal activity of Compound 1 was detected only against *E. coli*, with an MBC 2-4-fold higher than the MIC. The outer membrane of Gram-negative bacteria constitutes a unique protective barrier, incorporating efflux systems for foreign substances. The O-antigen, a polysaccharide with hydrophilic properties located on the outer face of the Gram-negative bacterial membrane, impedes the penetration of hydrophobic compounds through the outer layer [16], which may explain the resistance to tropylated aniline and its derivatives.

As evident from Table 2, the test compounds were primarily active against Gram-positive bacteria. The highest MIC and MBC values were observed for bacteria of the phylum Bacillota. Representatives of the phylum Actinomycetota exhibited greater susceptibility to the test compounds, with the exception of *C. ammoniagenes* IEGM 862. According to [17], an MBC/MIC ratio ≤4 indicates bactericidal activity, while a ratio ≥8 indicates bacteriostatic activity. In cases where MIC and MBC values were precisely determined, the corresponding MBC/MIC ratios were ≤4, further confirming bactericidal action. Only for Compound 2 against *M. smegmatis* GISK 107 was the MBC/MIC ratio equal to 8.

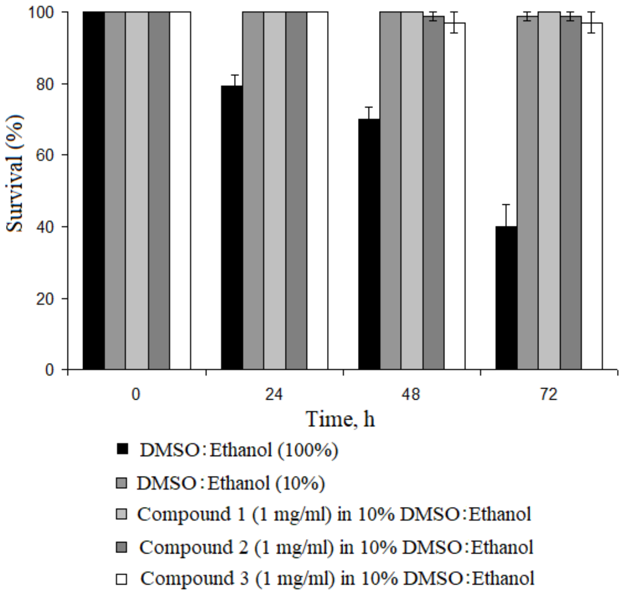

**Figure 4** – Survival of *G. mellonella* caterpillars after the introduction of solutions of tropylated aniline and its derivatives into the hemocoel

**Table 2** – Minimum inhibitory (MIC) and bactericidal (MBC) concentrations of tropylated aniline and its derivatives, µg/ml

| Microorganisms | | | Compound 1 | | Compound 2 | | Compound 3 | |
|---|---|---|---|---|---|---|---|---|
| | | | MIC | MBC | MIC | MBC | MIC | MBC |
| Gram-negative bacteria | | *E. coli* ATCC 25922 | 62.5 | 250 | 250 | >500 | >500 | >500 |
| | | *E. coli* M-17 | 125 | 250 | >500 | >500 | >500 | >500 |
| | | *P. fluorescens* ATCC 948 | 250 | >500 | >500 | >500 | >500 | >500 |
| | | *P. vulgaris* NCIMB 1475 | 250 | >500 | >500 | >500 | >500 | >500 |
| Gram-positive bacteria | Phylum Bacillota | *B. licheniformis* VKM B-1711D | 250 | 500 | 250 | 250 | 62.5 | 62.5 |
| | | *E. faecalis* NCIMB 13280 | 250 | 500 | 500 | 500 | 500 | 500 |
| | | *L. innocua* M-2 | 250 | 250 | >500 | >500 | 125 | 250 |
| | | *S. aureus* ATCC 25923 | 500 | 500 | 250 | 500 | 125 | 500 |
| | | *S. cohnii* VKM 3165 | 125 | 250 | 125 | 125 | 62.5 | 125 |
| | | *S. epidermidis* ATCC 12228 | >500 | >500 | 500 | 500 | 125 | 125 |
| | | *S. epidermidis* ATCC 29887 | 62.5 | 250 | 250 | 500 | 125 | 205 |
| | | *S. pyogenes* ATCC 8668 | 62.5 | 62.5 | 500 | 500 | 500 | 500 |
| | | *S. pyogenes* NCIMB 8884 | 500 | 500 | 500 | 500 | 250 | 500 |
| | Phylum Actino-mycetota | *C. ammoniagenes* IEGM 862 | 125 | 250 | >500 | >500 | 125 | 125 |
| | | *R. erythropolis* IEGM 10 | 7.8 | 7.8 | 62.5 | 62.5 | 3.9 | 7.8 |
| | | *R. equi* NCIMB 10027 | 7.8 | 15.6 | 31.2 | 62.5 | 15.6 | 15.6 |
| | | *M. smegmatis* GISK 107 | 1.95 | 7.8 | 1.95 | 15.6 | 15.6 | 31.2 |
| | | *M. smegmatis* mc$^2$ 155 | 1.95 | 7.8 | 3.9 | 15.6 | 15.6 | 31.2 |
| | | *M. avium* GISK 168 | 1.95 | 7.8 | 3.9 | 15.5 | 15.6 | 31.2 |

The efficacy of antimicrobial compounds, their binding to the cell, and penetration intensity depend directly on cell surface characteristics, including hydrophobicity. Assessment of test bacteria hydrophobicity via their adhesion to *n*-hexadecane showed that populations of Gram-negative bacteria lacked a cell fraction exhibiting affinity for this solvent. Minimal hydrophobicity was detected in the Gram-positive bacteria *L. innocua* M-2 (2.7%) and two strains of *S. pyogenes* ATCC 8668 and NCIMB 8884 (3.9% and 2.5%). A low level of hydrophobicity (23%) was found in the *E. faecalis* NCIMB 13280 culture (Table 3). Growth inhibition of Gram-positive bacteria with low cell surface hydrophobicity by tropylated aniline and its derivatives was only observed at high concentrations (250-500 µg/ml).

**Table 3** – Hydrophobicity of bacteria according to the MATH test with n-hexadecane

| Bacteria | | Hydrophobicity, % |
|---|---|---|
| Gram-negative bacteria | *E. coli* ATCC 25922 | 0 |
| | *E. coli* M-17 | 0 |
| | *P. fluorescens* ATCC 948 | 0 |
| | *P. vulgaris* NCIMB 1475 | 0 |
| Gram-positive bacteria | *B. licheniformis* VKM B-1711D | 44.0±2.97 |
| | *C. ammoniagenes* IEGM 862 | 48.5±7.0 |
| | *E. faecalis* NCIMB 13280 | 23.2±2.68 |
| | *L. innocua* M-2 | 2.7±1.2 |
| | *M. smegmatis* mc$^2$ 155 | 84.8±6.34 |
| | *M. smegmatis* GISK 107 | 92.5±2.54 |
| | *M. avium* GISK 168 | 90.2±3.32 |
| | *R. erythropolis* IEGM 10 | 55.8±2.84 |
| | *R. equi* NCIMB 10027 | 88.5±11.3 |
| | *S. aureus* ATCC 25923 | 42.0±8.6 |
| | *S. cohnii* VKM 3165 | 65.5±11.1 |
| | *S. epidermidis* ATCC 12228 | 75.8±9.5 |
| | *S. epidermidis* ATCC 29887 | 73.6±10.3 |
| | *S. pyogenes* ATCC 8668 | 3.9±1.1 |
| | *S. pyogenes* NCIMB 8884 | 2.5±0.8 |

To evaluate the influence of cell hydrophobicity level on susceptibility to the test substances, the investigated bacteria were divided into two groups based on cell wall type: Gram-positive (Group 1) and Gram-negative (Group 2). Comparison of these groups revealed a significant difference (p = 0.003) in the distribution of cell wall hydrophobicity, confirmed by the Mann-Whitney U test (Fig. 5A). Subsequently, the Gram-positive bacteria group (Group 1) was subdivided into two subgroups: one containing only representatives of the phylum Bacillota (Group 1a), and the other containing representatives of the phylum Actinomycetota (Group 1b). Significant differences (p = 0.012) in the distribution of cell wall hydrophobicity were also demonstrated between these subgroups of Gram-positive bacteria (Fig. 5B), with Actinomycetota bacteria exhibiting higher cell hydrophobicity levels.

The observed differences in hydrophobicity distribution are attributed to structural features of the cell walls in the compared bacterial groups. It is known that the low hydrophobicity of Gram-negative bacteria is provided by the lipopolysaccharide of the outer membrane. The hydrophobic properties of Gram-positive bacterial cell walls depend on the structure of the peptidoglycan layer. Specifically, the Actinobacteria assigned to Group 1b (*C. ammoniagenes*, *Mycobacterium* spp., *Rhodococcus* spp.) contain mycolic acids in their cell walls. The number of carbon atoms in mycolic acids varies significantly among different bacterial genera. For instance, corynebacteria contain mycolic acids with chain lengths of 20-36 carbon atoms. Bacteria of the genus *Rhodococcus* possess chains of 35-50 carbon atoms, while mycobacteria have mycolates with chain lengths of 60-98 carbon atoms [18, 19]. The structure of mycolic acids determines the permeability of the bacterial cell wall to various compounds and the overall surface hydrophobicity. The peptidoglycan of *Mycobacterium* is covalently linked to arabinogalactan. The termini of arabinogalactan are esterified with mycolic acids, forming the inner layer of the mycobacterial outer membrane, known as the mycomembrane, which dictates the physical and chemical properties of their cell surface [20].

The minimum inhibitory concentrations (MICs) of the test substances were analyzed similarly: a comparison was made between Gram-positive and Gram-negative bacterial groups (Group 1 vs Group 2) (Figure 6), followed by a comparison between the Gram-positive subgroups – Bacillota and Actinomycetota (Group 1a vs Group 1b) (Figure 7).

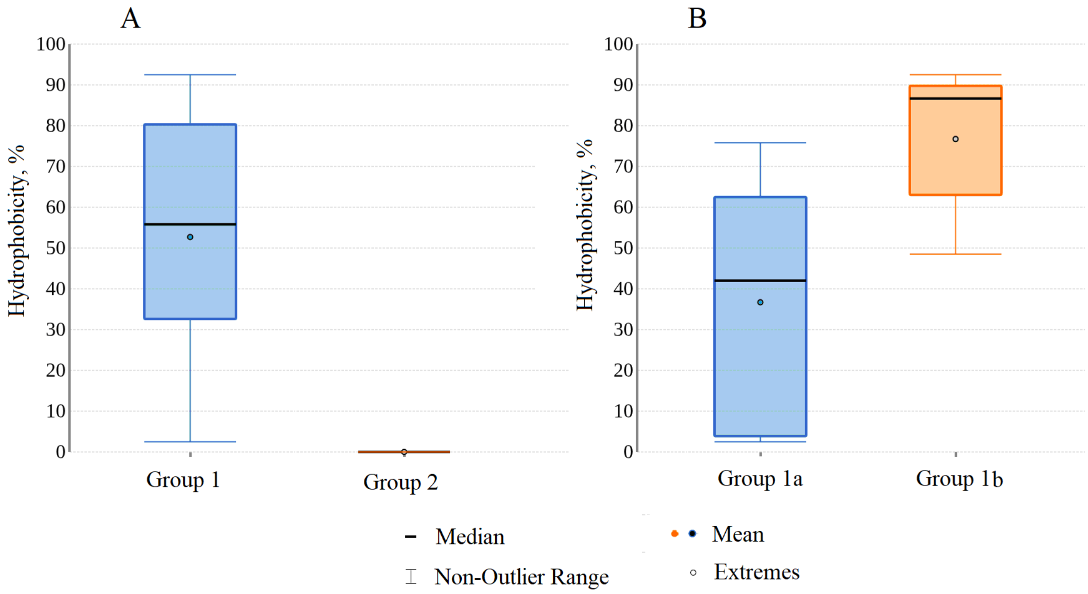

**Figure 5** – Distribution of hydrophobicity levels between Gram-positive (Group1) and Gram-negative (Group 2) bacteria (A) and of hydrophobicity levels of Gram-positive bacteria between *Bacillota* (Group 1a) and *Actinomycetota* (Group 1b): Boxplot visualization and Mann-Whitney U-test (A – *p*=0.003; B – *p*=0.012)

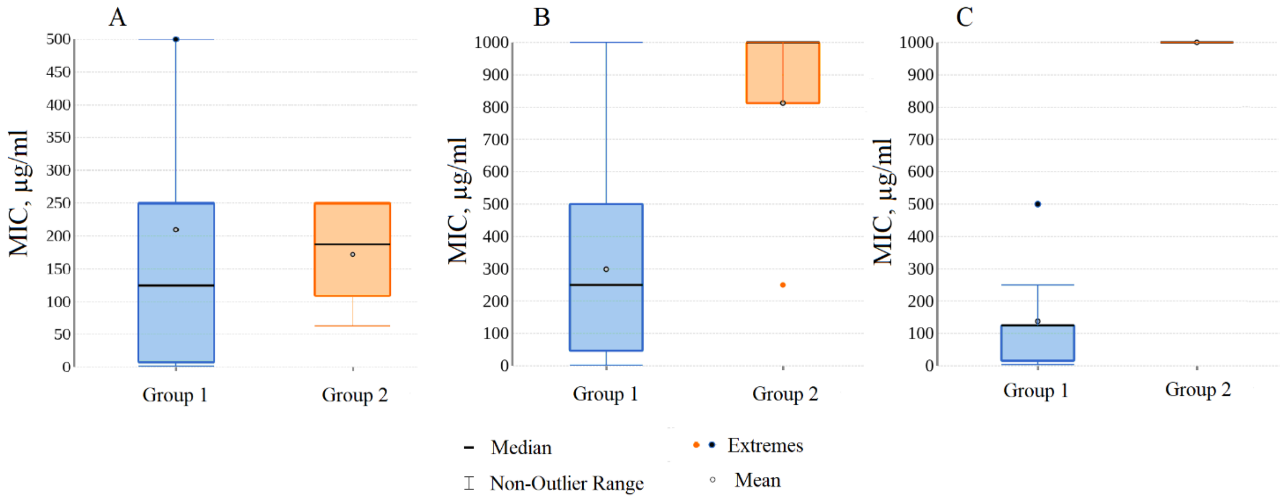

**Figure 6** – Analysis of the MICs of Compound 1 (A), Compound 2 (B) and Compound 3 (C) against Gram-positive and Gram-negative bacteria: Boxplot visualization and Mann-Whitney U test. (A – p=0.648; B – p=0,037; C – p=0,003)

When comparing antibacterial effects on Gram-positive and Gram-negative bacteria, analysis of the MICs of the three compounds showed no significant difference in the distribution of MIC values for Compound 1 (p=0.648) (Figure 6A). However, the median MIC values were relatively high, at 125 µg/ml for Gram-positive and 187.5 µg/ml for Gram-negative bacteria. Conversely, the distributions of susceptibility to Compounds 2 and 3 differed significantly between Gram-positive and Gram-negative bacterial groups (p = 0.037 and p = 0.003, respectively) (Figure 6B, C). Gram-negative bacteria exhibited high resistance to both derivatives of tropylated aniline. Gram-positive bacteria, in contrast, were highly susceptible to both compounds, with the greatest susceptibility observed towards the azomethine variant

(Compound 3). Overall, Figure 6 demonstrates that microorganisms with hydrophobic surfaces – the Gram-positive bacterial group – were more susceptible to the test substances than bacteria with hydrophilic cell walls – the Gram-negative microorganism group. This analysis indicates a direct relationship between the level of cell wall hydrophobicity and susceptibility to tropylated aniline and its derivatives.

Comparative analysis of susceptibility within the Gram-positive subgroups (Bacillota vs Actinomycetota) confirmed this observation (Figure 7). The susceptibility distributions for all three compounds differed significantly (p = 0.004 for Compound 1, p = 0.035 for Compound 2, p = 0.004 for Compound 3). Representatives of the phylum Bacillota, with hydrophobicity less than 40%, were more resistant to the test compounds, while the lowest MIC values against all compounds were detected for the most hydrophobic bacteria of the phylum Actinomycetota. Within the Actinomycetota group, the *C. ammoniagenes* IEGM 862 strain possessed the lowest hydrophobicity level and also exhibited the highest, atypical resistance to the investigated compounds. The extremes observed in the box plots of Figure 7 for Group 1b bacteria reflect the MIC values of the test compounds for the *C. ammoniagenes* IEGM 862 strain.

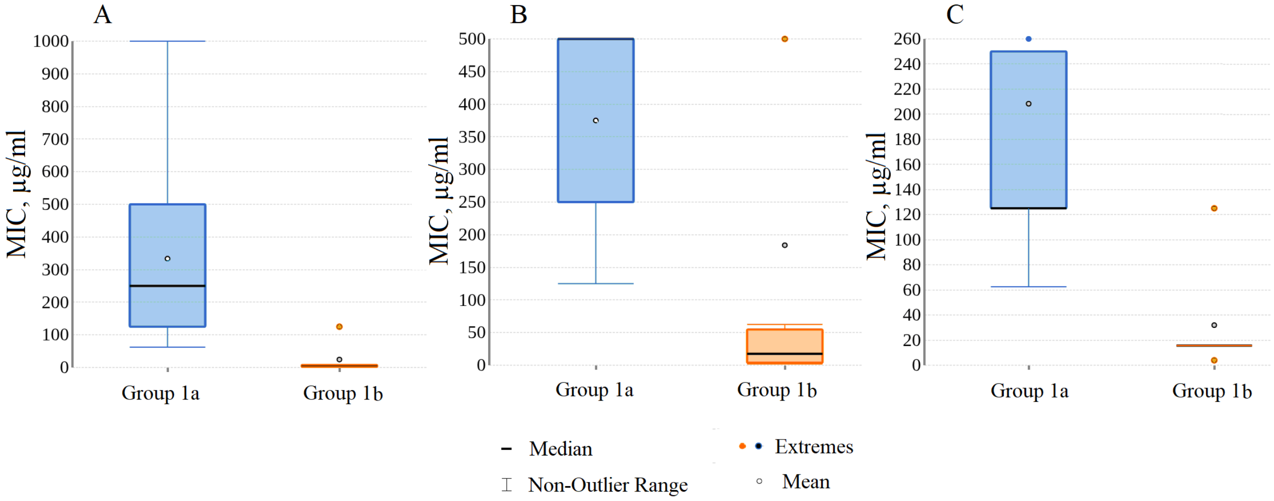

**Figure 7** – Analysis of the MICs of Compound 1 (A), Compound 2 (B) and Compound 3 (C) against *Bacillota* (Group 1a) and *Actinomycetota* (Group 1b) Gram-positive bacteria: Boxplot visualization and Mann-Whitney U test (A – p=0.004; B – p=0.035; C – p=0.004)

Thus, the most pronounced susceptibility to tropylated aniline and its derivatives was observed in bacteria with hydrophobic cell walls and high content of long-chain mycolic acids (*Rhodococcus* spp., *M. smegmatis*, *M. avium*), which can constitute 20-50% of the cell dry weight [21].

Tropylated aniline and its derivatives, being structural analogs of *para*-aminobenzoic acid, may competitively inhibit enzymes in the tetrahydrofolate biosynthesis pathway. Tetrahydrofolate is essential for the biosynthesis of purines, thymidylate, methionine, glycine, pantothenic acid, and N-formyl-methionyl tRNA. Inhibition of the folate pathway leads to depletion of tetrahydrofolate, cessation of cell growth, and potential cell death. Compounds with antifolate activity, similar to anticancer drugs (e.g., methotrexate, raltitrexed) and antibacterial agents (e.g., cotrimoxazole), are considered as novel therapeutic approaches for treating infections caused by tuberculous bacteria, including multidrug-resistant strains [22, 23]. The folate biosynthesis pathway offers multiple targets for small molecules with potential for tuberculosis therapy [23, 24].

The tropylium cation, a component of the compounds investigated in this work, may also possess biological activity. The natural compound tropodithietic acid (TDA), known for its broad-spectrum antibacterial action, is relevant. TDA biosynthesis involves dithiol formation, which oxidizes to a disulfide and increases the electron density of the tropylium oxide moiety. Consequently, TDA can chelate metals, providing the chemical basis for its biological activity. It has been shown that the action of neutral TDA on *E coli* functions via a proton antiporter mechanism. At elevated proton levels, the carboxyl group of TDA picks up $H^+$, allowing the neutral molecule to diffuse into the cell. In the pH-neutral cytosol, TDA releases the proton. The basicity of TDA, conferred by the tropylium oxide and α-carboxyl group, enables chelation of monovalent cations. This complex diffuses out of the cell, resulting in an exchange of $H^+$ for a monovalent cation such as $K^+$ [25].

## Conclusion

In conclusion, the non-toxic compounds synthesized via simple reactions of tropylium tetrafluoroborate and aniline demonstrate significant practical potential. The proposed methods for the synthesis of tropylated aniline and its derivatives make it possible to overcome production problems and scalability limitations inherent in other existing approaches. Due to its inherent reactivity, the tropylium cation readily forms covalent bonds with diverse substrates, generating reactive intermediates amenable to further chemical transformations. This positions it as a highly promising precursor for developing novel compounds, including those with broad-spectrum antibacterial activity.

The precise mechanism of antibacterial action for the investigated compounds remains to be fully elucidated. However, the structural features of tropylated aniline and its derivatives suggest potential antifolate activity and/or an ability to disrupt the proton membrane potential, analogous to mechanisms observed in derivatives of *para*-aminobenzoic acid and tropodithietic acid. Critically, the hydrophobicity of the target bacterial surface is a key determinant governing the binding of tropylated aniline and its derivatives to bacterial cells and the subsequent manifestation of antibacterial effects. The high affinity of these compounds for hydrophobic cell walls could form the basis for their use in combination therapies with other agents unable to penetrate such barriers. The potential synergistic effects of tropylated aniline and its derivatives with antibiotics targeting intracellular sites represent an important avenue for future research to identify effective combinations with both novel and established antimicrobial agents. Utilizing chemical compound-antibiotic combinations constitutes a primary strategy for addressing antibiotic resistance. The identified antibacterial effects of the obtained compounds against mycomembrane bacteria indicate their potential as anti-tuberculosis agents.

## Acknowledgments

The work was completed as part of the state task “Biodiversity of microorganisms in anthropogenically polluted ecosystems and functional-genetic mechanisms of their adaptation to stressful environmental conditions” (state registration number 124020500028-4).

## Conflict of interest

The authors declare that they have no conflicts of interest.

## References

1. Cotugno S, De Vita E, Frallonardo L, Novara R, et al. (2025) Antimicrobial Resistance and Migration: Interrelation Between Two Hot Topics in Global Health. *Ann Glob Health.*, vol. 91, no. 1, https://10.5334/aogh.4628.

2. Fischbach M.A., Walsh C.T. (2009) Antibiotics for emerging pathogens. *Science*. vol. 325, no 5944, pp. 1089-1093. https://10.1126/science.1176667.

3. Zahra F.T., Saeed A., Mumtaz K., Albericio F. (2023) Tropylium Ion, an Intriguing Moiety in Organic Chemistry. *Molecules*. vol. 28, no. 10. https://10.3390/molecules28104095 .

4. Mashkovskij M.D. (2002) Medicines [Lekarstvennye sredstva]. Moscow: Novaya volna. vol. 2 . pp. 432-433.

5. Enikeeva Z.M., Ibragimov A.A., Navruzov S.N., Aliev D.A. (2009) New drugs derived from tropolone alkaloids [Novye preparaty, poluchaemye iz tropolonovyh alkaloidov]. *Siberian J. Oncology*., no. 2, p. 70.

6. Mudrykh N. M., Akentyeva T. A., Zhakova S. N. (2024) Evaluation of the effect of azomethine on spring wheat seedlings [Ocenka dejstviya azometina na prorostki yarovoj pshenicy]. *Izvestiya nizhnevolzhsky agrouniversity complex*. vol. 78, no. 6, pp. 170-177. https://10.32786/2071-9485-2024-06-17.

7. Yunnikova L.P., Akent’eva T.A., Ésenbaeva V.V. (2015) Tropylation of Arylamines and Antimicrobial Activity of 4-(7-Cyclohepta-1,3,5-Trienyl)-N-(1-Cyclohepta-2,4,6-Trienyl)Aniline [Tropilirovanie arilaminov i antimikrobnaya aktivnost’ 4-(7-ciklogepta-1,3,5-trienil)- N-(1-ciklogepta-2,4,6-trienil)anilina]. *Pharmaceutical Chemistry Journal*. vol. 49, no. 4, pp. 243-245. https://10.1007/s11094-015-1263-3.

8. Akentyeva T.A., Makhmudov R.R. (2017) One-pot multicomponent synthesis of 4-(7-cyclohepta-1,3,5-trienyl)aniline [Odnoreaktornyj mnogokomponentnyj sintez proizvodnyh 4-(7-ciklogepta-1,3,5-trienil)aniline]. *Journal of General Chemistry*. vol. 87, no. 7, pp. 1204-1206. https://doi.org/10.1134/S1070363217070301

9. Akentyeva T.A., Yunnikova L.P., Esenbaeva V.V. (2018) Modified analysis 4-(7-cyclohepta-1,3,5-trienyl)aniline [Modificirovannyj sintez 4-(7-ciklogepta-1,3,5-trienil)anilina] *Butlerov Communications*, vol. 56, no. 11, pp. 128-130.

10. Akentyeva T.A. (2023) Method for obtaining low-toxic N-2-hydroxyphenylmethylene-41-(7-cyclohepta-1,3,5-trienyl)aniline [Sposob polucheniya malotoksichnogo N-2-gidroksifenilmetilen-41-(7-tsiklogepta-1,3,5-triyenil)anilina]. Patent № 2787769. Russian Federation.

11. Akentyeva T.A., Zhakova S.N. (2022) Method for producing low-toxic N-2-hydroxyphenylmethyl-41-(7-cyclohepta-1,3,5-trienyl)aniline exhibiting antimicrobial activity [Sposob polucheniya malotoksichnogo N-2-gidroksifenilmetil-41-(7-tsiklogepta-1,3,5-triyenil)anilina, prodolzhayushchego antimikrobnuyu aktivnost']. Patent № 2786532. Russian Federation.

12. Piatek M., Sheehan G., Kavanagh K. (2021) *Galleria mellonella*: The Versatile Host for Drug Discovery, In Vivo Toxicity Testing and Characterising Host-Pathogen Interactions. *Antibiotics (Basel)*. vol. 10, no. 12. https://10.3390/antibiotics10121545.

13. CLSI Documente M07-A10. (2015) Methods for dilution antimicrobial susceptibility tests for bacteria that grow aerobically, approved standard, 10th ed.; CLSI: Wayne, PA, USA, 35.

14. Nachtigall C., Weber C., Rothenburger S., et al. (2019) Test parameters and cell chain length of *Streptococcus thermophilus* affect the microbial adhesion to hydrocarbons assay: a methodical approach. *FEMS Microbiology Letters*, vol. 366, no. 12. https://doi.org/10.1093/femsle/fnz150

15. Yunnikova L.P., Akentyeva T.A. (2013) 4-(1-Cyclohepta-2,4,6-trienyl)aniline and its hydrochloride salt exhibiting antimicrobial activity [4-(1-Cyclohepta-2,4,6-trienyl)aniline i yego gidrokhloridnaya sol', proyavlyayushchiye antimikrobnuyu aktivnost']. Patent № 2479571. Russian Federation.

16. Farhana A., Khan Y.S. (2025) Biochemistry, Lipopolysaccharide/ In: StatPearls [Internet]. Treasure Island (FL): StatPearls Publishing. https://pubmed.ncbi.nlm.nih.gov/32119301/

17. Benjamin T., Adebare J., Remi Ramota R., Rachael K. (2012) Efficiency of some disinfectants on bacterial wound pathogens. *Life Science Journal*, vol. 9, no. 2, pp. 752-755. http://www.lifesciencesite.com

18. Sutcliffe I.C., Brown A.K., Dover L.G. (2010) The Rhodococcal Cell Envelope: Composition, Organisation and Biosynthesis. In: Alvarez, H. (eds) Biology of Rhodococcus. Microbiology Monographs, vol. 16. Springer, Berlin, Heidelberg. https://doi.org/10.1007/978-3-642-12937-7_2

19. Liu J., Nikaido H. (1999) A mutant of *Mycobacterium smegmatis* defective in the biosynthesis of mycolic acids accumulates meromycolates. *Proc Natl Acad Sci USA*, vol. 96, no 7, pp. 4011-4016. https://10.1073/pnas.96.7.4011.

20. Hart E.M., Bernhardt T.G. (2025) The mycomembrane. *Curr Biol*. vol. 35, no. 3. https://10.1016/j.cub.2024.11.002.

21. Burkovski A. (2018) The role of corynomycolic acids in Corynebacterium-host interaction. *Antonie Van Leeuwenhoek*, vol. 111, no. 5, pp. 717-725, https://10.1007/s10482-018-1036-6.

22. Heaslet H., Harris M., Fahnoe K., et al. (2009) Structural comparison of chromosomal and exogenous dihydrofolate reductase from *Staphylococcus aureus* in complex with the potent inhibitor trimethoprim. *Proteins*, vol.76, pp. 706-717. https://doi.org/10.1002/prot.22383

23. Thiede J.M., Kordus S.L., Turman B.J., et al. (2016) Targeting intracellular p-aminobenzoic acid production potentiates the anti-tubercular action of antifolates. *Sci Rep*. vol. 1, no. 6. https://10.1038/srep38083.

24. Hajian B., Scocchera E., Shoen C., et al. (2019) Drugging the Folate Pathway in Mycobacterium tuberculosis: The Role of Multi-targeting Agents. *Cell Chem Biol.* vol. 26, no. 6, pp. 781-791. https://10.1016/j.chembiol.

25. Wilson M.Z., Wang R., Gitai Z, Seyedsayamdost M.R. (2016) Mode of action and resistance studies unveil new roles for tropodithietic acid as an anticancer agent and the γ-glutamyl cycle as a proton sink. *Proc Natl Acad Sci USA*. vol. 113, no. 6, pp. 1630-1635. https://10.1073/pnas.1518034113.

***Information about authors:***

*Tatyana Polyudova – Candidate of Biological Sciences, Head of the Laboratory of Microbial Development Biochemistry, Institute of Ecology and Genetics of Microorganisms, Perm Federal Research Center, Ural Branch of the Russian Academy of Sciences (Perm, Russia, e-mail:polyudova@iegm.ru)*

*Tatyana A. Akentieva – Candidate of Chemical Sciences, Associate Professor of the Department of Ecology and Chemical Technologies Perm State Agro-Technological University named after academician D.N. Prianishnikov (Perm, Russia, e-mail: akentieva@hotmail.com)*

*Marina V. Antipeva – Candidate of Biological Sciences, Junior Researcher, Laboratory of Microbial Development Biochemistry, Institute of Ecology and Genetics of Microorganisms, Perm Federal Research Center, Ural Branch of the Russian Academy of Sciences (Perm, Russia, e-mail: m.antipeva@iegm.ru)*

*Artem Esaev - Candidate of Biological Sciences, Junior Researcher, Laboratory of Microbial Development Biochemistry, Institute of Ecology and Genetics of Microorganisms, Perm Federal Research Center, Ural Branch of the Russian Academy of Sciences (Perm, Russia, e-mail: a.esaev@iegm.ru)*

*Lidia P. Yunnikova - Doctor of Chemical Sciences, Professor of the Department of Ecology and Chemical Technology, Perm State Agro-Technological University named after academician D.N. Prianishnikov (Perm, Russia, e-mail: l.yunkova@iegm.ru)*

*Larisa P. Yunnikova - Junior Researcher, Laboratory of Microbial Development Biochemistry, Institute of Ecology and Genetics of Microorganisms, Perm Federal Research Center, Ural Branch of the Russian Academy of Sciences (Perm, Russia, e-mail: l.yunkova@iegm.ru)*

IRSTI 69.25.15 https://doi.org/10.26577/IJBCh20251827

N. Popov[1], V. Barabanov[2], S. Shalgimbayeva[3],
D. Batayeva[4], A. Zhumanova[3], A. Muratkyzy[3],
B. Abdullayeva[3*]

[1]Kazekoproekt LLP, Almaty, Kazakhstan
[2]Volga-Caspian Branch of the VNIRO Federal State Budgetary Institution, Astrakhan, Russia
[3]Al-Farabi Kazakh National University, Almaty, Kazakhstan
[4]Kazakh National Women's Teacher Training University, Almaty, Kazakhstan
*e-mail: abdullayeva.bagila1@gmail.com

*(Received 08 November 2025; received in revised form 23 December 2025; accepted 26 December 2025)*

# Feeding resources and key nutrients of commercial fish in the Ural-Caspian Basin

**Abstract.** The article presents information on hydrobiological monitoring in the Ural–Caspian Basin, including phytoplankton, zooplankton, and benthic communities in the Ural–Caspian Basin. The annual dynamics of hydrobiont biomass density have been established, showing seasonal variations with the highest values in summer and the lowest in winter. The qualitative and quantitative composition of aquatic organisms was studied depending on the discharge volume and flow levels of the Ural (Zhaiyk) River. In high-water years, the biomass of phytoplankton and the abundance of zooplankton increased by 1.4 and 2.2 times, respectively. In recent years, an increase in the biomass of gelatinous zooplankton has been observed. Among them, the comb jelly Mnemiopsis is spreading particularly actively, successfully colonizing shallow, low-salinity areas of the sea. This species is a major consumer of zooplankton, which negatively affects the food base of planktivorous fish and the juveniles of all ichthyofauna species in the Caspian Sea. An analysis was also conducted on the feeding preferences of anadromous, marine, semi-anadromous, and freshwater species inhabiting the Caspian Sea.

**Keywords:** forage base, abundance, biomass, ichthyofauna, fish diet

## Introduction

The development of fish stocks is largely determined by the state of the reservoir's food base, since at different stages of their life cycle, their diet includes planktonic organisms of both plant and animal origin, zoobenthos, and, for predatory species, representatives of the freshwater and marine ichthyofauna. Semi-anadromous and river fish mainly feed in the coastal zones of the Northern and Middle Caspian, which are influenced by freshwater inflow [1-8]. After spawning, the grown juveniles and adult individuals begin their downstream migration to feeding grounds in the Caspian Sea. These feeding grounds are generally restricted to the isobath with a salinity of 6–7 ‰ [9-11]. Sturgeons, herrings, sprats, and mullets feed not only in the Northern but also in the Middle and Southern Caspian [8, 12].

The Ural–Caspian basin plays a key role in the Republic of Kazakhstan in the reproduction and harvesting of fish resources. It includes the northeastern part of the Caspian Sea, where active efforts are being made to preserve and increase the populations of commercial fish species. In this area, feeding migrations occur on an abundant food base, followed by the formation of stocks of many fish populations.

The aim of this work was to assess the hydrobiological characteristics of the study area, including phytoplankton, zooplankton, and macrozoobenthos (at the group level), and to identify the main nutritional components of adult individuals of commercial fish species in the natural environment

To achieve the stated goal, it is necessary to address the following main objectives: to study the species diversity and seasonal changes in the abundance and biomass of aquatic organisms; to determine the influence of river discharge regimes on the increase of biological productivity of the studied groups; and to investigate and identify the main diet of commercial fish species under natural conditions

© 2025 al-Farabi Kazakh National University

## Materials and methods

In 2023, comprehensive scientific research was conducted in the Ural–Caspian basin, including the coastal zones of the Caspian Sea. The purpose of these studies was to examine hydrological and hydrobiological parameters, as well as to assess the distribution and abundance of aquatic biological resources in the Caspian Sea. The field expeditions were carried out during the winter, spring, summer, and autumn periods. Sampling maps are shown in Figure 1.

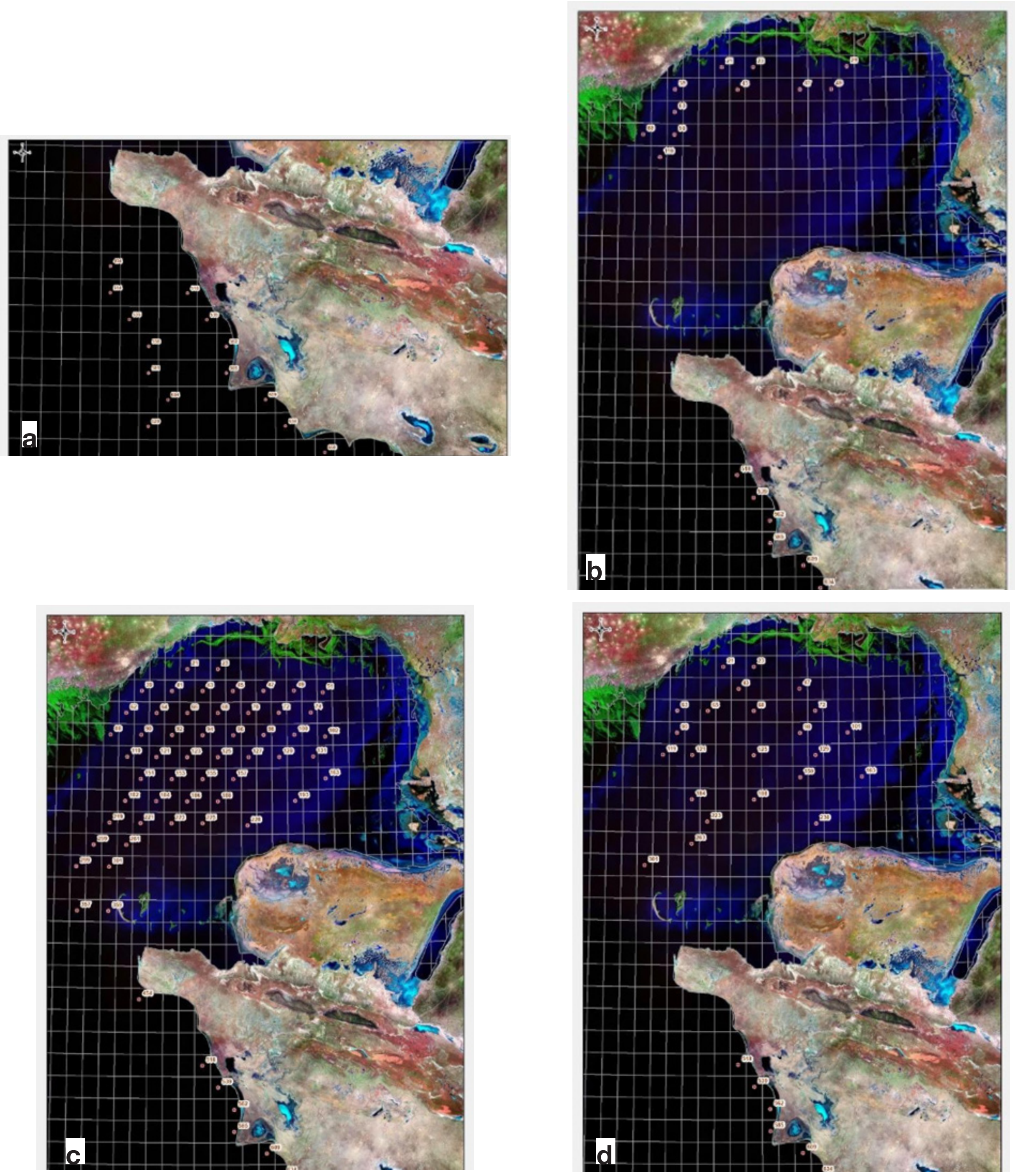

**Figure 1 –** Map-diagram of the observation station's location for hydrobiological and ichthyological sampling in (a) winter; (b) spring; (c) summer; (d) autumn

The results of studies on hydrobiological and ichthyological indicators in the Zhaiyk–Caspian basin in 2023 and during the comparative period of 2019–2022 were obtained from the reporting materials of Kazekoproekt LLP.

Phytoplankton samples were collected using Molchanov bathometers (GR-18) or BM-48, zooplankton samples – with an Apstein net, and benthos samples – with Petersen and Van Veen grab samplers, covering an area of 0.025 m². The processing of phytoplankton samples was carried out according to the method [13], zooplankton and zoobenthos by [14] at laboratory conditions. Phytoplankton samples were concentrated by centrifugation and examined by direct microscopic observation using a light microscope (OLYMPUS BX 41, Japan). Zooplankton was analyzed by direct microscopic examination with a binocular microscope (Levenhuk MED 900B, USA) using a Bogorov counting chamber. Zoobenthos was identified using a binocular microscope (Levenhuk MED 900B, USA), and biomass was determined using torsion and analytical balances (MT-HA203E, Mettler Toledo, Switzerland). The abundance and biomass of planktonic algae and invertebrates, including benthic organisms, were also quantified by [15-19].

The species composition of fish was taken from the recommendations on the allocation of total allowable catches (TAC) in the Atyrau region, following the territorial (administrative) principle within the waters of the Kazakhstan part of the Caspian Sea [20]. The methodology for dividing the TAC by regions is based on research data on the distribution of ichthyofauna and on data regarding the exploitation of fish resources, whose stocks are in a satisfactory condition.

Statistical processing of the research materials was carried out using standard methodologies. The main statistical parameters were calculated using the Microsoft Excel software package. To compare the mean values of several groups and to identify significant differences between them, analysis of variance (ANOVA – Analysis of Variance) was applied. The Statistica software was used for analysis of variance. Calculations were performed using Student's t-test.

$$t = \frac{\left(\bar{x}_1 + \bar{x}_2\right)}{\sqrt{\frac{s_1^2}{n_1}} + \sqrt{\frac{s_2^2}{n_2}}}$$

$\bar{x}_1$ – observed mean of first sample
$\bar{x}_2$ – observed mean of second sample
$s_1^2$ – standard deviation of first sample
$s_2^2$ – standard deviation of second sample
$n_1$ – sample size of first sample
$n_2$ – sample size of second sample

## Results and discussion

Phytoplankton is the primary producer of organic matter in a water body and serves as food for zooplankton and zoobenthos. During different seasons of the year, due to climatic conditions, the qualitative and quantitative composition of phytoplankton varies widely. At the end of February – beginning of March 2023, the phytoplankton community included 42 algal taxa from 5 divisions: Cyanophyta (blue-green algae) – 4, Bacillariophyta (diatoms) – 28, Myzozoa – 7, Ochrophyta – 1, and Chlorophyta (green algae) – 2. In terms of abundance and biomass, diatoms dominated, accounting for 75.6 mln inds/m³ and 1067.9 mg/m³, or 77.5% and 96.2% of the total phytoplankton, respectively. The average values were estimated at 97.5 mln inds/m³ and 1110.6 mg/m³ (Figure 5).

In April–May, the number of divisions (groups) remained unchanged; however, there was a sharp increase in newly appearing species, reaching 92 taxa. The most widely represented were Cyanophyta (blue-green algae) – 22 species (869.9 mln inds/m³ and 82.3 mg/m³), Bacillariophyta (diatoms) – 49 taxa (39.1 mln inds/m³ and 361.4 mg/m³), and Chlorophyta (green algae) – 15 species (127.0 mln inds/m³ and 36.5 mg/m³). The average abundance of phytoplankton increased 10.6 times (to 1033.4 mln inds/m³), while the biomass decreased 1.9 times (to 568.7 mg/m³) due to the dominance of small-sized and newly formed species.

During the summer period (June–August), the phytoplankton list included 170 algal species from 7 divisions: Cyanophyta (blue-green algae) – 38, Bacillariophyta (diatoms) – 79, Myzozoa – 10, Ochrophyta – 2, Charophyta – 4, Chlorophyta (green algae) – 34, and Euglenophyta – 3 species. The first three groups, compared to the spring indicators, continued to intensively increase their biopotential, which also included green algae. The number of taxa and the total abundance of phytoplankton (1935.7 mln inds/m³) reached their maximum values, with an average biomass of 1127.1 mg/m³. In the September samples, the quantitative and qualitative composition of aquatic plants remained at a fairly high level, although a tendency toward a decrease in the average number of taxa and their abundance was noted (Table 1).

**Table 1** – Phytoplankton of the eastern part of the Northern Caspian in 2023

| № | Number of taxa | Abundance, mln inds/m$^3$ | Biomass, mg/m $^3$ | Number of taxa | Abundance, mln inds/m$^3$ | Biomass, mg/m$^3$ | Number of taxa | Abundance, mln inds/m$^3$ | Biomass, mg/m$^3$ | Number of taxa | Abundance, mln inds/m$^3$ | Biomass, mg/m$^3$ |
|---|---|---|---|---|---|---|---|---|---|---|---|---|
|  | February-March |  |  | April-May |  |  | June-August |  |  | September |  |  |
| 1 | 4 | 10.6 ± 1.3 | 0.3 ± 0.1 | 22 | 869.9 ± 102.6 | 82.3 ± 8.3 | 381 | 1,672 ± 103 | 179.2 ± 8.5 | 31 | 1,487 ± 257 | 132.0 ± 21.5 |
| 2 | 28 | 75.6 ± 1.2 | 1,068 ± 106 | 49 | 30.1 ± 6.8 | 361.4 ± 32.3 | 79 | 94.4 ± 9.8 | 684.1 ± 75.9 | 74 | 83.6 ± 20.5 | 891.1 ± 106.3 |
| 3 | 7 | 2.6 ± 0.6 | 32.4 ± 9.3 | 5 | 2.5 ± 0.2 | 31.5 ± 5.3 | 10 | 6.5 ± 1.1 | 142.7 ± 32.5 | 12 | 10.2 ± 2.4 | 145.3 ± 25.6 |
| 4 | 1 | 0.6 ± 0.1 | 8.7 ± 1.2 | 1 | 4.0 ± 1.1 | 57.0 ± 4.2 | 2 | 2.6 ± 0.5 | 35.7 ± 8.6 | 1 | 1.9 ± 0.2 | 26.3 ± 3.5 |
| 5 | nd | nd | nd | nd | nd | nd | 4 | 2.6 ± 0.4 | 5.2 ± 1.1 | 1 | 1.9 ± 0.3 | 1.9 ± 0.2 |
| 6 | 2 | 8.0 ± 1.2 | 1.3 ± 0.2 | 15 | 127.0 ± 10.2 | 36.5 ± 3.2 | 34 | 156.5 ± 5.6 | 61.1 ± 6.5 | 17 | 185.3 ± 20.4 | 56.3 ± 5.8 |
| 7 | nd | nd | nd | nd | nd | nd | 3 | 1.5 ± 0.2 | 19.1 ± 3.5 | nd | nd | nd |
| ∑ | 42 | 97.4 | 1110.6 | 92 | 1033.5 | 568.7 | 170 | 1935.8 | 1127.1 | 136 | 1770.2 | 1252.9 |

Note: nd – not detected; №1. Cyanobacteria; №2 Bacillariophyta; №3. Miozoa; №4. Ochrophyta; №5. Charophyta; №6. Chlorophyta; №7. Euglenozoa

The analysis of the data showed that the seasonal dynamics of the phytoplankton species composition are characterized by a gradual increase in the number of taxa throughout the growing season. The highest species diversity is observed in summer and autumn. During the monitoring. a significant increase in the abundance and biomass of phytoplankton was recorded. mainly due to the development of certain species of filamentous and colonial cyanobacteria. diatoms. and green algae. which is typical for the studied region of the sea.

Zooplankton communities in aquatic ecosystems serve as a food source for aquatic invertebrates. juveniles. and planktivorous fish. Plankton responds relatively quickly to changes in the aquatic ecosystem and can serve as an indicator of its condition. including in the Zhaiyk–Caspian basin [21].

The dynamics of zooplankton abundance also exhibited a seasonal pattern. with concentrations increasing from the winter–spring to the summer–autumn period. In June–August. 50 zooplankton taxa were recorded in the samples. including 13 rotifers. 12 cladocerans. 10 copepods. 4 gelatinous species. and 11 other taxa. mostly facultative plankters. In February–March and April–May. the number of taxa did not exceed 19 and 23. respectively. During the summer. rotifers dominated in terms of abundance (54%). while copepods accounted for 40% of the total zooplankton population. The average zooplankton abundance in the summer period reached 108.640.9 mln inds/m$^3$. and the biomass was 1.983.4 mg/m$^3$. exceeding the values recorded in other seasons by 1.3–23.6 and 2.6–29.7 times. respectively. with the closest values observed by September (Table 2).

It is particularly important to note the increasing biomass of Jellyfish species. which in summer reached more than 88% (1749.8 mg/m$^3$) of the total zooplankton biomass. Among them. the accidentally introduced Warty comb jelly *Mnemiopsis leidyi* has successfully colonized the brackish areas of the sea. The rapid adaptation and wide distribution of the species have led to a sharp decline in the food base of planktivorous fish. This. in turn. has altered the composition of ichthyocenoses and the structure of trophic chains. Mnemiopsis. being an active consumer of pelagic fish eggs and larvae. has had a negative impact on the stocks of many pelagic species.

In February–March. the zoobenthos was represented by 21 species. with a clear dominance of crustaceans – 15 taxa (71.4%). Four species of worms (19.1%) and two species of mollusks (9.5%) were identified. Despite this species composition structure. the highest average biomass was recorded for mollusks – 31.103.0 mg/m$^2$ (91.4%). while worms were dominant in terms of abundance – 1.738.0 ind./m$^2$ (77.8%). followed by crustaceans – 400.0 ind./m$^2$ (17.9%). In April–May. despite a slight increase in the number of taxa within the same groups (29 taxa). the average abundance and biomass increased compared to the previous period by 2.8 and 1.8 times. respectively. This resulted in values of 6.368.0 ind./m$^2$ and 63.107.0 mg/m$^2$.

In the summer period. when the number of taxa increased to 41. mainly due to crustaceans. a decrease in abundance and biomass was observed across all taxonomic groups. The only exception was the biomass of worms. which reached 4.356.0 mg/m$^2$. In the September samples. with a slight decrease in species composition to 38 taxa compared to the summer values. a significant increase in biomass was again recorded for all groups of benthic organisms (Table 3).

In the formation of the biological productivity of the sea. including that of hydrobionts. the accumulation of river runoff from the catchment basin plays an essential role. The flow of the Ural River provides an inflow of freshwater and nutrients into the Caspian Sea. which is critically important for maintaining the ecosystem – primarily for phyto- and zooplankton. A decrease in river discharge due to climatic changes and anthropogenic impacts leads to a reduction in both the abundance and biomass of the fodder base. In addition. water pollution affects the qualitative and quantitative composition of the food base of the Zhaiyk–Caspian basin. The priority pollutants for the Atyrau region are suspended solids. magnesium. and chemical oxygen demand (COD) [22].

In 2019–2022. the annual discharge of the Ural River (measured at the Atyrau hydrological station) varied from 4.98 to 6.56 km$^3$/year (average 5.52 km$^3$/year). while the water level fluctuated between 330 and 375 cm (average 366 cm) [23-25]. The average number of phytoplankton taxa during the summer period of maximum development was 100. with an abundance of 1907.4 ind./m$^3$ and a biomass of 0.789 mg/m$^3$; for zooplankton. 41 taxa were recorded with an abundance of 50.155 ind./m$^3$ and a biomass of 2862.8 mg/m$^3$. A comparative analysis showed that in 2023. with an increase in river discharge (8.11 km$^3$/year) and water level (440 cm). a sharp rise in the number of taxonomic units. as well as in the biomass of phytoplankton and the abundance of zooplankton. was observed – by 1.4 times (1.127 mg/m$^3$) and 2.2 times (108.640.9 ind./m$^3$). respectively (Table 4).

**Table 2** – Zooplankton of the eastern part of the Northern Caspian in 2023

| № | Number of taxa | Abundance. mln inds/m$^3$ | Biomass. mg/m$^3$ | Number of taxa | Abundance. mln inds/m$^3$ | Biomass. mg/m$^3$ | Number of taxa | Abundance. mln inds/m$^3$ | Biomass. mg/m$^3$ | Number of taxa | Abundance. mln inds/m$^3$ | Biomass. mg/m$^3$ |
|---|---|---|---|---|---|---|---|---|---|---|---|---|
| | February-March | | | April-May | | | June-August | | | September | | |
| 1 | 3 | 1,163 ± 127 | 1.1 ± 0.2 | 7 | 2,185 ± 456 | 1.8 ± 0.3 | 13 | 58,289 ± 855 | 23.3 ± 5.8 | 8 | 22,346 ± 1,203 | 13.8 ± 2.5 |
| 2 | 3 | 79.4 ± 20.4 | 9.8 ± 2.3 | 4 | 477.7 ± 102.6 | 133.5 ± 21.4 | 12 | 1,772 ± 265 | 55.0 ± 10.4 | 6 | 237.5 ± 56.8 | 9.8 ± 1.2 |
| 3 | 6 | 1,793 ± 252 | 26.7 ± 6.5 | 6 | 7,993 ± 897 | 79.7 ± 15.6 | 10 | 43,971 ± 876 | 145.6 ± 25.6 | 6 | 50,998 ± 8,966 | 212.0 ± 12.6 |
| 4 | 1 | 1.3 ± 0.2 | 16.1 ± 5.8 | nd | Nd | nd | 4 | 57.4 ± 10.2 | 1,750 ± 159 | 5 | 191.1 ± 10.5 | 503.2 ± 68.6 |
| 5 | 6 | 1,565 ± 242 | 12.9 ± 2.0 | 6 | 3221 ± 325 | 17.3 ± 1.6 | 11 | 4,552 ± 457 | 9.7 ± 1.6 | 6 | 6,442 ± 866 | 12.8 ± 2.5 |
| ∑ | 19 | 4600.9 | 66.6 | 23 | 13876.1 | 232.3 | 50 | 108640.9 | 1983.4 | 31 | 80214.5 | 751.6 |
| Note: nd – not detected; №1. Rotatoria; №2. Cladocera; №3. Copepoda; №4. Jellyfish; №5. Others | | | | | | | | | | | | |

**Table 3** – Zoobenthos of the eastern part of the Northern Caspian in 2023

| № | Number of taxa | Abundance. inds/m$^3$ | Biomass. mg/m$^3$ | Number of taxa | Abundance. inds/m$^3$ | Biomass. mg/m$^3$ | Number of taxa | Abundance. inds/m$^3$ | Biomass. mg/m$^3$ | Number of taxa | Abundance. inds/m$^3$ | Biomass. mg/m$^3$ |
|---|---|---|---|---|---|---|---|---|---|---|---|---|
| | February-March | | | April-May | | | June-August | | | September | | |
| 1 | 4 | 1,738 ± 368 | 1,151 ± 322 | 8 | 3,302 ± 653 | 2,965 ± 659 | 7 | 2,129 ± 506 | 4,356 ± 106 | 8 | 3,633 ± 199 | 7,104 ± 1,109 |
| 2 | 2 | 97.0 ± 22.6 | 31,103 ± 5,688 | 2 | 236.0 ± 62.5 | 55,090 ± 1,165 | 4 | 45.0 ± 12.5 | 9,675 ± 189 | 3 | 87.0 ± 8.6 | 35,249 ± 8,366 |
| 3 | 15 | 400.0 ± 96.5 | 1,781 ± 424 | 19 | 2,830 ± 713 | 5,053±101 | 29 | 2,007 ± 486 | 1,247 ± 303 | 26 | 1,625 ± 168 | 3,908 ± 569 |
| 4 | nd | nd | nd | nd | nd | nd | 1 | 3.0 ± 0.2 | 1.0 ± 0.2 | n/d | n/d | n/d |
| 5 | nd | nd | nd | nd | nd | nd | nd | nd | nd | 1 | 5±1.1 | 0.2 ± 0.01 |
| ∑ | 21 | 2235 | 34035 | 29 | 6368 | 63108 | 41 | 4184 | 15279 | 38 | 5350 | 46261.2 |
| Note: nd – not detected; №1. Vermes; №2. Mollusca; №3. Crustacea; №4. Insecta; №5. Others | | | | | | | | | | | | |

**Table 4** – Comparative analysis of the dynamics of phyto- and zooplankton abundance and biomass in the Ural River under different water discharge levels

| Years | Discharge volume | Water levels | Phytoplankton | | | Zooplankton | | |
|---|---|---|---|---|---|---|---|---|
| | km³/year | cm | taxa units | ind./m³ | mg/m³ | taxa units | ind./m³ | mg/m³ |
| 2019–2022 | 5.52 | 354 | 100 | 1907 | 0.789 | 41 | 50155 | 2862.8 |
| 2023 | 8.11 | 440 | 170 | 1936 | 1.127 | 50 | 108641 | 1983.4 |
| Note: The results of studies on hydrobiological indicators in the Zhaiyk–Caspian basin in 2023 and during the comparative period of 2019–2022 were obtained from the reporting materials of Kazekoproekt LLP. | | | | | | | | |

The research results indicate that the decrease or increase in the concentration of hydrobionts throughout the year mainly reflects the seasonal dynamics of variability in the abundance and biomass of phyto-. zooplankton. and zoobenthos. with the highest values observed in the summer period. Over the years. the mass development of planktonic organisms has been greatly influenced by the volume of water discharge and water levels in the river. the increase of which promotes the growth of both taxonomic units and the overall productivity of hydrobionts. In 2023. due to the increase in hydrobiont abundance. the fish feeding base was in a satisfactory condition.

The species composition of the ichthyofauna in the Ural–Caspian Basin is diverse and includes both typically marine forms and migratory. semi-migratory. and freshwater fish species [7]. These fish utilize the full range of food organisms – from predation to consumption of phyto- and zooplankton. benthos. plants. and detritus. Since juvenile fish at early stages of development feed exclusively on planktonic organisms. Table 5 presents the species composition of fish along with the spectrum of their main food organisms in adulthood. based on the recommendations for the allocation of total allowable catches (TAC) within the Atyrau region. including recommendations for determining fishing effort standards for coastal fishing in the Caspian Sea [26]. Additionally. migratory species – sturgeons – should be mentioned. as their stocks have been severely depleted. and their artificial reproduction is carried out at the state level (Table 5).

**Table 5** – Commercial fish species and main food components of adult individuals in the natural environment

| № | Fish species | Main nutritional components of adult individuals* |
|---|---|---|
| Semi-anadromous and freshwater fish species | | |
| 1 | Zander – *Sander lucioperca* (L.. 1758) | Predator: feeds on fish and their juveniles (roach. white bream. carp. bream. bleak. sprat. and kilka). |
| 2 | Asp – *Aspius aspius* (L.. 1758) | Predator; even young-of-the-year individuals already start feeding on fish such as roach. bleak. rudd. white bream. and sabrefish. |
| 3 | Wels (European) catfish – *Silurus glanis* L.. 1758 | Predator: fish make up 86.7% of its diet (up to 27 species. mainly roach. bream. white bream. rudd. and carp); frogs account for 10.3%. |
| 4 | Pike – *Esox lucius* L.. 1758 | Predator: up to 22 species were found in its stomach (roach. bleak. rudd. carp. white bream. perch. and others). |
| 5 | European perch – *Perca fluviatilis* L.. 1758 | Predator: feeds on juveniles of commercial fish species. as well as gobies and bleak. |
| 6 | Common carp – *Cyprinus carpio* (L.. 1758) | Gastropods. chironomids. gammarids. worms. crustaceans. vegetation. detritus. |
| 7 | Caspian roach − *Rutilus rutilus caspicus* (Jakowlew. 1870) | Benthic organisms. mainly mollusks of the genera *Dreissena*. *Monodacna*. and *Didacna*. |
| 8 | Bream – *Abramis brama* L.. 1758 | Benthic crustaceans. mollusks. and worms. |
| 9 | Silver crucian carp – *Carassius auratus* (L.. 1758) | Bloodworms. small mollusks. and plants. |
| 10 | Rudd – *Scardinius erythrophthalmus* (L.. 1758) | Plants. algae. chironomid larvae. insects. worms. and small mollusks. |

*Continuation of the table*

| № | Fish species | Main nutritional components of adult individuals* |
|---|---|---|
| 11 | White bream – *Blicca bjoerkna* (L.. 1758) | Benthic organisms: bloodworms. worms. mollusks. and occasionally vegetation. |
| 12 | Sabrefish – *Pelecus cultratus* (L.. 1758) | Aquatic insect larvae. juvenile fish. and small crustaceans. |
| 13 | Vimba bream – *Vimba vimba* | Small mollusks. insect larvae. crustaceans. and worms. |
| 14 | Blue bream | Mainly small mollusks. crustaceans. and bloodworms. |
| Marine fish species | | |
| 15 | Common kilka *Clupeonella delicatula caspia* (Svetovidov. 1941) | Zooplankton feeders: copepods and mysids. |
| 16 | Anchovy kilka *Clupeonella engrauliformis* (Borodin. 1904) | Zooplankton: copepods and mysids. |
| 17 | Caspian shad *Alosa caspia caspia* (Eichwald. 1838) | Feeds mainly on zooplankton. primarily copepods. and juvenile fish. |
| 18 | Bigeye shad *Alosa saposchikowii* (Grimm. 1887) | Feeds on both fish (such as sprat and gobies) and crustaceans. |
| 19 | Golden grey mullet – *Liza aurata* (Risso. 1810) | Feeds on vegetation and detritus. |
| Anadromous fish species | | |
| 20 | Beluga – *Huso huso* (L.. 1759) | Predator: feeds on herring. roach. white bream. atherine. sprat. and gobies. The transition to feeding on fish occurs during the first months of life. |
| 21 | Russian sturgeon – *Acipenser gueldenstaedtii* Brandt.1833 | Feeds on both benthic invertebrates and fish (such as herring. atherine. sprat. and gobies). The transition to feeding on fish occurs at the age of two years. |
| 22 | Starry sturgeon – *Acipenser stellatus* Pallas.1771 | The diet is dominated by crustaceans; mollusks are of lesser importance. Among fish. sprat and gobies prevail. |
| Note: * according to [1, 7, 27, 28, 29] | | |

According to their ecological characteristics. the fish of the Ural–Caspian basin can be divided into four groups:

- River species are represented by 42 species and subspecies. accounting for 34.4% of the ichthyofauna composition. Throughout their life cycle. these fish inhabit the freshwaters of the river lower reaches. the desalinated areas of the sea. and the water bodies of the delta.
- Migratory fish include 18 species and subspecies (14.7%). Before reaching sexual maturity. they inhabit the sea. and for spawning. they migrate into rivers. far from the estuary. using specific sections of the riverbed and floodplain for reproduction. The migratory forms include the Caspian lamprey. all Caspian salmon species. all Caspian sturgeons except the sterlet. the Volga many-spined herring. the black-backed herring. the Caspian barbel. the Caspian roach. the shemaya. and others.
- Semi-anadromous fish are represented by 9 species and subspecies (7.4%). These fish feed in the desalinated areas of the sea and spawn in the river deltas formed during the flood season. Typical representatives of this group include bream. roach (vobla). common carp. pikeperch. white-eye bream. sabrefish. and others.
- Marine fish are the most numerous in terms of species diversity – 53 species and subspecies (43.5% of the ichthyofauna composition). The entire life cycle of these fish takes place in the sea. This group includes all three species of Caspian sprats (common. big-eyed. and anchovy sprat). herrings such as the Caspian shad. big-eyed shad. and Dolgin herring. as well as most Caspian gobies. the atherine. mullets (sharp-nosed and singil). and the marine pikeperch.

The state of sturgeon populations in the Ural–Caspian basin is assessed as unfavorable. which is largely explained by the impact of anthropogenic factors. The current critical situation is associated with the disruption of spawning and feeding conditions for sturgeon. irrational legal and large-scale illegal fishing. as well as economic activities in the rivers and the sea carried out without regard for the interests of fisheries management [30. 31. 32].

The stocks of marine fish remain stable. In recent years. there has been a recovery in sprat stocks. particularly for the common sprat [33].

Among semi-anadromous fish. the most abundant species are the roach (vobla) and bream. The commercial stock of vobla is in a depressed state. with its numbers declining due to the formation of low-yield generations corresponding to years of low water levels. Currently. bream is the most numerous species in the Ural–Caspian basin. However. its stocks have been decreasing in recent years due to a reduction in natural reproduction rates [7. 11].

At present. one of the main factors affecting the fish population in the Ural–Caspian basin is the decline in the level of the Caspian Sea. especially in its northern. shallowest part [7].

For aquatic biological resources. feeding conditions in the sea are deteriorating. as the shallow. highly productive zone of the Northern Caspian is shrinking year by year. It is bounded to the south by a sharp depth gradient separating it from fully marine waters. while to the north it is constantly being encroached upon by advancing land. Processes of restructuring in the composition of the ichthyofauna are taking place. associated with the decline in the abundance of some species and the increase of others. The ecological niches vacated by endemic species are being occupied by eurybiont species. whose prosperity does not depend on flood conditions. As the delta of the Ural River advances into the sea. the highly nutritious shallow and desalinated areas suitable for fish feeding are decreasing.

Commercial species. including semi-anadromous and freshwater fish. are largely represented by typical predators such as pikeperch. catfish. asp. pike. and perch. During their feeding migrations. these species inhabit the estuaries of river systems and the desalinated coastal areas of the sea. The main component of their diet in these zones is the juvenile fish of most ichthyofauna species found there. In particular. they prefer roach. bream. common carp. white bream. and bleak. while in marine waters their diet mainly includes sprat. herring. and gobies.

The remaining representatives of the commercial semi-anadromous and freshwater fish species (such as bream. roach. and common carp) feed on mollusks. crustaceans. worms. and may also consume plant material.

The dietary components of marine fish species vary significantly: Caspian sprats feed exclusively on zooplankton; mullet (singil) feed on algae and detritus; while marine herrings include sprats. gobies. and crustaceans in their diet.

The diet of adult sturgeon species is generally similar in composition. though there are significant species-specific differences in the quantitative structure of their feeding. Beluga sturgeon is a predator. feeding mainly on fish. It begins predatory feeding while still a juvenile in the river. although it also consumes mollusks. The Russian sturgeon feeds on crustaceans (worms. gammarids. mysids) and mollusks; its diet also includes fish such as sprats. gobies. and herrings. The stellate sturgeon (sevruga) feeds on invertebrates (crustaceans and worms) as well as fish. primarily gobies. herrings. and sprats.

## Conclusion

The formation of commercial fish stocks largely depends on the condition of the water body’s forage base. since at various stages of their life cycle the diet includes planktonic organisms of both plant and animal origin. zoobenthos. and. for predatory species. representatives of the freshwater and marine ichthyofauna. The Ural–Caspian basin. which encompasses the northeastern part of the Caspian Sea. plays a key role in the migratory routes and feeding of various fish species. This region provides a rich natural food base for the majority of aquatic biological resources.

Research shows that the abundance and composition of aquatic organisms vary throughout the year and can fluctuate within a wide range. The density of aquatic organism concentrations reflected the seasonal dynamics of changes in the abundance and biomass of phytoplankton. zooplankton. and zoobenthos from winter to autumn. with maximum values observed during the summer period.

Over the years. the mass development of planktonic organisms has been greatly influenced by the volume and level of river water releases. the increase of which contributes to the growth of both taxonomic diversity and the overall productivity of aquatic organisms. In 2023. under conditions of increased water discharge. the forage base of fish was in a satisfactory state due to the rise in the abundance of aquatic organisms. Comparative analysis showed that with an increase in river discharge (8.11 km$^3$/year) and water level (440 cm) compared to 2019–2022. there was a sharp rise in species diversity of taxonomic units. as well as in the biomass of phytoplankton and the abundance of zooplankton. which increased by 1.4 and 2.2 times. respectively. The discharge of the Ural (Zhaiyk) River continuously supplied the Caspian Sea with fresh water and nutrients. which was critically important for maintaining the ecosystem. particularly for phytoplankton and zooplankton. In the case of zoobenthos. such biomass fluctuations were not observed; rather. annual variations in biomass fluctuated around a relatively stable level.

As a negative factor. attention should be paid to the increasing biomass of gelatinous species. among which the accidentally introduced ctenophore Mnemiopsis leidyi has successfully colonized the brackish areas of the sea. Being a mass consumer of zooplankton. it contributes to the reduction of the forage base not only for planktivorous fish but also for the juveniles of nearly all fish species in the Caspian Sea.

The ichthyofauna of the Zhaiyk–Caspian basin includes anadromous fish species (sturgeons. blackback herring. whitefish). semi-anadromous species (roach. bream. pikeperch. common carp. catfish). freshwater species (silver bream. sabrefish. perch. blue bream. rudd. pike. etc.). as well as marine fish species (kilkas. atherina. marine herrings. mullet). The status of aquatic biological resources in the basin varies. The most depleted and vulnerable species include beluga sturgeon. Russian sturgeon. stellate sturgeon. and whitefish. Roach and blackback herring are in a depressed state. whereas populations of bream. common carp. catfish. and marine fish species remain relatively stable. The main factors affecting the abundance of commercially important fish species are low spring river discharges and the decline in the water level of the Caspian Sea.

The main group of commercially valuable species of interest for fish farming consists of typical predators (beluga. pikeperch. catfish. asp. and pike) or fish with a mixed diet that feed on both benthic invertebrates and other animals (sturgeon. stellate sturgeon). The remaining representatives of commercial resources. including semi-anadromous and freshwater fish species (such as bream. roach. common carp. and others). feed on mollusks. crustaceans. worms. and may also include plant material in their diet. Based on the literature review. the range of main forage organisms for producers of commercial fish species in natural conditions has been established. which can serve as a certain guideline when developing feed components for fish kept under artificial conditions.

## Conflict of interest

The authors declare that they have no conflicts of interest.

## References

1. Kazancheev E. N. (1981) Ryby Kaspijskogo morja. Opredelitel’ [Fishes of the Caspian Sea: Identification guide] Moscow: Legkaya i pishchevaya promyshlennost’. 168 p.

2. Koblitskaya A. F. (1966) Izuchenie neresta presnovodnyh ryb [Study of the spawning of freshwater fish]. 109 p.

3. Reshetnikova. Yu.S. (2002) Atlas presnovodnyh ryb Rossii V 2 t. T.1. [Atlas of Freshwater Fishes of Russia] Moscow: Nauka. pp. 16-377.

4. Ivanov V.P.. Komarova G.V. (2012). Ryby Kaspijskogo morja (sistematika. biologija. promysel) [Fishes of the Caspian Sea: Systematics. Biology. and Fishery] Astrakhan: Astrakhan State Technical University Press. 256 p.

5. Chavychalova N.I.. Taradina D.G.. Vasilchenko O.M.. Lardygina E.G. (2020) Efficiency of semi-anadromous and river fishes reproduction in different water modes of the Volga River. *Fisheries*. vol 2. 67–73. https://doi.org/10.37663/0131-6184-2020-2-67-73

6. Sokolsky A.F.. Kanbetov A.Sh.. Popov N.N. (2021) Contemporary ecological state of waters of the Caspian Sea during development of oil and gas deposits. *South Russ.-Ecol. Dev.*. vol. 16. no. 2(59). – pp. 98–107. https://doi.org/10.18470/1992-1098-2021-2-98-107

7. Ivanov V.P.. Paltsev V.N.. Shipulin S.V. (2023) Rybnye resursy Kaspijskogo morja [Fish resources of the Caspian Sea] Moscow: VNIRO Publishing House. 560 p. ISBN 978-5-85382-522-2.

8. Uteulieva T.A. (2020) Areal rasprostranenija i zapasov predprinimatelskih vidov ryb Zhajyk-Kaspijskogo bassejna [Distribution area and stocks of entrepreneurial fish species of the Zhaiyk-Caspian basin] *Bull. Kh. Dosmukhamedov Atyrau Univ.*. vol. 57. no. 2. – pp. 148-153.

9. Sidorova M.A. (1989) Kaspijskoe more: ihtiofauna i promyslovye resursy [Bream. In: The Caspian Sea: Ichthyofauna and Commercial Resources] Moscow: Nauka. Chapter 3. pp. 153–169.

10. Sidorova M.A. (2007) Jekologicheskie monitoringovye issledovanija na licenzionnom uchastke «Severnyj» OOO «Lukojl-Nizhnevolzhskneft’» (1997–2006 gg.): kollektivnaja monografija [Bream Abramis brama (Linnaeus. 1758). In: Ecological Monitoring Studies at the “Severny” Licensed Area of Lukojl-Nizhnevolzhskneft LLC (1997–2006): Collective Monograph.]. Astrakhan: CaspNIRKh Publishing House. pp. 351–356.

11. Levashina. N. V. (2020) Formirovanie populjacii leshha abramis brama (linnaeus. 1758) i promyslovoe ispol’zovanie ego zapasov v volzhsko-kaspijskom bassejne [Formation of the bream (Abramis brama Linnaeus. 1758) population and commercial use of its stocks in the Volga–Caspian basin] Abstract of the dissertation for the degree of Candidate of Biological Sciences. Astrackhan. Russia. 28 p.

12. Guseinov M.K. (2015) O biologicheskih resursah Kaspija [On the biological resources of the Caspian Sea]. *South Russ.-Ecol. Dev.*. vol. 10. no. 2. pp. 38–53. https://doi.org/10.18470/1992-1098-2015-2-38-53

13. Usachev P.I. (1961) Kolichestvennaja metodika sbora i obrabotki fitoplanktona. Tr. Vsesojuznogo gidrobiologicheskogo obshhestva [Quantitative method for collecting and processing phytoplankton. Proceedings of the All-Union Hydrobiological Society]. Moscow. vol. 9. pp. 411–415.

14. Instrukcija po sboru i obrabotke planktona (1977) [Instruction for the Collection and Processing of Plankton]. Moscow: VNIRO. 72 p.

15. Elenkin A.A. (1936) Sine-zelenye vodorosli SSSR [Blue-Green Algae of the USSR]. Moscow & Leningrad: Academy of Sciences of the USSR. 679 p.

16. Zenkevich L.A. (1963) Biologija morej SSSR [Biology of the Seas of the USSR]. Moscow: Academy of Sciences of the USSR. Publishing House. 739 p.

17. Zenkevich L.A.. & Zevina G.B. (1969) Flora i fauna. Kaspijskoe more [Flora and fauna. The Caspian Sea]. Moscow: Moscow State University Publishing House.

18. Birstein Ya.A.. Vinogradova L.G. (1968) Atlas bespozvonochnyh kaspijskogo morja [Atlas of Invertebrates of the Caspian Sea]. Moscow: Pishchevaya Promyshlennost. 430 p.

19. Proshkina-Lavrenko A.I.. Makarova I.V. (1968) Vodorosli planktona Kaspijskogo morya [Plankton algae of the Caspian Sea]. Leningrad: Nauka. 291 p.

20. Order of the Minister of Ecology. Geology and Natural Resources of the Republic of Kazakhstan No. 662 (2022). On approval of the Rules for determining total allowable catches and limits for the use of wildlife objects [Prikaz Ministra jekologii. geologii i prirodnykh resursov Respubliki Kazahstan № 662 ot 18 oktjabrja 2022 goda]. Astana. Kazakhstan.

21. Demesinova G.. Kamieva N. (2021) Sostojanie zooplanktona v osobo-ohranjaemyh prirodnyh territorijah Zhajyk-Kaspijskogo bassejna [The state of zooplankton in specially protected natural areas of the Zhaiyk Caspian basin]. Modern environmental policy: essence. theory and socio-economic priorities: proceedings of the International Scientific and Practical Conference. Astrakhan. Russia. pp. 38-43.

22. Zhanabayeva Z.. Musina A.. Aktymbaeva A. and others. (2024) Sovremennoe sostojanie kachestva vody Zhajyk-Kaspijskogo bassejna v Kazakhstane [The current state of water quality in the Zhaiyk-Caspian basin in Kazakhstan] *Geogr. Water Resour.*. no. 4. pp. 67-74. https://doi.org/10.55764/2957-9856/2024-4-67-74.40

23. Zagidullina A.R.. Smagulov Z.. Birimbayeva L.M.. Sailaubek A.M. (2024) Tendencii mnogoletnih izmenenij stoka osnovnyh rek. formirujushhihsja v Zhajyk-Kaspijskom vodohozjajstvennom bassejne [Trends of long-term changes in the flow of the main rivers forming in the Zhaiyk-Caspian water basin] *Geogr. Water Resour.*. no 2. pp.15-26. https://doi.org/10.55764/2957-9856/2024-2-15-26.9

24. Zagidullina A.. Dostaeva A.. Sailaubek A.. Alzhanov O. (2025) Regularities of territorial distribution of river resources of the Urals – Caspian water management basin. *Bull. L.N. Gumilyov Eurasian Natl. Univ.: Chem. Geogr. Ecol. Ser*. no. 2. 151 p.. https://doi.org/10.32523/2616-6771-2025-151-2-183-196

25. Meteorological and hydrological databases [Electronic resource] (accessed on 30.08.2025). https://www.kazhydromet.kz/meteo_db.

26. Kadimov E. L. (2020) O rekomendacijah po opredeleniju normativov promyslovogo usilija pri osushhestvlenii pribrezhnogo lova na zakreplennyh rybopromyslovyh uchastkah Kaspijskogo morja. u poberezh'ja [Recommendations for determining the standards of fishing efforts in the context of carrying out coastal fishing in fixed fishing areas at the coast of the Caspian Sea]. *Bull. Kh. Dosmukhamedov Atyrau Univ*. vol. 57. no. 2.. pp. 87-94.

27. Asylbekova. S.Z. (2016) Akklimatizacija ryb i vodnyh bespozvonochnyh v vodoemah Kazahstana: rezul'taty i perspektivy [Acclimatization of fish and aquatic invertebrates in the water bodies of Kazakhstan: results and prospects]. Doctoral dissertation (Biological Sciences). Almaty. Kazakhstan. 348 p.

28. Popov N.N.. Kuanysheva G.A. (2022) Ocenka sovremennogo sostojanija okunevyh ryb v Severo-Vostochnoj chasti Kaspijskogo morja [Assessment of the current state of perch fish in the Northeastern part of the Caspian Sea]. Problems of integrated security of the Caspian macroregion: Proceedings of the International Scientific and Practical Conference. Astrakhan. Russia. pp. 161-167.

29. Popov N.N.. Kurochkina T.F. (2022) Vstrechayemost i biologicheskiye pokazateli rybtsa (vimba vimba) v kazakhstanskom sektore kaspiyskogo morya v 2021 godu [Occurrence and biological indicators of tuna (vimba vimba) in the Kazakh sector of the Caspian Sea in 2021]. Modern environmental policy: essence. theory and socio-economic priorities: Proceedings of the II International Scientific and Practical Conference. Astrakhan. Russia. pp. 56-61.

30. Kamelov A.K. (2023) Osetrovye ryby Zhajyk – Kaspijskogo bassejna. Monografija [Sturgeon fish of the Zhaiyk – Caspian basin. The monograph] NCOC NV Publishing House. Atyrau. 268 p.

31. Lepilina I.N.. Vasilyeva T.V.. Abdusamadov A.S. (2010) Sostojanie zapasov kaspijskih osetrovyh v mnogoletnem aspekte (literaturnyj obzor) [The state of Caspian sturgeon stocks in long-term aspect (review of literature)] *South Russ.-Ecol. Dev.*. no. 3.. pp. 57-65. https://doi.org/10.18470/1992-1098-2010-3-57-65

32. Lepilina I.N.. Vlasenko A.D.. Konopleva I.V.. Safaraliev I.A.. Chaplygin V.A. (2020) Raspredelenie. chislennost'. zapasy i ulovy osetrovyh v Kaspijskom bassejne [Distribution. abundance. stocks and catches of sturgeons in the Caspian basin] Astrakhan: Astrakhan State Technical University. 241 p.

33. Razinkov V.P. (2022) Sovremennye osobennosti biologii. sostojanija zapasov i promysla anchousovidnoj kil'ki (Slupeonella engrauliformis (Borodin. 1904)) v Kaspijskom more [Modern features of biology. stocks and fishing of anchovy sprat (Clupeonella engrauliformis (Borodin. 1904)) in the Caspian Sea] Abstract of the thesis for the degree of Candidate of Biological Sciences. Astrakhan. Russia. 25 p.

***Information about authors:***

*Nikolay Popov – Leader Specialist, Kazekoproekt LLP (Almaty, Kazakhstan, e-mail: fich63@mail.ru).*

*Vitaliy V. Barabanov – Senior Researcher, Laboratory of Riverine and Semi-Aquatic Fishes, Volga-Caspian Branch of the VNIRO Federal State Budgetary Institution (KaspNIRKh) (Astrakhan, Russia, e-mail: barabanov2411@yandex.ru).*

*Saule Shalgimbayeva – Candidate of Biological Sciences, Assistant Professor, Department of Zoology, Histology and Cytology, Faculty of Biology and Biotechnology, Al-Farabi Kazakh National University (Almaty, Kazakhstan, e-mail: s.saule777@gmail.com).*

*Dariga Batayeva – PhD, Acting Associate Professor, Institute of Natural Science, Kazakh National Women's Teacher Training University (Almaty, Kazakhstan, e-mail: batayeva.d@qyzpu.edu.kz).*

*Arailym Zhumanova – Bachelor's Student, Department of Zoology, Histology and Cytology, Faculty of Biology and Biotechnology, Al-Farabi Kazakh National University (Almaty, Kazakhstan, e-mail: zhumanovaraika@gmail.com).*

*Alua Muratkyzy – Bachelor's Student, Department of Zoology, Histology and Cytology, Faculty of Biology and Biotechnology, Al-Farabi Kazakh National University (Almaty, Kazakhstan, e-mail: aluamuratkyzy@gmail.com).*

*Bagila Abdullayeva – Candidate of Biological Sciences, Senior Lecturer, Department of Zoology, Histology and Cytology, Faculty of Biology and Biotechnology, Al-Farabi Kazakh National University (Almaty, Kazakhstan, e-mail: abdullayeva.bagila1@gmail.com).*

IRSTI 31.15.15:31.15.25:31.21.25:31.27.22:34.27.19:34.47.15 https://doi.org/10.26577/IJBCh20251828

A.V. Sharov[1*], P.A. Nikolaychuk[1, 2], A.A. Tereshkina[1, 3], A.V. Dostovalova[1],
Y.A. Enova[1], D.S. Popova[1], D.A. Rychkova[1], A.Y. Kurochkina[1],
V.V. Savinova[1], A.N. Nakoskin[1], I.V. Shipitsyna[4], O.V. Filisteev[1],
S.T. Lwin[5], M.M. Zaw[5], Z. Minthein[6], Z.Y.M. Oo[1, 7]

[1]Kurgan State University, Kurgan, Russia
[2]Scientific-Educational Centre of Chemistry and Chemical Technology of Novosibirsk State University, Novosibirsk, Russia
[3]Ural Federal University named after the first President of Russia B.N. Yeltsin, Yekaterinburg, Russia
[4]National Ilizarov Medical Research Centre for Traumatology and Orthopedics, Kurgan, Russia
[5]Medical Research Centre, Nay Pyi Taw, Myanmar
[6]Medical Academy, Yangon, Myanmar
[7]Science Research Centre of the Republic of the Union of Myanmar, Nay Pyi Taw, Myanmar
*e-mail: sharow84@gmail.com

*(Received 28 May 2025; received in revised form 19 December 2025; accepted 26 December 2025)*

# A Schiff base 4-chloro-2-((pyridin-3-ylimino)methyl)phenol: crystal structure details, computational study, proteolytic properties, molecular docking, *in vivo* toxicity and *in vitro* antibacterial activity

**Abstract.** IIn the present study, a synthesis, computational modeling and experimental investigation of 4-chloro-2-((pyridin-3-ylimino)methyl)phenol was reported. A Hirshfeld surface analysis was used for elucidation of interatomic contacts to the crystal structure of the substance. A DFT analysis was used for geometry optimisation, modeling of both vibrational and absorption spectra of three tautomeric forms and their comparison with the experimental spectra. The compound exists in the enolimine form in organic solvents, and the addition of water leads to the appearance of the ketoenamine form. A molecular docking was used for estimation of binding of three tautomeric forms with some proteins of *Staphylococcus* aureus and *Pseudomonas aeruginosa*. The ionisation constants in hydroethanolic mixtures are equal to 4.16, 8.55 and 10.43. The results of the antimicrobial tests of microamounts of 4-chloro-2-((pyridin-3-ylimino)methyl)phenol deposited onto the surface of titanium alloy of medical grade against the same microbials, and of the toxicity test of this compound with laboratory mice were provided. An inhibitory activity against *Pseudomonas aeruginosa* was revealed. No significant toxicity effects of the compound on the laboratory mice was detected.

**Keywords:** Schiff base, crystal structure, Hirshfeld surface analysis, computational study, DFT, molecular docking, toxicity, antibacterial activity.

## Introduction

The secondary imines or the Schiff bases [1], namely the condensation products of aldehydes and amines, are of extensive interest to the researchers for more than 100 years due to a very simple one-pot synthesis procedure and a wide range of potentially practically applicable properties [1–5]. Particularly, several imines have demonstrated antimicrobial properties against common pathogens [6–28], the details are presented in Table S1. Among their diversity, Schiff bases based on salicylic aldehyde, similar compounds, and their derivatives could be pointed out separately. They are characterised by the presence of an intramolecular hydrogen bond and the ability to form various tautomeric enolimine and ketoenamine forms [29–36]. The equilibria of formation of these forms are usually shifted under the influence of external factors, in particular, solvents with different polarity. A variety of their interesting properties of practical significance include optical properties, the complexation ability, the ability to bind nucleic acids, and a wide range of biological properties [10, 19, 27, 37–44].

An attention was recently drawn to the derivatives of salicylic aldehyde with a heterocycle in the amine residue, including from the point of view of their possible application in medicinal chemistry.

© 2025 al-Farabi Kazakh National University

This is due, among other things, to the wide use of heterocyclic compounds in medicine [45,46]. First of all, the condensation products of salicylic aldehyde and *ortho*-, *meta*-, and *para*-aminopyridines is of interest. The literature contains several information on the structure, optical properties, complex formation, and biological activity of 2-aminopyridine and 4-aminopyride derivatives [47–56]. However, such staring attention was not yet paid to 3-aminopyridine derivatives, despite their potentially interesting properties. For example, unlike 2- and 4-aminopyridine, 3-aminopyridine has fairly strong basic properties in aqueous solutions due to the redistribution of electron density between the amine nitrogen in the *meta*-position and the heterocyclic nitrogen [57]. This can affect the equilibria of keto-enol tautomerism of Schiff bases and, as a consequence, the properties of the substance in various environments.

In the present study the results of detailisation of the crystal structure using computer algorithms, DFT analysis of the structure and main characteristics of the molecule, determination of some physicochemical properties, molecular docking and *in vitro* analysis of the antimicrobial activity of 4-chloro-2-((pyridin-3-ylimino)methyl)phenol, a compound based on 5-chlorosalicylic aldehyde and 3-aminopyridine, are presented.

Because derivatives of salicylaldehide already demonstrated antimicrobial properties [10, 19], it was also important to test the antimicrobial properties of the synthesised compound. However, instead of using organic solvents for testing, the model samples of the surface of orthopedic implants from medical titanium covered by electrodeposited calcium phosphate material and Schiff base were prepared.

*In vitro* studies were conducted on cultures of both *Staphylococcus aureus* and *Pseudomonas aeruginosa*, namely, the common pathogens that cause infections complicating the osteogenesis processes after surgery. The toxicity of 4-chloro-2-((pyridin-3-ylimino)methyl)phenol was also tested *in vivo* using laboratory mice.Introduction should consist of justification of importance of the field, theoretical and practical significance of the topic, the meaning of the narrow problem, solution for the problem or formulation of hypothesis, the objectives of the work.

## Materials and methods

*Reagents and equipment*

5-chlorosalicylaldehyde (Shanghai Macklin Biochemical Technology Co. Ltd, China), 3-aminopyridine (Sisco Research Laboratories Pvt Ltd., India), calcium nitrate (Reakhim LLC, Russia), ammonium dihydrophosphate (Reakhim LLC, Russia), potassium chloride (Reakhim LLC, Russia), nitric acid (Èkos-1 LLC, Russia), sulphuric acid (Èkos-1 LLC, Russia), ammonium hydroxide (Èkos-1 LLC, Russia), potassium hydroxide (Reakhim LLC, Russia), barium chloride (Reakhim LLC, Russia), barium hydroxide (Reaktiv-Express LLC, Russia), spectral grade potassium bromide (Sigma-Aldrich, USA), standard buffer solutions for pH calibration (Reakhim LLC, Russia), Muller-Hinton agar (Agat-Med LLC, Russia), xylazine, tiletamine, zolazepam and chlorhexidine (obtained from local pharmacies, Russia), and assay kits for determination of liver enzymes (Vital LLC, Russia) were used without further purification. Methanol (Èkos-1 LLC, Russia), ethanol (Èkos-1 LLC, Russia), propan-1-ol (Èkos-1 LLC, Russia), propan-2-ol (Èkos-1 LLC, Russia), butan-1-ol (Èkos-1 LLC, Russia), butan-2-ol (Èkos-1 LLC, Russia), acetone (Èkos-1 LLC, Russia), acetonitrile (Èkos-1 LLC, Russia), chloroform (Èkos-1 LLC, Russia), hexane (Èkos-1 LLC, Russia), toluene (Èkos-1 LLC, Russia) were redistilled before use.

The distilled water was produced using the aquadistiller Puridest PD 4D (Lauda Scientific GmbH, Germany). The samples were weighted using the analytical balance Vibra HT-224RCE (Schinko Denshi Co. Ltd., Japan). Infrared spectra were recorded using the spectrophotometer FT-801 (Simeks LLC, Russia) in KBr pellets. 1H NMR spectra were registered using the spectrometer Bruker DRX-400 (Bruker Corporation, Germany). Absorption spectra were recorded using the spectrophotometer ХРОМАТРОН XT-500D (LabTex LLC, Russia). The ionometer Mettler-Toledo SevenCompact (Mettler Toledo Corp., Switzerland) equipped with the pH Sensor InLab Expert Pro-ISM (Mettler Toledo Corp., Switzerland) was used for pH measurement and potentiometric titrations. The dry-air thermostat TS-1/20 SPU (JSC «Smolenskoe special'noe konstruktorsko-tehnologičeskoe bûro sistem programmnogo upravleniâ», Russia) was used for sample incubation in microbial tests. The abacterial air medium box BAVnp-01-«Laminar-C»-1,2 Lorica (CJSC «Laminarnye sistemy», Russia) was used for working with bacterial cultures.

Laboratory mice of CBA strain were kindly provided by pharmaceutical company LLC Binnopharm Group, Russia as the gift.

*Synthesis of the compound*

A Schiff base (4-chloro-2-((pyridin-3-ylimino)methyl)phenol, compound **I**, see Figure 1) was obtained in an ethanolic medium using a condensation reaction of 5-chlorosalicylaldehyde and 3-aminopyridine. To the solution of 5-chlorosalicylaldehyde (1.0292 g, 6.57 mmol) in 10 ml of ethanol, a solution of 3-aminopyridine (0.6188 g, 6.57 mmol) in 10 ml of ethanol were gradually added. The reaction mixture was boiled with the reflux condenser during 4 hours, then cooled to the room temperature. The formed orange precipitate was filtered, washed several times with cold ethanol and dried in vacuum. The yield was 1.4663 g (96 %).

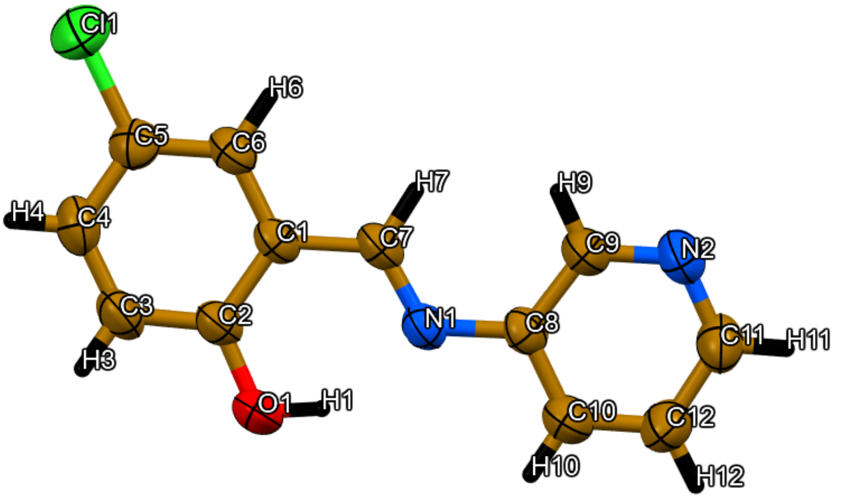

**Figure 1** – Molecular structure of compound **I** obtained in [47] by X-Ray crystallography

*Compound characterisation*

$^1$H NMR spectra were registered at the frequency of $^1$H equal to 400 MHz in $CDCl_3$. The chemical shifts are depicted relatively to trimethylsilane. IR spectra were registered with the spectral resolution of 4.1 cm$^{-1}$ and the scan number equal to 32 in the potassium bromide pellets. UV-spectra of the compound **I** solutions in the different solvents as well as in hydroethanolic mixtures were registered in quartz cuvettes with the optical path length equal to 1 cm. The scan range was from 190 to 800 nm with the step of 1 nm.

The ionisation constants of **I** were determined with hydroethanolic mixtures with the ethanol mass fraction of 73% by potentiometric titration with the combined pH sensor. The electrode was calibrated using the standard buffer solutions. The corrected pH values in the hydroethanolic mixtures were calculated from the electrode readings using the method proposed by Bates [58], where the medium effect was determined from the experimental data [58, 59]. The measurements were made at the temperature of 298 K and the ionic strength of 0.01 M, maintained by the potassium chloride. The titration of the compound **I** solution was carried out by either hydrochloric acid or potassium hydroxide. Potassium hydroxide was pre-purified from the presence of carbonates by barium hydroxide.

*Hirshfeld surface analysis*

The Hirshfeld surfaces [60–62] of **I** were generated using the Crystal Explorer 17 software [62]. The original crystal structure was taken from the CCDC database with deposition number 1869718 [63, 64]. The 2D fingerprint plots were generated with the Crystal Explorer 17 software and used for description of the intermolecular interactions, including contacts between the pairs of atoms.

*Quantum chemical calculations*

The geometry of the ground state (in gas phase), electronic (in alcoholic solution) и vibrational (in gas phase) spectra were calculated by the density functional theory (DFT) using GaussView 6.0 molecular visualisation program and Gaussian 09 [65, 66], Revision D.01 program package. The functional Becke-3-parametr-Lee-Yang-Parr (B3LYP) and the basis set 6-311++G(d,p) [67 – 69] were employed. The correspondence of the calculated bands in the IR spectra to vibrations of specific atoms or groups of atoms was established using VEDA software [70]. The HOMO and LUMO orbitals and MEP surfaces were generated based on the optimised geometry for the ground state of substance **I** in the gas phase.

*Molecular docking*

The molecular docking procedure was implemented for some proteins (mainly of the cell walls) of *Staphylococcus aureus* and *Pseudomonas aeruginosa*.

Crystal structures of proteins for the molecular docking procedure were taken from the RCSB Protein Data Bank [71]. Processing of molecular models, as well as visualisation of the results of interactions between **I** and active centers of proteins, were performed in BIOVIA Discovery Studio 2020 and AutoDock tools software. Molecular docking was performed with the AutoDock Vina software [72, 73].

*Preparation of the samples containing micro-amounts of Schiff base for in vitro anti-microbial testing*

The samples have a form of the disks with a diameter of 5 mm and a height of 1 mm made of medical grade titanium alloy Ti-6Al-4V covered by a calcium phosphate coating with additives of **I**. The metal disks were pre-cleaned in an ultrasonic bath and degreased using acetone. Before the precipitation of calcium phosphate, anodic oxidation of titanium was carried out in a 0.5 M $H_2SO_4$ solution [74, 75]. The samples serve as anodes, and a copper cathode was used. Anodisation was carried out at a direct current voltage of 25 V for 1 minute at room temperature. After oxidation, the samples were washed in an ultrasonic bath with distilled water and dried using the filter paper.

The electrolyte for the precipitation of phosphates contained 0.042 M $Ca(NO_3)_2$ and 0.025 M $NH_4H_2PO_4$ [74]. The pH value of the electrolyte was adjusted to 4.1 using nitric acid or ammonium hydroxide solutions. Electrolysis was carried out for 2 hours at a direct current voltage of 4 V. A titanium sample served as a cathode, and graphite rod as an anode. After electrolysis, the samples were washed in distilled water and dried in air. At the last stage, the samples were impregnated with 1 mM ethanol solution of **I** and dried afterwards. The content of the Schiff base in the samples was determined by its extraction from the samples with ethanol, followed by spectrophotometric analysis.

*Spectrophotometric determination of (4-chloro-2-((pyridin-3-ylimino)methyl)phenol*

The concentration of the compound **I** in the ethanolic extracts were determined spectrophotometrically. For this, ten disks (described in the previous section) covered by calcium phosphate and impregnated with compound **I** were immersed into 5 ml of ethanol, vigorously shaken, immersed into another 5 ml of ethanol and vigorously shaken again. The resulting ethanolic solutions were combined, and the content of compound **I** was measured spectrophotometrically at the wavelength of 355 nm with the molar extinction coefficient equal to 1900 $m^2$/mol. The analytical performance of the method is as follows: linearity range equals 0.1 – 20 mg/L, with LOD 0.015 mg/L, and LOQ 0.05 mg/L, recovery studies revealed the relative uncertainty of 3.5% for the 1 mg/L solution, and reproducibility studies revealed the relative standard deviation of 3.2% ($f$ = 5, p = 0.95) for the 1 mg/L solution of compound **I**.

*In vitro antimicrobial tests*

The museum strains *Staphylococcus aureus* ATCC 25923, *Pseudomonas aeruginosa* ATCC 27853, Escherichia coli ATCC 25922 were used as test cultures. A suspension (corresponding to the 0.5 McFarland standard [76]) of the studied microorganism was seeded on a Petri dish with a dense nutrient medium (Muller-Hinton agar, Agat-Med LLC, Russia). The disks described previously were applied to the surface of the agar with microbial cultures. The cultures were incubated in a dry-air thermostat TS-1/20 SPU (JSC «Smolenskoe special'noe konstruktorsko-tehnologičeskoe bûro sistem programmnogo upravleniâ», Russia) for 24 hours at a temperature of 35±1˚C. The results were recorded based on the absence or presence of microorganism growth around the disk, measuring the diameter of the growth inhibition zone.

*In vivo toxicity tests using laboratory mice*

For the toxicity test 10 male adult laboratory mice (*Mus musculus*, BCA strain) weighting 20–35 g were randomly divided into two groups. For general anaesthesia the animals were treated by the 0.2 mg/ml solutions of xylazine, tiletamine and zolazepam, the hair was partially removed, the freed skin surface was disinfected by chlorhexidine, and the compound I in physiological solution with the quantity of 0.2 mg/kg was injected subcutaneously. The second group of mice remained the control group. After 14 days the mice were sacrificed, and the fresh blood samples were taken. The content of aspartate transaminase and alanine aminotransferase in the blood samples were estimated spectrophotometrically. The bodies were dissected, and the tissues were examined for inflammation, fibrosis, vascularisation, and neoplasm. The hearts and the livers were also weighted. For each group the average masses of mice, their hearts and livers, their standard deviations and confidence intervals ($f$ = 4, $p$ = 0.95) were estimated. The results of both groups were compared using the Wilcoxon signed rank test.

*Spectrophotometric determination of aspartate transaminase and alanine aminotransferase in laboratory mice blood serum*

The concentration of the liver enzymes in the samples of mice blood serum was determined according to the method described in work [77] using the commercially available assay kits (B 01.05 and B 02.05, Vital LLC, Russia). The determination of alanine aminotransferase is based on the enzyme-catalysed transformation of L-alanine and α-ketoglutarate into pyruvic acid and L-glutamate with subsequent oxidation of nicotinamide adenine dinucleotide by formed pyruvic acid with the help of the enzyme lactate dehydrogenase. A reagent in the kit (B 01.05, Vital LLC, Russia) contained the solutions of 400 mmol/l L-alanine, 75 mmol/l Tris-HCl buffer, 1040 U/l lactate dehydrogenase, 3 mmol/l α-ketoglutarate and 0.036 mmol/l NADH. Freshly taken mice blood samples were centrifuged over 15 min at 3000 rpm, 0.2 ml of obtained serum was mixed with 2.0 ml of the reagent, incubated at 37$^o$C, and the absorbance of the resulting solution at 340 nm against distilled water was registered in quartz cuvette with optical path length of 1 cm over 3 minutes. The activity of alanine aminotransferase in U/l was calculated from the rate of absorbance decrease as 1746 . dA/dt. A unit activity of the enzyme corresponds to catalysed transformation of 16.67 nmol/s of L-alanine.

The determination of aspartate transaminase is based on the enzyme-catalysed transformation of L-aspartate and α-ketoglutarate into oxaloacetate and L-glutamate with subsequent oxidation of nicotinamide adenine dinucleotide by formed oxaloacetate with the help of the enzyme malate dehydrogenase. A reagent in the kit (B 02.05, Vital LLC, Russia) contained the solutions of 192 mmol/l L-aspartate, 64 mmol/l Tris-HCl buffer, 480 U/l lactate dehydrogenase, 480 U/l malate dehydrogenase, 2.4 mmol/l α-ketoglutarate and 0.036 mmol/l NADH. Again, 0.2 ml of obtained serum was mixed with 2.0 ml of the reagent, incubated at 37 oC, and the absorbance of the resulting solution at 340 nm against distilled water was registered in quartz cuvette with optical path length of 1 cm over 3 minutes. The activity of aspartate transaminase in U/l was calculated from the rate of absorbance decrease as 1746 . dA/dt. A unit activity of the enzyme corresponds to catalysed transformation of 16.67 nmol/s of L-aspartate.

The analytical performance of both test kits as stated by manufacturer is as follows: linearity range 10 – 190 U/l, LOQ 7 U/l, relative uncertainty and relative standard deviation less than 5%.

For each group the average values of enzyme activities, their standard deviations and confidence intervals (f = 4, p = 0.95) were estimated. The results of both groups were compared using the Wilcoxon signed rank test.

## Results and discussion

*$^1$H NMR spectroscopy*

The experimental $^1$H NMR spectrum of compound I recorded at 400MHz in CDCl3 revealed the following bands: 12.74 (1H, Ar-OH), 8.76 (1H, Ar-CH=N-), 8.57-7.00 (7H, Ar-H). For comparison, the model NMR spectrum of this compound predicted by the online tool nmrdb.org [78] revealed the bands 6.88 (1H), 7.37 (1H), 7.46-7.66 (2H), 7.91 (1H), 8.48 (1H), 8.62 (1H), 8.90 (1H). As one might see, the experimental and predicted spectra coincide well.

*Crystal structure and Hirshfeld surface analysis*

The formulae and schemas of tautomeric transformations of the compound **I** are presented in Figure 1. In accordance with the data of monocrystal X-ray difractometry (CCDC number 1869718 [60]), the compound **I** crystallises in monoclinic singony, a space group $P2_1/n$. The cell parameters: a = 4.5628 Å, b = 19.3486 Å, c = 12.0485 Å, α = 90°, β = 95.27, γ = 90°, Z = 4 [61]. The compound **I** in its crystalline state is predominantly represented by the enolimine form. The structure is characterised by an intermolecular hydrogen bond O11–H12···N15 (bond length O11–H12 equals 0.90(3) Å, bond length H12···N15 equals 1.84(3) Å, angle O11–H12···N15 equals 145(3)°). The geometric structure of enolimine, *cis*-ketoenamine and *trans*-ketoenamine forms obtained by using the B3LYP/6-311++G(d,p) method is presented in Figure 2.

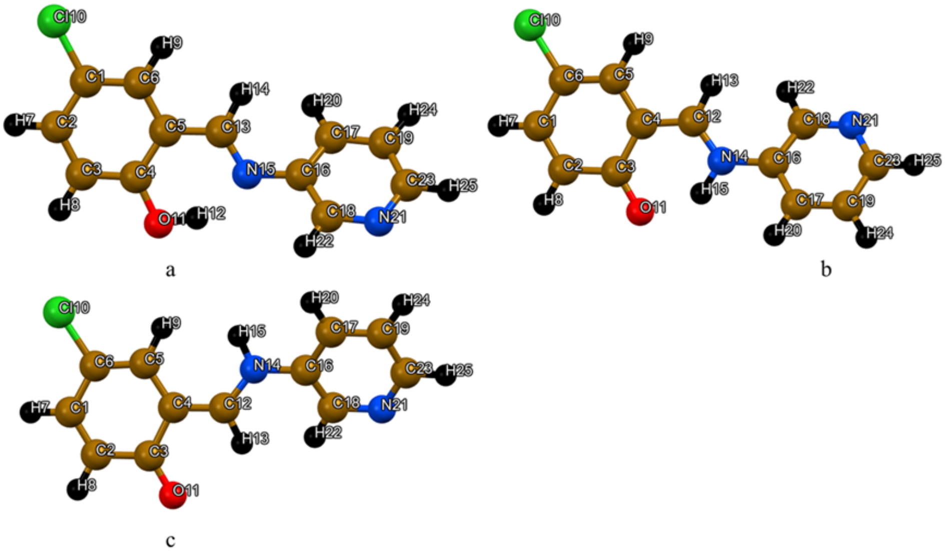

**Figure 2 –** Molecular structure of compound **I** tautomeric forms obtained by B3LYP/6-311++G(d,p) method (a – enolimine, b – *cis*-ketoenamine c – *trans*-ketoenamine)

**Table 1 –** Selected bond lengths (Å) and angles (°) in the experimental structure of I [47] and optimized structure of enol-imine form of I using the B3LYP/6-311++G(d,p) method

| | Experimental [47] | Calculated | | Experimental [47] | Calculated |
|---|---|---|---|---|---|
| | | | *Bond lengths* | | |
| C1–C2 | 1.388(3) | 1.398 | C19–C23 | 1.378(3) | 1.393 |
| C1–C6 | 1.374(2) | 1.382 | C16–C18 | 1.394(2) | 1.403 |
| C2–C3 | 1.370(3) | 1.388 | C1–Cl10 | 1.742(2) | 1.764 |
| C3–C4 | 1.391(3) | 1.399 | C4–O11 | 1.352(2) | 1.345 |
| C4–C5 | 1.409(2) | 1.418 | O11–H12 | 0.900(3) | 0.997 |
| C5–C6 | 1.402(2) | 1.407 | N11–C12 | 1.478(5) | 1.472 |
| C5–C13 | 1.449(2) | 1.452 | C13–N15 | 1.279(2) | 1.288 |
| C12–C13 | 1.516(6) | 1.537 | N15–C16 | 1.418(2) | 1.407 |
| C16–C17 | 1.394(2) | 1.399 | C23–N21 | 1.333(3) | 1.340 |
| C17–C19 | 1.379(3) | 1.389 | N21–C18 | 1.336(3) | 1.333 |
| | | | *Bond angles* | | |
| C1–C2–C3 | 119.6(2) | 120.8 | C2–C1–Cl10 | 119.2(1) | 119.4 |
| C2–C3–C4 | 120.9(2) | 120.5 | C3–C4–O11 | 119.0(1) | 118.7 |
| C3–C4–C5 | 119.6(2) | 119.5 | C4–O11–H12 | 111.0(2) | 107.3 |
| C4–C5–C6 | 118.8(1) | 119.3 | C13–N15–C16 | 121.5(1) | 121.4 |
| C1–C6–C5 | 120.1(2) | 120.4 | N15–C16–C18 | 118.2(1) | 117.8 |
| C6–C5–C13 | 119.4(1) | 119.2 | C19–C23–N21 | 122.8(2) | 123.0 |
| C16–C17–C19 | 119.5(2) | 118.7 | C18–N21–C23 | 117.5(2) | 117.8 |
| C17–C19–C23 | 117.1(2) | 117.8 | C16–C18–N21 | 124.0(2) | 123.7 |
| C17–C16–C18 | 118.4(4) | 117.8 | | | |
| | | | *Dihedral angles* | | |
| C1–C2–C3–C4 | –0.6(8) | –0.1 | C6–C5–C13–N15 | –2.2(2) | –0.23 |
| C2–C3–C4–C5 | 1.8(3) | 0.1 | C5–C13–N15–C16 | 179.1(1) | 177.6 |

*Continuation of the table*

| | Experimental [47] | Calculated | | Experimental [47] | Calculated |
|---|---|---|---|---|---|
| C3–C4–C5–C6 | –1.7(2) | 0.1 | C13–N15–C16–C17 | 2.3(3) | –34.0 |
| C4–C5–C6–C1 | –0.5(2) | –0.1 | N15–C16–C17–C19 | –179.2(2) | –179.1 |
| C2–C1–C6–C5 | 0.6(3) | 0.1 | C16–C17–C19–C23 | 0.2(3) | 0.5 |
| C6–C1–C2–C3 | –0.7(3) | 0.0 | C18–N21–C23–C19 | –0.6(3) | –0.2 |
| C3–C4–O11–H12 | –179.2(2) | –179.4 | C16–C18–N21–C23 | –0.2(3) | –1.0 |
| Cl10–C1–C2–C3 | –179.9(1) | –179.9 | | | |

Generally, a good agreement between the experimental and calculated values of bond lengths, bond angles and dihedral angles for enolimine form of **I** (Table 1) is observed. Thus, the differences between the bond lengths are about 0.01 Å. A notable exception is the dihedral angle C13–N15–C16–C17, which value according to the experimental data is about 2°. The calculated dihedral angle C13–N15–C16–C17 equals 34°. A similar picture is observed in the paper [47]. A possible explanation of this phenomenon might be the presence of the network of intermolecular interactions in the crystal structure that makes the molecule **I** flat. The geometric parameters of both *cis*- and *trans*-ketoenamine forms obtained by using the B3LYP/6-311++G(d,p) method are listed in Table S2.

In order to obtain additional information on intermolecular interactions in the crystal structure of compound **I** a Hirshfeld surface, including 2D fingerprints of interatomic contacts, was generated and studied. The model data were obtained using a CrystalExplorer 17 software. In addition to the 2D fingerprints the the enrichment ratios ($E$) of the intermolecular contacts were estimated in order to determine the contributions of different elements to the intermolecular interactions [79]. The appearance of the Hirshfeld surface of the compound **I** on the parameters denote normalised distance $d_{norm}$, shape index and curvedness is presented in Figure 3. The red areas on the $d_{norm}$ surfaces depict the presence of intermolecular hydrogen bonds C–H···O and C–H···N. The donors and the acceptors in the frameworks of corresponding interactions are presented on the shape index surface.

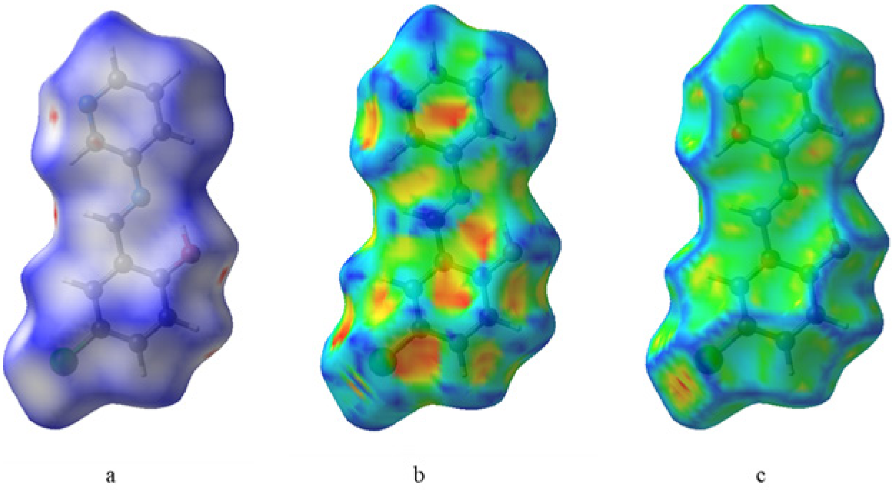

**Figure 3** – Molecular Hirshfeld surfaces of form II of tautomeric forms of compound **I** obtained by B3LYP/6-311++G(d,p) method (a – normalized distance $d_{norm}$, b – shape index, c – curvedness)

Figure 4 presents 2D fingerprint plots for all atoms participating in intermolecular interactions, as well as for atomic pairs H···X (X = H, C, N, O, Cl). Paired contacts H···N and H···O on the 2D fingerprint plots have the form of keen pikes with the heights at di ≈ 1.1, de ≈ 0.7 (di ≈ 0.7, de ≈ 1.1, total 1.8 nm) and di ≈ 1.0, de ≈ 0.7 (di ≈ 0.7, de ≈ 1.0, total 1.7 nm). These contacts correspond to the hydrogen bonds C–H···O and C–H···N. The similar sums (or minimal distances between atoms) for other paired contacts equal: H···H – 1.4 nm, H···C – 2.2 nm, H···Cl – 2.2 nm, C···C – 2.6 nm, and C···N – 2.7 nm. The mutual contacts C···C, H···O and H···Cl, C···N, Cl···Cl are preferred for the structure of the compound **I**, because the enrichment ratio values for these paired mutual contacts exceed unity (Table 2). The contacts of hydrogen atoms are somewhat less preferable (E = 0.92), this could be explained by the largest proportion of the surface occupied by hydrogen, carbon and chlorine atoms.

The distribution of intermolecular interaction energies relative to the central molecule was calculated using the method B3LYP/6-31G(d,p). The calculation results are listed Table 3, and the visualisation of the interacting molecules is presented in Figure 5. It was revealed that the largest contribution to the total interaction energy was made by the dispersive interactions. This is mostly typical for molecules packed parallel to each other along the planes of aromatic rings. (Table 3, Figure 5). For such molecules, the dispersion interaction energy equals 62 kJ/mol. The strongest electrostatic interactions (10.5 kJ/mol) apparently correspond to hydrogen bonds C–H···O and C–H···N.

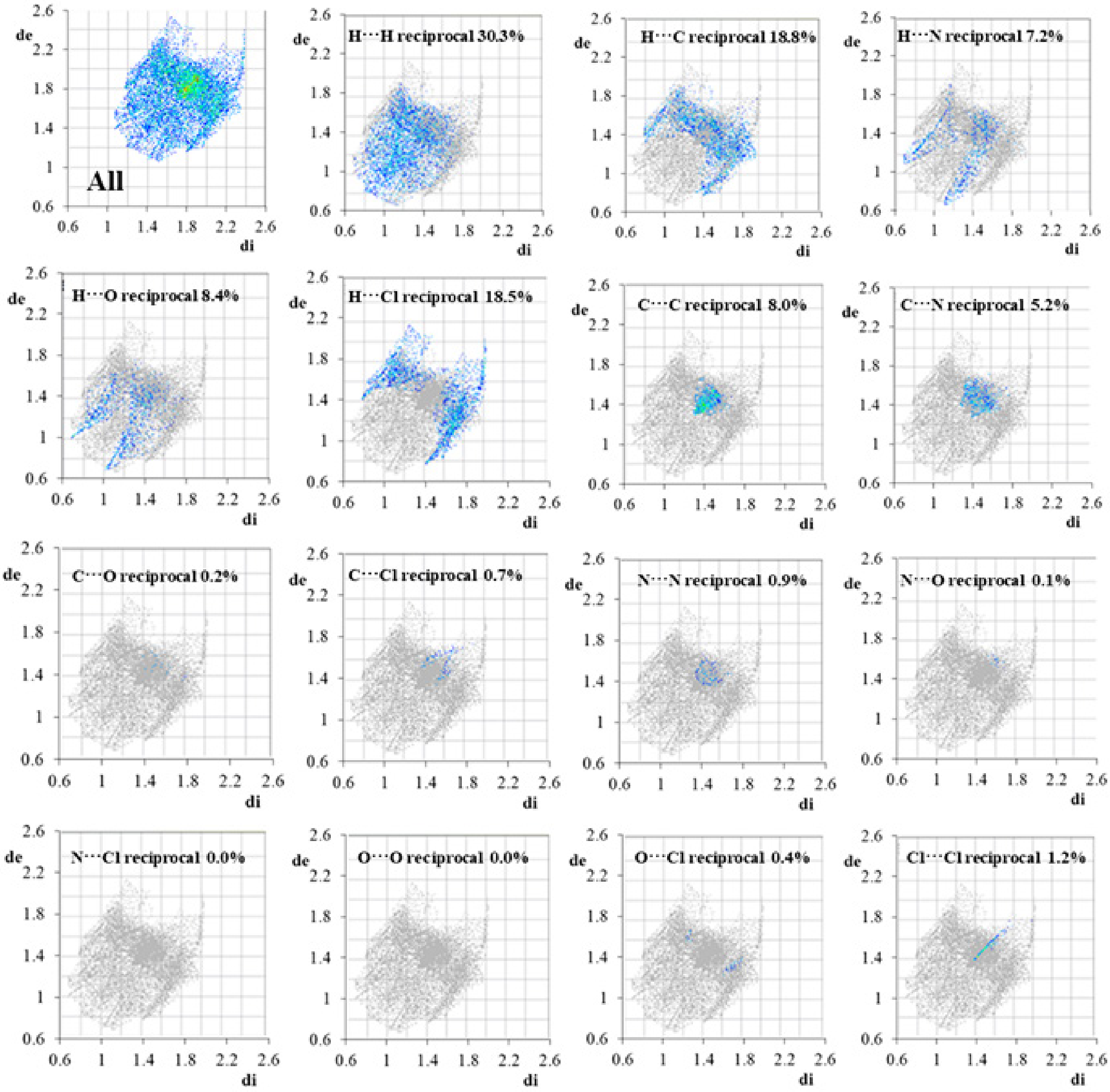

**Figure 4** – Total 2D and decomposed 2D fingerprint plots of observed contacts for compound **I** crystal structure

**Table 2 –** Hirshfeld contact surface and it characteristics for compound **I**

| | H | C | N | O | Cl |
|---|---|---|---|---|---|
| Contacts (*C*, %)[a] | | | | | |
| H | 30.3 | – | – | – | – |
| C | 18.8 | 8.0 | – | – | – |
| N | 7.2 | 5.2 | 0.9 | – | – |
| O | 8.4 | 0.2 | 0.1 | 0.0 | – |
| Cl | 18.5 | 0.7 | 0.0 | 0.4 | 1.2 |
| Surface (*S*, %) | | | | | |
| | 56.8 | 20.5 | 7.2 | 4.5 | 11.0 |
| Random contacts (*R*, %) | | | | | |
| H | 32.3 | – | – | – | – |
| C | 23.2 | 4.2 | – | – | – |
| N | 8.2 | 3.0 | 0.5 | – | – |
| O | 5.2 | 1.8 | 0.5 | 0.2 | – |
| Cl | 12.5 | 4.6 | 1.6 | 1.0 | 1.2 |
| Enrichment (*E*)[b] | | | | | |
| H | 0.93 | – | – | – | – |
| C | 0.81 | 1.90 | – | – | – |
| N | 0.88 | 1.73 | – | – | – |
| O | 1.62 | 0.11 | – | – | – |
| Cl | 1.48 | 0.15 | 0.00 | 0.40 | 1.00 |

[a] Values are obtained from CrystalExplorer 17. [b] The “enrichment ratios” were not computed when the “random contacts” were lower than 0.9%, as they are not meaningful.

**Table 3 –** Interaction energies (kJ/mol) calculated with the B3LYP/6-31G(d,p) energy model for the crystal structure of compound **I**

| | No | Symmetry operation | R | E_ele | E_pol | E_dis | E_rep | E_tot |
|---|---|---|---|---|---|---|---|---|
| 🟥 | 2 | x, y, z | 4.56 | -8.7 | -1.2 | -61.7 | 35.1 | -42.1 |
| 🟧 | 2 | -x+1/2, y+1/2, -z+1/2 | 9.97 | -2.7 | -0.4 | -8.7 | 4.7 | -7.8 |
| 🟨 | 2 | x+1/2, -y+1/2, z+1/2 | 9.55 | -1.1 | -0.1 | -4.4 | 1.5 | -4.1 |
| 🟩 | 2 | x+1/2, -y+1/2, z+1/2 | 8.72 | -6.4 | -1.7 | -9.9 | 9.4 | -10.9 |
| 🟩 | 2 | x+1/2, -y+1/2, z+1/2 | 6.28 | -10.5 | -2.7 | -17.3 | 14.4 | -19.3 |
| 🟦 | 2 | x+1/2, -y+1/2, z+1/2 | 6.67 | -2.6 | -1.1 | -12.7 | 7.7 | -9.9 |
| 🟦 | 1 | -x, -y, -z | 12.13 | -2.5 | -0.2 | -3.9 | 0.0 | -6.1 |
| 🟪 | 2 | -x+1/2, y+1/2, -z+1/2 | 10.20 | -2.0 | -0.6 | -11.9 | 7.1 | -8.6 |
| 🟪 | 1 | -x, -y, -z | 11.00 | 1.5 | -0.7 | -8.4 | 2.4 | -4.7 |

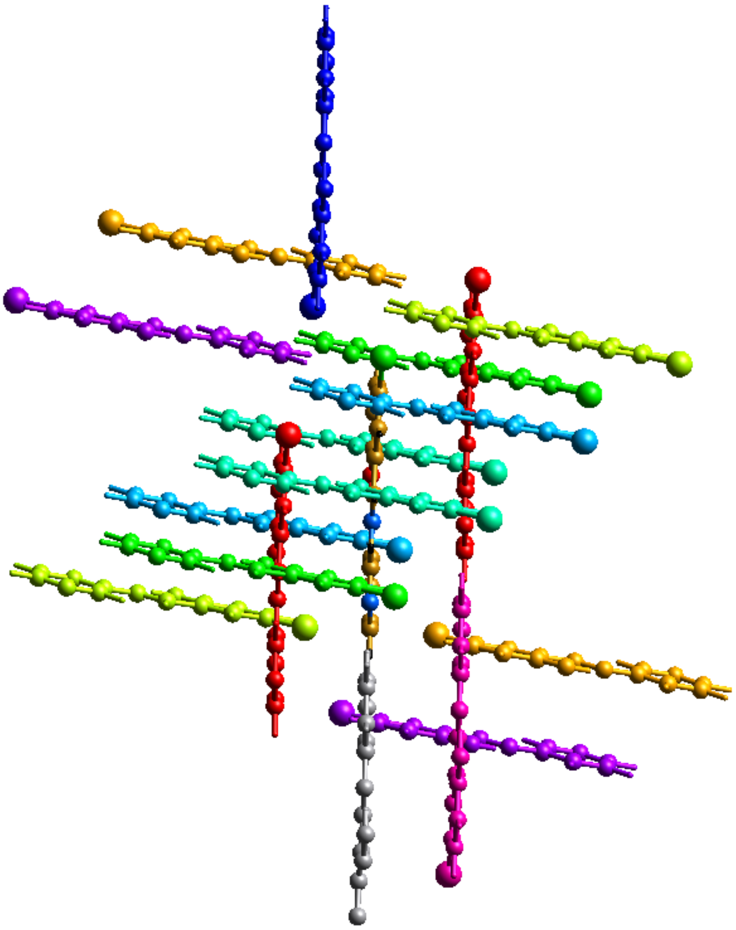

**Figure 5 –** The color-coded interaction mapping within 3.8 Å of the centering molecule in the crystal structure of compound **I**, calculated with the B3LYP/6-31G(d,p) energy model

*Vibrational analysis*

To calculate the vibration frequencies appearing in IR spectra for both enolimine, *cis*-, and *trans*-ketoenamine forms of the compound **I**, a DFT method was used. The experimental and predicted IR spectra are presented in Figure 6.

It is well known that the predicted wavenumbers of vibrational bands are usually some higher than the experimental ones. [80]. This fact was taken into account while interpreting the absorption bands in the experimental spectrum and their comparison with the bands of calculated spectra. It is important to note that the comparison of the experimental and calculated bands in the range from 4000 to 1700 cm$^{-1}$ was not conducted, because the position of bands corresponding to valence oscillations of hydroxyl groups located in this region is heavily influenced by intermolecular interactions in the crystal structure, including C–H···O and C–H···N. Thus in the experimental spectrum there is a broad peak related to hydroxyl groups with the maximum at 3430 cm$^{-1}$, and in the calculated spectra an analogous high intensity band is present at 3143 cm$^{-1}$. Table 4 provides a decoding of vibrational modes and a comparison of the frequencies of calculated and experimental vibrations. Coinciding frequencies are highlighted in bold, taking into account the reduction factor of 1.021457 for calculated frequencies. As expected, the match was best for the enolimine form, which gives another confirmation of its prevalence in crystalline state of compound **I**. The vibrational modes for *cis*- and *trans*-ketoenamine forms of compound **I** are listed in Tables S3 and S4.

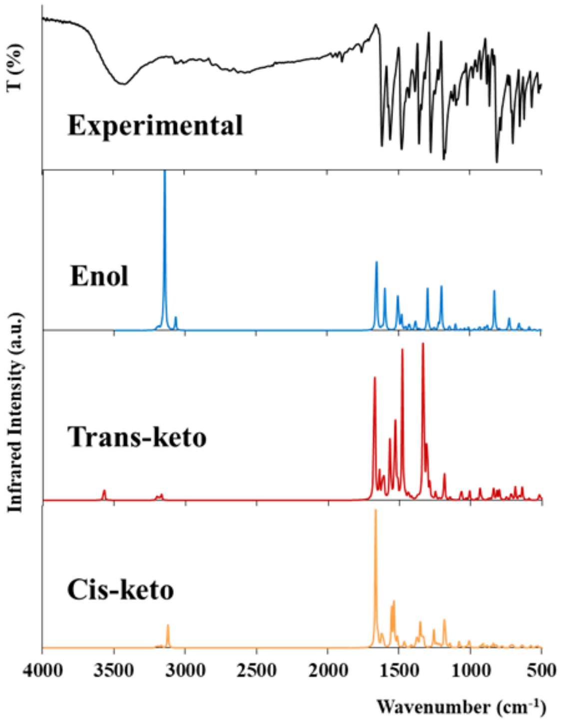

**Figure 6 –** The experimental IR spectrum of compound **I** in solid state, and calculated IR spectra of its different tautomeric forms

**Table 4 –** The vibration modes in the calculated IR spectrum (Figure 7) of the ground state of enol-imine form of compound **I** and the peaks of the experimental IR spectrum

| Calculated molecular vibration (PED, %)[a] | Calculated frequency (cm$^{-1}$) | Calculated intensity (km·mol$^{-1}$) | Experimental frequency (cm$^{-1}$)/ Intensity |
|---|---|---|---|
| *v*O11–H12 (100) | 3206 | 1.89 | 3425/ Medium |
| *v*C17–H20 + *v*C19–H24 (100) | 3198 | 10.99 | 3067/ Low |
| *v*C2–H7 + *v*C3–H8 (13); *v*C6–H9 (87) | 3194 | 0.35 | 3050/ Low |
| *v*C2–H7 + *v*C3–H8 (87); *v*C6–H9 (13) | 3192 | 6.54 | 3008/ Low |
| *v*C17–H20 (100) | 3184 | 14.02 | 2989/ Low |
| *v*C23–H25 (87); *v*C18–H22 + *v*C23–H25 (13) | 3164 | 9.50 | 2971/ Low |
| *v*C23–H25 (13); *v*C18–H22 + *v*C23–H25 (87) | 3157 | 15.44 | 1959/ Low |
| *v*O11–H12 (97) | 3143 | 944.21 | 1929/ Low |
| *v*C13–H14 (98) | 3067 | 81.69 | 1896/ Low |
|  |  |  | 1818/ Low |
|  |  |  | 1758/ Low |
| *v*N15–C13 + *v*C1–C6+ *v*C3–C4 + *v*C1–C2 + *v*C2–C3 (53) | **1657** | **207.79** | **1617/High** |
| *v*N15–C13 + *v*C1–C6+ *v*C3–C4 + *v*C19–C23 + *v*C2–C3 (50) | 1653 | 31.34 | Not detected |
| *v*C2–C3+ *v*C5–C6 + *v*C1–C6 + *v*C3–C4 + *v*N21–C18 *v*N21–C23 (11); *v*C17–C19 + *v*C5–C6 (39) | **1615** | **13.75** | **1572/ Low** |
| *v*C16–C17 + *v*C19–C23 (53) | 1600 | 11.97 | Not detected |
| *v*N15–C13 + *v*C5–C6+ *v*C1–C2 (50); *β*H12–O11–C4 (12); *β*H7–C2–C3 + *β*H8–C3–C4 + *β*H9–C6–C5 (10) | **1594** | **249.11** | **1555/ High** |

*Continuation of the table*

| Calculated molecular vibration (PED, %)[a] | Calculated frequency (cm$^{-1}$) | Calculated intensity (km·mol$^{-1}$) | Experimental frequency (cm$^{-1}$)/ Intensity |
|---|---|---|---|
| *β*H12–O11–C4 (19); *β*H9–C6–C5 + *β*H8–C3–C4 + *β*H7–C2–C3 (16) | **1506** | **1701.20** | **1479/ High** |
| *ν*C17–C19 + *ν*N21–C18+ *ν*N21–C23 (14); *β*H9–C6–C5 (12) + *β*H8–C3–C4 + *β*H7–C2–C3 (15); *β*H20–C17–C19 + *β*H22–C18–N21 + *β*H25–C23–N21 (11); *β*H22–C18–N21 + *β*H25–C23–N21 + *β*H14–C13–N15 (20) | **1500** | **99.36** | **1450/ Medium** |
| *β*H12–O11–C4 (12); *β*H9–C6–C5 + *β*H8–C3–C4 + *β*H7–C2–C3 (17); *β*C1–C2–C3 + *β*C2–C1–C6 + *β*C2–C3–C4 (10) | **1478** | **92.58** | **1435/ Medium** |
| *β*H12–O11–C4 (10); *β*H22–C18–N21 + *β*H25–C23–N21 + *β*H14–C13–N15 + *β*H24–C19–N23 (31) | 1451 | 23.48 | Not detected |
| *ν*C2–C3+ *ν*C5–C6 + *ν*C1–C6 + *ν*C3–C4 + *ν*N21–C18 + *ν*N21–C23 (22); *β*H12–O11–C4 (11); *β*H14–C13–N15 + *β*H9–C6–C5 + *β*H25–C23–N21 + *β*H8–C3–C4 (18) | **1424** | **52.28** | **1384/ Medium** |
| *β*H14–C13–N15 + *β*H9–C6–C5 + *β*H22–C81–N21 + *β*H25–C23–N21 (57) | **1381** | **72.07** | **1355/ High** |
| *β*H20–C17–C19 + *β*H22–C18–N21 + *β*H25–C23–N21 + *β*H24–C19–C23 (65) | **1356** | **10.45** | **1338/ Medium** |
| *ν*C1–C6+ *ν*C1–C2 + *ν*C5–C13 (64) | **1340** | **5.11** | **1314/ Low** |
| *ν*O11–C4+ *ν*C5–C13 + *ν*C3–C4 (40); *β*H14–C13–N15 + *β*H9–C6–C5 + *β*H25–C23–N21 + *β*H8–C3–C4 (12) | **1295** | **231.18** | **1274/ High** |
| *ν*N21–C18+ *ν*N21–C23 + *ν*C19–C23 (63) | 1283 | 5.65 | |
| *ν*N15–C16 (10); *β*H14–C13–N15 + *β*H9–C6–C5 + *β*H25–C23–N21 + *β*H8–C3–C4 (24) | **1259** | **2.42** | **1243/ Medium** |
| *ν*N15–C16 (19); *ν*C5–C13+ *ν*C3–C4 + *ν*N15–C16 (13); *β*H14–C13–N15 + *β*H9–C6–C5 + *β*H25–C23–N21 + *β*H8–C3–C4 (12); *β*H22–C18–N21 + *β*H25–C23–N21 + *β*H14–C13–N15 (10) | **1249** | **18.26** | **1219/ Low** |
| *ν*C17–C19 + *ν*N21–C18+ *ν*N21–C23 (12); *β*H22–C18–N21 + *β*H25–C23–N21 + *β*H14–C13–N15 + *β*H24–C19–N23 (11); *β*H22–C18–N21 + *β*H25–C23–N21 + *β*H14–C13–N15 (23) | 1218 | 32.63 | Not detected |
| *ν*C5–C13+ *ν*C3–C4 + *ν*N15–C16 (32) | **1199** | **293.30** | **1170/ High** |
| *ν*C2–C3+ *ν*C5–C6 + *ν*C1–C6 + *ν*C3–C4 + *ν*N21–C18 + *ν*N21–C23 (16); *β*H7–C2–C3 + *β*H8–C3–C4 + *β*H9–C6–C5 (47) | **1147** | **9.89** | **1125/ Medium** |
| *ν*C17–C19 + *ν*N21–C18+ *ν*N21–C23 (26); *β*H20–C17–C19 + *β*H24–C19–C23 (51) | 1139 | 22.60 | Not detected |
| *ν*C1–C2 + *ν*C2–C3 (39); *ν*Cl10–C1 (11); *β*H9–C6–C5 + *β*H8–C3–C4 + *β*H7–C2–C3 (26) | **1100** | **36.46** | **1080/ Medium** |
| *ν*C19–C23 + *ν*N21–C23+ C17–C19 (54); *β*H22–C18–N21 + *β*H25–C23–N21 + *β*H14–C13–N15 + *β*H24–C19–N23 (10) | **1062** | **9.97** | **1037/ Low** |
| *β*C18–N21–C23 + *β*C17–C19–C23 + *β*C19–C23–N21 (72) | **1034** | **14.83** | **1010/ Medium** |
| *τ*H14–C13–N15–C16 (82) | 1009 | 17.85 | |
| *τ*H24–C19–C23–N21 (70) | **1004** | **0.36** | **975/ Low** |
| *τ*H7–C2–C3–C4 + *τ*H8–C3–C4–C5 (72) | **969** | **1.49** | **954/ Low** |
| *τ*H20–C17–C19–C23 + *τ*H22–C18–N21–C23 + *τ*H25–C23–N21–C18 (72) | 965 | 7.50 | Not detected |

*Continuation of the table*

| Calculated molecular vibration (PED, %)[a] | Calculated frequency ($cm^{-1}$) | Calculated intensity ($km \cdot mol^{-1}$) | Experimental frequency ($cm^{-1}$)/ Intensity |
|---|---|---|---|
| *τ*H22–C18–N21–C23 + *τ*H25–C23–N21–C18 (66); *τ*C17–C19–C23–N21 + *τ*C18–N21–C23–C19 (66) | **938** | **5.19** | **923/ Medium** |
| *τ*H9–C6–C5–C4 (72); *τ*C1–C6–C5–C13 (10) | **894** | **19.21** | **880/ Medium** |
| *v*N15–C16 (10); *β*C19–C23–N21 + *β*C5–C13–N15 + *β*C1–C2–C3 + *β*C18–N21–C23 + *β*C16–C17–C19 (44) | **877** | **33.61** | **861/ Medium** |
| *τ*H12–O11–C4–C3 (40); *τ*H7–C2–C3–C4 + *τ*H8–C3–C4–C5 (45) | **845** | **1.87** | **830/ Low** |
| *τ*H12–O11–C4–C3 (51); *τ*H7–C2–C3–C4 + *τ*H8–C3–C4–C5 (25) | **825** | **210.86** | **805/ High** |
| *τ*H24–C19–C23–N21 (58) | 823 | 31.11 | Not detected |
| *v*C1–C2 + *v*C2–C3 (14); *v*O11–C4 (12); *β*C1–C2–C3 + *β*C2–C1–C6 + *β*C2–C3–C4 (22) | **791** | **7.9** | **787/ Medium** |
| *τ*H9–C6–C5–C4 (11); *τ*H7–C2–C3–C4 + *τ*H8–C3–C4–C5 (10); *τ*H7–C2–C3–C4 + *τ*H8–C3–C4–C5 (13); *τ*C1–C6–C5–C13 + *τ*C1–C2–C3–C4 + *τ*C3–C2–C1–C6 + *τ*C2–C1–C6–C5 (10); out-of-planeO11–C3–C5–C4 (29) | **737** | **2.91** | **726/ Low** |
| *β*C5–C13–N15 + *β*C6–C15–C13 + *β*C19–C23–N21 + *β*C17–C19–C23 (28); *τ*C18–N21–C23–C19 + *τ*C16–C17–C19–C23 (14) | **723** | **62.49** | **710/ Low** |
| *β*C5–C13–N15 + *β*C6–C15–C13 + *β*C19–C23–N21 + *β*C17–C19–C23 (17); *τ*H22–C18–N21–C23 + *τ*H25–C23–N21–C18 (12); *τ*C18–N21–C23–C19 + *τ*C16–C17–C19–C23 (27) | **718** | **30.07** | **700/ High** |
| *β*C2–C3–C4 + *β*C1–C6–C5 + *β*C1–C2–C3 (40); *v*Cl10–C1 (16); *β*C2–C1–C6 + *β*C1–C2–C3 + *β*C1–C6–C5 (11) | **654** | **53.39** | **646/ Medium** |
| *β*C18–N21–C23 + *β*C17–C19–C23 (72) | **634** | **15.58** | **622/ Medium** |
| *β*C2–C1–C6 + *β*C1–C2–C3 + *β*C1–C6–C5 (11); *β*C16–C17–C19 + *β*C6–C5–C13 (27) | **581** | **16.67** | **568/ Medium** |
| *τ*C3–C2–C1–C6 + *τ*C2–C1–C6–C5 (60) | 578 | 5.88 | Not detected |
| *β*C18–C16–N15 + *β*C13–N15–C16 + *β*C6–C15–C13 + *β*C16–C1z7–C19 (16); out-of-planeN15–C17–C18–C16 + *τ*C2–C1–C6–C5 (35) | **543** | **7.97** | **520/ Low** |
| *β*C18–C16–N15 + *β*C13–N15–C16 + *β*C6–C15–C13 + *β*C16–C17–C19 (33); *τ*C1–C6–C5–C13 (10); out-of-planeN15–C17–C18–C16 + *τ*C2–C1–C6–C5 (15) | 504 | 4.85 | 516/ Low |

*Global reactivity descriptors and molecular orbitals*

In Table 5 the values of the global reactivity descriptors, calculated using B3LYP 6-311++G(d,p) for molecules in the gas phase are provided. A total energy is minimal for the enoimine form of the compound **I**. It is also worth noting the higher global chemical hardness of this form, which points the resistance of the electronic shell to deformation. Both of these parameters indicate the higher stability of the enolimine form. The highest occupied and the lowest unoccupied molecular orbitals for all three forms are localised mainly throughout the whole molecule (see Figure 7). The special features include localisation on the chlorine atom only for HOMO, as well as lower electron density of HOMO and LUMO on the nitrogen atom of the heterocycle.

**Table 5 –** Dipole moment, frontier molecular HOMO and LUMO orbitals and descriptors for three forms of compound **I** in gas phase, obtained by using the B3LYP/6-311++G(d,p) method

| Parameter | Enol form | *Cis*-keto form | *Trans*-keto form |
|---|---|---|---|
| Total energy (eV) | –30145.44228 | –30145.32565 | –30145.01196 |
| Dipole moment (Debye) | 3.89751 | 5.942917 | 8.738414 |
| $E_{\mathrm{HOMO}}$ (eV) | –0.23729 | –0.22019 | –0.21759 |
| $E_{\mathrm{LUMO}}$ (eV) | –0.08962 | –0.10001 | –0.10392 |
| $\Delta E_{\mathrm{LUMO-HOMO}} = E_{\mathrm{LUMO}} - E_{\mathrm{HOMO}}$ (eV) | 0.14767 | 0.12018 | 0.11367 |
| Ionization energy, $I = -E_{\mathrm{HOMO}}$ (eV) | 0.23729 | 0.22019 | 0.21759 |
| Electron affinity, $A = -E_{\mathrm{LUMO}}$ (eV) | 0.08962 | 0.10001 | 0.10392 |
| Electronegativity, $\chi = (I + A)/2$ (eV) | 0.16346 | 0.16010 | 0.16076 |
| Chemical potential, $\mu = -\chi$ (eV) | –0.16346 | –0.16010 | –0.16076 |
| Global chemical hardness, $\eta = (I - A)/2$ (eV) | 0.07384 | 0.06009 | 0.05684 |
| Global chemical softness, $S = 1/(2\eta)$ (eV$^{-1}$) | 6.77186 | 8.32085 | 8.79740 |
| Global electrophilicity index, $\omega = \mu^2/(2\eta)$ (eV) | 0.18093 | 0.21328 | 0.22734 |
| Global nucleophilicity index, $E = \mu \times \eta$ (eV$^2$ ) | –0.01207 | –0.00962 | –0.00914 |

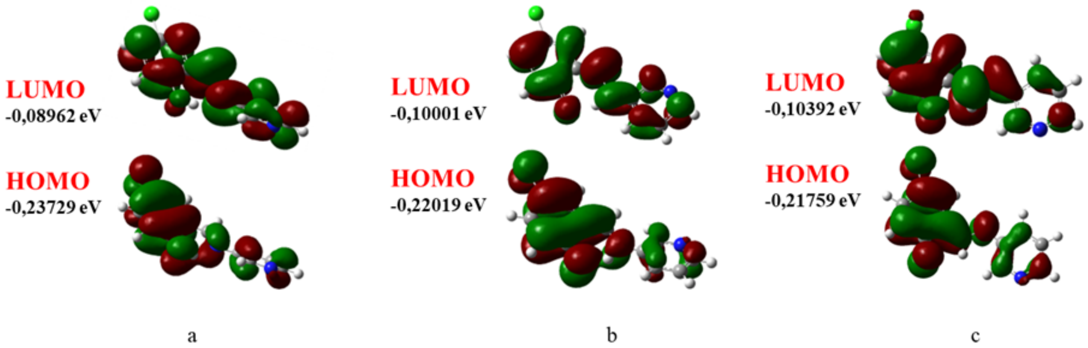

**Figure 7 –** Views on the electronic isosurfaces of LUMO and HOMO molecular orbitals of tautomeric forms of compound **I** obtained by using the B3LYP/6-311++G(d,p) method (a – enolimine, b – *cis*-keto-namine c – *trans*-ketoenamine; results under 0.02 a.u. isovalue)

The ionisation potential (I) and the affinity to electrons (A) were estimated as follows: I = −E (HOMO), A = −E (LUMO) [49]. Thus, a decrease in the values of I corresponds to an increase in electron-donating capacity, and an increase in A corresponds to an increase in electron-accepting capacity. For all forms of the compound **I** the ionisation energy lies in the range of 0.21 – 0.25 eV, and the affinity to electrons is about 0.1 eV. These values indicate more expressed electron donor ability of the compound.

For a general reactivity assessment, some additional characteristics calculated from the difference in the LUMO and HOMO energies, were also calculated [81]. Low electronegativity values (0.15 – 0.17 eV) also indicate the predominantly electron donor properties of the molecules.

*Molecular electrostatic potential surfaces*

The visualisation of electrophilic and nucleophilic centres of different forms of the compound **I** was carried out using molecular electrostatic potential (MEP) surfaces (see Figure 8).

The red and blue zones on the MEP surfaces depict nucleophilic and electrophilic centres respectively. As expected, the nucleophilic centres are the oxygen, nitrogen and chlorine atoms. For the enolimine form (Figure 8a) the nucleophilicities of oxygen and heterocyclic nitrogen are close to each other. For the ketoenamine forms (Figure 8b, c) this characteristic is far more pronounced for oxygen atom. The most pronounced electrophilic centre is the hydrogen at the carbon atom adjacent to the imine nitrogen.

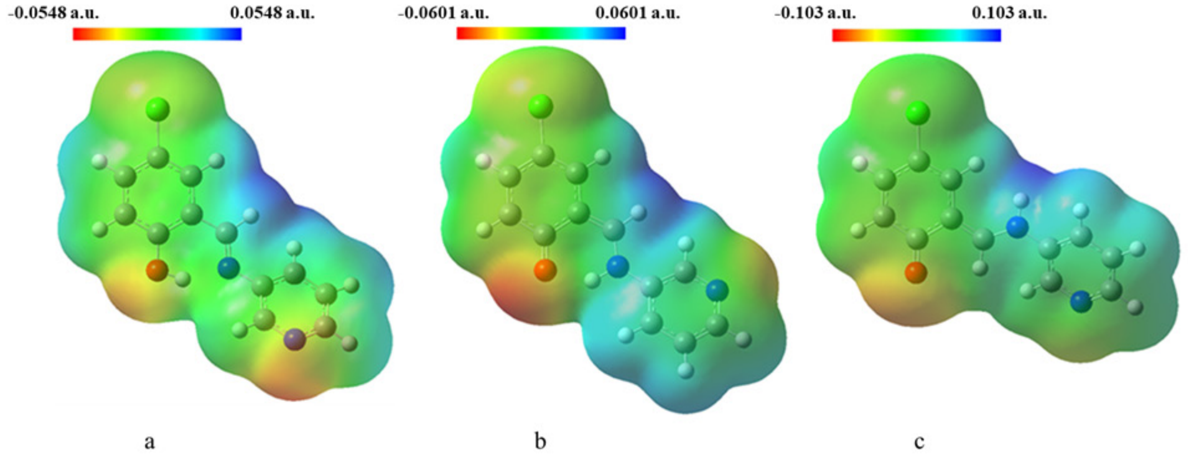

**Figure 8 –** View of the molecular electrostatic potential surfaces of compound **I**, obtained by using the B3LYP/6-311++G(d,p) method (a – enolimine, b – *cis*-keto-namine c – *trans*-ketoenamine; results under 0.004 a.u. isovalue)

*Absorption spectroscopy*

The calculated according to B3LYP 6-311++G(d,p) and the experimental UV-spectra of the compound **I** solution in ethanol are presented in Figure 9. The calculated spectra of the *cis*- and *trans*-ketoenamine forms of the compound **I** (Figures 9b, c) contain bands at 428 and 521 nm characteristic for these forms. The maxima of absorption band of enoimine form are located below 400 nm. A good agreement between the experimental spectrum (Figure 9d) and the calculated spectrum of enolimine form (Figure 9a) is observed. In the experimental and calculated spectra, the absorption maxima and bands at 357 and 355 nm; 301 and 312 nm; 210 and 224 nm closely coincide.

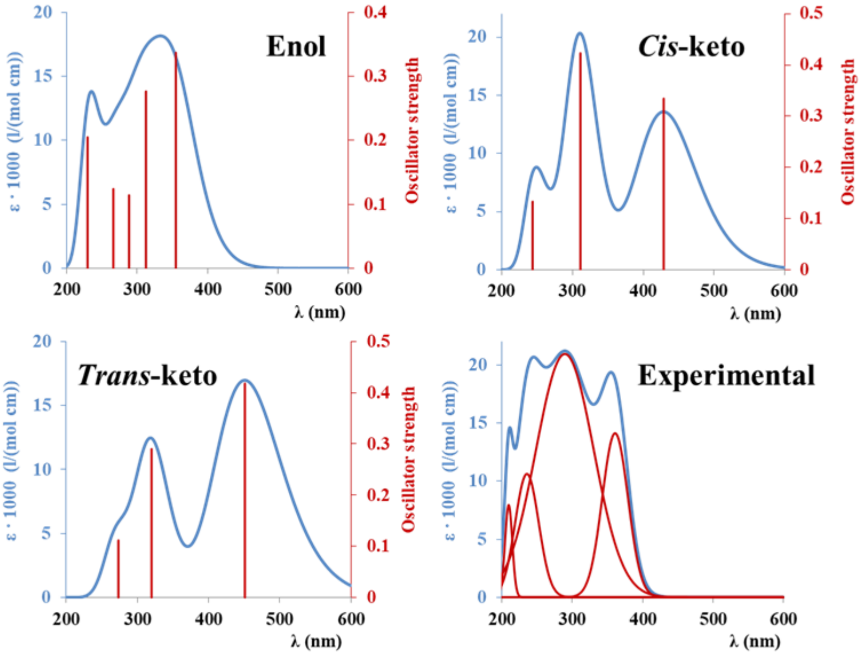

**Figure 9 –** The calculated absorption spectra of different tautomeric forms of compound **I** obtained by using the TD-DFT/B3LYP/6-311++G(d,p) method and experimental UV-vis spectrum of compound **I** in ethanol

The UV-spectra of the compound **I** in different both polar and non-polar solvents were also recorded and analysed for better understanding of the influence of medium on the tautomerism of this Schiff base. These spectra are presented in Figure 10. The UV-spectra in different alcohols are presented separately.

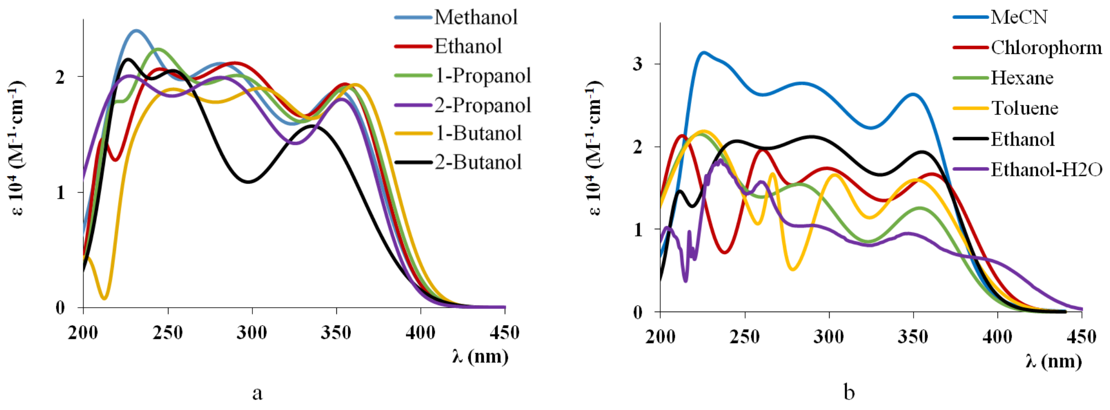

a b

**Figure 10 –** Experimental UV-spectra of compound **I** in different solvents

The absorption bands corresponding to the π → π* and n → π* transitions are located in the ultraviolet region. The bands corresponding to the π→ π* transition in more polar solvents such as ethanol and chloroform are located at 209 and 215 nm correspondingly. A series of solvents sorted by the location of the longer wavelength band corresponding to the n → π* transition is as follows: toluene (351 nm) – hexane (352 nm) – acetonitrile (353 nm) – ethanol (357 nm) – chloroform (363 nm). Therefore, the increase of the solvent polarity apparently shifts the hydrogen atom from O11 toward N15. The spectrum of the compound **I** in the ethanol-water mixture containing 76 weight % ethanol is worth noting separately. An introduction of water somewhat shifts the position of the n→ π* transition band of enolimine form, but reveals a band at 400 nm, related with the ketoenamine form.

### *Ionisation constants*

An oxygen-containing group and two nitrogen-containing groups are the acid-base centres in the structure of the compound **I**. Generally, the proteolytic equilibria of the compound **I** might be presented as follows [82]:

$$H_3A^{2+} \overset{K_1}{\rightleftarrows} H_2A^{+} \overset{K_2}{\rightleftarrows} HA \overset{K_3}{\rightleftarrows} A^{-} \qquad (1)$$

The neutral form HA exists as the mixture of both enolimine and ketoenamine forms. The evaluation of the equilibrium constants of tautomeric transformations of the compound falls outside the scope of the present study. Only the acidity constants $K_1 - K_3$ are to be determined.

At the first step the UV-spectra of the compound **I** at different pH values in water-ethanolic mixtures with the 73 weight percent ethanol were recorded. The obtained spectra are presented in Figure 11a. There are several isosbestic points at 303, 361 and 364 nm. The absorbances of each solution at 390 nm were determined and plotted against the pH value (see Figure 11b). The jumps are present on the curve at the pH ranges 4.7 – 5.7 and 7.0 – 10.0. The potentiometric titration of the mixture was conducted (see Section 2.4) for more accurate analysis. The titration curve is presented in Figure 11c. The experimental curves were processed implementing the KEV algorithm [83] for estimation of ionic equilibrium constants. The obtained ionisation constant values are listed in Table 6. Apparently, p$K_{a1}$ corresponds to the dissociation of protonated pyridine nitrogen, p$K_{a2}$ – to the protonation of imine nitrogen, and p$K_{a3}$ – to the protonation of hydroxyl group [82].

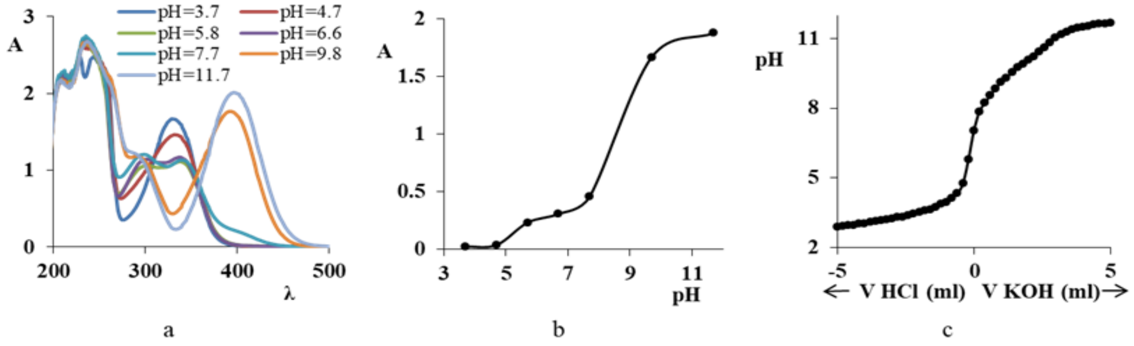

**Figure 11** – UV-spectra of compound **I** in different pH (a), dependence of the absorption value on pH (b) and the titrimetric curve of compound **I** (c) in ethanol-water media (73% ethanol by weight)

**Table 6** – Acidity constants of compound **I** in a water-ethanol mixture (73% ethanol by weight) obtained by potentiometric titration

| p$K_{a1}$ | p$K_{a2}$ | p$K_{a3}$ |
|---|---|---|
| 4.16 | 8.55 | 10.43 |

*Molecular docking*

To roughly estimate the level of binding energies of the compound **I** with target proteins, the molecular docking methodology was employed. The models of the structure of some proteins from the cell walls of *Staphylococcus aureus* (predominantly, sortase), factors of invasion LasA and LasB, hemolytic proteins LipA and LipB and Lasl protein of *Pseudomonas aeruginosa*, see Table 7. The original ligands (downloaded together with the protein structures from the PDB) were removed and the affinity calculation was performed for their binding sites. In the case of multiple original ligands, molecular docking was performed for the binding sites of each of them and the lowest affinity value obtained was recorded. In addition, the docking procedure for the known antibiotics azithromycin and ampicillin was performed on the same proteins.

**Table 7** – Intermolecular interactions energies of gram-positive and gram-negative microorganisms proteins with original ligands, antibiotic molecules and tautomeric forms of **I**

| No | PDB code | Protein | Binding energy (kcal/mol) | | | | | |
|---|---|---|---|---|---|---|---|---|
| | | | Initial ligand[a] | Azithromycin | Ampicillin | Compound **I** | | |
| | | | | | | Enol form | *Cis*-keto form | *Trans*-keto form |
| Gram-positive bacteria proteins (*Staphylococcus aureus*) | | | | | | | | |
| 1 | 2KID | Sortase A with (PHQ) LPA(B27) peptide | –6.8 | –6.9 | –6.9 | –5.2 | –5.7 | –5.6 |
| 2 | 6R1V | Sortase A with 6-(hydroxymethyl)-3-oxidanyl-2-(thiophen-3-ylmethyl)pyran-4-one | –5.1 | –7.1 | –6.7 | **–5.7** | **–5.7** | **–5.7** |
| 3 | 4LFD | Sortase B with (CBZ) NPQ(B27) peptide | –6.9 | –7.6 | –7.4 | –6.5 | –6.5 | –6.5 |
| 4 | 1QXA | Sortase B with Gly3 | –4.6 | –7.6 | –6.4 | **–6.5** | **–6.4** | **–6.3** |
| 5 | 1QWZ | Sortase B | –4.7 | –7.6 | –7 | **–6.5** | **–6.6** | **–6.6** |
| 6 | 1QX6 | Sortase B with E64 | –5.7 | –8.1 | –7.1 | **–6.4** | **–6.5** | **–6.0** |
| Gram-negative bacteria proteins (mainly *Pseudomonas aeruginosa*) | | | | | | | | |
| 7 | 3IT7 | LasA elastase | –4,9 | –9.1 | –8.0 | **–6.5** | **–6.5** | **–6.5** |

*Continuation of the table*

| No | PDB code | Protein | Binding energy (kcal/mol) | | | | | |
|---|---|---|---|---|---|---|---|---|
| | | | Initial ligand[a] | Azithromycin | Ampicillin | Compound **I** | | |
| | | | | | | Enol form | *Cis*-keto form | *Trans*-keto form |
| 8 | 7NLM | LasB elastase | –5.8 | –7.4 | –7.0 | **–6.2** | **–6.0** | **–6.1** |
| 9 | 9G3R | LecA lectin with a synthetic thiogalactoside | –5,6 | –7,3 | –6.0 | –5.5 | –5.0 | –5.2 |
| 10 | 5A6Y | LecB lectin with mannose-alpha1,3mannoside | –6.0 | –6.2 | –5.6 | –5.2 | –5.1 | –5.2 |
| 11 | 1RO5 | AHL Synthase LasI | –4.6 | –8.9 | –7.0 | **–7.0** | **–6.9** | **–6.8** |

[a] (from top to bottom) Initial ligand = (phenylmethyl) N-[(2S)-4-methyl-1-oxidanylidene-1-[(2S)-2-[[(2S)-1-oxidanylidene-1-[[(2S,3R)-3-oxidanyl-1-sulfanyl-butan-2-yl]amino]propan-2-yl]carbamoyl]pyrrolidin-1-yl]pentan-2-yl]carbamate; 6-(hydroxymethyl)-3-oxidanyl-2-(thiophen-3-ylmethyl)pyran-4-one; (phenylmethyl) N-[(2S)-4-azanyl-1-[(2S)-2-[[(2S)-5-azanyl-1,5-bis(oxidanylidene)-1-[[(2S,3R)-3-oxidanyl-1-sulfanyl-butan-2-yl]amino]pentan-2-yl]carbamoyl]pyrrolidin-1-yl]-1,4-bis(oxidanylidene)butan-2-yl] carbamate; trimethyl-(2-sulfanylethyl)azanium; trimethyl-(2-sulfanylethyl)azanium; [amino-[4-[[(2S)-2-[[(2S)-2,4-dihydroxy-4-oxo-butanoyl]amino]-4-methyl-pentanoyl]amino]butylamino]methylidene]azanium; (2R,3R)-2,3-dihydroxybutanedioic acid and propane-1,2,3-triol; (S)-2-mercapto-N-(4-methoxyphenyl)-4-methylpentanamide; (2R,3R,4S,5R,6S)-2-(hydroxymethyl)-6-sulfanyl-oxane-3,4,5-triol and 2-(2-hydroxyethyloxy)ethanol; (2S,3S,4S,5S,6R)-6-(hydroxymethyl)oxane-2,3,4,5-tetrol and propane-1,2,3-triol; sulfate.

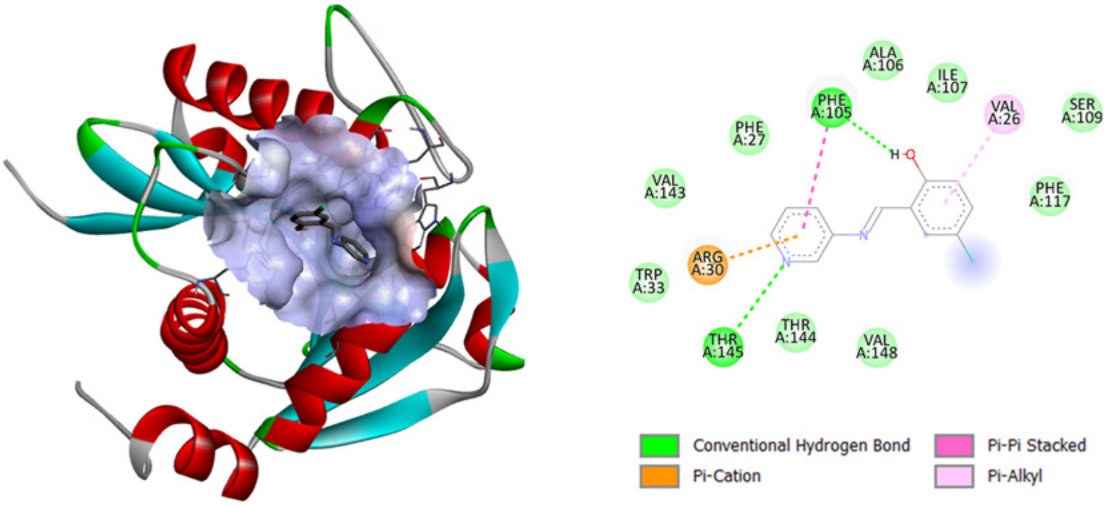

**Figure 12 –** Molecular docking results of compound **I** and *Pseudomonas aeruginosa* Synthase LasI

Generally, it is worth noting that the binding energies are close to each other, at a level of 5.5 – 6.5 kcal/mol. In most cases, the indicated energies are lower for the compound **I** than for the initial ligands (marked in bold in Table 7). At the same time, the affinity value comparable with that of used antibiotics is reached by the compound **I** only in the case of sortase B of *Staphylococcus aureus* and Lasl protein of *Pseudomonas aeruginosa*. For the last one the visualisation model of indicated interaction is presented in Figure 12. A binding of the molecule of enolimine form of compound **I** is is provided by hydrogen and π···π interactions with phenylalanine, π···alkyl interactions with valine, and hydrogen bonds with tyrosine. It is also worth noting the almost complete absence of differences in affinities between the tautomeric forms.

### *Antimicrobial activity in vitro*

The method of obtaining the samples for *in vitro* testing is described in Section 2.9. An average mass of the compound **I** on the surface of each disc, determined according to the method described in Section 2.9, is about 10 μg, which roughly corresponds to the minimal inhibitory content of the substance isomeric to compound **I** that was determined in the paper [47]. At the same time the substance under study was present on the disc surface in its solid state. The results of the testing are collected in Table 8.

**Table 8 –** Bacteria growth inhibition zones around samples

| Bacteria | Growth inhibition zone (mm) | | |
|---|---|---|---|
| | Ti6Al4V | Ti6Al4V with calcium phosphate | Ti6Al4V with calcium phosphate and compound **I** |
| *Pseudomonas aeruginosa* | Continuous growth | 4±1 | 9±1 |
| *Escherichia coli* | Continuous growth | Continuous growth | Continuous growth |
| *Staphylococcus aureus* | Continuous growth | Continuous growth | Continuous growth |

As could be seen from the data of Table 8, no meaningful activity of the compound in relation to *Staphylococcus aureus* ATCC 25923, *Escherichia coli* ATCC 25922 was recorded, but a limited antimicrobial effect in relation to *Pseudomonas aeruginosa* ATCC 27853 was noted. For the alloy Ti6Al4V covered with calcium phosphate this effect might be related to the presence of $TiO_2$ on its surface.

*Toxicity of compound*

The toxicity of the compound **I** was estimated according to the ProTox online tool [84], and the predicted toxicity class is 4 out of 6, with $LD_{50}$ equal to 370 mg/kg. According to prediction, the compound might exhibit neurotoxicity, respiratory toxicity and immunotoxicity, and additionally be toxic to the environment. The detailed report is provided in Supplementary Information (Figure S1).

In order to check the effect of the compound on living organism, the *in vivo* tests with laboratory mice were conducted. Based on the visual inspection right after dissection, no abscesses or other local signs of inflammation were observed in any animal. The results of weighing the internal organs of the experimental animals are given in Table 9. To evaluated the organ conditions objectively, the ratios of the organ mass to the animal mass were calculated.

The results of determination of liver enzymes are summarised in Table 10.

**Table 9 –** Average masses of organs of laboratory mice at day 14 after injection of compound **I**

| Group | Weight of organs, g | | Weight of organs divided by weight of mouse | | Weight of mouse, g |
|---|---|---|---|---|---|
| | Heart | Liver | Heart | Liver | |
| Control | 0,108±0,004 | 1,26±0,07 | 0,0054±0,0003 | 0,063±0,005 | 20,0±0,5 |
| Injection of 0.2 mg/kg of compound **I** | 0,111±0,007 | 1,26±0,07 | 0,0045±0,0004 | 0,051±0,004 | 24,8±0,6 |

**Table 10 –** Activity of liver enzymes in the fresh blood samples of laboratory mice at day 14 after injection of compound **I**

| Group | Activity, U/l | |
|---|---|---|
| | Alanine aminotransferase | Aspartate transaminase |
| Norm [86] | 26 – 89 | 59 – 140 |
| Control | 74 ± 3 | 84 ± 7 |
| Injection of 0.2 mg/kg of compound **I** | 86 ± 2 | 86 ± 2 |

The results were compared using the Wilcoxon signed rank test [85], and neither organ masses, nor liver enzyme activities of mice in control and experimental groups revealed statistically significant differences. Although the darkening of the liver edges was noticed for the mice of experimental group, the activities of liver enzymes in the blood samples were still within their normal ranges [86]. The obtained data indicate that the implantation of compound **I** in the late postoperative period does not cause significant toxic shifts in the metabolism of mice.

*Intestinal absorption prediction pathway of compound*

The intestinal absorption pathway of the compound **I** was predicted using the SwissADME online tool [87], see Figure S2. According to the prediction, the compound has a good blood-brain barrier crossing probability. No active efflux of the compound by the P-glycoprotein is also predicted.

## Discussion

The combination of the presented results indicates the existence of the compound **I** predominantly in the enolimine form in the solid state. At the same time, in solutions in organic solvents, this form is also mainly present. With an increase in the polarity of the solvent, some displacement of the hydrogen atom from oxygen to the imine nitrogen takes place. Similar results are observed for a number of related compounds, including salicylideneaniline, salicylidene-2-aminopyridine, 5-chlorosalicylidene-2-aminopyridine [47, 80, 82]. In aqueous-alcoholic solutions of the compound **I**, the keto-enamine tautomeric form is present.

The obtained ionisation constant values correspond to dissociation of protonated pyridine nitrogen, protonation of imine nitrogen, and protonation of hydroxyl group

The molecular docking results indicate that only for some proteins the binding energies of the compound **I** are approaching those for ampicillin and azithromycin. For the related (and according to the data from [64] – the same) compound the values of minimum inhibitory concentration (MIC) in DMFA solution were evaluated in the paper [47], and these values are 30 times higher than these of ampicillin. This is fundamentally consistent with the calculated data presented in the present study. At the same time, fairly high level of toxicity of the compound **I** is assumed. Based on this it was quite important to test the antimicrobial activity of the compound under two given conditions. The first is the usage of a model that approximates the compound **I** to the real conditions of potential use on the implant surface. At the same time, the used form of the compound does not imply dissolution in toxic solvents. The second is testing the activity for low compound contents, in the MIC range for analogous substances. The results obtained indicate the prospects for using the compound **I** as an antimicrobial substance. Further work will be related to experimental studies related to the search for optimal antimicrobial activity with minimal toxicological impact on warm-blooded organisms.

## Conclusion

In the present study, the detailed results of computational studies of 4-chloro-2-((pyridin-3-ylimino)methyl)phenol is reported. The molecules in the crystal structure are mainly linked to each other by C–H···O and C–H···N hydrogen bonds. Most of the Hirschfeld surface is formed by mutual contacts of H···X (X = H, C, N, O, Cl) and C···X (X = C, N, O, Cl).

Comparison of the results of computer modeling and experimental studies indicates the predominant existence of the compound in the enolimine form in organic solvents. At the same time, the introduction of water leads to the appearance of the ketoenamine form.

The calculated results of molecular docking do not reveal any differences in the effect on a number of proteins of *Staphylococcus aureus* and *Pseudomonas aeruginosa*, while the affinity values themselves are either lower or are approaching those for reference antibiotics.

An inhibitory effect of microgram amounts of the compound on the surface of a medical titanium alloy on the development of *Pseudomonas aeruginosa* in vitro was detected.

No significant toxicity effects of the studied compound on the laboratory mice was detected.

## Supplementary Materials

The following supporting information is available: Figure S1 – The prediction of toxicity of the compound I by the Pro-Tox online tool; Figure S2 – The prediction of intestinal absorption and blood-brain barrier penetration of the compound I by the SwissADME online tool; Table S1 – Antibacterial activity of different secondary amines; Table S2 – Selected bond lengths (Å) and angles (°) in the optimized structure of cis-ketoenamine and trans-ketoenamine form of compound I using the B3LYP/6-311++G(d,p) method; Table S3 – The vibration modes in the calculated IR spectrum (Figure 7) of the ground state of cis-ketoenamine form of compound I, obtained by using the DFT/B3LYP/6-311++G(d,p) method; Table S4 – The vibration modes in the calculated IR spectrum (Figure 7) of the ground state of trans-ketoenamine form of compound I, obtained by using the DFT/B3LYP/6-311++G(d,p) method.

## Acknowledgments

This research was funded by Ministry of Science and Higher Education of Russian Federation, project topic "Materials and technologies for design and development of implants", state contract number 1023041400091-5-3.2.10;2.4.2.

The animal study protocol was approved by the Ethics Committee of Kurgan State University (protocol number 1 from 28th April 2025).

The authors are grateful to the pharmaceutical company Binnopharm Group for providing laboratory mice as the gift.

## Abbreviations

The following abbreviations are used in this manuscript:

| | |
|---|---|
| HOMO | Highest occupied molecular orbital |
| LUMO | Lowest unoccupied molecular orbital |
| DFT | Density functional theory |
| NMR | Nuclear magnetic resonance |
| IR | Infrared |
| UV | Ultraviolet |
| MEP | Molecular electrostatic potential |
| MIC | Minimum inhibitory concentration |
| DMFA | Dimethylformamide |
| CCDC | The Cambridge Crystallographic Data Centre |
| LOD | Limit of detection |
| LOQ | Limit of quantification |
| NADH | Nicotinamide adenine dinucleotide |
| PDB | Protein databank |

## Conflict of interest

The authors declare that they have no conflicts of interest.

## References

1. Schiff, H. (1864). Eine neue Reihe organischer Basen. *Annalen der Chemie und Pharmacie*, vol. *131, no 1, pp.* 118–119.
2. Sacconi, L. (1966). Tetrahedral complexes of nickel(II) and copper(II) with schiff bases. *Coordination Chemistry Reviews, vol. 1, no 1–2*, pp. 126–132. https://doi.org/10.1016/s0010-8545(00)80165-4.
3. Li, P.; Niu, M.; Hong, M.; Cheng, S.; Dou, J. (2014). Effect of structure and composition of nickel(II) complexes with salicylidene Schiff base ligands on their DNA/protein interaction and cytotoxicity. *Journal of Inorganic Biochemistry, vol. 137*, pp. 101–108. https://doi.org/10.1016/j.jinorgbio.2014.04.005.
4. Aggarwal, N.; Kumar, R.; Dureja, P.; Rawat, D. S. (2009). Schiff bases as potential fungicides and nitrification inhibitors. *Journal of Agricultural and Food Chemistry*, vol. *57, no 18*, pp. 8520–8525. https://doi.org/10.1021/jf902035w.
5. Raczuk, E.; Dmochowska, B.; Samaszko-Fiertek, J.; Madaj, J. (2022). Different Schiff Bases–Structure, Importance and Classification. *Molecules*, vol. 27, no 3, article 787. https://doi.org/10.3390/molecules27030787.
6. Al-Amiery, A. A.; Al-Majedy, Y. K.; Ibrahim, H. H.; Al-Tamimi, A. A. (2012). Antioxidant, antimicrobial, and theoretical studies of the thiosemicarbazone derivative Schiff base 2-(2-imino-1-methylimidazolidin-4-ylidene)hydrazinecarbothioamide (IMHC). *Organic and Medicinal Chemistry Letters*, vol. *2, no 1, article* 4. https://doi.org/10.1186/2191-2858-2-4.
7. Ceyhan, G.; Çelik, C.; Uruş, S.; Demirtaş, İ.; Elmastaş, M.; Tümer, M. (2011). Antioxidant, electrochemical, thermal, antimicrobial and alkane oxidation properties of tridentate Schiff base ligands and their metal complexes. *Spectrochimica Acta Part A Molecular and Biomolecular Spectroscopy*, vol. *81, no 1*, pp. 184–198. https://doi.org/10.1016/j.saa.2011.05.106.
8. Mermer, A.; Demirbas, N.; Uslu, H.; Demirbas, A.; Ceylan, S.; Sirin, Y. (2019). Synthesis of novel Schiff bases using green chemistry techniques; antimicrobial, antioxidant, antiurease activity screening and molecular docking studies. *Journal of Molecular Structure*, vol. *1181*, pp. 412–422. https://doi.org/10.1016/j.molstruc.2018.12.114.
9. Teran, R.; Guevara, R.; Mora, J.; Dobronski, L.; Barreiro-Costa, O.; Beske, T.; Pérez-Barrera, J.; Araya-Maturana, R.; Rojas-Silva, P.; Poveda, A.; Heredia-Moya, J. (2019). Characterization of antimicrobial, antioxidant, and leishmanicidal activities of Schiff base derivatives of 4-Aminoantipyrine. *Molecules*, vol. *24, no 15*, article 2696. https://doi.org/10.3390/molecules24152696.
10. Hasi, Q.-M.; Fan, Y.; Yao, X.-Q.; Hu, D.-C.; Liu, J.-C. (2016). Synthesis, characterization, antioxidant and antimicrobial activities of a bidentate Schiff base ligand and its metal complexes. *Polyhedron*, vol. *109*, pp. 75–80. https://doi.org/10.1016/j.poly.2016.01.052.
11. Parekh, J.; Inamdhar, P.; Nair, R.; Baluja, S.; Chanda, S. (2005). Synthesis and antibacterial activity of some Schiff bases derived from 4-aminobenzoic acid. *Journal of the Serbian Chemical Society*, vol. *70, no 10*, pp. 1155–1162. https://doi.org/10.2298/jsc0510155p.
12. Imran, S.; Taha, M.; Ismail, N.; Khan, K.; Naz, F.; Hussain, M.; Tauseef, S. (2014). Synthesis of Novel Bisindolylmethane Schiff bases and Their Antibacterial Activity. *Molecules*, vol. *19, no 8*, pp. 11722–11740. https://doi.org/10.3390/molecules190811722.

13. Nair, R.; Shah, A.; Baluja, S.; Chanda, S. (2006). Synthesis and antibacterial activity of some Schiff base complexes. *Journal of the Serbian Chemical Society, vol. 71, no 7*, pp. 733–744. https://doi.org/10.2298/jsc0607733n.

14. Tehrani, K. H. M. E.; Hashemi, M.; Hassan, M.; Kobarfard, F.; Mohebbi, S. (2015). Synthesis and antibacterial activity of Schiff bases of 5-substituted isatins. *Chinese Chemical Letters*, vol. *27, no 2*, pp. 221–225. https://doi.org/10.1016/j.cclet.2015.10.027.

15. Malladi, S.; Isloor, A. M.; Isloor, S.; Akhila, D. S.; Fun, H.-K. (2011). Synthesis, characterization and antibacterial activity of some new pyrazole based Schiff bases. *Arabian Journal of Chemistry*, vol. *6, no 3, pp.* 335–340. https://doi.org/10.1016/j.arabjc.2011.10.009.

16. Chohan, Z. H.; Scozzafava, A.; Supuran, C. T. (2003). Zinc Complexes of Benzothiazole-derived Schiff Bases with Antibacterial Activity. *Journal of Enzyme Inhibition and Medicinal Chemistry*, vol. *18, no 3, pp.* 259–263. https://doi.org/10.1080/1475636031000071817.

17. Vashi, K.; Naik, H. B. (2004). Synthesis of Novel Schiff Base and Azetidinone Derivatives and their Antibacterial Activity. *Journal of Chemistry*, vol. *1, no 5, pp.* 272–275. https://doi.org/10.1155/2004/158924.

18. Asiri, A. M.; Khan, S. A. (2010). Synthesis and Anti-Bacterial Activities of Some Novel Schiff Bases Derived from Aminophenazone. *Molecules*, vol. *15, no 10, pp.* 6850–6858. https://doi.org/10.3390/molecules15106850.

19. Mondal, S.; Mandal, S. M.; Mondal, T. K.; Sinha, C. (2015). Structural characterization of new Schiff bases of sulfamethoxazole and sulfathiazole, their antibacterial activity and docking computation with DHPS protein structure. *Spectrochimica Acta Part A Molecular and Biomolecular Spectroscopy*, vol. *150*, pp. 268–279. https://doi.org/10.1016/j.saa.2015.05.049.

20. Cheng, K.; Zheng, Q.-Z.; Qian, Y.; Shi, L.; Zhao, J.; Zhu, H.-L. (2009). Synthesis, antibacterial activities and molecular docking studies of peptide and Schiff bases as targeted antibiotics. *Bioorganic & Medicinal Chemistry*, vol. *17, no 23, pp.* 7861–7871. https://doi.org/10.1016/j.bmc.2009.10.037.

21. El-Gammal, O. A.; Mohamed, F. Sh.; Rezk, G. N.; El-Bindary, A. A. (2021). Synthesis, characterization, catalytic, DNA binding and antibacterial activities of Co(II), Ni(II) and Cu(II) complexes with new Schiff base ligand. *Journal of Molecular Liquids*, vol. *326*, article 115223. https://doi.org/10.1016/j.molliq.2020.115223.

22. Wang, X.; Yin, J.; Shi, L.; Zhang, G.; Song, B. (2014). Design, synthesis, and antibacterial activity of novel Schiff base derivatives of quinazolin-4(3H)-one. *European Journal of Medicinal Chemistry*, vol. *77*, pp. 65–74. https://doi.org/10.1016/j.ejmech.2014.02.053.

23. Anacona, J. R.; Rodriguez, J. L.; Camus, J. (2014). Synthesis, characterization and antibacterial activity of a Schiff base derived from cephalexin and sulphathiazole and its transition metal complexes. *Spectrochimica Acta Part A Molecular and Biomolecular Spectroscopy*, vol. *129*, pp. 96–102. https://doi.org/10.1016/j.saa.2014.03.019.

24. Goszczyńska, A.; Kwiecień, H.; Fijałkowski, K. (2015). Synthesis and antibacterial activity of Schiff bases and amines derived from alkyl 2-(2-formyl-4-nitrophenoxy)alkanoates. *Medicinal Chemistry Research*, vol. *24, no 9, pp.* 3561–3577. https://doi.org/10.1007/s00044-015-1397-6.

25. Ommenya, F. K.; Nyawade, E. A.; Andala, D. M.; Kinyua, J. (2020). Synthesis, Characterization and Antibacterial Activity of Schiff Base, 4-Chloro-2-{(E)-[(4-Fluorophenyl)imino]methyl}phenol Metal (II) Complexes. *Journal of Chemistry*, vol. *2020*, article 1745236. https://doi.org/10.1155/2020/1745236.

26. Reiss, A.; Florea, S.; Caproiu, T.; Stanica, N. (2009). Synthesis, characterization, and antibacterial activity of some transition metals with the Schiff base N-(2-furanylmethylene)-3-aminodibenzofuran. *Turkish Journal of Chemistry*, vol. *33, no 6, pp.* 775–783. https://doi.org/10.3906/kim-0807-31.

27. Chaudhary, N. K.; Mishra, P. (2017). Metal complexes of a novel Schiff base based on penicillin: characterization, molecular modeling, and antibacterial activity study. *Bioinorganic Chemistry and Applications*, vol. *2017*, article 6927675. https://doi.org/10.1155/2017/6927675.

28. Yin, X.; Chen, J.; Yuan, W.; Lin, Q.; Ji, L.; Liu, F. (2011). Preparation and antibacterial activity of Schiff bases from O-carboxymethyl chitosan and para-substituted benzaldehydes. *Polymer Bulletin*, vol. *68, no 5, pp.* 1215–1226. https://doi.org/10.1007/s00289-011-0599-4.

29. Hadjoudis, E.; Vittorakis, M.; Moustakali-Mavridis, I. (1987). Photochromism and thermochromism of schiff bases in the solid state and in rigid glasses. *Tetrahedron*, vol. *43, no 7, pp.* 1345–1360. https://doi.org/10.1016/s0040-4020(01)90255-8.

30. Ogawa, K.; Kasahara, Y.; Ohtani, Y.; Harada, J. (1998). Crystal structure change for the thermochromy of N-Salicylideneanilines. the first observation by x-ray diffraction. *Journal of the American Chemical Society*, vol. *120, no 28, pp.* 7107–7108. https://doi.org/10.1021/ja980972v.

31. Alarcón, S. H.; Olivieri, A. C.; Sanz, D.; Claramunt, R. M.; Elguero, J. (2004). Substituent and solvent effects on the proton transfer equilibrium in anils and azo derivatives of naphthol. Multinuclear NMR study and theoretical calculations. *Journal of Molecular Structure*, vol. *705, no 1–3*, pp. 1–9. https://doi.org/10.1016/s0022-2860(03)00208-4.

32. Filarowski, A.; Koll, A.; Sobczyk, L. (2009). Intramolecular Hydrogen Bonding in o-hydroxy Aryl Schiff Bases. *Current Organic Chemistry*, vol. *13, no 2, pp.* 172–193. https://doi.org/10.2174/138527209787193765.

33. Minkin, V. I.; Tsukanov, A. V.; Dubonosov, A. D.; Bren, V. A. (2011). Tautomeric Schiff bases: Iono-, solvato-, thermo- and photochromism. *Journal of Molecular Structure*, vol. *998, no* 1–3, pp. 179–191. https://doi.org/10.1016/j.molstruc.2011.05.029.

34. Zhao, J.; Ji, S.; Chen, Y.; Guo, H.; Yang, P. (2011). Excited state intramolecular proton transfer (ESIPT): from principal photophysics to the development of new chromophores and applications in fluorescent molecular probes and luminescent materials. *Physical Chemistry Chemical Physics*, vol. *14, no 25, pp.* 8803–8817. https://doi.org/10.1039/c2cp23144a.

35. Hadjoudis, E.; Chatziefthimiou, S.; Mavridis, I. (2009). Anils: Photochromism by H-Transfer. *Current Organic Chemistry*, vol. *13, no 3, pp.* 269–286. https://doi.org/10.2174/138527209787314797.

36. Panchal, P. K.; Parekh, H. M.; Pansuriya, P. B.; Patel, M. N. (2006). Bactericidal activity of different oxovanadium(IV) complexes with Schiff bases and application of chelation theory. *Journal of Enzyme Inhibition and Medicinal Chemistry*, vol. *21, no 2, pp.* 203–209. https://doi.org/10.1080/14756360500535229.

37. Yildirim, N.; Yildiz, M. (2018). A Schiff base sensor selective to anions, biological activity and spectral studies. *Journal of the Turkish Chemical Society Section A Chemistry*, vol. *5, no 3*, pp. 1271–1278. https://doi.org/10.18596/jotcsa.431554.

38. Yıldız, M.; Karpuz, Ö.; Zeyrek, C. T.; Boyacıoğlu, B.; Dal, H.; Demir, N.; Yıldırım, N.; Ünver, H. (2015). Synthesis, biological activity, DNA binding and anion sensors, molecular structure and quantum chemical studies of a novel bidentate Schiff base derived from 3,5-bis(triflouromethyl)aniline and salicylaldehyde. *Journal of Molecular Structure*, vol. *1094*, pp. 148–160. https://doi.org/10.1016/j.molstruc.2015.03.047.

39. Dege, N.; Gökce, H.; Doğan, O. E.; Alpaslan, G.; Ağar, T.; Muthu, S.; Sert, Y. (2022). Quantum computational, spectroscopic investigations on N-(2-((2-chloro-4,5-dicyanophenyl)amino)ethyl)-4-methylbenzenesulfonamide by DFT/TD-DFT with different solvents, molecular docking and drug-likeness researches. *Colloids and Surfaces A Physicochemical and Engineering Aspects*, vol. *638*, article 128311. https://doi.org/10.1016/j.colsurfa.2022.128311.

40. Yıldız, M.; Tan, E.; Demir, N.; Yıldırım, N.; Ünver, H.; Kiraz, A.; Mestav, B. (2015). Synthesis and spectral, antimicrobial, anion sensing, and DNA binding properties of Schiff base podands and their metal complexes. *Russian Journal of General Chemistry*, vol. *85, no 9, pp.* 2149–2162. https://doi.org/10.1134/s1070363215090200.

41. Adeel-Sharif, H. M.; Ahmed, D.; Mir, H. (2015). Antimicrobial salicylaldehyde Schiff bases: synthesis, characterization and evaluation. *Pakistan Journal of Pharmaceutical Sciences*, vol. *28, no 2, pp.* 449–455.

42. Shi, L.; Ge, H.-M.; Tan, S.-H.; Li, H.-Q.; Song, Y.-C.; Zhu, H.-L.; Tan, R.-X. (2006). Synthesis and antimicrobial activities of Schiff bases derived from 5-chloro-salicylaldehyde. *European Journal of Medicinal Chemistry*, vol. *42, no 4, pp.* 558–564. https://doi.org/10.1016/j.ejmech.2006.11.010.

43. Montaser, A. S.; Wassel, Ahmed. R.; Al-Shaye'a, O. N. (2018). Synthesis, characterization and antimicrobial activity of Schiff bases from chitosan and salicylaldehyde/$TiO_2$ nanocomposite membrane. *International Journal of Biological Macromolecules*, vol. *124*, pp. 802–809. https://doi.org/10.1016/j.ijbiomac.2018.11.229.

44. Jesmin, M.; Ali, M. M.; Salahuddin, M. S.; Habib, M. R.; Khanam, J. A. (2008). Antimicrobial Activity of Some Schiff Bases Derived from Benzoin, Salicylaldehyde, Aminophenol and 2,4 Dinitrophenyl Hydrazine. *Mycobiology*, vol. *36, no 1, article* 70. https://doi.org/10.4489/myco.2008.36.1.070.

45. Jampilek, J. (2019). Heterocycles in medicinal chemistry. *Molecules*, vol. *24, no 21, article* 3839. https://doi.org/10.3390/molecules24213839.

46. Heravi, M. M.; Zadsirjan, V. (2020). Prescribed drugs containing nitrogen heterocycles: an overview. *RSC Advances*, vol. *10, no 72, pp.* 44247–44311. https://doi.org/10.1039/d0ra09198g.

47. Yildirim, N.; Demir, N.; Alpaslan, G.; Boyacioğlu, B.; Yildiz, M.; Ünver, H. (2018). DFT calculation, biological activity, anion sensing studies and crystal structure of (E)-4-chloro-2-((pyridin-2-ylimino)-methyl)phenol. *Journal of the Serbian Chemical Society*, vol. *83, no 6, pp.* 707–721. https://doi.org/10.2298/jsc171001009y.

48. Dueke-Eze; Fasina, C. U.; Idika. (2011). Synthesis, electronic spectra and inhibitory study of some Salicylaldehyde Schiff bases of 2-aminopyridine. *African Journal of Pure and Applied Chemistry*, vol. *5, no 2, pp.* 13–18. https://doi.org/10.5897/ajpac.9000160.

49. Barboza, C. A.; Germino, J. C.; Duarte, L. G. T. A.; Quites, F. J.; Vazquez, P. A. M.; Atvars, T. D. Z. (2016). Photoacidity of the N -salicylidene-5-chloroaminopyridine. *Journal of Luminescence*, vol. *184*, pp. 268–272. https://doi.org/10.1016/j.jlumin.2016.12.045.

50. Sliwa, M.; Mouton, N.; Ruckebusch, C.; Aloïse, S.; Poizat, O.; Buntinx, G.; Métivier, R.; Nakatani, K.; Masuhara, H.; Asahi, T. (2009). Comparative investigation of ultrafast photoinduced processes in Salicylidene-Aminopyridine in solution and solid state. *The Journal of Physical Chemistry C*, vol. *113, no 27, pp.* 11959–11968. https://doi.org/10.1021/jp901849a.

51. Zhao, L.; Sui, D.; Wang, Y. (2015). Luminescent properties of N-salicylidene-3-aminopyridine and selective sensing behavior to $Ba^{2+}$. *Journal of Luminescence*, vol. *162*, pp. 81–86. https://doi.org/10.1016/j.jlumin.2015.02.038.

52. Moustakali-Mavridis, I.; Hadjoudis, E.; Mavridis, A. (1978). Crystal and molecular structure of some thermochromic Schiff bases. *Acta Crystallographica Section B*, vol. *34, no 12, pp.* 3709–3715. https://doi.org/10.1107/s0567740878011930.

53. Goyat, G.; Malik, A.; Vikas; Verma, K. K.; Garg, S. (2018). Spectroscopic and Biological Studies of 3,5-Dichlorosalicylaldehyde-3-Aminopyridine Schiff Base and their Tellurium(IV) Complexes. *International Journal of Scientific Research in Science Engineering and Technology*, vol. *4, no 1, pp.* 755–762. https://doi.org/10.32628/ijsrset1841205.

54. Moustakali-Mavridis, I.; Hadjoudis, B.; Mavridis, A. (1980). Structure of thermochromic Schiff bases. II. Structures of N-salicylidene-3-aminopyridine and N-(5-methoxysalicylidene)-3-aminopyridine. *Acta Crystallographica Section B*, vol. *36, no 5, pp.* 1126–1130. https://doi.org/10.1107/s0567740880005432.

55. Vinita, G.; Sanchita, S.; Gupta, Y. K. (2013). Synthesis and Antimicrobial Activity of some Salicylaldehyde Schiff bases of 2-aminopyridine. *Research Journal of Chemical Sciences*, vol. *3, no 9, pp.* 26–29.

56. Cimerman, Z.; Galic, N.; Bosner, B. (1997). The Schiff bases of salicylaldehyde and aminopyridines as highly sensitive analytical reagents. *Analytica Chimica Acta*, vol. *343, no 1–2*, pp. 145–153. https://doi.org/10.1016/s0003-2670(96)00587-9.

57. Angyl, S. J.; Angyal, C. L. (1952). 268. The tautomerism of N-hetero-aromatic amines. Part I. *Journal of the Chemical Society (Resumed)*, pp. 1461–1466. https://doi.org/10.1039/jr9520001461.

58. Bates, R. G. (1964). *Determination of pH, Theory and Practice.* Wiley, New York, pp. 222-230.

59. Gelsema, W. J.; De Ligny, C. L.; Remijnse, A. G.; Blijleven, H. A. (1966). pH-Measurements in alcohol-water mixtures, using aqueous standard buffer solutions for calibration. *Recueil Des Travaux Chimiques Des Pays-Bas*, vol. *85, no 7, pp.* 647–660. https://doi.org/10.1002/recl.19660850702.

60. Spackman, M. A.; Jayatilaka, D. (2008). Hirshfeld surface analysis. *CrystEngComm*, vol. *11, no 1, pp.* 19–32. https://doi.org/10.1039/b818330a.

61. Spackman, M. A.; McKinnon, J. J. (2002). Fingerprinting intermolecular interactions in molecular crystals. *CrystEngComm*, vol. *4, no 66, pp.* 378–392. https://doi.org/10.1039/b203191b.

62. Spackman, P. R.; Turner, M. J.; McKinnon, J. J.; Wolff, S. K.; Grimwood, D. J.; Jayatilaka, D.; Spackman, M. A. (2021). CrystalExplorer: a program for Hirshfeld surface analysis, visualization and quantitative analysis of molecular crystals. *Journal of Applied Crystallography*, vol. *54, no 3, pp.* 1006–1011. https://doi.org/10.1107/s1600576721002910.

63. Rodić, M. (2020). CCDC 1869718: Experimental Crystal Structure Determination. *The Cambridge Structural Database*. https://doi.org/10.5517/ccdc.csd.cc20rlhw.

64. Rodić, M. (2018). Comments on DFT calculation, biological activity, anion sensing studies and crystal structure of (E)-4-chloro-2-((pyridin-2-ylimino)-methyl)phenol by Nuray Yıldırım, Neslihan Demir, Gökhan Alpaslan, Bahadir Boyacıoğlu, Mustafa Yıldız, and Huseyin Ünver, published in the Journal of the Serbian Chemical Society, volume 83, issue 6, 2018, pp. 707-721. *Journal of the Serbian Chemical Society*, vol. *84, no 1, pp.* 111–116. https://doi.org/10.2298/jsc180925082r.

65. Dennington, R.; Keith, T. A.; Millam, J. M. (2016). *GaussView Version 6.0.* Semichem Inc., Shawnee Mission, KS.

66. Frisch, M.J.; Trucks, G.W.; Schlegel, H.B.; Scuseria, G.E.; Robb, M.A.; Cheeseman, J.R.; Scalmani, G.; Barone, V.; Mennucci, B.; Petersson, G.A. et al. (2009). *Gaussian 09, Revision D.01*. Gaussian. Inc., Wallingford.

67. Krishnan, R.; Binkley, J. S.; Seeger, R.; Pople, J. A. (1980). Self-consistent molecular orbital methods. XX. A basis set for correlated wave functions. *The Journal of Chemical Physics*, vol. *72, no 1, pp.* 650–654. https://doi.org/10.1063/1.438955.

68. Becke, A. D. (1993). Density-functional thermochemistry. III. The role of exact exchange. *The Journal of Chemical Physics*, vol. *98, no 7, pp.* 5648–5652. https://doi.org/10.1063/1.464913.

69. Frisch, M. J.; Pople, J. A.; Binkley, J. S. (1984). Self-consistent molecular orbital methods 25. Supplementary functions for Gaussian basis sets. *The Journal of Chemical Physics*, vol. *80, no 7, pp.* 3265–3269. https://doi.org/10.1063/1.447079.

70. Jamróz, M. H. (2013). Vibrational Energy Distribution Analysis (VEDA): Scopes and limitations. *Spectrochimica Acta Part A Molecular and Biomolecular Spectroscopy*, vol. *114*, pp. 220–230. https://doi.org/10.1016/j.saa.2013.05.096.

71. Berman, H. M.; Battistuz, T.; Bhat, T. N.; Bluhm, W. F.; Bourne, P. E.; Burkhardt, K.; Feng, Z.; Gilliland, G. L.; Iype, L.; Jain, S.; Fagan, P.; Marvin, J.; Padilla, D.; Ravichandran, V.; Schneider, B.; Thanki, N.; Weissig, H.; Westbrook, J. D.; Zardecki, C. (2002). The Protein Data Bank. *Acta Crystallographica Section D Biological Crystallography*, vol. *58, no 6, pp.* 899–907. https://doi.org/10.1107/s0907444902003451.

72. Trott, O.; Olson, A. J. (2009). AutoDock Vina: Improving the speed and accuracy of docking with a new scoring function, efficient optimization, and multithreading. *Journal of Computational Chemistry*, vol. *31, no 2, pp.* 455–461. https://doi.org/10.1002/jcc.21334.

73. Morris, G. M.; Huey, R.; Lindstrom, W.; Sanner, M. F.; Belew, R. K.; Goodsell, D. S.; Olson, A. J. (2009). AutoDock4 and AutoDockTools4: Automated docking with selective receptor flexibility. *Journal of Computational Chemistry*, vol. *30, no 16, pp.* 2785–2791. https://doi.org/10.1002/jcc.21256.

74. Kuo, M. C.; Yen, S. K. (2002). The process of electrochemical deposited hydroxyapatite coatings on biomedical titanium at room temperature. *Materials Science and Engineering C*, vol. *20, no 1–2*, pp. 153–160. https://doi.org/10.1016/s0928-4931(02)00026-7.

75. Zhang, Y.-Y.; Tao, J.; Pang, Y.-C.; Wang, W.; Wang, T. (2006). Electrochemical deposition of hydroxyapatite coatings on titanium. *Transactions of Nonferrous Metals Society of China*, vol. *16, no 3, pp.* 633–637. https://doi.org/10.1016/s1003-6326(06)60112-x.

76. McFarland, J. (1907). The nephelometer: an instrument for media used for estimating the number of bacteria in suspensions used for calculating the opsonic index and for vaccines. *Journal of American Medical Association*, vol. 49, no 14, pp. 1176-1178. 10.1001/jama.1907.25320140022001f.

77. Arnold, P. M.; Parslow, G. R. (1995). Designing a coupled assay system for aspartate aminotransferase. *Biochemical Education*, vol. *23, no 1, pp.* 40–41. https://doi.org/10.1016/0307-4412(94)00116-7.

78. Banfi, D.; Patiny, L. (2008). www.nmrdb.org: Resurrecting and processing NMR spectra on-line *Chimia*, vol. *62, no 4, pp.* 280-281. https://doi.org/10.2533/chimia.2008.280.

79. Jelsch, C.; Ejsmont, K.; Huder, L. (2014). The enrichment ratio of atomic contacts in crystals, an indicator derived from the Hirshfeld surface analysis. *International Union of Crystallography Journal*, vol. *1, no 2, pp.* 119–128. https://doi.org/10.1107/s2052252514003327.

80. Moosavi-Tekyeh, Z.; Dastani, N. (2015). Intramolecular hydrogen bonding in N-salicylideneaniline: FT-IR spectrum and quantum chemical calculations. *Journal of Molecular Structure*, vol. *1102*, pp. 314–322. https://doi.org/10.1016/j.molstruc.2015.09.001.

81. Geerlings, P.; De Proft, F.; Langenaeker, W. (2003). Conceptual Density Functional Theory. *Chemical Reviews*, vol. *103, no 5, pp.* 1793–1874. https://doi.org/10.1021/cr990029p.

82. Galić, N.; Cimerman, Z.; Tomišić, V. (1997). Tautomeric and protonation equilibria of Schiff bases of salicylaldehyde with aminopyridines. *Analytica Chimica Acta*, vol. *343, no 1–2*, pp. 135–143. https://doi.org/10.1016/s0003-2670(96)00586-7.

83. Meshkov, A. N.; Gamov, G. A. (2019). KEV: A free software for calculating the equilibrium composition and determining the equilibrium constants using UV–Vis and potentiometric data. *Talanta*, vol. *198*, pp. 200–205. https://doi.org/10.1016/j.talanta.2019.01.107.

84. Banerjee, P.; Kemmler, E.; Dunkel, M.; Preissner, R. (2024). ProTox 3.0: a webserver for the prediction of toxicity of chemicals. *Nucleic Acids Research*, vol. *52, no W1, pp.* W513–W520. https://doi.org/10.1093/nar/gkae303.

85. Wilcoxon, F. (1945). Individual comparisons by ranking methods. *Biometrics Bulletin*, vol. *1, no 6, pp.* 80–83. https://doi.org/10.2307/3001968.

86. Mirošnikov, M. V.; Makarova, M. N. (2021). Variabel'nost' biohimičeskih pokazatelej krovi i ustanovlenie referensnyh intervalov v dokliničeskih issledovaniâh. Soobŝenie 4: myši. *Laboratornye životnye dlâ naučnyh issledovanij*, no *3*, pp. 63–69. https://doi.org/10.29296/2618723X-2021-03-08.

87. Daina, A.; Zoete, V. (2016). A BOILED-Egg to predict gastrointestinal absorption and brain penetration of small molecules. *ChemMedChem*, vol. *11, no 11, pp.* 1117–1121. https://doi.org/10.1002/cmdc.201600182.

***Information about authors:***

*Artem V. Sharov – PhD, Senior Researcher, Laboratory of Advanced Materials for Industry and Biomedicine, Kurgan State University (Kurgan, Russia, e-mail: sharow84@gmail.com)*

*Pavel A. Nikolaychuk – PhD, Senior Researcher, Scientific-Educational Centre of Chemistry and Chemical Technology of Novosibirsk State University (Novosibirsk, Russia, e-mail: pavel.nikolaychuk@kgsu.ru)*

*Anastasia A. Tereshkina –M. Sc. Junior Researcher, Ural Federal University named after the first President of Russia Boris Nikolaevich Yeltsin (Yekaterinburg, Russia, e-mail: an-terrr@mail.ru)*

*Alena V. Dostovalova – M.Sc., Junior Researcher, Laboratory of Advanced Materials for Industry and Biomedicine, Kurgan State University (Kurgan, Russia, e-mail: alenka_01_45@mail.ru)*

*Yulia A. Enova – M.Sc., Junior Researcher, Laboratory of Advanced Materials for Industry and Biomedicine, Kurgan State University (Kurgan, Russia, e-mail: julia_qwer19@mail.ru)*

*Darya S. Popova – M.Sc., Junior Researcher, Laboratory of Advanced Materials for Industry and Biomedicine, Kurgan State University (Kurgan, Russia, e-mail: nikitina.dar@mail.ru)*

*Darya A. Rychkova – M.Sc., Junior Researcher, Laboratory of Advanced Materials for Industry and Biomedicine, Kurgan State University (Kurgan, Russia, e-mail: dariaruchkova25@gmail.com)*

*Alena Y. Kurochkina – M.Sc., Junior Researcher, Laboratory of Advanced Materials for Industry and Biomedicine, Kurgan State University (Kurgan, Russia, e-mail: aleona.kurochkina@yandex.ru)*

*Valentina V. Savinova – M.Sc., Junior Researcher, Laboratory of Advanced Materials for Industry and Biomedicine, Kurgan State University (Kurgan, Russia, e-mail: savinovavalenrina21@mail.ru)*

*Aleksander N. Nakoskin – PhD, Senior Researcher, Laboratory of Advanced Materials for Industry and Biomedicine, Kurgan State University (Kurgan, Russia, e-mail: Nakoskin_A@mail.ru)*

*Irina V. Shipitsyna – PhD, Researcher, National Ilizarov Medical Research Centre for Traumatology and Orthopaedics (Kurgan, Russia, e-mail: IVSchimik@mail.ru)*

*Oleg V. Filisteev – PhD, Senior Researcher, Laboratory of Advanced Materials for Industry and Biomedicine, Kurgan State University (Kurgan, Russia, e-mail: filisteev.oleg@gmail.com)*

*Soe T. Lwin – PhD, Senior Researcher, Medical Research Centre (Nay Pyi Taw, Myanmar, e-mail: drthihalwin2012@gmail.com)*

*Min M. Zaw – PhD, Senior Researcher, Medical Research Centre (Nay Pyi Taw, Myanmar, e-mail: mrzaw710@gmail.com)*

*Zaw Minthein – PhD, Senior Researcher, Medical Academy (Yangon, Myanmar, e-mail: zawminthein@gmail.com)*

*Zaw Y.M. Oo – PhD, Senior Researcher, Science Research Centre of the Republic of the Union of Myanmar (Nay Pyi Taw, Myanmar, e-mail: zawyemawoo@gmail.com)*

IRSTI 31.25.15 https://doi.org/10.26577/IJBCh20251829

F.A. Amirli[1], R.F. Khankishiyeva[1, 2, 3, 4], A.F. Mammadova[1*],
S.T. Bayramova[1], G.G. Azizova[1], K.B. Iravanlı[1]

[1]Azerbaijan State Oil and Industry University, Baku, Azerbaijan
[2]Institute of Radiation Problems, Baku, Azerbaijan
[3]Azerbaijan University of Architecture and Construction Baku, Azerbaijan
[4]Scientific-Research Institute Geotechnological Problems of Oil, Gas and Chemistry, Baku, Azerbaija
*e-mail: aynur.memmedova@asoiu.edu.az

*(Received 9 December 2025; received in revised form 23 December 2025; accepted 25 December 2025)*

# Reactive compatibilization of EPDM/PA6 blends with dicumyl peroxide: structure–property relationships

**Abstract.** In this study, binary blends based on ethylene–propylene–diene rubber (EPDM) and polyamide-6 (PA6) were systematically prepared with varying PA6 contents ranging from 10 to 40 phr. Dicumyl peroxide (DCP) was employed as a reactive compatibilizer in order to promote chemical linkages between the elastomeric and thermoplastic components and thereby enhance interfacial adhesion. The blending process was carried out in a Banbury internal mixer under controlled temperature and shear conditions, ensuring homogeneous distribution of the polyamide phase within the EPDM matrix, and the obtained compounds were subsequently compression molded to produce uniform test specimens.

The effect of increasing PA6 concentration on the physicomechanical, thermal, and morphological characteristics of the blends was extensively investigated. Tensile testing demonstrated that the incorporation of higher amounts of PA6 significantly increased tensile strength, modulus, and Shore hardness, which can be attributed to the reinforcing action of the rigid polyamide domains and the formation of peroxide-induced covalent interfacial linkages. Thermal gravimetric analysis further revealed an improvement in thermal stability with rising PA6 content, while differential scanning calorimetry and dynamic mechanical analysis indicated a gradual upward shift in storage modulus and in the glass transition behavior, consistent with the contribution of the stiff thermoplastic phase.

On the other hand, elongation at break and overall elasticity decreased as the PA6 fraction was raised, reflecting the stiffer and less deformable nature of the dispersed polyamide particles. Scanning electron microscopy (SEM) images confirmed that optimal phase dispersion and strong interfacial adhesion were obtained in blends containing approximately 20–30 phr PA6 together with 1.0–1.2 phr DCP. These particular formulations offered the best balance between mechanical strength, flexibility, and heat resistance. Overall, the results demonstrate that peroxide-compatibilized EPDM/PA6 blends possess tunable and application-oriented properties suitable for engineering uses where both mechanical robustness and thermal durability are simultaneously required.

**Keywords:** EPDM, PA6, reactive compatibilization, dicumyl peroxide, mechanical properties, thermal stability, morphology.

## Introduction

Elastomer/thermoplastic blends have attracted significant interest because they combine the elasticity of rubbers with the rigidity and thermal stability of thermoplastics, resulting in balanced performance properties [1–3]. These hybrid systems provide tunable mechanical and thermal behavior and are widely applied in automotive parts, cable insulation, construction, and various engineering devices [4–6].

Ethylene–propylene–diene rubber (EPDM) is a widely used nonpolar elastomer, valued for its resistance to ozone, weathering, and chemicals, as well as its high elasticity and low glass transition temperature [7,8]. However, its relatively low stiffness and tensile strength restrict its application in engineering fields that require enhanced mechanical performance [9]. To overcome these limitations, EPDM is often blended with rigid thermoplastics.

Polyamide-6 (PA6) is a semi-crystalline thermoplastic that exhibits high tensile strength, modulus,

© 2025 al-Farabi Kazakh National University

thermal stability, and excellent oil and abrasion resistance [10]. Incorporating PA6 into EPDM increases stiffness and strength while maintaining some elasticity [11]. However, the fundamental challenge arises from their incompatibility: EPDM is nonpolar, whereas PA6 is strongly polar, leading to poor interfacial adhesion, phase separation, and reduced mechanical performance [12,13].

Compatibilization strategies have therefore been widely explored. Maleic anhydride–grafted polymers, such as EPDM-g-MA and SEBS-g-MA, can create covalent bonds at the interface and improve adhesion [14,15]. Despite their effectiveness, these compatibilizers present disadvantages, including high cost, additional synthesis steps, and limited stability under certain conditions [16]. An alternative and cost-effective approach is reactive compatibilization using peroxides.

Dicumyl peroxide (DCP) has been reported as an efficient compatibilizer for EPDM/PA6 blends [17]. Upon decomposition, DCP generates free radicals that promote crosslinking in the EPDM phase and grafting reactions at the EPDM/PA6 interface [18]. This improves phase dispersion, tensile strength, and thermal resistance, although excessive peroxide content can reduce flexibility [19,20].

Previous studies have shown that increasing PA6 loading enhances modulus and tensile strength but reduces elongation at break and overall elasticity [21,22]. Some reports indicate that intermediate PA6 contents (20–30 phr) provide an optimal compromise between strength and elasticity [23]. Morphological studies further confirm that DCP improves phase dispersion and interfacial bonding compared to uncompatibilized blends [24].

Research gap and aim of the study: Although progress has been made, most studies have focused either on maleic anhydride–based compatibilizers or on limited peroxide dosages, leaving open questions about the systematic effect of DCP across a wide PA6 concentration range. The present work addresses this gap by preparing EPDM/PA6 blends with 10–40 phr PA6, compatibilized with DCP, and investigating their mechanical, thermal, and morphological properties. The aim is to identify compositions that achieve an optimal balance between strength, elasticity, and thermal stability, while offering practical insights for industrial polymer blend design.

## Materials and methods

For this investigation, commercially available ethylene–propylene–diene rubber (EPDM) (Keltan® 4450, DSM Elastomers, Netherlands) was selected as the elastomeric matrix. This grade contains 50 wt.% ethylene and 5.2 wt.% ENB, which ensures good elasticity and processability. Polyamide-6 (PA6) (Ultramid® B27, BASF, Germany) with a relative viscosity of 2.7 (96% $H_2SO_4$ solution) was used as the thermoplastic component owing to its high stiffness and thermal stability. Dicumyl peroxide (DCP) (Perkadox® BC-40, Akzo Nobel, Netherlands, 40% active content) was employed both as a crosslinking agent and a reactive compatibilizer, enabling radical-induced grafting at the EPDM/PA6 interface.

*Formulation of Blends*

The compositions of the blends were defined on a phr basis (parts per hundred parts of rubber), with EPDM fixed at 100 phr (Table 1). To systematically investigate the influence of PA6 loading, its content was varied from 10 to 40 phr, while DCP was introduced at 1.0–1.2 phr. The selected range was based on preliminary trials, which indicated that lower PA6 loadings had negligible reinforcing effects, whereas very high loadings compromised elasticity.

**Table 1** – Formulation of EPDM/PA6 blends

| Sample Code | EPDM (phr) | PA6 (phr) | DCP (phr) |
|---|---|---|---|
| E10 | 100 | 10 | 1.0 |
| E20 | 100 | 20 | 1.0 |
| E30 | 100 | 30 | 1.2 |
| E40 | 100 | 40 | 1.2 |

*Blend Preparation*

The compounding was carried out using a Banbury internal mixer (Haake Rheomix, 160 mL chamber). The mixing parameters were optimized to promote sufficient dispersion of PA6 within the EPDM matrix and to activate the peroxide without excessive degradation. The chamber temperature was maintained at 180°C, with a rotor speed of 60 rpm, and a total mixing time of 8 minutes.

The mixing procedure was as follows:

EPDM was first masticated for 2 minutes to reduce its viscosity and improve incorporation of the thermoplastic phase.

PA6 was then gradually introduced to the chamber to avoid agglomeration and ensure uniform distribution.

Finally, DCP was added to initiate in-situ compatibilization through peroxide decomposition and radical generation.

The compounded materials were subsequently passed through a two-roll mill (Polymix 150L, Germany) at 70°C to obtain uniform sheets. This step was crucial to eliminate unmixed domains and to prepare samples suitable for molding.

*Molding and Curing*

Test specimens were produced by compression molding using a Carver laboratory hot press. The molding was conducted at 190°C under a pressure of 10 MPa for 15 minutes, conditions chosen to balance peroxide crosslinking with thermoplastic flow. Following molding, the sheets were cooled to ambient temperature under natural air circulation. Dumbbell-shaped specimens were cut according to ASTM D412 for mechanical testing.

To comprehensively evaluate the blends, a multi-method characterization approach was employed:

*Mechanical Properties*: Tensile strength, elongation at break, and modulus were measured according to ASTM D412 using an Instron 3365 universal testing machine at a crosshead speed of 500 mm/min. Hardness was determined with a Shore A durometer (ASTM D2240). These tests were performed to quantify reinforcement effects of PA6 and the efficiency of peroxide compatibilization.

*Thermal Stability* (TGA): Thermogravimetric analysis was conducted on a TA Q50 in a nitrogen atmosphere, heating from 30 to 700°C at 10°C/min. The degradation onset temperature ($T_{10}\%$) and maximum decomposition temperature ($T_{max}$) were used to assess improvements in thermal resistance imparted by PA6.

*Dynamic Mechanical Analysis* (DMA): Performed on a TA Q800 in tensile mode from –100°C to 100°C, at a heating rate of 3°C/min and a frequency of 1 Hz. The storage modulus (E′) and tan δ curves were analyzed to understand viscoelastic behavior and interfacial bonding.

*Morphology* (SEM): Fractured tensile specimens were sputter-coated with gold and observed under SEM (JEOL JSM-6610LV, 15 kV). This analysis was essential to correlate mechanical performance with phase morphology and to visually confirm the effectiveness of DCP-induced compatibilization.

## Results and discussion

The mechanical performance of the EPDM/PA6 blends compatibilized with DCP is summarized in Table 2.

**Table 2** – Mechanical properties of EPDM/PA6 blends

| Sample | PA6 (phr) | Tensile Strength (MPa) | Elongation at Break (%) | Modulus (MPa) | Hardness (Shore A) |
|---|---|---|---|---|---|
| E10 | 10 | 9.8 | 280 | 3.5 | 64 |
| E20 | 20 | 13.6 | 240 | 5.2 | 68 |
| E30 | 30 | 15.2 | 210 | 6.0 | 72 |
| E40 | 40 | 16.0 | 180 | 7.3 | 76 |

The results clearly demonstrate a progressive increase in tensile strength, modulus, and hardness with increasing PA6 content. This behavior can be attributed to the reinforcing effect of PA6 domains, which restrict EPDM chain mobility and improve stiffness. At the same time, elongation at break decreases, reflecting reduced flexibility due to higher thermoplastic loading.

The optimum balance was achieved for 20–30 phr PA6 (E20, E30), where tensile strength improved significantly while maintaining moderate elasticity. Similar observations have been reported in literature, where intermediate PA6 levels provided a compromise between toughness and stiffness [21–23].

Thermogravimetric analysis results are presented in Table 3.

**Table 3** – TGA results of EPDM/PA6 blends

| Sample | PA6 (phr) | $T_{10}\%$ (°C) | $T_{max}$ (°C) | Residue at 700°C (%) |
|---|---|---|---|---|
| E10 | 10 | 328 | 460 | 2.8 |
| E20 | 20 | 336 | 468 | 3.2 |
| E30 | 30 | 343 | 474 | 3.5 |
| E40 | 40 | 350 | 480 | 4.0 |

The onset of degradation ($T_{10}\%$) increased from 328°C (E10) to 350°C (E40), indicating that PA6 improves thermal stability. The maximum degradation temperature ($T_{max}$) also shifted positively, which suggests stronger interfacial bonding due to peroxide-induced compatibilization. The higher char residue at elevated PA6 loadings is consistent with the inherently stable aromatic structure of PA6.

Thus, incorporation of PA6 not only reinforces mechanical properties but also delays thermal decomposition, enhancing the suitability of these blends for engineering applications where heat resistance is critical.

DMA analysis further supports the reinforcing effect of PA6 (Table 4).

**Table 4** – DMA parameters of EPDM/PA6 blends

| Sample | PA6 (phr) | Storage Modulus E′ (25°C, MPa) | $T_g$ (°C, tanδ peak) |
|---|---|---|---|
| E10 | 10 | 12.5 | –61 |
| E20 | 20 | 18.2 | –58 |
| E30 | 30 | 22.7 | –55 |
| E40 | 40 | 26.5 | –52 |

The storage modulus (E′) increased steadily with PA6 loading, confirming enhanced stiffness and restricted chain mobility. Moreover, the glass transition temperature (Tg) shifted from –61°C to –52°C as PA6 content increased, which reflects improved interfacial adhesion and constrained segmental motion of EPDM chains.

The broadening and slight reduction in tan δ peak intensity at higher PA6 loadings indicate that DCP-mediated compatibilization effectively reduced interfacial friction, leading to improved stress transfer across phases [22–28].

SEM micrographs of the fractured surfaces revealed distinct differences in phase dispersion depending on PA6 loading. At low PA6 contents (E10), relatively large and poorly adhered PA6 domains were observed. However, with the incorporation of DCP, the morphology significantly improved, especially at 20–30 phr PA6, where finer and more homogeneous dispersion was evident.

At higher PA6 loadings (E40), partial agglomeration and rigid particle domains were visible, which explains the reduced elongation at break despite improved tensile strength. These observations confirm that DCP-induced grafting reactions enhanced compatibility between the nonpolar EPDM matrix and polar PA6 phase.

The graph demonstrates (Fig.1) that tensile strength increases markedly with higher PA6 loadings, which can be attributed to the reinforcing effect of the rigid thermoplastic domains restricting the mobility of EPDM chains. In contrast, elongation at break decreases progressively, reflecting the loss of flexibility as the blends become stiffer.

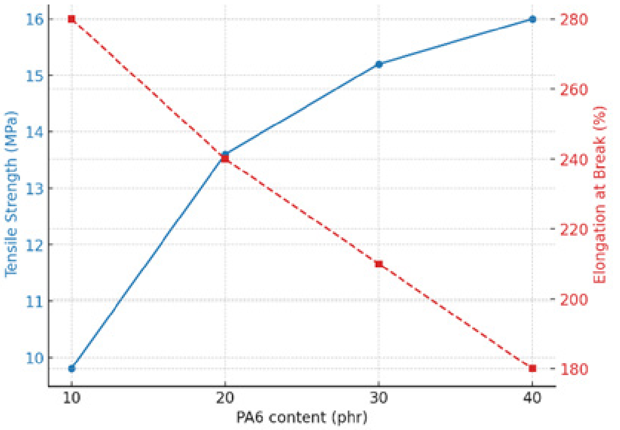

**Figure 1** – Variation of tensile strength and elongation at break of EPDM/PA6 blends compatibilized with DCP as a function of PA6 content

When PA6 is added, stiffness increases, but the same tendency is observed for elastomer-thermoplastic systems when elasticity is compromised. The optimal balance between strength and elasticity is obtained at moderate concentrations (20-30 phr PA6), without loss of retention and expansion.

Figure 2 shows the effect of PA6 on the modulus and hardness of EPDM/PA6 blends.

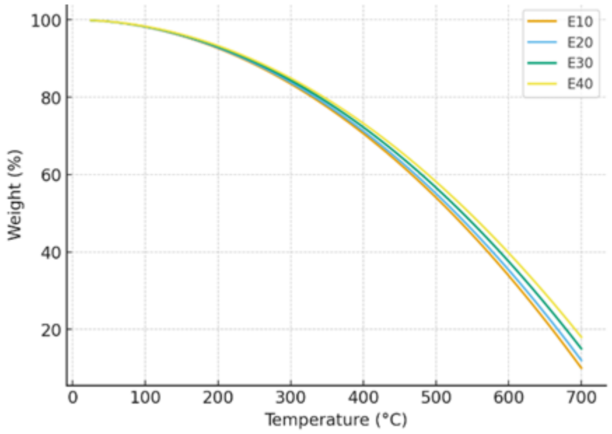

**Figure 2** – Effect of PA6 loading on modulus and hardness of EPDM/PA6 blends

Both modulus and A-hardness increase in the same way with increasing PA6 concentration. Since PA6 domains act as rigid reinforcements, the resistance to deformation under tension in the blends increases. The transition from a soft elastomeric material to a harder elastomeric-thermoplastic is fully confirmed as the hardness increases. These results confirm the suitability of such blends for engineering applications where high stiffness resistance and dimensional stability are required, such as automotive parts and cable insulation.

As shown in Figure 3, the thermal decomposition of EPDM/PA6 blends strongly depends on the PA6 content. The shift of the TGA curves towards higher temperatures and the increasing residual yield are in full agreement with the data presented in Table 3 and confirm the increased thermal stability of blends with higher PA6 loading (Figure 4).

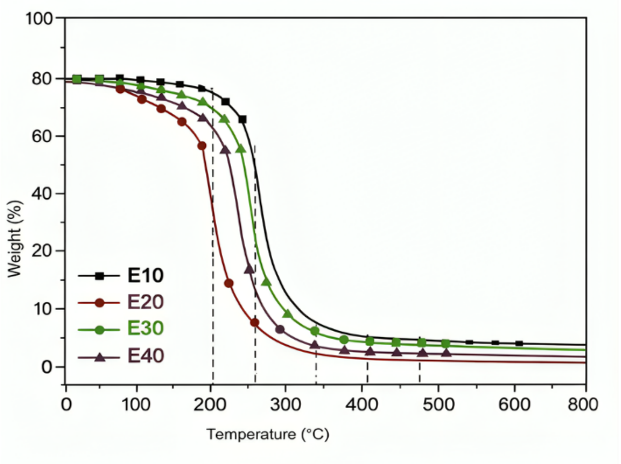

**Figure 3** – TGA curves of EPDM/PA6 mixed with different PA6 compositions

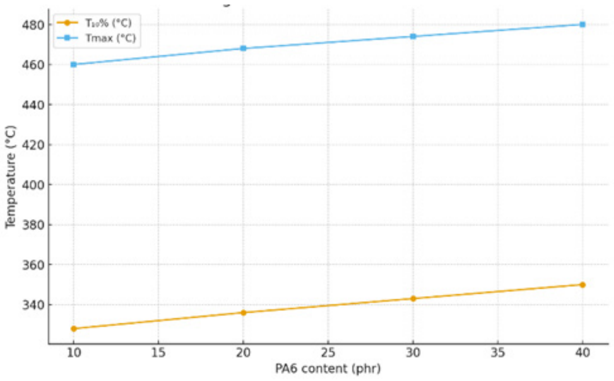

**Figure 4** – Dependence of T$_{max}$ from PA6 content in EPDM/PA6

Figure 5 shows the temperature variation of the storage modulus (E′) for EPDM/PA6 blends due to the strengthening effect of PA6 as well as the adaptation by DCP.

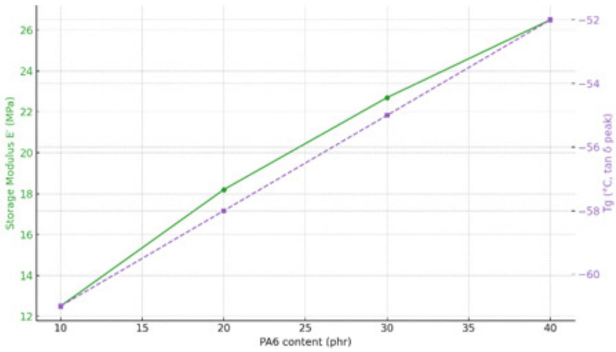

**Figure 5** – Storage modulus (E′) of EPDM/PA6 blends versus temperature, the stiffening effect of PA6 and the adaptation by DCP

The dynamic mechanical analysis results show that the storage modulus (E′) increases steadily with PA6 loading. This confirms the increased stiffness and energy storage capacity. Also, the glass transition temperature (Tg, observed from the tanδ peak) shifts upwards from –61°C to –52°C. At this time, stronger interfacial interactions reflect limited chain mobility. The decrease in tanδ peak intensity and lower interfacial friction at higher PA6 levels indicate more efficient stress transfer between phases, which fully proves the effectiveness of peroxide-induced adaptation.

As shown in Figure 6, the SEM micrographs illustrate the fractured surface morphology of EPDM/PA6 blends, where samples E10, E20, E30, and E40 exhibit variations in dispersion and interfacial adhesion.

E10 (10 phr PA6): Large, irregular PA6 domains are clearly visible with distinct boundaries, reflecting poor interfacial adhesion. This morphology corresponds to moderate tensile strength and high elongation at break. Poor adhesion leads to voids and poor stress transfer in the thermoplastic phase dispersed from the EPDM matrix. As a result, the material exhibits a strong effect at low tensile strength, which maintains a high elongation at break, which mainly affects the toughness of the rubber.

E20 (20 phr PA6): According to the SEM images provided, it shows a fine morphology with smaller uniformly dispersed PA6 particles. The difference between the interfaces is less noticeable, which indicates that the DCP-induced grafting reactions are good, indicating that the polar PA6 and non-polar EPDM phases are well matched. This fine dispersion also results in high levels of strength and modulus while maintaining the existing elasticity.

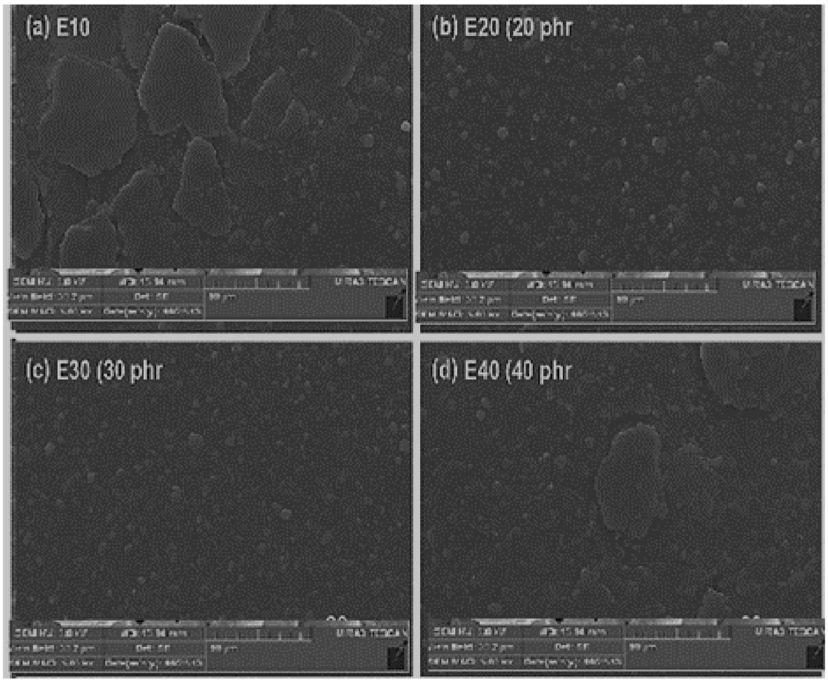

(a) E10, (b) E20, (c) E30, and (d) E40

**Figure 6** – High-magnification SEM micrographs of EPDM/PA6 blends

E30 (30 phr PA6): The most homogeneous morphology is achieved at this composition. PA6 particles are finely dispersed and well bonded to the EPDM matrix, resulting in excellent stress transfer and the best balance of stiffness and toughness [34]. The strong interfacial adhesion allows efficient stress transfer across the two phases, leading to the best overall balance of stiffness, toughness, and elongation. This explains why the E30 blend is identified as the optimal composition in terms of mechanical performance.

E40 (40 phr PA6): Agglomeration of PA6 domains reappears, leading to localized stress concentrations and premature fracture during deformation. This explains the reduced elongation at break despite further increases in tensile strength and hardness [29–32]. At high PA6 loadings, the micrographs reveal the reappearance of agglomerated PA6 clusters and microcracks around rigid particles. These features act as stress concentrators, which promote brittle fracture and reduce elongation at break, even though tensile strength and hardness continue to increase. Thus, the excessive thermoplastic fraction undermines toughness and flexibility.

The SEM observations clearly demonstrate that 20–30 phr PA6 (E20–E30) offers the most favorable morphology, where PA6 domains are sufficiently small, uniformly dispersed, and well-bonded to the EPDM matrix due to DCP-induced compatibilization. This composition provides an optimal compromise:

- improved tensile strength and stiffness (due to effective reinforcement by PA6);
- maintained elasticity and toughness (due to the continuous rubbery EPDM phase);
- enhanced interfacial adhesion (due to peroxide-initiated grafting).

In contrast, 10 phr PA6 is insufficient to achieve meaningful reinforcement, while 40 phr PA6 causes phase agglomeration and embrittlement. Therefore, the 20–30 phr range is the most suitable ratio for engineering applications demanding a balance of mechanical strength, flexibility, and thermal stability.

## Conclusion

In this study, EPDM/PA6 blends compatibilized with dicumyl peroxide (DCP) were systematically prepared and characterized in terms of mechanical, thermal, and morphological properties. The results collectively highlight the decisive role of PA6 content and peroxide-induced compatibilization in tailoring the performance of elastomer/thermoplastic systems.

The results of the tests showed that the inclusion of PA6 in the blends significantly increased the tensile strength, modulus of elasticity and hardness. This is explained by the reinforcing effect of the hard thermoplastic phases. Also, increasing the amount of PA6 showed a loss of elasticity, while simultaneously reducing the elongation at break. The optimum limit between strength and elasticity was achieved at 20–30 phr PA6; at these contents, the blends provided sufficient strength as well as acceptable elongation.

The results of the thermal analysis confirmed that PA6 improved the thermal stability of the blends. As the amount of PA6 increased, both the initial decomposition temperature ($T_{10}\%$) and the maximum decomposition temperature ($T_{max}$) gradually shifted towards higher values. This, together with the higher char residue observed at higher loadings, indicates a positive effect of the PA6 and DCP-induced adaptation on the overall thermal resistance of the blends.

Dynamic mechanical analysis confirmed the stiffening effect of PA6, showing a systematic increase in storage modulus and a shift of the glass transition temperature ($T_g$) towards higher values. These results reflect the strengthening of interfacial adhesion and the limitation of chain mobility. This is also attributed to peroxide-mediated grafting reactions at the EPDM/PA6 interface.

Morphological analysis by SEM directly demonstrated the effect of PA6 concentration on phase dispersion. At low PA6 content (E10), large and poorly bonded phase domains were observed, which is consistent with low strength and high elongation. At other PA6 proportions (E20–E30), finely dispersed and well-bonded PA6 particles were obtained, confirming effective tailoring. It also explained the superiority of mechanical properties. At high PA6 content (E40), however, microcracking of the particles was observed, which led to a decrease in impact strength despite an increase in tensile strength.

Overall, the findings demonstrate that DCP is an efficient reactive compatibilizer for EPDM/PA6 blends, enabling improved phase adhesion and tunable property profiles. The optimal formulations were identified at 20–30 phr PA6 with 1.0–1.2 phr DCP, providing the best trade-off between tensile strength, toughness, thermal stability, and morphological uniformity. These compositions are therefore promising for industrial applications–such as automotive parts, cable insulation, and structural components–where a balance of elasticity, strength, and heat resistance is critical.

The mechanical and thermal results obtained in this study are not only of laboratory interest but also highly relevant for industrial applications. In particular, the EPDM/PA6 blends containing 20–30 phr PA6, which demonstrated tensile strengths in the range of 13–15 MPa while maintaining adequate elasticity, are promising for automotive engineering components such as vibration-damping parts, heat- and oil-resistant seals in the engine compartment, and shock-absorbing elements.

The improvement in thermal stability, with the onset degradation temperature increasing from 328°C to 350°C, further indicates that these blends can be effectively employed in cable insulation materials and energy transport systems where elevated temperatures are encountered. Moreover, the enhanced modulus and hardness suggest their suitability for structural components requiring dimensional stability and durability under mechanical stress.

Therefore, scaling the mechanical and thermal findings to real-world applications clearly demonstrates that DCP-compatibilized EPDM/PA6 blends are not limited to fundamental research but offer significant potential in automotive, construction, and energy infrastructure sectors, where a combination of flexibility, mechanical robustness, and heat resistance is essential.

## Acknowledgments

The authors gratefully acknowledge the support provided by Tekoplast Company.

## Conflict of interest

The authors declare that they have no conflicts of interest.

## References

1. Kumar R., et al. (2021) Mechanical performance and sustainability of polymer composites: A critical review. *Materials Science Forum*, 1012, pp.1. https://doi.org/10.4028/www.scientific.net/MSF.1012.1.

2. Movlayev I.G., Mammadova A.F. (2024) Determination of the main parameters of the modified epoxide oligomer. *Int. Sci. J. Eng. Agric*., 3(6), pp. 95. https://doi.org/10.46299/j.isjea.20240306.09.

3. Amirli F.A., Movlayev I.H., Aliyeva G.A., Mammadova A.F. (2023) Compositions based on modified and filled epoxy oligomer. *Processes of Petrochemistry and Oil Refining*, 24(4), pp. 689. https://doi.org/10.36719/1726-4685/96/689-696.

4. Mammadov S., Mammadova G., Khankishiyeva R., Azizova G., Movlayev İ., Mammadov J. (2023) The effect of composition and structure of NBR-based elastomer blends in the vulcanization process and study of their aging by exposure to heat and radiation. *Chemistry & Chemical Technology*, 17(4), pp. 829. https://doi.org/10.23939/chcht17.04.829.

5. Aghamaliyev Z.Z., Naghiyeva M.V., Rasulov Ch.K. (2018) Synthesis of 2-Hydroxy-3-(methylcyclohexenyl-isopropyl)-5-methylbenzylaminoethylnonyl imidazolines as thermostabilizers to polypropylene. *Materials Science Forum*, 935, pp. 155. https://doi.org/10.4028/www.scientific.net/MSF.935.155.

6. Amirli F.A., Azizova G.G., Mammadova A.F., Iravanli K.B. (2025) Study of the features of vulcanization and the character of vulcanization structures of nitrile butadiene rubber. *Processes of Petrochemistry and Oil Refining*, Special issue, 2025, pp. 259-264. https://doi.org/10.62972/1726-4685.si2025.1.259.

7. Klyuchnikov O.R., Deberdeev R.Ya., Zaikov G.E. (2006) Low-temperature vulcanisation of unsaturated rubbers by C-nitrose systems. *International Polymer Science and Technology*, 3, pp. 51. https://doi.org/10.1177/0307174X0603300810.

8. Amirli F.A., Movlayev I.H., Mammadova A.F. (2025) Study of the rheological properties of the mixture of terminal ethylene–propylene rubber with benzenamine-modified phenol–formaldehyde oligomer. *Processes of Petrochemistry and Oil Refining*, 26(1), pp. 229–239. https://doi.org/10.62972/1726-4685.2025.1.229.

9. Dyshyn O., Habibov I., Suleymanova A., Abasova S., Malikov R., Khankishiyeva T. (2023) Identifying the mechanism of formation of a natural nanocomposite in polymer composite materials. *Eastern-European Journal of Enterprise Technologies*, 2(6-122), pp. 24. https://doi.org/10.15587/1729-4061.2023.277587.

10. Park G., Kim Y.-H., Kim D. S., et al. (2010) Morphology and vulcanizate properties of ethylene-propylene-diene rubber/styrene-butadiene rubber blends. *Journal of Nanoscience and Nanotechnology*, 10(5), pp. 3720. https://doi.org/10.1166/jnn.2010.2348.

11. Mammadov S., Mammadova G., Khankishiyeva R., Amirov F., Azizova G., Movlaev I., Mammadov J. (2023) Investigation of the rheological structural parameters of a network of NBR-based vulcanizates with the participation of chlorine-containing compounds. *Journal of New Technology and Materials*, 13(1), pp. 70.

12. Mammadov S., Mammadova G., Khankishiyeva R., Amirov F., Azizova G., Movlaev I., Mammadov J. (2023) Properties of vulcanizates based on nitrile butadiene rubber in the occurrence of halomethyl-containing compounds. *Functional Materials*, 30(3), pp. 393. http://dx.doi.org/10.15407/fm30.03.393.

13. Ibragimova M.C., Amirov F.A., Bayramova S.T. (2020) Investigation of reactivity of the petroleum polymer pitch on the basis of gasoil fraction. *Processes of Petrochemistry and Oil Refining*, 24(3), pp. 347.

16. Ma L., Yang W., Guo H. (2019) Effect of cross-linking degree of EPDM phase on the morphology evolution and crystallization behavior of thermoplastic vulcanizates based on polyamide 6 (PA6)/ethylene-propylene-diene rubber (EPDM) blends. *Polymers*, 11(9), pp. 1375. https://doi.org/10.3390/polym11091375.

17. Lin X., Li Y., Zhang Z., Liu J. (2020) Reactive compatibilization of polyamide 6 with olefin block copolymers: morphology, rheology and mechanical properties. Polymers, 12(5), pp. 1123. https://doi.org/10.3390/polym12051123.

18. Hel C.L., Smith A.B., Jones D.R. (2020) Thermoplastic vulcanizates: new insight on rubber morphology and phase behavior. *Polymers*, 12(10), pp. 2315. https://doi.org/10.3390/polym12102315.

19. Amirli F., Khankishiyeva R., Movlayev I., Mammadova A. (2025) Properties of NBR/modified EPDM rubber compositions. *Physics and Chemistry of Solid State*, 26(3), pp. 549-555. https://doi.org/10.15330/pcss.26.3.549-555.

20. Song L.F., Müller K., Becker M. (2023) Effects of ethylene-propylene-diene monomer characteristics on TPV performance and morphology. *Polymers*, 15(2), pp. 345. https://doi.org/10.3390/polym15020345.

21. Çakır N.Y., Wang S., Roberts I. (2023) Unlocking the potential use of reactive POSS as a compatibilizer and coagent in peroxide-cured TPVs. *Polymers*, 15(7), pp. 1489. https://doi.org/10.3390/polym15071489.

22. Piontek A., Vernaez O., Kabasci S. (2020) Compatibilization of poly(lactic acid) (PLA) and bio-based EPDM via reactive extrusion with different coagents. *Polymers*, 12(3), pp. 605. https://doi.org/10.3390/polym12030605.

23. Ma L., Guo H., Yang W. (2019) In-situ dynamic vulcanization and interfacial compatibilization in PA6/EPDM TPVs: effects on crystallization and mechanical performance. *Journal of Applied Polymer Science*, 136(14), pp. 47215.

24. Mirzaee R., Park S. (2020) Modeling and optimizing toughness and rigidity in PA6/SBR blends using experimental design and reactive compatibilization. *Polymer*, 188, pp. 122121. https://doi.org/10.1016/j.polymertesting.2020.106346.

25. Tang Q., Li Y., Zhou X. (2022) Morphological evolution and damping properties of dynamically vulcanized TPVs: role of curing degree and compatibilizer. *Materials*, 15(5), pp. 1789.

26. Ma L., Guo H. (2019) Effect of peroxide dosage on morphology and mechanical properties of PA6/EPDM blends. *Materials*, 12(18), pp. 2953.

27. Bhattacharya A.B., Fernández M. (2020) Automotive applications of thermoplastic vulcanizates: review and perspectives. *Polymer Reviews*, 60(4), pp. 585-612.

28. Mirzaee R., Zhao K. (2020) Optimizing compatibilizer type and loading for PA6/EPDM based blends: mechanics and morphology. *Polymer Engineering & Science*, 60(9), pp. 2030-2042.

29. Maity A., Naskar K., Bhowmick A.K. (2016) Peroxide-induced compatibilization in elastomer/thermoplastic blends: mechanism and processing. *Polymer International*, 65(11), pp. 1360-1374.

30. Li L., Zhang T. (2012) Characterization of PA6/EPDM-g-MA/HDPE ternary blends: phase morphology and mechanical performance. *Polymer*, 53(8), pp. 1702-1710.

31. Nakason C., Praserthdam P. (2013) Thermoplastic natural rubber based on polyamide-12 and EPDM: morphology by reactive compatibilization. *Journal of Elastomers & Plastics*, 45(3), pp. 245-261.

32. Zhu L., Wang H. (2018) Core-shell morphology effects on mechanical properties in PA6/HDPE/compatibilizer systems. *Macromolecules*, 51(20), pp. 8202-8214.

33. Cui Z., Sun L. (2023) Effect of crosslinking agent dosage on the morphology and thermal stability of TPVs based on various rubbers. *Composites Part A: Applied Science and Manufacturing*, 164, pp. 106771.

34. Helms G., Noordermeer J. (2014) Peroxide-induced dynamic vulcanization and interfacial compatibilization methodologies: a review. *Biomacromolecules*, 15(6), pp. 2038-2052.

***Information about authors:***

*Fariz Amirli – Professor, Doctor of Technical Sciences, Azerbaijan State Oil and Industry University (Baku, Azerbaijan, e-mail: fariz.amirli@asoiu.edu.az).*

*Rana Khankishiyeva – Doctor of Philosophy in Radiation Materials Science, Azerbaijan State Oil and Industry University; Institute of Radiation Problems; Azerbaijan University of Architecture and Construction; Scientific-Research Institute Geotechnological Problems of Oil, Gas and Chemistry (Baku, Azerbaijan, e-mail: rana.khankishiyeva@azmiu.edu.az).*

*Aynur Mammadova – PhD candidate, Azerbaijan State Oil and Industry University (Baku, Azerbaijan, e-mail: aynur.memmedova@asoiu.edu.az).*

*Samira Bayramova – Researcher, Azerbaijan State Oil and Industry University (Baku, Azerbaijan, e-mail: bayramova.samira.t@gmail.com).*

*Gunel Azizova – Researcher, Azerbaijan State Oil and Industry University (Baku, Azerbaijan, e-mail: azizova.gunel@asoiu.edu.az).*

*Konul Iravanli – Researcher, Azerbaijan State Oil and Industry University (Baku, Azerbaijan, e-mail: iravanli.konul@asoiu.edu.az).*

IRSTI 31.19.15 https://doi.org/10.26577/IJBCh202518210

M.M. Burkitbayev[1], U.Zh. Dzhusipbekov[2], G.O. Nurgalieva[2],
Z.K. Bayakhmetova[2], D. Duisenbai[2], Sh.N. Nazarkulova[1*],
I.V. Matveyeva[1, 3], Ye.Yu. Yarovaya[1]

[1]Al-Farabi Kazakh National University, Almaty, Kazakhstan
[2]JSC A.B. Bekturov Institute of Chemical Sciences, Almaty, Kazakhstan
[3]Kazakh-British Technical University, Almaty, Kazakhstan
*e-mail: sholpan.nazarkulova@kaznu.edu.kz

*(Received 29 May 2025; received in revised form 12 November 2025; accepted 19 November 2025)*

# Assessment of natural radionuclides content in humate-containing fertilizers

**Abstract.** Humic substances (HS) possess significant physiological activity and play a crucial role in enhancing soil properties and plant productivity. This study is devoted to the determination of the content of natural radionuclides in humate-containing samples obtained from natural raw materials of Kazakhstan. Five samples, including both solid and liquid fertilizers, were prepared and analyzed. Key parameters such as elemental composition, content of carboxyl and phenolic groups, and the yield of free humic acids were determined. The concentrations of uranium-238, uranium-234, thorium-232, thorium-230, thorium-228, polonium-210, and lead-210 isotopes were measured using alpha-spectrometric and alpha-beta radiometric methods. Results indicated that the liquid fertilizer exhibited the lowest radionuclide activities, while the solid samples showed varying levels of radioactive isotopes, with the highest activity recorded in sample A2. Nonetheless, the specific activities of all measured radionuclides complied with the national radiation safety standards (SanPiN 2.6.1.2523-09), confirming the fertilizers' safety for agricultural use. This work highlights the importance of radiation monitoring in fertilizers and the potential of humate-containing materials as environmentally friendly agricultural enhancers. The findings contribute to the development of sustainable agricultural practices through the safe utilization of natural organomineral fertilizers derived from local raw materials.

**Keywords:** Humic substances, natural radionuclide, fertilizers, uranium series, activity concentration.

## Introduction

Fertilizers can increase crop yields by an average of 50-80% by eliminating nutrient deficiencies in the soil. Nutrients include macronutrients (nitrogen, phosphorus, potassium), mesonutrients (sulfur, calcium, magnesium) and micronutrients (iron, molybdenum, zinc, boron, cobalt, copper, manganese). These elements are part of fertilizers, divided into 5 main types: nitrogen, potassium, phosphorus, micronutrients and complex or compound mineral fertilizers [1].

Humic substances (HS) are characterized by high physiological activity due to their structural features and physicochemical properties [2-5]. Humic substances activate the metabolism and reproduction of beneficial soil microflora, enhance the protective mechanism of plants against the effects of unfavorable physical, chemical and biological factors, and contribute to increased productivity of agricultural crops and product quality. In addition, HS have a complex effect on the soil, improving its physical, chemical and biological properties, maintaining the organo-mineral balance of soils and promoting the restoration and increase of soil fertility. Liquid humate-containing fertilizers containing a balanced set of biologically active humic substances, macro- and microelements have high biological efficiency and minimal negative impact on the ecosystem and are used to stimulate physiological processes in plants, increase the yield and quality of agricultural products, increase the absorption of nutrients and plant resistance to chemical, physical and biological stress [5-8].

Along with increasing crop yields, the use of fertilizers has negative consequences, such as soil pollu-

© 2025 al-Farabi Kazakh National University

tion and potential contamination of agricultural products, and the entry into the food chain of elements with high toxicity associated with the specificity of specific fertilizers, for example, phosphorus fertilizers contain heavy metals, radioactive isotopes of some metals, and potassium fertilizers often contain impurities of chlorine and a radioactive isotope of potassium, while excessive use of nitrogen fertilizers causes the accumulation of nitrates in plants [9]. Thus, an important characteristic of any fertilizer, both mineral and organic, is quality, which implies a minimum content of pollutants in the composition and control of fertilizers for their content.

The uranium industry has played a significant role in the economy of modern Kazakhstan, which has been a major source of uranium for more than 50 years [10]. The long-term and intensive activities of the uranium industry have left a legacy of environmental pollution [11]. The well-developed uranium industry affects the radio ecological situation of the region [12], where three isotopes of uranium occur in nature. These include U-238, U-235, and U-234. The potential harmfulness of radionuclides is based on their long half-lives and chemical behavior [13].

Determining the content of radioactive elements in fertilizers helps assess radiation safety and compliance of fertilizers with sanitary rules and hygienic standards [14-18]. Due to usage of fertilizers can increase the number of radionuclides in the soil and groundwater and their subsequent entry into the human body. Broad meanings of radionuclide activity concentrations vary among countries, and there is no specific legislation defining maximum permissible limits for radioisotopes in fertilizers.

## Materials and methods

Sample A1 was obtained by interaction of the tetrahydrate ammonium heptamolybdate [$(NH_4)_6Mo_7O_{24}$ .$4H_2O$)] with 1% sodium humate solution at a temperature of 40°C for 60 min at a ratio of the initial components of 0.5:100 (weight/volume). Ammonium molybdate was purchased from LLC Scientific and Production Firm "Baltic Manufacture" (St. Petersburg, Russia).

Sample A2 was obtained from brown coal of the Oikaragay deposit (Almaty region) using 2% NaOH (1:8 weight/volume) for 1 hour at 25°C with vigorous stirring and its precipitation by adding hydrochloric acid to pH 1-2. The precipitate was filtered, washed with distilled water until a negative reaction for chloride ion, and dried in a drying cabinet at a temperature of 70-80°C.

Sample A3 was extracted from brown coal of the Oikaragay deposit (Almaty region). The extraction process was carried out with a 2% NaOH solution (1:8 weight/volume) for 1 hour at 25°C with vigorous stirring. The suspension was centrifuged, and the filtrate was dried in a vacuum oven at 105°C.

Sample A4 is brown coal from the Oikaragay deposit in the Almaty region.

Sample A5 was obtained by extraction from brown coal of the Oikaragay deposit (Almaty region) with a 2% solution of $NH_4OH$ (1:8 weight/volume for 1 hour at 25°C with vigorous stirring. The suspension was centrifuged, and the filtrate was dried in a vacuum oven at 105°C.

In humate-containing samples were determined the release of free humic acids by chemical analysis [19], the amount of carboxyl groups and phenolic hydroxyls was determined using the calcium acetate and barite methods [20]. The elemental composition of humate-containing samples was determined using a Thermo analyzer FlashSmart (Thermo Scientific company, USA). The molybdenum content was determined using an inductively coupled plasma atomic emission spectrometer of the iCAP PRO XP Duo brand (Thermo Fisher Scientific, USA). The characteristics of humate-containing samples are given in the Table 1.

**Table 1** – Characteristics of humate-containing samples

| Sample | Elemental composition, on a dry ash-free basis, % | | | | | Content of acidic groups, on a dry ash-free basis, mg-eq/g | | Yield of free humic acids based on dry ash-free basis, % |
|---|---|---|---|---|---|---|---|---|
| | C | H | N | O | Mo | COOH | Phenolic hydroxyl | |
| A1 | 54.51 | 3.80 | 5.23 | 35.64 | 0.27 | 1.76 | 0.70 | 38.40 |
| A2 | 60.1 4 | 4.14 | 1.4 1 | 28. 32 | - | 1. 18 | 1.67 | 81.07 |
| A3 | 42.40 | 3 .02 | 1.2 9 | 30.6 4 | . | 2 .12 | 2.87 | 74.10 |
| A4 | 53.61 | 4.21 | 1.43 | 28.92 | . | 0.33 | 2.40 | 55.00 |
| A5 | 55.63 | 3.44 | 1.57 | 33.32 | - | 1.30 | 0.75 | 54.12 |

Determination of uranium isotopes in solid humate-containing and liquid organomineral fertilizers by the alpha-spectrometric method was carried out in three stages:

1. Decomposition of the sample (in the case of liquid samples, the concentration method was used);
2. Preliminary radiochemical preparation of samples;
3. Alpha spectrometric determination of uranium isotopes.

Decomposition of solid humate-containing samples was carried out by treating them with solutions of strong acids after roasting at high temperatures to remove organic substances. Concentration of uranium isotopes in liquid fertilizers was carried out by evaporation in a glass beaker over low heat, preventing the sample from boiling.

Preliminary radiochemical preparation of samples included concentration of uranium isotopes from a solid sample, extraction separation from interfering radionuclides, and preparation of a counting sample by electrolytic method.

The samples were isolated and purified by extraction with tributyl phosphate in toluene. The nitric acid solution containing uranium isotopes, concentrated in a smaller volume, was transferred to a separatory funnel, freshly purified TBP solution in toluene was added and extracted for 5 minutes.

Next, uranium was re-extracted, for which the organic phase was washed with distilled water. The combined aqueous re-extract was evaporated to dryness, moistened with concentrated nitric acid, and again evaporated to dryness to remove traces of organic matter.

The preparation of the counting sample was carried out by the method of electrolytic deposition of uranium isotopes on a steel disk. To achieve the best peak resolution on the alpha-spectrogram, it is necessary that the uranium isotopes be applied to a polished steel substrate in a thin, uniform layer. For this purpose, the dry residue containing uranium isotopes was dissolved in a mixture of $HNO_3$, Trilon B, $NH_4Cl$, $(NH_4)_2C_2O_4$. The pH of the solution was maintained at 7-8. Then, the solution containing uranium isotopes was transferred in bulk to an electrolytic cell and the electrodeposition of purified isotopes was carried out at a constant current of 1 A.

To determine thorium isotopes in the liquid sample, radiochemical preparation was carried out, which included:

- concentration of thorium isotopes,
- separation and isolation of thorium isotopes (separation of macrocomponents, polonium, radium, plutonium, uranium),
- preparation of a counting sample.

For solid samples, radiochemical preparation consisted of:

- decomposition,
- separation and isolation of thorium isotopes (separation of macrocomponents, polonium, radium, plutonium, uranium),
- preparation of a counting sample.

The method is selective and is focused on determining only the isotopes of thorium-232, thorium-230 and thorium-228. The possible interfering effect of radionuclides with similar alpha radiation energies (uranium-234, uranium-238, polonium-210, radium-226, plutonium-238, americium-241) was eliminated during the radiochemical preparation of samples.

The separation and extraction of thorium isotopes from accompanying interfering alpha-emitting natural radionuclides with similar alpha-radiation energies (isotopes of uranium, radium, polonium, etc.) was carried out on ion-exchange resins. The ion-exchange resins were pre-treated, including obtaining a resin of a certain fraction, removing interfering components, and bringing the resin to the required pH value.

The preparation of the counting sample was carried out by electrolytic deposition on a low-background disk at a constant current ($I = 1$ A).

Losses during analysis were monitored by adding a thorium-234 solution to the sample, followed by comparison of the integral beta particle count rate from the working preparation (counting sample) and from a specially prepared comparison sample of identical geometry.

Uranium and thorium isotopes were measured using the alpha-spectrometric method on the Alpha – analyst alpha -spectrometer from Canberra with the appropriate software. This method allows identifying an isotope by energy and intensity, determining its activity and content in the sample. For this purpose, the device was pre-calibrated by energy and efficiency. Background values were determined before the measurement.

The alpha spectrometer "Canberra" (USA) is a specialized spectrometric system designed for detailed analysis of alpha-emitting radionuclides (in particular, uranium and thorium isotopes). The device includes a silicon semiconductor detector of the PIPS (Passivated Implanted Planar Silicon) type, placed in a vacuum chamber, which ensures low background and high energy resolution (no worse than 20-25 keV). The advantage of the design is high sensitivity when measuring low-energy alpha quanta (from 3 to 8 MeV), which is especially important when studying natural radionuclides in organo-mineral matrices. The counting sample was prepared by applying a thin (up to 100 μg/cm²) precipitant to a disk carrier, followed by drying and stabilization of the layer. The spectrum clearly showed peaks of alpha decay of U-238, U-234, Th-232 isotopes and their daughter products, which allowed for qualitative and quantitative analysis at the level of Bq/kg units.

To determine polonium-210 and lead-210 isotopes in solid humate-containing and liquid organomineral fertilizers by the alpha-beta radiometric method, a variant of simultaneous spontaneous electrochemical precipitation of Po-210 and Bi-210 (= Pb-210) in radiochemically pure form on substrates made of stainless corrosion-resistant Ni – Ti steel was implemented. In this case, the precipitation of Pb-210 on Fe is practically excluded, and its determination was carried out by beta radiation of daughter Bi-210. Radionuclides are leached from 5 g of air-dry crushed sample with a mixture of $HNO_3$, HCl and $H_2O_2$, after which $HClO_4$ is added to the filtrate and the solution is evaporated to wet salts to remove traces of $HNO_3$. The salts are dissolved in 0.5 M HCl and then Po-210 and Bi-210 are deposited on one side of the steel substrate for 2 hours. Isotope measurements were carried out in the range of 10-36 hours after spontaneous currentless deposition on an alpha-beta radiometer with a silicon detector for measuring low activities UMF-2000 (JSC NPP Doza, Moscow, Russia), as recommended in the methodology (MI No. FR 15382).

The UMF-2000 radiometer is the device equipped with a low-background counter with a protection system from external radiation and an automated recorder of counting information. The design of the radiometer includes a removable cassette with a sample, located in a fixed geometry opposite the counting device. Due to its high sensitivity (detection threshold of about 0.05 Bq/cm² with a 10-minute exposure) and ease of use, the UMF-2000 is optimal for this work. Its use is especially justified when it is necessary to confirm data obtained by the spectrometric method, as well as for preliminary screening of the radioactivity level.

The combined use of two methods ensured the reliability of measurements, expanded the analytical range (in terms of registration energies) and made it possible to obtain substantiated data on the distribution of natural radionuclides in the studied fertilizers. The relevance of using these devices in this work is due to their high reliability, representativeness of the results and compliance with modern requirements for radiometric control of substances of natural origin.

## Results and discussion

The results of radiometric analysis of five samples of humate-containing preparations are presented in Figures 1-7. The highest activity values of uranium and thorium radionuclides were recorded in sample A4, where the activity of U-238 reached 202±14 Bq/kg, and U-234 – 245±15 Bq/kg. At the same time, the minimum levels of these radionuclides were observed in sample A1, which suggests significant differences in the original mineral composition of the raw materials or in the concentration processes during production.

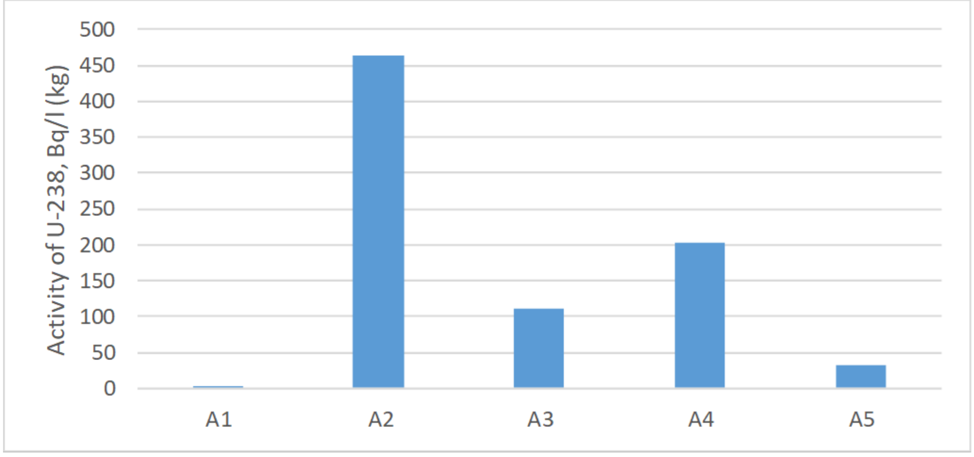

**Figure 1** – Content of uranium-238 isotope in the analyzed samples

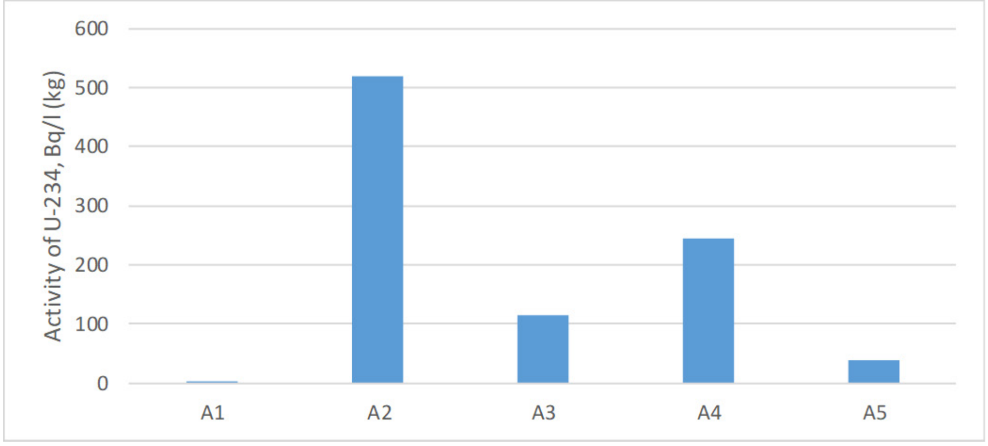

**Figure 2** – Content of uranium-234 isotope in the analyzed samples

A similar pattern is also characteristic of radionuclides of the thorium series: the highest activity of Th-232 and its daughter isotopes (Th-230 and Th-228) was recorded in samples A2 and A4, which indicates the presence of thorium-containing components of natural origin in these samples.

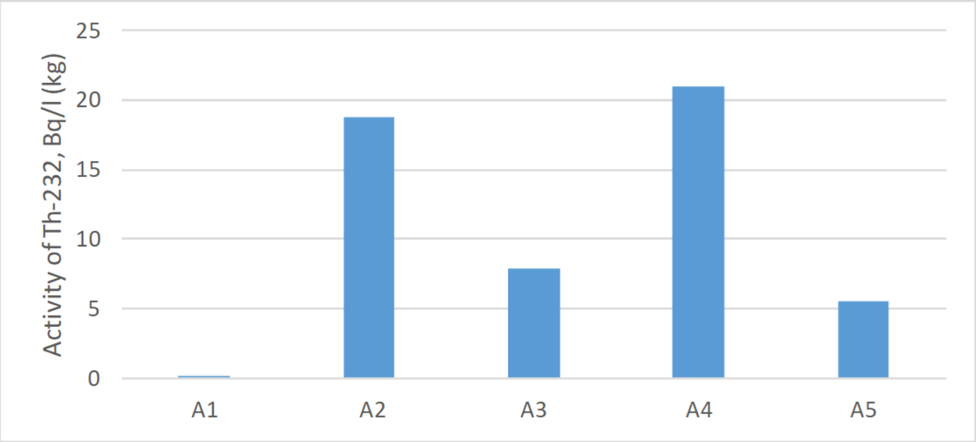

**Figure 3** – Content of thorium-232 isotope in the analyzed samples

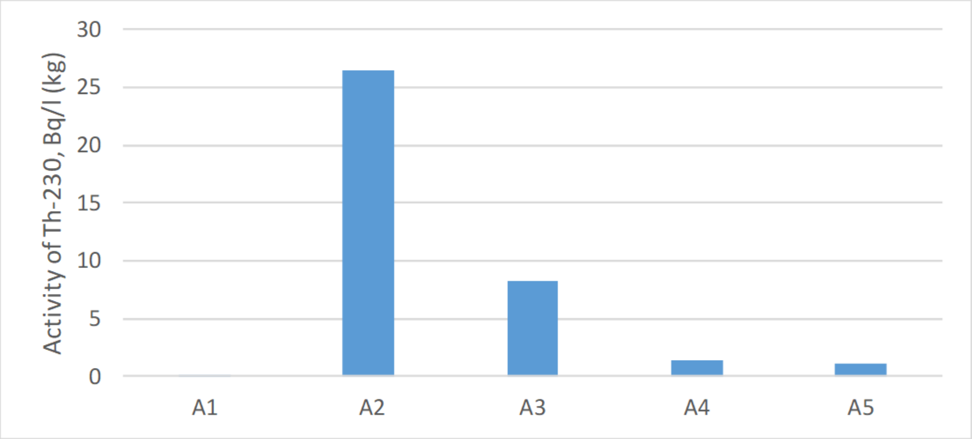

**Figure 4** – Content of thorium-230 isotopes in the analyzed samples

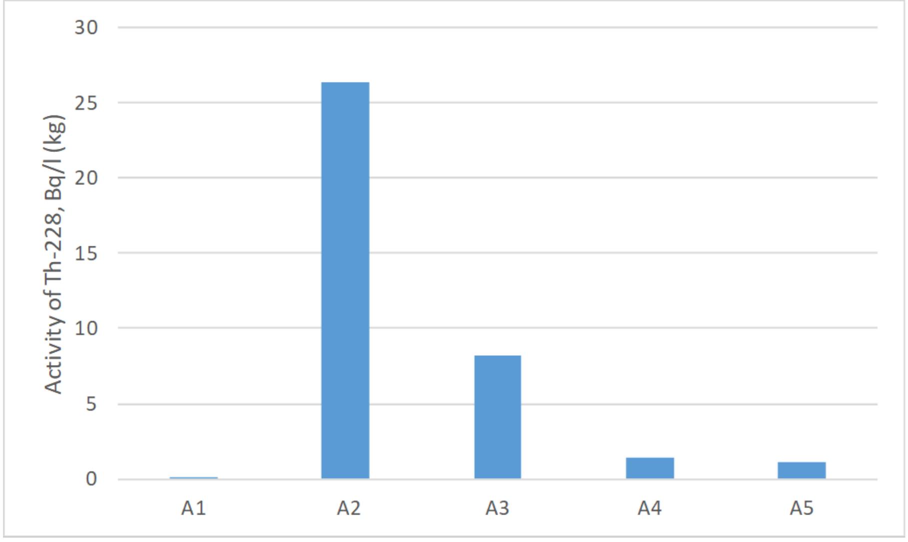

**Figure 5** – Content of thorium-228 isotopes in analyzed samples

The radioactivity of Po-210 and Pb-210 also correlates with the concentration of uranium. Their values are highest in the samples A2 (119 and 513 Bq/kg, respectively) and A3 (112 and 483 Bq/kg), which indicates the enrichment of these products with radionuclides from the uranium-radium series. Probably, during the processing of organomineral components, sorption accumulation of these radionuclides occurred, especially in the presence of humic acids, which have a high complexing capacity [21].

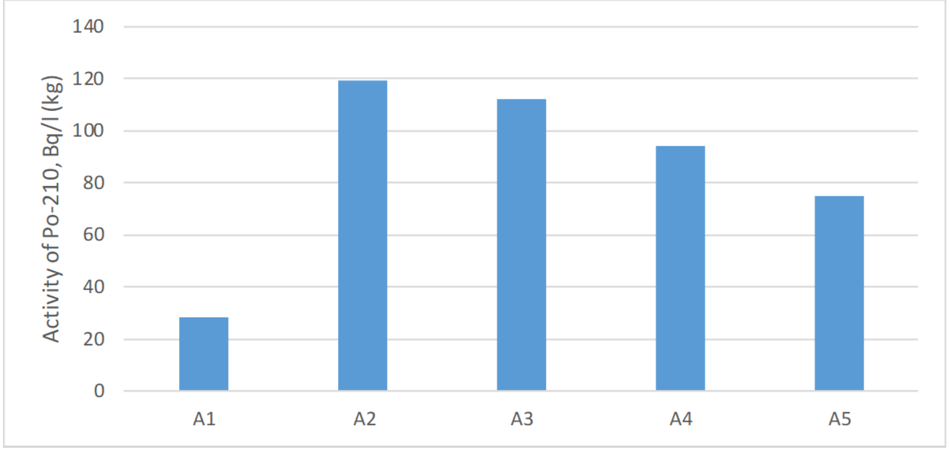

**Figure 6** – Content of polonium-210 isotope in samples

Comparison of the radionuclide composition with the expected content of humic substances shows that higher concentrations of U-238, Th-232 and Po-210 are characteristic of fertilizers containing an active organic matrix. This confirms the role of humic acids as factors enhancing the migration and retention of radionuclides in the solid phase.

Thus, it can be concluded that the content of natural radionuclides in humate-containing fertilizers is determined not only by the origin of the raw materials, but also by the degree of complexation with humic substances. These results are consistent with previously published data [22], where the influence of organic matter on the behavior of radionuclides in the soil-plant system was emphasized. Such a dependence is especially significant when assessing environmental risks when using fertilizers based on natural organomineral components.

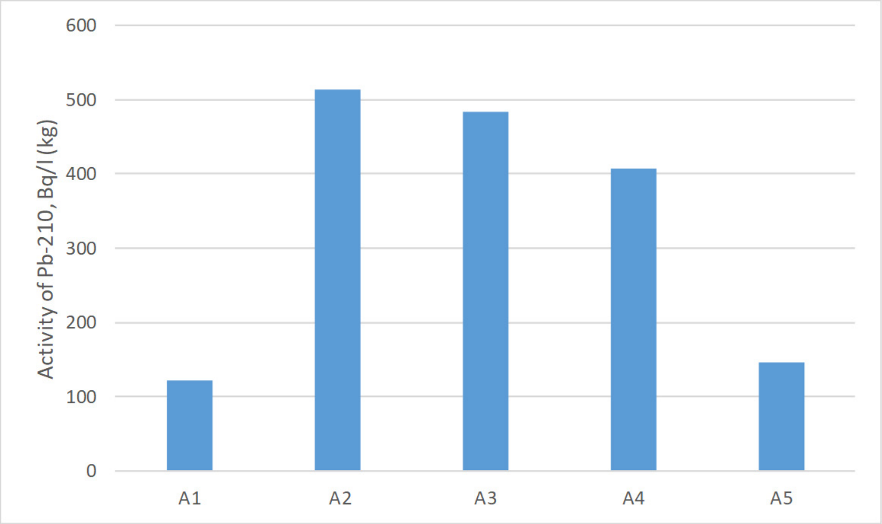

**Figure 7** – Content of lead-210 isotope in samples

To assess the reliability of the experimental data obtained on the activity of radionuclides in samples of humate-containing fertilizers, statistical processing of the results was carried out. The main calculation indicators were: arithmetic mean, standard deviation, confidence interval, and variation coefficient. The processing was performed for all studied radionuclides: U-238, U-234, Th-232, Th-230, Th-228, Po-210, and Pb-210.

The arithmetic mean was calculated using the formula:

$$\bar{x} = (1/n) \cdot \sum x_i \qquad (1)$$

where $\bar{x}$ is arithmetic mean, $x_i$ is individual values, n is number of measurements.

The standard deviation (unbiased) was defined as:

$$s = \sqrt{[(1 / (n - 1)) \cdot \sum(x_i - \bar{x})^2]} \qquad (2)$$

where s is standard deviation, $\bar{x}$ is average value.

Confidence interval (at 95% significance level):

$$CI = \bar{x} \pm t * (s / \sqrt{n}) \qquad (3)$$

where CI is confidence interval, t is Student's coefficient, s is standard deviation, n is number of measurements.

The coefficient of variation (in percent) is calculated using the formula:

$$CV = (s / \bar{x}) \cdot 100\% \qquad (4)$$

where CV is coefficient of variation, s is standard deviation, $\bar{x}$ is average value.

These formulas were used to analyze the distribution of radiometric measurement results, including to assess the variability of the content of the studied radionuclides in samples of humate-containing preparations. They provided an objective quantitative interpretation of the data and allowed statistical comparison between different preparations. Table 2 presents the statistical parameters for all the studied radionuclides.

**Table 2** – Statistical parameters of all studied radionuclides

| Radionuclide | Average value | Standard deviation | Confidence interval (95%) | Coefficient of variation (%) |
|---|---|---|---|---|
| U-238 | 4224.20 | 8940.41 | ±7836.61 | 211.65 |
| U-234 | 5106.85 | 10851.44 | ±9511.71 | 212.49 |
| Th-232 | 10.67 | 8.91 | ±7.81 | 83.46 |
| Th-230 | 7.44 | 11.07 | ±9.71 | 148.79 |
| Th-228 | 7.44 | 11.07 | ±9.71 | 148.79 |
| Po-210 | 85.60 | 36.45 | ±31.95 | 42.58 |
| Pb-210 | 334.40 | 186.74 | ±163.68 | 55.84 |

The presented data show that the greatest variability was demonstrated by U-238 and U-234 radionuclides, which may be due to the characteristics of the initial raw materials and the uneven distribution of uranium in the humic matrix. The lowest values of the variation coefficient are observed for Po-210 and Pb-210, which indicates a more uniform distribution of these radionuclides across the samples, probably due to stable sorption bonds with organic matter. Such differences in statistical parameters must be taken into account when assessing the radiation safety of humate-containing fertilizers, especially in the context of long-term impact on the soil-plant system and potential migration of radionuclides in agrobiocenoses.

Such results are consistent with reference data indicating a significant influence of the organic component of fertilizers on the distribution of natural radionuclides. Further research is expected to examine the contribution of specific fractions of humic substances to the retention of uranium and thorium series, using chromatographic fractionation methods and surface radiospectral analysis.

## Conclusion

The minimum activity of uranium isotopes was determined in the liquid sample (A1), which indicates a low level of radiation contamination in this sample. However, in the solid humate-containing samples, a higher activity of both uranium isotopes is observed compared to the liquid sample. Specifically, the activity of uranium-238 varies from 463±22 Bq/kg in sample A2 to 33±3 Bq/kg in sample A5, and for the uranium-234 isotope, these values are 519±22 Bq/kg in A2 and 38±3 Bq/kg in A5. Thus, it can be concluded that the humate-containing solid samples have a higher radiation activity than the liquid ones. Also, the minimum values of the activity of thorium isotopes were recorded in the liquid sample (A1). However, the highest content of the thorium-232 isotope was recorded in sample A4, which indicates a higher concentration of this isotope in this sample. As for the thorium-230 and thorium-228 isotopes, the maximum activity was detected in sample A2, which also confirms a certain variability in the content of radionuclides in different types of samples.

For the isotopes polonium-210 and lead-210, the minimum values were established in the liquid sample A1, where the activity was 75±6 Bq/l for polonium-210 and 147±11 Bq/l for lead-210. At the same time, in solid humate-containing samples, the maximum activity of these isotopes is observed in sample A2, where it is 119±9 Bq/kg for polonium-210 and 513±36 Bq/kg for lead-210. These results confirm the high concentration of these radionuclides in solid samples, especially in humate-containing ones.

The specific activity of natural radionuclides in the studied humate-containing samples complies with the requirements of paragraph 5.3.6 of Sanitary rules and regulations 2.6.1.2523-09 "Radiation Safety Standards (NRB-99/2009)", which means compliance with radiation norms and standards. Thus, the use of these fertilizers for their intended purpose is permitted without restrictions on the radiation factor, which makes them safe for use in agriculture.

## Acknowledgments:

The work was carried out under the program of targeted funding of scientific research for 2023-2025, implemented by the Committee of Science of the Ministry of Science and Higher education of the Republic of Kazakhstan, under the program BR27101179.

## Conflict of interest

The authors declare that they have no conflicts of interest.

## References

1. Potetnya K.M. (2019) Role and Types of Fertilizers in Agriculture. *Scientific and Technical Bulletin: Technical Systems in Agriculture*, no. 5 (5). pp. 25-33 (In Russ.)
2. Klavins M., Grandovska S., Obuka V., Ievinsh G. (2021) Comparative Study of Biostimulant Properties of Industrially and Experimentally Produced Humic Substances. *Agronomy*, vol. 6, no. 11, pp. 1250-1263. https://doi.org/10.3390/agronomy11061250.
3. Shehata A.S., Heba Y.A. Morsy, Marwa A.H. Shady, Wafaa M.T. El-Etr (2023). Ammonium Humate Application Techniques and their Influence on Crop Productivity and Sandy Soil Properties. *J. of Soil Sciences and Agricultural Engineering*, vol. 14, no 9, pp. 297-308. https://doi.org/10.21608/jssae.2023.230850.1183.
4. Marenych M.M., Hanhur V.V., Len O.I., Hangur Y.M., Zhornyk I.I., Kalinichenko A.V. (2019) The Efficiency of Humic Growth Stimulators in Pre-Sowing Seed Treatment and Foliar Additional Fertilizing of Sow Areas of Grain and Industrial Crops. *Agron. Res. no.* 17, pp. 194-205. http://dx.doi.org/10.15159/ar.19.023

5. 4. Şanlı A., Cansever G., Zehra Ok F. (2024**)** Effects of Humic Acid Applications along with Reduced Nitrogen Fertilization on Potato Tuber Yield and Quality. **T***urkish Journal of Agriculture – Food Science and Technology*, vol. 12, no. s4, pp. 2895-2900. https://doi.org/10.24925/turjaf.v12is4.2895-2900.7367.

6. Semenyuk O.V. (2023**)** Efficiency of using liquid complex organomineral fertilizers for pre-sowing treatment of winter wheat seeds. *Agriculture*, no. 7, pp. 25–28. https://doi.org/10.24412/0044-3913-2023-7-25-28.

7. Artemyeva K.S., Skrylnyk E.V. (2018) Efficiency of application of liquid organo-mineral fertilizers under spring barley in the conditions of climate change. *Soil Science and Agrochemistry,* no. 1, pp. 148-154. https://soil.belal.by/jour/article/view/662 (In Russ.).

8. Amirov M.F., Safiullin A.Ya. (2023) Effect of complex organomineral fertilizers on the yield and grain quality of spring wheat in the conditions of the Pre-Kama region of the Republic of Tatarstan. *Agrobiotechnol. and digital agriculture*, vol. 6, no. 2, pp. 1-6. https://doi.org/10.12737/2782-490X-2023-6-11.

9. Uzakov Z., Khalikova S., Egamberdiev A. (2018) Environmental problems of the use of mineral fertilizers. *Symbol of Science: international Scientific Journal*, no. 4, pp. 35-37. (In Russ.).

10. Matveyeva I., Jaćimović R., Planinšek P., Stegnar P., Smodiš B., Burkitbayev M. (2014) Assessment of the main natural radio nuclides, minor and trace elements in soils and sediments of the Shu valley (near the border of Kazakhstan and Kyrgyzstan). *J Radioanal Nucl Chem., no.* 299(3), pp. 1399–1409. https://doi.org/10.1007/s10967-013-2902-3.

11. Matveyeva I, Jaćimović R, Planinšek P, Smodiš B, Burkitbayev M. 2016. Uptake of uranium, thorium and radium isotopes by plants growing in dam impoundment Tasotkel and the Lower Shu region (Kazakhstan). *Radiochimica Acta,* no. 104, pp. 51–57. https://doi.org/10.1515/ract-2015-2457.

12. Nursapina N., Diyarov A., Matveyeva I., Nazarkulova Sh., Ponomarenko O. (2022) Uranium isotopes in food and effect on health of Southern Kazakhstan citizens. *Food additives & Contaminants: Part B*, vol. 15, no. 1, pp. 56–61 https://doi.org/10.1080/19393210.2021.2010810.

13. Van T.T., Bat L.T., Nhan D.D, Quang N.H., Cam B.D., Hung L.V. (2019) Estimation of radionuclide concentrations and average annual committed effective dose due to ingestion for the population in the Red River Delta, Vietnam. *Environ Manage,* vol. 63, pp. 444–454. https://doi.org/10.1007/s00267-018-1007-8.

14. Eke C. (2022) Investigation of Some Properties of Chemical Fertilizers Using Gamma-ray Spectrometry and Energy Dispersive X-ray Fluorescence Spectrometry. *Instrum. Exp. Tech.,* vol. 65, pp. 482–490. https://doi.org/10.1134/S0020441222030149.

15. e Silva C.R., de Oliveira F.M. (2023**)** Natural radioactivity in mineral phosphate fertilizers and its impacts on human health: an overview. *Environ. Sci. Pollut. Res*., vol. 30, pp. 118149-118160. https://doi.org/10.1007/s11356-023-30467-y.

16. Tamilarasi A., Sathish V., Chandrasekaran A. (2023) Assessment of gamma dose and annual effective dose rate for commonly used fertilizer samples in agriculture field with a statistical approach. *Radiat. Prot. Dosim. v*ol. 199 (2), pp. 95–106. https://doi.org/10.1093/rpd/ncac227.

17. Hassan N.M., Chang B.U., Tokonami S., (2017**)** Comparison of natural radioactivity of commonly used fertilizer materials in Egypt and Japan. *J.Chem.,* vol. 9182768, pp. 1-8. https://doi.org/10.1155/2017/9182768/.

18. Alharbi W. R. (2013**)** Natural Radioactivity and Dose Assessment for Brands of Chemical and Organic Fertilizers Used in Saudi Arabia. *J. Mod. Phys.*, vol. 4, no. 3, pp. 344-348. https://doi.org/10.4236/jmp.2013.43047.

19. GOST 9517-1994 (1996) *S*olid fuel. Methods for determining the yield of humic acids [GOST 9517-1994 Ugli burye i kamennye. Metody opredeleniya vyhoda guminovyh kislot]. Minsk: Publishing House of Standards, 8 p. https://ohranatruda.ru/upload/iblock/ad0/4294820847.pdf.

20. Orlov D.S., Grishina L.A. (1981**)** Praktikum po khimii gumusa [Workshop on the chemistry of humus]. Moscow: MSU**,** 271 p. https://www.studmed.ru/orlov-ds-grishina-la-praktikum-po-himii-gumusa_8caa68f7d7c.html.

21. Trofimov D.E., Aksenova L.V., et al. (2019) Behavior of Po-210 and Pb-210 in soils. *Radioecology*, no. 3, pp. 22–30. (In Russ.).

22. Panfilov Yu.V., Stepanov A.V., et al. (2020) Content of radionuclides in fertilizers. *Agroecology*, no. 4, pp. 42–47.(In Russ.).

***Information about authors:***

*Mukhambetkali Burkitbayev – Doctor of Chemical Sciences, Professor of Al-Farabi KazNU (Almaty, Kazakhstan, e-mail: mukhambetkali.burkitbayev@kaznu.edu.kz).*

*Umirzak Zhumasilovich Dzhusipbekov – Doctor of Technical Sciences, Professor, JSC «A.B. Bekturov Institute of Chemical Sciences» (Almaty, Kazakhstan, e-mail: omirzak1952@gmail.ru).*

*Gulzipa Oryntayevna Nurgalieva – Doctor of Chemical Sciences, JSC «A.B. Bekturov Institute of Chemical Sciences» (Almaty, Kazakhstan, e-mail: N_gulzipa@mail.ru).*

*Zamira Kenesbekovna Bayakhmetova – Candidate of Chemical Sciences, JSC «A.B. Bekturov Institute of Chemical Sciences» (Almaty, Kazakhstan, e-mail: zamirabkz@mail.ru).*

*Dulat Duisenbai – Junior Researcher, JSC «A.B. Bekturov Institute of Chemical Sciences» (Almaty, Kazakhstan, e-mail: dulat_211@mail.ru).*

*Sholpan Nurlanovna Nazarkulova – PhD, Senior Lecturer of Al-Farabi KazNU (Almaty, Kazakhstan, e-mail: Sholpan.nazarkulova@kaznu.edu.kz).*

*Ilona Valeriyevna Matveyeva – PhD, Associate Prof. of Kazakh-British Technical University (Almaty, Kazakhstan, e-mail: ilona.matveyeva@kaznu.edu.kz).*

*Yelena Yuriyevna Yarovaya – PhD, Senior Lecturer of Al-Farabi KazNU (Almaty, Kazakhstan, e-mail: yarovayayu@mail.ru).*

International Journal of Biology and Chemistry 18, № 2 (2025)

IRSTI 31.21.27 https://doi.org/10.26577/IJBCh202518211

F. Islamoğlu

Recep Tayyip Erdoğan University, Rize, Turkey
e-mail: fatih.islamoglu@erdogan.edu.tr

*(Received 28 April 2025; received in revised form 18 September 2025; accepted 11 October 2025)*

# Determination of ADMET properties of substituted-piperidine-3-carboxamide derivatives with potential use in the treatment of Crohn's disease

**Abstract.** In this study, ADME studies were carried out on seven different substituted-piperidine-3-carboxamide derivatives compounds, which were considered as drug active ingredients that can be used in the treatment of Chron's disease with docking studies that were done in our previous studies. In this context, these molecules were examined in terms of physicochemical properties, lipophilicity, water solubility, absorption property, distribution property, metabolism property, toxicity property, environmental toxicity property, tox21 pathway property, and medicinal chemistry property. According to the results obtained, it was concluded that (E)-4-((4-(((4-bromopyridin-1(2H)-yl)methylene)amino)-3-(4-methoxy phenyl)-5-oxo-4,5-dihydro-1H-1,2,4-triazol-1-yl)methyl) piperazine-1-carboxylic acid molecule is the most ideal molecule that can be used in the treatment of Chron's disease in terms of ADME properties among the molecules studied.

**Keywords**: Crohn's disease, piperidine-3-carboxamide derivatives, ADME properties, physicochemical properties, toxicity property, medicinal chemistry property.

## Introduction

A chronic inflammatory disease of the digestive tract, Crohn's disease is a member of the inflammatory bowel disease (IBD) group [1]. Although it can occur anywhere in the digestive tract, it most frequently occurs in the ileum, the end of the small intestine, and the colon, the beginning of the large intestine [2]. Crohn's disease can lead to ulcers by thickening the intestinal wall. Crohn's disease symptoms can range from minor to severe and differ from person to person. Anal fissures or fistulas, fever, weariness, diarrhea, cramping and soreness in the abdomen, and loss of appetite are common symptoms [3]. Although the precise origin of Crohn's disease is unknown, environmental factors, immune system issues, and genetic predisposition are believed to be involved [4]. A number of tests and procedures are used to diagnose Crohn's disease. These include MRI, CT scans, or x-rays with barium, stool tests to screen for infection or bleeding, colonoscopy or upper endoscopy to image the digestive tract, and blood tests to check for inflammation and diseases like anemia [5]. Crohn's disease has no known cure, although a number of therapeutic approaches are employed to manage symptoms and bring the condition into remission. Anti-inflammatory medications, immunosuppressants, antibiotics, and biological therapies are the most crucial ones. Other measures include limiting particular meals and providing nutritional assistance, and treating intestinal obstruction or fistulas when medicine is ineffective [6]. Serious side effects include intestinal blockage, deep ulcers throughout the digestive tract, aberrant connections between the intestines and other organs, malnourishment, arthritis, skin issues, and inflammation of the eyes can result from Crohn's disease if it is not treated or is not treated well enough [7]. A balanced diet, stress management, regular checkups with the doctor, and following the treatment plan are just a few of the lifestyle adjustments needed to control Crohn's disease symptoms and enhance quality of life [8].

When developing a new medication, the ADMET concept is essential for assessing its pharmacological characteristics. It establishes a drug's safety, effectiveness, and physiological behavior. Before moving on to clinical trials, choosing a successful therapeutic candidate and reducing any risks requires evaluating ADMET characteristics during the drug development process [9]. Potential drug candidates' ADMET characteristics are assessed both *in vitro*, or in a lab setting, and *in silico*, or through computer modeling.

© 2025 al-Farabi Kazakh National University

At this point, molecules with favorable metabolism, low toxicity, favorable distribution, and high absorption are chosen [10]. Selected medication candidates are examined for ADMET characteristics in animal models during preclinical research. Important information about the drug's safety can be found in toxicological studies [11]. Regulatory bodies (such as the FDA and EMA) submit ADMET data for the medicine's approval. These statistics are used to evaluate the medication's safety and effectiveness [12].

## Materials and Methods

*Studied molecules*. In this study seven different piperidine-3-carboxamide derivative molecules:

- (E)-4-((3-(4-chlorophenyl)-5-oxo-4-((pyridin-1(2H)-ylmethylene)amino)-4,5-dihydro-1H-1,2,4-tri- azol-1-yl)methyl)piperazine-1-carboxylic acid (1);
- (E)-4-((5-oxo-4-((pyridin-1(2H)-ylmethylene) amino)-3-(p-tolyl)-4,5-dihydro-1H-1,2,4-triazol-1-yl)methyl)piperazine-1-carbo xylic acid (2);
- (E)-4-((3-(4-fluorophenyl)-4-(((4-methylpyridin-1(2H)-yl)methylene)amino)-5-oxo-4,5-di hydro-1H-1,2,4-triazol-1-yl)methyl)piperazine-1-carboxylic acid (3);
- (E)-4-((4-(((4-chloro pyridin-1(2H)-yl)methylene)amino)-3-(4-hydroxyphenyl)-5-oxo-4,5-dihydro-1H-1,2,4-triazol-1-yl)methyl)piperaz ine-1-carboxylic acid (4);
- (E)-4-((4-(((4-bromopyridin-1(2H)-yl) methylene)amino)-3-(4-methoxy phenyl)-5-oxo-4,5-dihydro-1H-1,2,4-triazol-1-yl)methyl) piperazine-1-carboxylic acid (5);
- (E)-4-((4-(((4-bromopyridin-1(2H)-yl)methylene)amino)-3-(4-fluorophenyl)-5-oxo-4,5-dihydro-1H-1,2,4-triazol-1-yl)methyl)piperazine-1-carboxylic acid (6);
- (E)-4-((4-(((4-bromopyridin-1(2H)-yl)methylene)amino)-3-(4-hydroxyphenyl)-5-oxo-4,5-dihydro-1H-1,2,4-triazol-1-yl)methyl)piperaz ine-1-carboxylic acid (7)

that have not yet been synthesized and not yet registered in the literature have been selected. The aim of this study is not only to propose a new active ingredient for Crohn's disease A visual showing the molecular structures of the compounds studied is given in Figure 1.

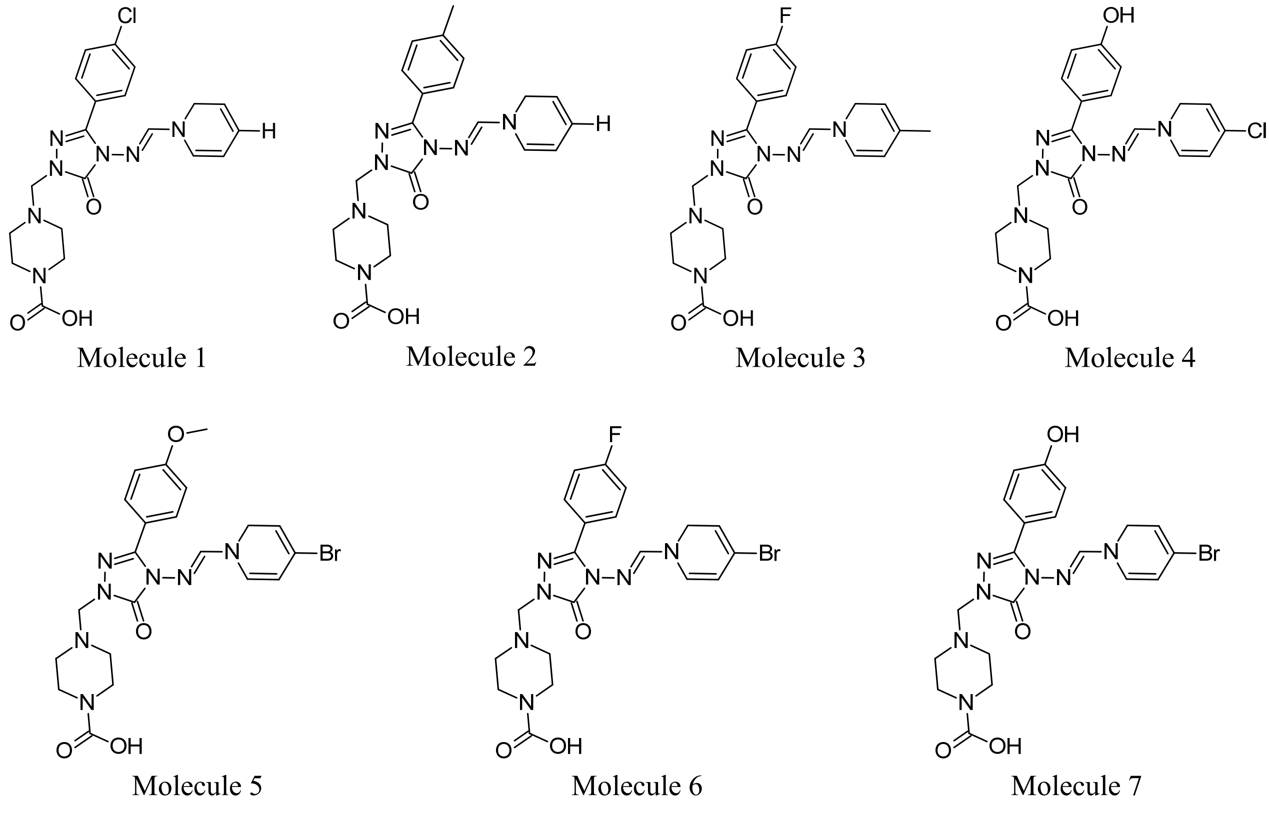
Molecule 1 Molecule 2 Molecule 3 Molecule 4

Molecule 5 Molecule 6 Molecule 7

**Figure 1** – Molecular formulas of studied piperidine-3-carboxamide derivatives

*Computer program used*. In this study, the ADMETlab 3.0 and SwissADME computer programs were used for all calculations. ADMETlab 3.0 is an *in silico* (computer-based) tool used in drug discovery and development processes to predict the ADMET (absorption, distribution, metabolism, excretion, and toxicity) properties of molecules. This platform provides great convenience to researchers in the evaluation of pharmacokinetic and toxicological properties and has been widely used in studies in the literature [13-16]. Among the main features of ADMETlab 3.0, we can say that it has a comprehensive database, uses multiple prediction models, has a user-friendly interface, provides fast and reliable results, and has advanced features. SwissADME is a web-based tool for predicting pharmacokinetic and pharmacodynamic properties of molecules used in drug discovery and development processes. This platform is widely used to assess ADME properties and drug similarity, especially for drug candidate molecules.

*Physicochemical properties*. In the process of discovering a new drug, the physicochemical properties of molecules are critical to the efficacy, safety and pharmacokinetic behavior of the drug candidate. These properties determine how the molecule behaves in the body, how it interacts with the target protein and its potential toxicological risks [17]. From this point, physicochemical properties molecular weight, volume, density, number of heavy atom, number of aromatic heavy atom, number of hydrogen bond acceptors (nHA), number of hydrogen bond donors (nHD), number of rotable bonds (nRot), number of rings (nRing), number of atoms in the biggest ring (MaxRing), number of heteroatoms (nHet), formal charge (fChar), number of rigid bonds (nRig), flexibility, number of stereo centers, topological polar surface area (TPSA), molar recractivity, $sp^3$ hybridization rate (fraction $Csp^3$), the logarithm of aqueous solubility (logS), the logarithm of the n-octanol/water distribution coefficient (logD), acid dissociation constant (pKa), melting point, and boiling point were calculated for all studied molecules. The results obtained (together with the optimal values) are given in Table 1. All data are colored for a better visual understanding of the results. Here, the data obtained are colored green if they are good (in the range of optimal values), orange if they are moderate, and red if they are poor.

*Lipophilicity*. Lipophilicity properties of the molecules were analyzed in detail according to iLOGP (a physics-based technique that uses the generalized-born and solvent accessible surface area (GB/SA) model created by Daina and colleagues to compute the free energies of solvation in n-octanol and water) [18], WLOGP (an atomistic approach based on topological descriptors and fragments) [19], MLOGP (based on topological indices and the linear relationship between structure and logP) [20], XLOGP3 (an atomistic approach that incorporates corrective factors and a knowledge-based library) [21], and SILICOS-IT (a hybrid fragment/topological method that uses seven topological descriptors and 27 fragments) [22]. The data obtained were averaged, and the results were given as consensus log Po/w. The data obtained regarding the lipophilicity property are given in Table 2.

*Water solubility*. Water solubility is examined according to three different methods in SwissADME. These are ESOL [23], Ali [24], and SILICOS-IT [22], respectively. The water solubility of our candidate molecules through these three models were examined. Molecules with high water solubility are generally better absorbed from the gastrointestinal tract and have higher bioavailability, facilitating passive diffusion of molecules across the cell membrane. Water solubility affects the rate of binding of molecules to plasma proteins, the distribution of molecules to different tissues, and the interaction of molecules with metabolic enzymes. Molecules with high water solubility are more easily excreted by the kidneys. Molecules with low water solubility can accumulate in the body and cause toxic effects [25]. The data obtained as a result of the calculations are given in Table 3.

*Absorption properties*. Caco-2 Permeability (Caco-2 permeability is an *in vitro* assay widely used in drug discovery to predict the absorption of drugs from the gut), MDCK Permeability (MDCK permeability refers to an *in vitro* assay used to assess the permeability of drug candidates across cell membranes), PAMPA (Parallel Artificial Membrane Permeability Assay is an *in vitro* assay used to assess the permeability of drug candidates across a synthetic membrane that simulates passive diffusion through biological membranes) [26], Pgp-inhibitor (understanding the role of P-gp inhibitors is crucial for predicting drug absorption, bioavailability and distribution), Pgp-substrat (A P-glycoprotein (P-gp) substrate refers to a drug or compound transported by P-glycoprotein (P-gp), an efflux carrier protein that plays a role in limiting the absorption and bioavailability of certain drugs), human intestinal absorption (HIA, refers to the percentage of an orally administered drug that is absorbed from the human intestine and enters the systemic circulation), $F_{20\%}$ (an $F_{20}$ of 20% means that 20% of the orally administered drug dose is absorbed and enters the bloodstream), $F_{30\%}$ (an $F_{30}$ of 30% means that 30% of the orally administered drug dose is absorbed and enters the bloodstream), and $F_{50\%}$ (an $F_{50}$ of 50% means that 20% of the orally administered drug dose is absorbed and enters the bloodstream) parameters from absorption property were analyzed. The data obtained for absorption properties are given in Table 4.

*Distribution property*. Distribution features plasma protein binding (PPB, describes how much a drug binds to plasma proteins (such as albumin or α1-acid glycoprotein) [27] while in the bloodstream), steady-state volume of distribution (VDss, refers to the theoretical volume that must be evenly distributed for the total amount of drug to result in the same concentration as in steady-state plasma), blood-brain barrier penetration (BBB, refers to the ability of a drug to cross the blood-brain barrier and reach the central nervous system) [28], the fraction unbound in plasms (Fu, refers to the fraction of a drug in the bloodstream that remains unbound to plasma proteins), organic anion transporting polypeptide 1B1 (OATP1B1) inhibitor (it refers to a compound that inhibits the activity of the OATP1B1 transporter), organic anion transporting polypeptide 1B3 (OATP1B3) inhibitor (it refers to a compound that inhibits the activity of the OATP1B3 transporter), breast cancer resistance protein (BCRP) inhibitor (refers to a compound that inhibits the activity of the breast cancer resistance protein transporter) [29], and finally multidrug pesistance protein 1 (MRP1) inhibitor (refers to a compound that inhibits the activity of the protein 1 transporter associated with multidrug resistance) were analyzed. The data obtained for distribution properties are given in Table 5.

*Metabolism property*. As metabolism properties, CYP1A2 inhibitor (refers to a compound that inhibits the activity of the enzyme cytochrome P450 1A2), CYP1A2 substrate (refers to a compound (such as a drug) that is metabolized by the enzyme cytochrome P450 1A2), CYP2C19 inhibitor (refers to a compound that inhibits the activity of the enzyme CYP2C19, which is part of the cytochrome P450 (CYP) enzyme family), CYP2C19 substrate (refers to a drug or compound metabolized by the enzyme CYP2C19, which is part of the cytochrome P450 enzyme family), CYP2C9 inhibitor (refers to a compound that inhibits the activity of the enzyme CYP2C9, which is part of the cytochrome P450 family of enzymes involved in the metabolism of many drugs), CYP2C9 substrate (refers to a compound or drug that is metabolized primarily by the enzyme CYP2C9, a member of the cytochrome P450 enzyme family), CYP2D6 inhibitor (means a compound or drug that inhibits the activity of the enzyme CYP2D6, a member of the cytochrome P450 enzyme family), CYP2D6 substrate (refers to a compound or drug metabolized by the enzyme CYP2D6, which is part of the cytochrome P450 enzyme family), CYP3A4 inhibitor (a substance that slows down or blocks the activity of the enzyme CYP3A4, one of the most important enzymes in the cytochrome P450 family), CYP3A4 substrate (a drug or compound metabolized by the enzyme CYP3A4, one of the most important enzymes in the cytochrome P450 family), CYP2B6 inhibitor (a compound that reduces or blocks the activity of the CYP2B6 enzyme, part of the cytochrome P450 family involved in drug metabolism), CYP2B6 substrate (a compound metabolized by the enzyme CYP2B6, which belongs to the cytochrome P450 family), CYP2C8 inhibitor (is a substance that interferes with the activity of the CYP2C8 enzyme, part of the Cytochrome P450 family involved in drug metabolism), and human liver microsome stability (HLM) stability (an important parameter for assessing metabolic stability) were analyzed. CLplasma, meaning plasma clearance, which is an important parameter in the excretion phase of ADMET studies, and $T_{1/2}$ (half-life), which refers to the time it takes for the concentration of a drug in plasma to decrease by half, were examined within the scope of excretion properties. The data obtained for metabolism and excretion properties are given in Table 6.

**Table 1** – Physicochemical properties (together with the optimal values) of molecules

| **Physicochemical Property** | **Molecule 1** | **Molecule 2** | **Molecule 3** | **Molecule 4** | **Molecule 5** | **Molecule 6** | **Molecule 7** |
|---|---|---|---|---|---|---|---|
| Formula | $C_{20}H_{22}ClN_7O_3$ | $C_{21}H_{25}N_7O_3$ | $C_{21}H_{24}FN_7O_3$ | $C_{20}H_{22}ClN_7O_4$ | $C_{21}H_{24}BrN_7O_4$ | $C_{20}H_{21}BrFN_7O_3$ | $C_{20}H_{22}BrN_7O_4$ |
| Molecular Weight (g/mol, Optimal:100~600) | 443.150 | 423.200 | 441.19 | 459.14 | 517.11 | 505.09 | 503.09 |
| Volume (Å³, Optimal:200 ~ 600) | 415.081 | 417.166 | 423.234 | 423.871 | 445.24 | 425.221 | 427.944 |
| Density (g/cm³, Optimal:1.0 ~ 1.5) | 1.068 | 1.014 | 1.042 | 1.083 | 1.161 | 1.188 | 1.176 |
| N. Heavy Atom (Optimal:20 ~ 70) | 31 | 31 | 32 | 32 | 33 | 32 | 32 |
| N. Aromatic Heavy Atom (Optimal:0 ~ 15) | 11 | 11 | 11 | 11 | 11 | 11 | 11 |
| nHA (Optimal:0 ~ 12) | 10.0 | 10.0 | 10.0 | 11.0 | 11.0 | 10.0 | 11.0 |
| nHD (Optimal:0 ~ 7) | 1.0 | 1.0 | 1.0 | 2.0 | 1.0 | 1.0 | 2.0 |
| nRot (Optimal:0 ~ 11) | 6.0 | 6.0 | 6.0 | 6.0 | 7.0 | 6.0 | 6.0 |
| nRing (Optimal:0 ~ 6) | 4.0 | 4.0 | 4.0 | 4.0 | 4.0 | 4.0 | 4.0 |
| MaxRing (Optimal:0 ~ 18) | 6.0 | 6.0 | 6.0 | 6.0 | 6.0 | 6.0 | 6.0 |
| nHet (Optimal:1 ~ 15) | 11.0 | 10.0 | 11.0 | 12.0 | 12.0 | 12.0 | 12.0 |
| fChar (Optimal:-4 ~ 4) | 0.0 | 0.0 | 0.0 | 0.0 | 0.0 | 0.0 | 0.0 |
| nRig (Optimal:0 ~ 30) | 26.0 | 26.0 | 26.0 | 26.0 | 26.0 | 26.0 | 26.0 |
| Flexibility (nRot /nRig, Optimal:0.1 ~ 0.4) | 0.231 | 0.231 | 0.231 | 0.231 | 0.269 | 0.231 | 0.231 |
| Stereo Centers (Optimal: ≤ 2) | 0.0 | 0.0 | 0.0 | 0.0 | 0.0 | 0.0 | 0.0 |
| TPSA (Å², Optimal:0 ~ 140) | 99.2 | 99.2 | 99.2 | 119.43 | 108.43 | 99.2 | 119.43 |
| Molar Recractivity (cm³/mol, Optimal:40 ~ 130) | 128.63 | 128.59 | 128.38 | 130.44 | 137.98 | 131.45 | 133.51 |
| Fraction Csp³ (Optimal:0.25 ~ 0.65) | 0.30 | 0.33 | 0.33 | 0.30 | 0.33 | 0.30 | 0.30 |
| logS (Optimal -4 ≤ LogS ≤ 0) | -1.773 | -1.928 | -1.966 | -2.278 | -2.137 | -1.824 | -2.378 |
| logD (0 < LogP < 3) | 1.379 | 1.360 | 1.29 | 1.062 | 1.337 | 1.289 | 1.092 |
| pKa (Acid) (Optimal:3 ~ 7) | 3.051 | 3.463 | 3.896 | 3.919 | 4.345 | 3.423 | 4.019 |
| Melting point (°C, Optimal 50 ~ 250) | 192.617 | 189.594 | 199.294 | 201.583 | 193.899 | 199.123 | 201.001 |
| Boiling point (°C, Optimal 150 ~ 400) | 261.529 | 266.401 | 261.321 | 288.841 | 270.879 | 266.124 | 289.524 |

**Table 2** – Lipophilicity properties of molecules

| **Lipophilicity Properties*** | **Molecule** | | | | | | |
|---|---|---|---|---|---|---|---|
| | **1** | **2** | **3** | **4** | **5** | **6** | **7** |
| Log Po/w (iLOGP) | 3.55 | 3.64 | 3.84 | 3.20 | 3.95 | 3.76 | 2.56 |
| Log Po/w (XLOGP3) | -0.17 | -0.44 | -0.79 | -0.81 | -0.42 | -0.29 | -0.75 |
| Log Po/w (WLOGP) | 0.50 | 0.16 | 0.80 | 0.12 | 0.58 | 1.13 | 0.28 |
| Log Po/w (MLOGP) | 3.33 | 3.06 | 3.44 | 2.56 | 2.89 | 3.54 | 2.67 |
| Log Po/w (SILICOS-IT) | -0.47 | -0.59 | -0.19 | -0.96 | -0.39 | -0.02 | -0.93 |
| Consensus Log Po/w | 1.35 | 1.16 | 1.42 | 0.82 | 1.32 | 1.62 | 0.77 |
| Note: *Log Po/w <0: hydrophilic; 0<Log Po/w <3: balanced lipophilicity; 3<Log Po/w <5: high lipophilicity; Log Po/w >5: extremely lipophilic | | | | | | | |

**Table 3** – Water solubility properties of molecules

| **Molecule** | **Water Solubility** | | | | | | | | |
|---|---|---|---|---|---|---|---|---|---|
| | **Log $S_1$** | **Solubility** | **Class** | **Log $S_2$** | **Solubility** | **Class** | **Log $S_3$** | **Solubility** | **Class** |
| **1** | -2.35 | 1.98 mg/mL<br>$4.45.10^{-3}$ mol/L | Soluble | -1.46 | $1.55.10^{1}$ mg/mL<br>$3.48.10^{-2}$ mol/L | Very Soluble | -1.58 | $1.18.10^{1}$ mg/mL<br>$2.65.10^{-2}$ mol/L | Soluble |
| 2 | -2.05 | 3.73 mg/mL<br>$8.81.10^{-3}$ mol/L | Soluble | -1.18 | $2.81.10^{1}$ mg/mL<br>$6.64.10^{-2}$ mol/L | Very Soluble | -1.37 | $1.82.10^{1}$ mg/mL<br>$4.30.10^{-2}$ mol/l | Soluble |
| **3** | 1.94 | 5.10 mg/mL<br>$1.15.10^{-2}$ mol/L | Very Soluble | -0.81 | $6.67.10^{1}$ mg/mL<br>$1.53.10^{-1}$ mol/L | Very Soluble | -1.85 | 6.26 mg/mL<br>$1.42.10^{-2}$ mol/L | Soluble |
| **4** | -2.04 | 4.20 mg/mL<br>$9.13.10^{-3}$ mol/L | Soluble | -1.22 | $2.78.10^{1}$ mg/mL<br>$6.04.10^{-2}$ mol/L | Very Soluble | -1.20 | $2.88.10^{1}$ mg/mL<br>$6.25.10^{-2}$ mol/L | Soluble |
| **5** | -2.57 | 1.38 mg/mL<br>$2.67.10^{-3}$ mol/L | Soluble | -1.39 | $2.10.10^{1}$ mg/mL<br>$4.05.10^{-2}$ mol/L | Very Soluble | -2.80 | 4.33 mg/mL<br>$8.36.10^{-3}$ mol/L | Soluble |
| **6** | -2.65 | 1.12 mg/mL<br>$2.21.10^{-3}$ mol/L | Soluble | -1.33 | $2.35.10^{1}$ mg/mL<br>$4.64.10^{-2}$ mol/L | Very Soluble | -2.24 | 2.89 mg/mL<br>$5.70.10^{-3}$ mol/L | Soluble |
| **7** | -2.35 | 2.24 mg/mL<br>$4.44.10^{-3}$ mol/L | Soluble | -1.28 | $2.64.10^{1}$ mg/mL<br>$5.24.10^{-2}$ mol/L | Very Soluble | -1.39 | $2.05.10^{1}$ mg/mL<br>$4.06.10^{-2}$ mol/L | Soluble |

**Table 4** – Absorption properties of molecules

| Absorption Property | Molecule 1 | Molecule 2 | Molecule 3 | Molecule 4 | Molecule 5 | Molecule 6 | Molecule 7 |
|---|---|---|---|---|---|---|---|
| Caco-2 Permeability<br>(Optimal: higher than Log -5.15) | -5.156 | -5.095 | -5.264 | -5.374 | -5.303 | -5.221 | -5.331 |
| MDCK Permeability<br>(low permeability: $<2.10^{-6}$ cm/s,<br>medium permeability: $2\text{-}20.10^{-6}$ cm/s,<br>high passive permeability: $>20.10^{-6}$ cm/s) | -4.600 | -4.733 | -4.759 | -4.951 | -4.788 | -4.834 | -4.905 |
| PAMPA<br>(log Peff <0, Category 0, low-permeability<br>log Peff >2.5, Category 1, high-permeability) | 0.728 | 0.856 | 0.758 | 0.957 | 0.614 | 0.612 | 0.945 |
| Pgp-inhibitor<br>(Category 1: Inhibitor,<br>Category 0: Non-inhibitor) | 0.003 | 0.003 | 0.004 | 0.000 | 0.001 | 0.007 | 0.000 |
| Pgp-substrate | 0.006 | 0.017 | 0.021 | 0.030 | 0.008 | 0.005 | 0.015 |
| HIA | 0.395 | 0.638 | 0.371 | 0.637 | 0.841 | 0.156 | 0.555 |
| $F_{20\%}$ | 0.600 | 0.920 | 0.732 | 0.953 | 0.767 | 0.244 | 0.897 |
| $F_{30\%}$ | 0.998 | 0.999 | 0.997 | 0.999 | 0.997 | 0.983 | 0.999 |
| $F_{50\%}$ | 0.905 | 0.948 | 0.850 | 0.991 | 0.933 | 0.460 | 0.977 |

**Table 5** – Distribution properties of molecules

| Distribution Property | Molecule 1 | Molecule 2 | Molecule 3 | Molecule 4 | Molecule 5 | Molecule 6 | Molecule 7 |
|---|---|---|---|---|---|---|---|
| PPB | 94.576 | 91.356 | 74.509 | 85.82 | 93.535 | 93.563 | 89.665 |
| VDss | -0.124 | -0.185 | -0.060 | -0.244 | -0.133 | -0.066 | -0.065 |
| BBB | 0.001 | 0.000 | 0.000 | 0.000 | 0.000 | 0.003 | 0.000 |
| Fu | 4.301 | 6.835 | 18.001 | 12.456 | 6.395 | 6.252 | 8.200 |
| OATP1B1 inhibitor | 0.111 | 0.168 | 0.089 | 0.155 | 0.125 | 0.079 | 0.137 |
| OATP1B3 inhibitor | 0.615 | 0.546 | 0.557 | 0.839 | 0.892 | 0.690 | 0.845 |
| BCRP inhibitor | 0.000 | 0.000 | 0.000 | 0.000 | 0.000 | 0.000 | 0.000 |
| MRP1inhibitor | 0.181 | 0.283 | 0.416 | 0.456 | 0.438 | 0.514 | 0.604 |

**Table 6** – Metabolism and excretion properties of molecules

| Metabolism Property | Molecule 1 | Molecule 2 | Molecule 3 | Molecule 4 | Molecule 5 | Molecule 6 | Molecule 7 |
|---|---|---|---|---|---|---|---|
| CYP1A2 inhibitor | 0.000 | 0.000 | 0.000 | 0.000 | 0.000 | 0.000 | 0.000 |
| CYP1A2 substrate | 0.000 | 0.000 | 0.000 | 0.000 | 0.000 | 0.000 | 0.000 |
| CYP2C19 inhibitor | 0.335 | 0.391 | 0.392 | 0.037 | 0.021 | 0.065 | 0.015 |
| CYP2C19 substrate | 0.000 | 0.000 | 0.000 | 0.000 | 0.000 | 0.000 | 0.000 |
| CYP2C9 inhibitor | 0.900 | 0.961 | 0.955 | 0.934 | 0.993 | 0.992 | 0.976 |
| CYP2C9 substrate | 0.188 | 0.032 | 0.016 | 0.001 | 0.002 | 0.001 | 0.000 |
| CYP2D6 inhibitor | 0.000 | 0.000 | 0.004 | 0.000 | 0.000 | 0.001 | 0.001 |
| CYP2D6 substrate | 0.000 | 0.002 | 0.003 | 0.000 | 0.002 | 0.000 | 0.000 |
| CYP3A4 inhibitor | 0.000 | 0.000 | 0.000 | 0.005 | 0.000 | 0.000 | 0.001 |
| CYP3A4 substrate | 0.002 | 0.002 | 0.007 | 0.000 | 0.000 | 0.000 | 0.000 |
| CYP2B6 inhibitor | 0.031 | 0.014 | 0.066 | 0.093 | 0.122 | 0.155 | 0.062 |
| CYP2B6 substrate | 0.000 | 0.000 | 0.000 | 0.000 | 0.000 | 0.000 | 0.000 |
| CYP2C8 inhibitor | 0.985 | 0.793 | 0.950 | 0.946 | 0.996 | 0.992 | 0.996 |
| HLM Stability | 0.064 | 0.116 | 0.681 | 0.171 | 0.258 | 0.061 | 0.080 |
| Excretion Property | | | | | | | |
| $CL_{plasma}$ | 2.944 | 3.367 | 3.170 | 3.391 | 3.498 | 2.516 | 3.366 |
| $T_{1/2}$ | 0.965 | 0.931 | 0.929 | 1.146 | 0.966 | 1.071 | 1.259 |

*Toxicity property*. Toxicity properties, hERG blockers (the hERG gene encoding a potassium ion channel that plays a critical role in the electrical activity of the heart, particularly in the repolarization of the cardiac action potential) [30], hERG Blockers (10 μM), drug-induced liver injury (DILI), AMES mutagenicity (AMES mutagenicity testing helps identify compounds that can cause genetic mutations) [31], rat oral acute toxicity, FDA maximum recommended daily dose [32] (FDAMDD), skin sensitization, Log Kp (cm/s, skin permeation), carcinogenicity (assesses the potential of a compound to cause cancer after long-term exposure), eye corrosion, eye irritation, respiratory, human hep atotoxicity (refers to the toxic effects of a substance on the human liver), drug-induced nephrotoxicity (nephrotoxicity refers to the adverse effects of drugs or their metabolites on kidney function, which can lead to conditions such as acute kidney injury, chronic kidney disease, and even kidney failure in severe cases), ototoxicity (refers to the potential for medicines or chemicals to cause damage to the inner ear, resulting in hearing loss, tinnitus or balance problems), hematotoxicity (refers to the adverse effects of a drug or compound on blood and its components, including red blood cells, white blood cells, platelets and bone marrow cells), genotoxicity, RPMI-8226 immunitoxicity, A549 cytotoxicity, Hek293 cytotoxicity, and drug-induced neurotoxicity were examined. The data obtained for toxicity properties are given in Table 7.

*Environmental toxicity property*. Environmental toxicity properties, bioconcentration factors (it is a critical metric for assessing the potential for a compound to accumulate in biological organisms), inhibition growth concentration 50 ($IGC_{50}$) [33], lethal concentration 50% for freshwater microorganisms ($LC_{50}FM$), and lethal concentration 50% for daphnia magna ($LC_{50}DM$) were analyzed. The data obtained for environmental toxicity properties are given in Table 8.

*Tox21 pathway property*. Tox21 pathway property, NR-AhR (provides valuable information on potential metabolic, immune, endocrine and carcinogenic toxicity), NR-AR (important for assessing endocrine toxicity, reproductive risks and cancer potential), NR-AR-LBD (refers to a specific assay targeting the nuclear receptor pathway for the androgen receptor ligand-binding domain), NR-aromatase (help us detect and understand the interactions between compounds and the aromatase enzyme), NR-ER (helps us understand endocrine disruption and its implications for human health and safety), NR-ER-LBD (interaction of compounds with the ligand binding domain of the estrogen receptor, which plays a crucial role in mediating hormonal responses and signaling pathways helps us understand), NR-PPAR-gamma (identify compounds that interact with the receptor and help predict their effects on metabolism, toxicity and therapeutic potential), SR-ARE (helps to understand how compounds affect cellular oxidative stress and activation of detoxification pathways), SR-ATAD5 (a valuable tool for assessing DNA damage response and repair mechanisms), SR-HSE (helps assess how compounds interact with the cellular heat shock response, a fundamental stress adaptation mechanism), SR-MMP (helps to evaluate the interaction of compounds with matrix metalloproteinases), and SR-p53 (assess how compounds affect the p53 pathway, which plays a central role in regulating the cellular response to DNA damage [34], oxidative stress and other genotoxic insults) were analyzed. The data obtained for Tox21 pathway properties are given in Table 9.

*Medicinal chemistry property*. Lastly, medicinal chemistry properties, quantitative estimate of drug-likeness (QED), globally accessible surface area (GASA), synthetic accessibility score (Synth), the proportion of $sp^3$-hybridized carbon atoms (Fsp3), molecular complexity estimation – 18 (MCE-18), natural product similarity score (NPscore), Lipinski Rule, Ghose Rule, Veber Rule, Egan Rule, Muegge Rule, Pfizer Rule, Glaxo Smith Kline (GSK) Rule, Golden Triangle, pan-assay interference compounds (PAINS), Brenk Rule, antibiotic-like activity related to mechanism nuclear magnetic resonance (ALARM NMR), Bristol-Myers Squibb (BMS), Chelator Rule, colloidal aggregators, firefly luciferase (FLuc) inhibitors, blue fluorescence, green fluorescence, reactive compounds, promiscuous compounds, synthetic accessibility (SA), and leadlikeness were examined in ADMET properties [35,36]. The data obtained for medicinal chemistry properties are given in Table 10.

**Table 7** – Toxicity properties of molecules

| Toxicity Property | Molecule 1 | Molecule 2 | Molecule 3 | Molecule 4 | Molecule 5 | Molecule 6 | Molecule 7 |
|---|---|---|---|---|---|---|---|
| hERG Blockers | 0.099 | 0.058 | 0.066 | 0.030 | 0.053 | 0.050 | 0.036 |
| hERG Blockers (10 μM) | 0.210 | 0.140 | 0.113 | 0.113 | 0.087 | 0.102 | 0.094 |
| DILI | 0.995 | 0.987 | 0.988 | 0.948 | 0.998 | 0.995 | 0.994 |
| AMES Mutagenicity | 0.131 | 0.218 | 0.495 | 0.612 | 0.725 | 0.710 | 0.641 |
| Rat Oral Acute Toxicity | 0.336 | 0.263 | 0.353 | 0.395 | 0.457 | 0.693 | 0.513 |
| FDAMDD | 0.425 | 0.402 | 0.645 | 0.772 | 0.874 | 0.932 | 0.904 |
| Skin Sensitization | 0.204 | 0.186 | 0.261 | 0.685 | 0.599 | 0.576 | 0.795 |
| Log Kp (cm/s, Skin Permeation) | -9.130 | -9.200 | -9.550 | -9.680 | -9.760 | -9.590 | -9.910 |
| Carcinogenicity | 0.528 | 0.596 | 0.888 | 0.813 | 0.961 | 0.959 | 0.945 |
| Eye Corrosion | 0.001 | 0.001 | 0.001 | 0.056 | 0.137 | 0.271 | 0.171 |
| Eye Irritation | 0.146 | 0.357 | 0.295 | 0.755 | 0.867 | 0.893 | 0.938 |
| Respiratory | 0.640 | 0.717 | 0.611 | 0.991 | 0.985 | 0.980 | 0.975 |
| Human Hep atotoxicity | 0.782 | 0.791 | 0.826 | 0.707 | 0.535 | 0.588 | 0.534 |
| Drug-induced Nephrotoxicity | 0.988 | 0.972 | 0.991 | 0.873 | 0.919 | 0.982 | 0.801 |
| Ototoxicity | 0.237 | 0.200 | 0.182 | 0.247 | 0.132 | 0.137 | 0.112 |
| Hematotoxicity | 0.206 | 0.192 | 0.357 | 0.188 | 0.198 | 0.175 | 0.091 |
| Genotoxicity | 1.000 | 1.000 | 1.000 | 1.000 | 1.000 | 1.000 | 1.000 |
| RPMI-8226 Immunitoxicity | 0.018 | 0.021 | 0.023 | 0.028 | 0.039 | 0.029 | 0.024 |
| A549 Cytotoxicity | 0.002 | 0.001 | 0.002 | 0.003 | 0.001 | 0.002 | 0.001 |
| Hek293 Cytotoxicity | 0.072 | 0.024 | 0.059 | 0.114 | 0.060 | 0.072 | 0.121 |
| Drug-induced Neurotoxicity | 0.807 | 0.783 | 0.831 | 0.749 | 0.877 | 0.923 | 0.837 |

**Table 8** – Environmental toxicity properties of molecules

| Environmental Toxicity Property | Molecule 1 | Molecule 2 | Molecule 3 | Molecule 4 | Molecule 5 | Molecule 6 | Molecule 7 |
|---|---|---|---|---|---|---|---|
| Bioconcentration Factors | 0.439 | 0.291 | 0.194 | 0.497 | 0.579 | 0.452 | 0.547 |
| $IGC_{50}$ | 3.134 | 2.946 | 2.862 | 3.200 | 3.294 | 3.128 | 3.267 |
| $LC_{50}FM$ | 3.929 | 3.561 | 3.467 | 3.959 | 4.172 | 3.928 | 4.057 |
| $LC_{50}DM$ | 4.531 | 4.255 | 4.229 | 4.613 | 4.699 | 4.524 | 4.680 |

**Table 9** – Tox21 pathway properties of molecules

| Tox21 Pathway Property | Molecule 1 | Molecule 2 | Molecule 3 | Molecule 4 | Molecule 5 | Molecule 6 | Molecule 7 |
|---|---|---|---|---|---|---|---|
| NR-AhR | 0.011 | 0.010 | 0.004 | 0.010 | 0.007 | 0.003 | 0.009 |
| NR-AR | 0.027 | 0.027 | 0.035 | 0.052 | 0.051 | 0.040 | 0.065 |
| NR-AR-LBD | 0.001 | 0.000 | 0.001 | 0.000 | 0.001 | 0.001 | 0.000 |
| NR-Aromatase | 0.003 | 0.001 | 0.002 | 0.015 | 0.001 | 0.001 | 0.005 |
| NR-ER | 0.025 | 0.029 | 0.011 | 0.427 | 0.009 | 0.004 | 0.180 |
| NR-ER-LBD | 0.001 | 0.000 | 0.000 | 0.018 | 0.000 | 0.000 | 0.004 |
| NR-PPAR-gamma | 0.000 | 0.000 | 0.000 | 0.000 | 0.000 | 0.000 | 0.000 |
| SR-ARE | 0.920 | 0.779 | 0.672 | 0.962 | 0.786 | 0.822 | 0.971 |
| SR-ATAD5 | 0.001 | 0.001 | 0.000 | 0.002 | 0.000 | 0.000 | 0.001 |
| SR-HSE | 0.157 | 0.097 | 0.102 | 0.080 | 0.131 | 0.156 | 0.131 |
| SR-MMP | 0.023 | 0.004 | 0.006 | 0.242 | 0.006 | 0.013 | 0.150 |
| SR-p53 | 0.032 | 0.006 | 0.008 | 0.068 | 0.016 | 0.013 | 0.100 |

**Table 10** – Medicinal chemistry properties of molecules

| Medicinal Chemistry Property | **Molecule 1** | **Molecule 2** | **Molecule 3** | **Molecule 4** | **Molecule 5** | **Molecule 6** | **Molecule 7** |
|---|---|---|---|---|---|---|---|
| QED | 0.558 | 0.577 | 0.560 | 0.512 | 0.460 | 0.492 | 0.469 |
| GASA | 1.000 | 1.000 | 1.000 | 1.000 | 1.000 | 1.000 | 1.000 |
| Synth | 3.000 | 3.000 | 3.000 | 3.000 | 3.000 | 3.000 | 3.000 |
| Fsp$^3$ | 0.300 | 0.333 | 0.333 | 0.300 | 0.333 | 0.300 | 0.300 |
| MCE-18 | 52.462 | 51.857 | 54.214 | 54.846 | 54.214 | 54.846 | 54.846 |
| NPscore | -1.065 | -0.975 | -1.032 | -0.827 | -0.906 | -1.170 | -0.756 |
| Lipinski Rule | 0.000 | 0.000 | 0.000 | 0.000 | 1.000 | 0.000 | 1.000 |
| Ghose Rule | 0.000 | 0.000 | 0.000 | 1.000 | 1.000 | 1.000 | 1.000 |
| Veber Rule | 0.000 | 0.000 | 0.000 | 0.000 | 0.000 | 0.000 | 0.000 |
| Egan Rule | 0.000 | 0.000 | 0.000 | 0.000 | 0.000 | 0.000 | 0.000 |
| Muegge Rule | 0.000 | 0.000 | 0.000 | 0.000 | 0.000 | 0.000 | 0.000 |
| Pfizer Rule | 0.000 | 0.000 | 0.000 | 0.000 | 0.000 | 0.000 | 0.000 |
| GSK Rule | 1.000 | 1.000 | 1.000 | 1.000 | 1.000 | 1.000 | 1.000 |
| Golden Triangle | 0.000 | 0.000 | 0.000 | 0.000 | 1.000 | 1.000 | 1.000 |
| PAINS | 0 alerts | 0 alerts | 0 alerts | 0 alerts | 0 alerts | 0 alerts | 0 alerts |
| Brenk | 2 alerts | 2 alerts | 2 alerts | 2 alerts | 2 alerts | 2 alerts | 2 alerts |
| ALARM NMR | 0 alerts | 0 alerts | 0 alerts | 2 alerts | 2 alerts | 1 alerts | 2 alerts |
| BMS | 0 alerts | 0 alerts | 0 alerts | 0 alerts | 0 alerts | 0 alerts | 0 alerts |
| Chelator Rule | 0 alerts | 0 alerts | 0 alerts | 0 alerts | 0 alerts | 0 alerts | 0 alerts |
| Colloidal aggregators | 0.133 | 0.057 | 0.155 | 0.434 | 0.443 | 0.496 | 0.495 |
| FLuc inhibitors | 0.290 | 0.435 | 0.341 | 0.316 | 0.538 | 0.307 | 0.387 |
| Blue fluorescence | 0.194 | 0.137 | 0.207 | 0.137 | 0.213 | 0.117 | 0.092 |
| Green fluorescence | 0.672 | 0.546 | 0.604 | 0.622 | 0.631 | 0.629 | 0.636 |
| Reactive compounds | 0.004 | 0.002 | 0.001 | 0.005 | 0.004 | 0.004 | 0.007 |
| Promiscuous compounds | 0.039 | 0.028 | 0.004 | 0.025 | 0.001 | 0.001 | 0.006 |
| SA (Synthetic Accessibility) | 4.190 | 4.320 | 4.310 | 4.260 | 4.330 | 4.230 | 4.260 |
| Leadlikeness | 1.000 | 1.000 | 1.000 | 1.000 | 1.000 | 1.000 | 1.000 |

## Result and Discussion

When the physicochemical properties were examined for the seven molecules studied, it was determined that the molar refractivity (MR) values for molecules 4, 5, 6, and 7 were slightly higher than the ideal values and that the molecules met the desired conditions in all other parameters. MR is a measure that reflects the polarizability of a molecule, the volume of the electron cloud, and its steric properties (volumetric size). The hydrophobic interaction potential of the molecule also influences molar refractivity at the point of binding with the target protein. This in turn affects the binding affinity. It also provides indirect information on how far the molecule can diffuse into tissues. For good oral bioavailability, an ideal molar refractivity value in the range $40 \leq MR \leq 130$ is desirable. Since the deviation observed in the MR values for molecules 4, 5, 6, and 7 was very small, all values were considered acceptable. Molar refractivity values of molecules were given Figure 2.

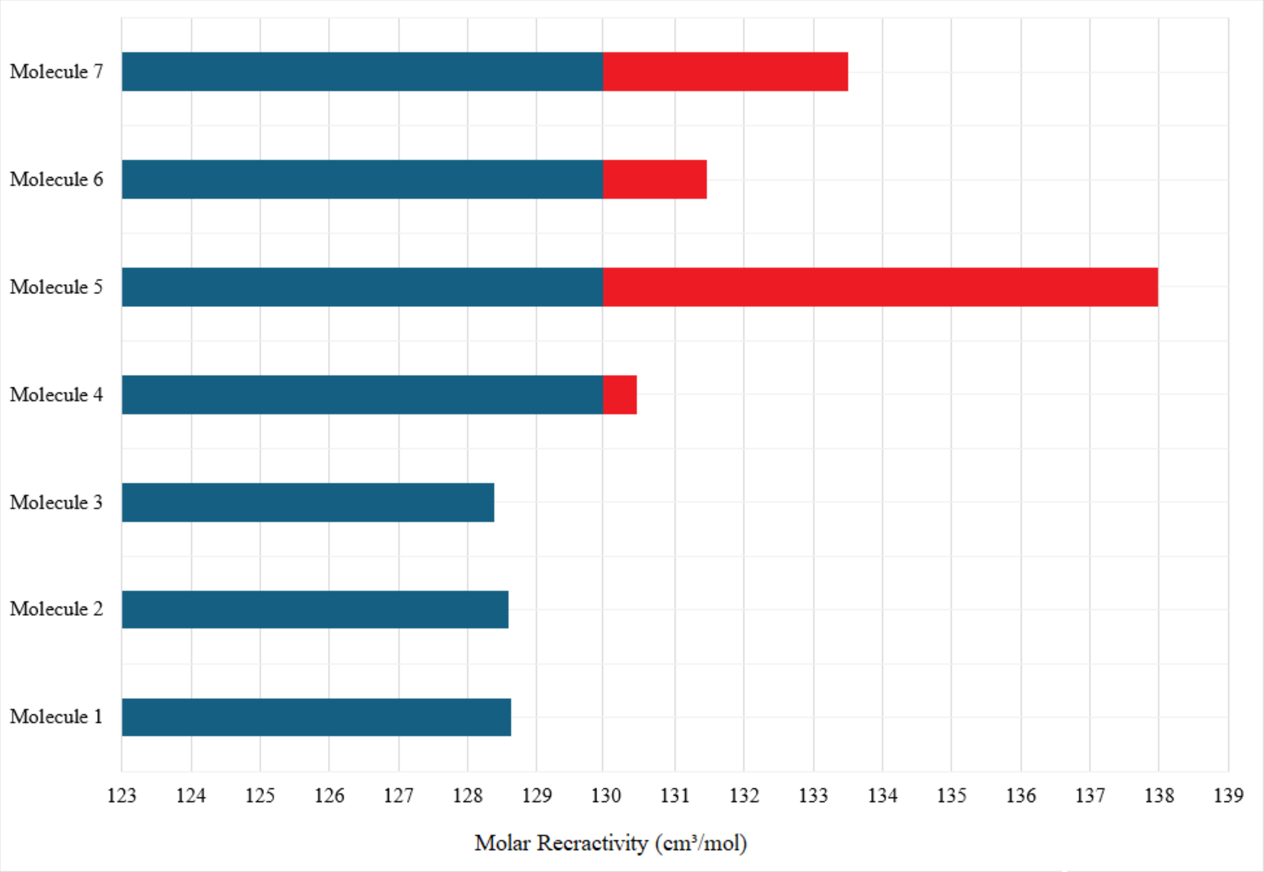

**Figure 2** – Molar refractivity values of molecules

In order for the molecules to show good absorption and solubility potential, a lipophilicity (Log Po/w) value between 0 and 3 is desired. This range is considered the ideal range. This range is especially important for a good oral bioavailability and solubility balance. When the lipophilicity values of our molecules are examined, it is seen that the consensus Log Po/w values of all the molecules studied are within this ideal range. This shows us that all of our molecules can be characterized as suitable molecules in terms of lipophilicity. Lipophilicity values of molecules were given Figure 3.

When the water solubility values calculated according to ESOL, Ali, and SILICOS-IT methods and given in Table 3 were analyzed, it was found that all molecules were soluble. Water solubility plays a critical role in terms of ADME properties. Because water solubility directly affects the absorption, distribution, metabolism, and excretion of a drug candidate molecule in the body. Such that the molecule must be dissolved in water to be absorbed through the digestive tract (GI tract), and highly soluble molecules show rapid and complete absorption. For passage through the cell membrane, molecules must first be dissolved in aqueous media. Even lipophilic compounds cannot be absorbed unless they are slightly dissolved in water. Water-soluble molecules can reach the target tissues by circulating freely in the plasma. The balance of solubility and lipophilicity is critical for central nervous system drugs. Enzymes in the liver (CYP450) have easier access to water-soluble molecules. It determines the half-life of the drug by affecting metabolic stability. High-solubility molecules are more suitable for excretion in urine. The visual representation of these data obtained is given in Figure 4.

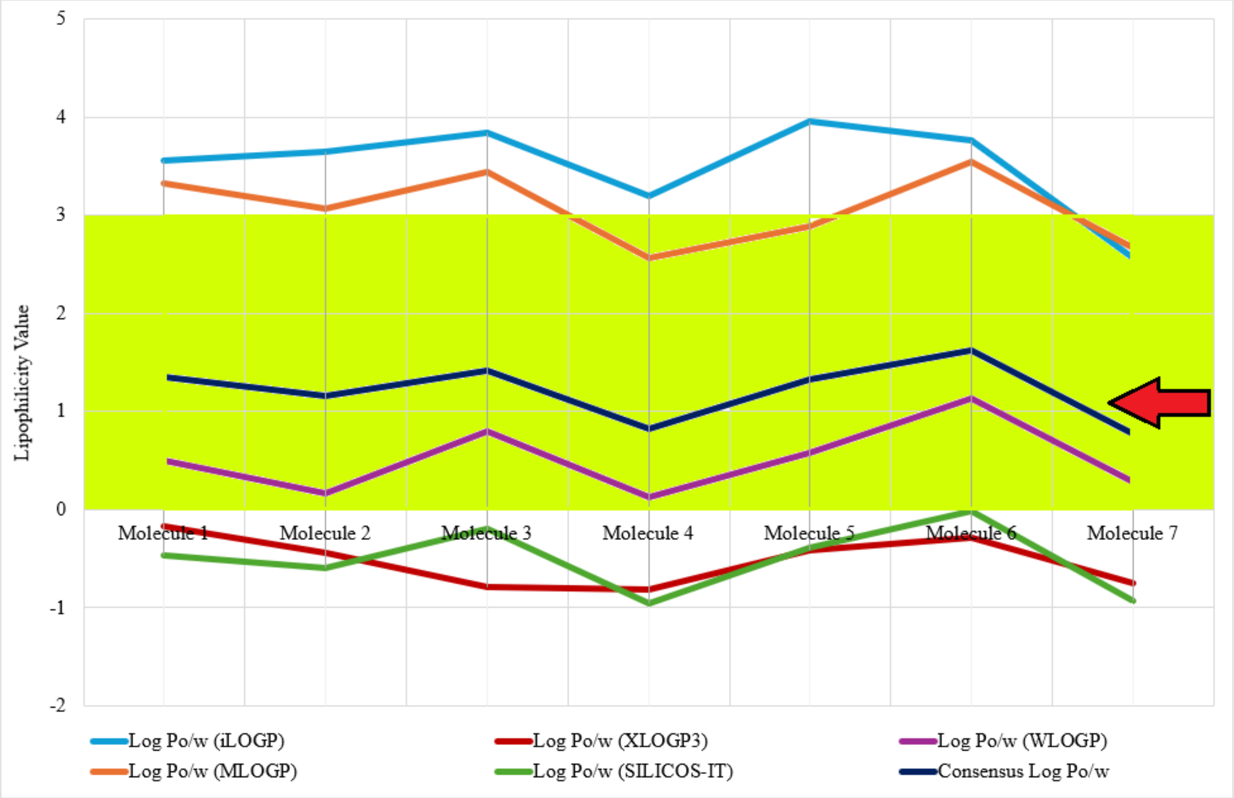

**Figure 3** – Lipophilicity values of molecules

When the absorption properties values of the molecules given in Table 4 were analyzed, it was found that only molecule 2 was ideal in terms of Caco-2 Permeability, no molecule was ideal in terms of MDCK Permeability, and molecule 5 and molecule 6 were found to be evaluable in terms of PAMPA. It was observed that all molecules were ideal in terms of Pgp-inhibitor and Pgp-substrate. In terms of HIA, $F_{20\%}$, $F_{30\%}$, and $F_{50\%}$, the values obtained from molecule 6 were found to have better values compared to other molecules. When the molecules were analyzed in terms of distribution properties, generally good results were obtained in terms of other properties except for VDss property. In terms of metabolism and excretion properties, it was observed that all data except CYP2C9 inhibitor and CYP2C8 inhibitor values were suitable for all molecules studied, and in terms of excretion property, it was observed that the values for CLplasma were very good and $T_{1/2}$ values were partially ideal. In terms of toxicity properties, very good values were obtained for all molecules for hERG Blockers, hERG Blockers (10 μM), rat oral acute toxicity, ototoxicity, hematotoxicity, RPMI-8226 immunotoxicity, skin sensitization, A549 Cytotoxicity, and Hek293 Cytotoxicity. In terms of environmental toxicity properties, ideal results were obtained for all the substances studied. The visual graph of these data is given in Figure 5. In terms of Tox21 pathway properties, good results were obtained for all molecules except SR-ARE.

**Figure 4** – Water solubility values of molecules

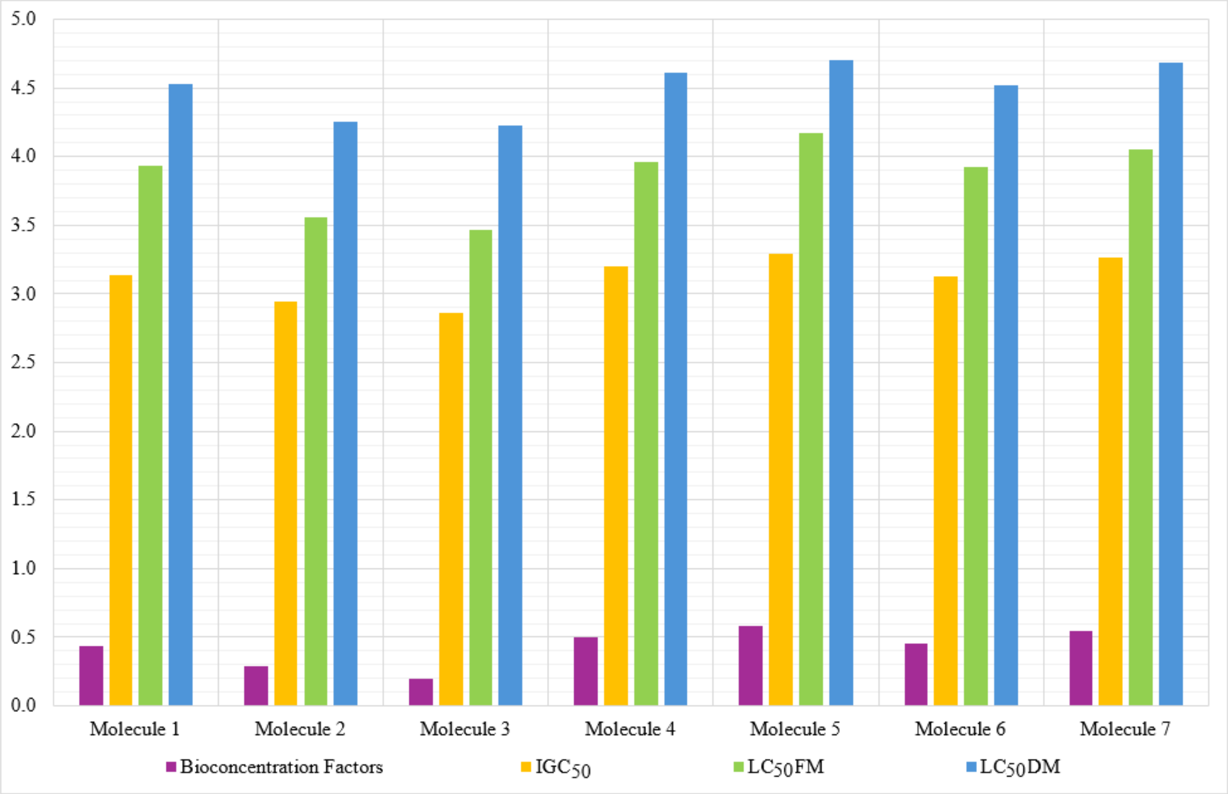

**Figure 5** – Environmental toxicity properties of molecules

Finally, when the medicinal chemistry property values were examined, it was observed that the results obtained for all molecules in terms of Synth, MCE-18, Veber Rule, Egan Rule, Muegge Rule, Pfizer Rule, PAINS, BMS, Chelator Rule, Colloidal Aggregators, FLuc Inhibitors, Blue Fluorescence, Reactive Compounds, Promiscuous Compounds, and SA (Synthetic Accessibility) were very good.

## Conclusion

In this study, it was concluded that molecule 5 ((E)-4-((4-(((4-bromopyridin-1(2H)-yl) methylene) amino)-3-(4-methoxyphenyl)-5-oxo-4,5-dihydro-1H-1,2,4-triazol-1-yl)methyl)piperazi-ne-1-carboxylic acid) can be considered as a drug candidate to be used in the treatment of this disease and advanced studies can be carried out when the physicochemical properties, lipophilicity, water solubility, absorption property, distribution property, metabolism property, toxicity property, environmental toxicity property, tox21 pathway property, and medicinal chemistry properties of seven different substituted-piperidine-3-carboxamide derivatives compounds that can be used in the treatment of Crohn's disease are examined.

## Conflict of interest

The authors declare that they have no conflicts of interest.

## References

1. Beaty W., Katragadda A., Condos R., Dane B., Sarkar S., Shaffer E., Chang S.N. (2024) Pulmonary Crohn's disease masquerading as lymphoma. *ACG Case Rep. J.*, vol. 11, no. 1, pp. 1-3.
2. Hattori Y., Kobayashi K., Katsumata T., Saigenji K., Watanabe M., Okayasu I. (2007) Clinicopathologic features of Crohn's disease with free intestinal perforation. *Hepatogastroenterol.*, vol. 54, no. 73, pp. 135-139.
3. Banjar N.A., Abdulwahab S.A., AlDrees S.E., Binsaeed S.Y., Alajmi N.S., Sardidi H.O., Alsaif M.A., Aldakhil S.S., Aljoufi F.S., Fakieha A.Y., Alfayez L.H., Alshehri G.S., Aldhahri T.M. (2018) Early diagnosıs of Crohn's disease symptoms and management. *Indo Am. J. Pharm. Sci.*, vol 51, no. 12, pp. 16392-16400.
4. Nanau R.M., Neuman M.G. (2012) Metabolome and inflammasome in inflammatory bowel disease. *Transl. Res.*, vol. 160, no. 1, pp. 1-28.
5. Af Björkesten C.G., Jussila A., Kemppainen H., Hallinen T., Soini E., Mankinen P., Valgardsson S., Veckman V., Nissinen R., Naessens D., Molander P. (2019) Relationship of faecal calprotectin and long-term outcomes in finnish patients with Crohn's disease: retrospective multi-centre chart review study. *Scand. J. Gastroenterol.*, vol. 54, no. 10, pp. 1226-1232.
6. Stallmach A., Stallhofer J., Schmidt C., Atreya R., Grunert P.C. (2025) Treatment of severe flares in Crohn's disease and ulcerative colitis. *Inn. Med.*, vol. 66, no. 1, pp. 22-30.
7. Bollegala N., Griller N., Bannerman H., Habal M., Nguyen G.C. (2019) Ultrasound vs endoscopy, surgery, or pathology for the diagnosis of small bowel Crohn's disease and its complications. *Inflamm. Bowel Dis.*, vol. 25, no. 8, pp. 1313-1338.
8. Shaler C.R., Elhenawy W., Coombes B.K. (2019) The onique lifestyle of Crohn's disease-associated adherent-invasive escherichia coli. *J. Mol. Biol.*, vol. 431, no. 16, pp. 2970-2981.
9. Norinder U., Bergström C.A.S. (2006) Prediction of ADMET properties. *ChemMedChem.*, vol. 1, no. 9, pp. 920-937.
10. Daoud N.E.H., Borah P., Deb P.K., Venugopala K.N., Hourani W., Alzweiri M., Bardaweel S.K., Tiwari V. (2021) ADMET profiling in drug discovery and development: perspectives of in silico, in vitro and integrated approaches. *Curr. Drug Metab.*, vol. 22, no. 7, pp. 503-522.
11. Cheng F.X., Li W.H., Liu G.X., Tang Y. (2013) In silico ADMET prediction: recent advances, current challenges and future trends. *Curr. Top. Med. Chem.*, vol. 13, no. 11, pp. 1273-1289.
12. Riley R.J., Kenna J.G. (2004) Cellular models for ADMET predictions and evaluation of drug-drug interactions. *Curr. Opin. Drug Discov. Devel.*, vol. 7, no. 1, pp. 86-99.
13. Elbasyouni A., Prabhu D., Akindoyin E.O., Adebiyi V.G., Aremu B.M., Ilori C.T., Olagookun F.I., Ogunlakin A.D., Adesanya E.O. (2025) In silico-based investigation of the molecular mechanism of Artocarpus communis seed hexane fraction against metabolic syndrome. *J. Mol. Model.*, vol. 31, no. 2, pp. 1-12.
14. Sherefedin U., Belay A., Gudishe K., Kebede A., Kumela A.G., Feyisa T., Mahamud J.H., Fekadu S. (2025) Physicochemical properties and drug likeness of hydroxycinnamic acids and their molecular docking with caffeine and amoxicillin: potential anticancer drugs. *Results Chem.*, vol. 13. pp. 1-15.
15. Popovici L.F., Brinza I., Gatea F., Badea G.I., Vamanu E., Oancea S., Hritcu L. (2025) Enhancement of cognitive benefits and anti-anxiety effects of phytolacca americana fruits in a zebrafish (danio rerio) model of scopolamine-induced memory impairment. *Antioxidants*, vol. 14, no. 1, pp. 1-48.
16. Wang Y.W., Wang L., Li Y.F. (2025) Organophosphorus pesticides management strategies: prohibition and restriction multi-category multi-class models, environmental transformation risks, and special attention list, *Toxics*, vol. 13, no. 1, pp. 1-19.
17. Staneva Y., Iliev I., Georgieva S., Merdjanova A. (2024) In silico prediction of physicochemical properties and drug-likeness of omega-3 fatty acids. *Ovidius Univ. Ann. Chem.*, vol. 35, no. 2, pp. 118-125.

18. Daina A., Michielin O., Zoete V. (2014) iLOGP: A simple, robust, and efficient description of n-octanol/water partition coefficient for drug design using the gb/sa approach. *J. Chem. Inf. Model.*, vol. 54, no. 12, pp. 3284-3301.

19. Wildman S.A., Crippen G.M. (1999) Prediction of physicochemical parameters by atomic contributions. *J. Chem. Inf. Comput. Sci.*, vol. 39, no. 5, pp. 868-873.

20. Moriguchi I., Shuichi H., Liu Q., Nakagome I., Matsushita Y. (1992) Simple method of calculating octanol/water partition coefficient. *Chem. Pharm. Bull.*, vol. 40, no. 1, pp. 127-130.

21. Cheng T., Zhao Y., Li X., Lin F., Xu Y., Zhang X., Li Y., Wang R., Lai L. (2007) Computation of octanol-water partition coefficients by guiding an additive model with knowledge. *J. Chem. Inf. Model.*, vol. 47, no. 6, pp. 2140-2148.

22. Klimoszek D., Jelen M., Dolowy M., Morak-Mlodawska B. (2024) Study of the lipophilicity and ADMET parameters of new anticancer diquinothiazines with pharmacophore substituents. *Pharmaceuticals*, vol. 17, no. 6, pp. 725-745.

23. Delaney J.S. (2004) ESOL: Estimating aqueous solubility directly from molecular structure. *J. Chem. Inf. Comput. Sci.*, vol. 44, no. 3, pp. 1000-1005.

24. Ali J., Camilleri P., Brown M.B., Hutt A.J., Kirton S.B. (2012) Revisiting the general solubility equation: in silico prediction of aqueous solubility incorporating the effect of topographical polar surface area. *J. Chem. Inf. Model.*, vol. 52, no. 2, pp. 420-428.

25. Bhanushali J.S., Dhiman S., Nandi U., Bharate S.S. (2022) Molecular interactions of niclosamide with hydroxyethyl cellulose in binary and ternary amorphous solid dispersions for synergistic enhancement of water solubility and oral pharmacokinetics in rats. *Int. J. Pharm.*, vol. 626, pp. 122-144.

26. Shah P., Jogani V., Mishra P., Mishra A.K., Bagchi T., Misra A. (2007) Modulation of ganciclovir intestinal absorption in presence of absorption enhancers. *J. Pharm. Sci.*, vol. 96, no. 10, pp. 2710-2722.

27. Yang Y.D., Engkvist O., Llinàs A., Chen H.M. (2012) Beyond size, ionization state, and lipophilicity: influence of molecular topology on absorption, distribution, metabolism, excretion, and toxicity for druglike compounds. *J. Med. Chem.*, vol. 55, no. 8, pp. 3667-3677.

28. Maness L.M., Banks W.A., Kastin A.J. (1997) Investigation of blood-brain barrier penetration and central nervous system distribution of peptides and proteins by in vivo autoradiography. *STP Pharma Sci.*, vol. 7, no. 1, pp. 12-16.

29. Maliepaard M., Scheffer G.L., Faneyte I.F., Van Gastelen M.A., Pijnenborg A.C.L.M., Schinkel A.H., Van de Vijver M.J., Scheper R.J., Schellens J.H.M. (2001) Subcellular localization and distribution of the breast cancer resistance protein transporter in normal human tissues. *Cancer Res.*, vol. 61, no. 8, pp. 3458-3464.

30. Braga R.C., Alves, V.M., Silva M.F.B., Muratov E., Fourches D., Liao L.M., Tropsha A., Andrade C.H. (2015) Pred-hERG: A novel web-accessible computational tool for predicting cardiac toxicity. *Mol. Inform.*, vol. 34, no. 10, pp. 698-701.

31. Lynch A.M., Sasaki J.C., Elespuru R., Jacobson-Kram D., Thybaud V., De Boeck M., Aardema M.J., Aubrecht J., Benz R.D., Dertinger S.D., Douglas G.R., White P.A., Escobar P.A., Fornace A., Honma M., Naven R.T., Rusling J.F., Schiestl R.H., Walmsley R.M., Yamamura E., Van Benthem J., Kim J.H. (2011) New and emerging technologies for genetic toxicity testing. *Environ. Mol. Mutagen.*, vol. 52, no. 3, pp. 205-223.

32. Vetsa S., Zhang S., Kay W., Kelkar N., Ghosh A., Alam S., Hoopes P.C., Moshirfar M. (2024) Ocular toxicities of FDA-approved antibody drug conjugates. *Cutan. Ocul. Toxicol.*, vol. 43, no. 4, pp. 316-327.

33. Çankaya N., Kebiroglu M.H., Temüz M.M. (2024) A comprehensive study of experimental and theoretical characterization and in silico toxicity analysis of new molecules. *Drug Chem. Toxicol.*, vol. 47, no. 6, pp. 1226-1240.

34. Parfett C.L., Desaulniers D. (2017) A Tox21 approach to altered epigenetic landscapes: assessing epigenetic toxicity pathways leading to altered gene expression and oncogenic transformation in vitro. *Int. J. Mol. Sci.*, vol. 18, no. 6, pp. 1-76.

35. Scotti L., Scotti M.T. (2019) Studies of ADMET properties in medicinal chemistry – part-I. *Curr. Top. Med. Chem.*, vol. 19, no. 29, pp. 2641-2642.

36. Scotti L., Scotti M.T. (2019) Studies of ADMET properties in medicinal chemistry – part-II, *Curr. Top. Med. Chem.*, vol. 19, no. 29, pp. 2742-2742.

***Information about author:***

*Fatih İslamoğlu – Professor, Faculty of Science and Arts, Department of Chemistry, Recep Tayyip Erdoğan University (Rize, Turkey, e-mail: fatih.islamoglu@erdogan.edu.tr).*

International Journal of Biology and Chemistry 18, № 2 (2025)

IRSTI 53.01.97 https://doi.org/10.26577/IJBCh202518212

A. Niyazbekova[1*], A. Niyazbayeva[2*], N. Dalabayeva[2*],
L. Baytlesova[1], T.A. Shakirov[1], M. Almagambetova[3],
G. Gubaidullina[4], Z. Kanapia[2]

[1]West Kazakhstan Innovation Technology University, Uralsk, Kazakhstan
[2]Al-Farabi Kazakh National University, Almaty, Kazakhstan
[3]Zhangir Khan West Kazakhstan Agrarian Technical University, Uralsk, Kazakhstan
[4]L.N. Gumilyov Eurasian National University, Astana, Kazakhstan
*e-mail: almagulni63@mail.ru, nazgulds81@gmail.com

# The influence of some trivalent metal cations on the structure and corrosion properties of phosphates

**Abstract.** This study presents an investigation into the inhibitory properties of phosphate-based systems used for the protection of metals against corrosion. Various types of phosphates are examined, including ortho-, di-, and cyclophosphates, as well as their interactions with metals in aggressive environments. Special attention is given to the influence of iron modifier ions on the efficiency of corrosion inhibition. The potential of modifying phosphate systems to enhance protective properties is analyzed.

The aim of this research is to study and apply complex inhibitors that provide a high level of protection for steel structures against corrosion. The material used for the investigation is carbon structural steel of ordinary quality, compliant with the European standard S235JR (EN 10025-2). Various inorganic phosphate formulations modified with trivalent iron, aluminum, and lanthanum ions were selected as inhibitors

Shifts in spectral bands were observed, corresponding to the deformation vibrations of hydroxyl groups and Al-O bonds. These shifts suggest interactions between the ionic dopants and the phosphate matrix. Specifically, bands shifted from 735 to 671 cm$^{-1}$. Similarly, the band associated with Al-O interactions changed from 530 to 555 cm$^{-1}$, while the $HPO_4^-$ band shifted from 940 to 979 cm$^{-1}$ in the presence of $Al^{3+}$ ions. Deviations in the vibrational frequencies of Al-O and $HPO_4^-$ indicate changes in chemical bonding and increased reactivity of the inhibitors.

Scanning electron microscopy (SEM) provided high-resolution images and elemental composition of corrosion deposits on the steel surface. The method revealed the distribution of elements: oxygen (36.17%), iron (26.79%), phosphorus (4.72%), as well as minor amounts of sodium (0.78%) and aluminum (1.39%) in corrosion products, and allowed localization of protective layers.

The results of this study demonstrate that modifying phosphates with trivalent iron, aluminum, and lanthanum ions leads to significant changes in their inhibitory properties.

**Keywords:** corrosion, inhibitor, orthophosphates, degree of protection, depth index.

## Introduction

The wide variety of available corrosion inhibitors today does not diminish the relevance of developing new formulations with comprehensive protective properties [1], due to the substantial economic losses caused by corrosion processes and the necessity for effective and cost-efficient solutions to protect industrial equipment [2]. Modification of phosphates using cations from the p- and d-block elements represents a promising approach to creating materials with improved inhibitory properties compared to existing analogs [3]. The incorporation of these ions alters the structure and properties of the phosphates, which in turn affects their protective characteristics. This effect is further influenced by factors such as the pH of the medium, as well as the nature and concentration of the phosphate, helping to determine the conditions under which inhibitors are most effective.

Corrosion of metals is a pressing problem in chemical science. Therefore, it is necessary to use inhibitors to protect metals from corrosion. Phosphate-based systems are used as inhibitors. Phosphates are compounds containing phosphorus. However, phos-

© 2025 al-Farabi Kazakh National University

phates have their own peculiarities in their use as inhibitors.

Phosphate systems can be modified to protect against corrosion. Further research is required to optimize the composition and structure of modified phosphate systems and to study their interaction mechanisms with metal surfaces at the molecular level [4].

Modifying the phosphate matrix with p- and d-block metal cations offers a targeted approach to altering their structure and properties. This is primarily due to differences in the size, charge, and chemical reactivity of these ions [5]. The incorporation of metal ions into the phosphate structure leads to variations in physicochemical characteristics, opening up possibilities for the design of functional materials with tailored properties [6].

The relevance of research in this field stems from the urgent need to address corrosion – a significant economic problem for industry, particularly in the metallurgical sector. The search for effective methods to protect equipment from corrosion damage, especially the development of new corrosion inhibitors, remains a priority research area [7-10].

Despite the wide variety of available corrosion inhibitors, optimizing corrosion protection technologies continues to be a topical issue. This is due to the diversity of service environments and operational conditions throughout the equipment life cycle [11-12]. The development of inhibitors with multifunctional action and resistance to changing environmental factors is therefore a key objective.

Current trends in corrosion protection focus on the following key aspects:

- Conducting in-depth analyses of the corrosion behavior of structural materials in various environments (atmosphere, soils, aqueous media) to develop predictive models and methods for forecasting corrosion resistance.
- Developing effective monitoring and diagnostic systems to assess the condition of corrosion protection in metallic structures under real-world operational conditions.
- Carrying out fundamental and applied research in the areas of electrodeposition and chemical-catalytic deposition of metallic and alloy coatings, including the development of nanostructured coatings using electrochemical techniques.
- Study of passivation and behavior of metallic materials in aqueous solutions of containing corrosion inhibitors. Study of adsorption mechanisms of inhibitors on material surfaces using analytical methods.

Particular attention is currently being paid to the development of environmentally friendly corrosion inhibitors [13, 14], including compounds and complexes derived from catalytic production waste and spent catalysts. Promising examples of such inhibitors include organopolymolybdates, aromatic and aliphatic amines, hydrazides of organic acids, and triazoles containing Zn, Ni, Al, Co ions and their respective salts.

The inhibition mechanism occurs as follows: due to chemisorption, there is an interaction between the d-electrons of iron atoms. Industrial approaches are important in solving corrosion-related problems.

It is necessary to develop new inhibitor compositions with combining chemical and physical methods [15].

## Materials and methods

This study is devoted to investigating the efficiency of complex corrosion inhibitors based on sodium phosphates in aqueous environments. Reagents of analytical grade purity were used for the preparation of phosphate inhibitor solutions. The phosphate compound solutions were prepared using distilled water, with precise weighing of the required amount of each substance to achieve the desired concentration.

The primary components of the inhibitor system included solutions with a concentration of 0.1 mol/L: sodium dihydrogen phosphate ($NaH_2PO_4$), disodium hydrogen phosphate ($Na_2HPO_4$), trisodium phosphate ($Na_3PO_4$), disodium dihydrogen pyrophosphate ($Na_2H_2P_2O_7$), tetrasodium pyrophosphate ($Na_4P_2O_7$), sodium trimetaphosphate ($Na_3P_3O_9$), and sodium hexametaphosphate ($Na_6P_6O_{18}$).

To modify the inhibitor properties and enhance their protective efficiency, trivalent metal ions $Al^{3+}$, $Fe^{3+}$, and $La^{3+}$ were used. Solutions of these trivalent ions were prepared by dissolving the respective metal salts. The concentration of each solution was 0.1 mol/L. All solutions were prepared using pure distilled water and filtered prior to use to eliminate possible impurities.

The selection of $Al^{3+}$, $Fe^{3+}$, and $La^{3+}$ as modifying ions was based on their structural characteristics and high complexation ability. Trivalent cations exhibit high reactivity, which facilitates their incorporation into the crystalline structure of phosphate compounds. The introduction of a trivalent ion provides charge compensation for the phosphate anion ($P^{5+}$), stabilizes the phosphate matrix structure, and consequently enhances the protective properties of the resulting inhibitor coating.

Corrosion tests were conducted in accordance with the procedures specified by state standards [16], using steel samples of the following chemical composition (wt.%): Fe – 98.36; C – 0.2; Mn – 0.5; Si – 0.15; P – 0.04; S – 0.05; Cr – 0.3; Ni – 0.2; Cu – 0.2 [12]. This steel grade was selected due to its widespread use in corrosion studies and its relatively simple chemical structure, which facilitates the analysis of its behavior in aggressive environments.

Work method: First, the steel samples were ground and polished to a smooth surface. The grinding was done using abrasive discs with grit sizes of 220, 500 and 1200. Then, they were polished with a polishing paste. After polishing, the samples were degreased using organic solvents (acetone or ethanol). All traces of oil and contaminants were removed. Thus, they were cleaned of impurities. The experiments were conducted at a constant temperature of 25±2°C. The volume of the solution in each test tube or container was 500 ml. All solutions were mixed using magnetic stirrers. The duration of the experiments ranged from 24 to 480 hours.

To evaluate the corrosion behavior of the material, the following methods were applied: gravimetric analysis to determine the corrosion rate based on the mass loss of the specimens; photocolorimetric analysis to determine the concentration of iron ions ($Fe^{3+}$) in the corrosive medium using the reaction with potassium thiocyanate [17, 18] potentiometric analysis for measuring the pH of aggressive environments using a combined glass electrode and ionomer.

Infrared (IR) spectroscopy for the identification of functional groups and compounds present in the corrosion products were employed in order to analyze the composition and structure of corrosion deposits. The deposit samples were dried and placed into a spectrometer, where the absorption spectrum was measured in the range of 4000–400 $cm^{-1}$; scanning electron microscopy (SEM) was used to visualize the morphology and microstructure of the corrosion deposits. The samples were examined at high resolution, which allowed the identification of specific features in the shape and distribution of corrosion products on the specimen surfaces.

Quantitative characteristics of corrosion processes were calculated using standard formulas. The uncertainty of measurements was assessed using Student's *t*-test at a confidence level of 0.95 [19].

The phosphorus(V) oxide ($P_2O_5$) content was determined by a photocolorimetric method based on the formation of a colored phosphovanadomolybdate complex. The optical density of the complex solution was measured using a photocolorimeter. This method allows for the determination of $P_2O_5$ content in complex matrices. The relative error of the determination was ±1%, and the color stability of the complex was maintained for several hours. The analysis was performed in accordance with standard methodology [20].

Thus, this study is based on the use of modern analytical methods to obtain reliable data on the corrosion behavior of materials in aggressive media and the effectiveness of phosphate inhibitors, enabling precise and objective evaluation of their protective performance.

## Results and discussion

Studies of the inhibitory ability of multicomponent orthophosphate systems

The study of the inhibitive efficiency of multicomponent phosphate systems involved the creation of 27 different systems containing phosphate compounds. During the experimental work, potentiometric and photocolorimetric analyses were carried out, enabling the assessment of the concentrations of modifying ions, iron, and phosphate ions in the solution, as well as their influence on corrosion processes. The concentration of modifier ions, iron and phosphate ions in the solution, as well as their effect on corrosion processes.

Figure 1 illustrates the dependence of the modifier ion concentration on the content of aluminum, iron, and phosphates when disodium hydrogen phosphate was replaced. In the initial stages of the experiment, a gradual transition of iron from the metal plate into the solution occurred in the form of ions. The amount of iron in the aqueous medium decreases. The concentrations of both modifier ions and phosphate ions decrease [21].

Figure 2 illustrates the dependence of the corrosion rate on the nature of the modifying ions at various component ratios in the system containing disodium hydrogen phosphate. The lowest corrosion rate was observed in the composition with disodium hydrogen phosphate at a 3:1 ratio in the presence of aluminum ions. The protection efficiency reached 79.14%. The inhibitive effect is attributed to the formation of complex aluminum hydroxyphosphate compounds, which create a protective film on the metal surface [22].

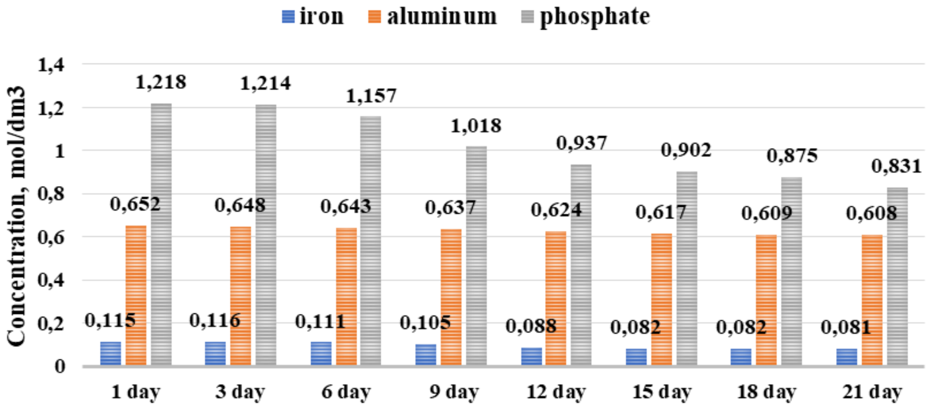

**Figure 1 –** Dynamics of the concentration of lanthanum, iron, and phosphate ions in the sodium hydrophosphate system

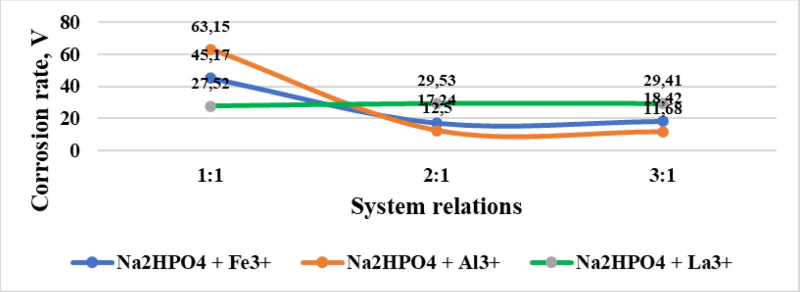

**Figure 2 –** The effect of the nature of modifier ions on the corrosion rate in the sodium hydrophosphate system of different ratios

Systems containing aluminum exhibited a clear trend: the higher the phosphate content, the lower the corrosion rate. This correlates with the formation of hydroxyphosphate compounds in an alkaline environment. These compounds provide a high degree of corrosion protection, as confirmed by both thermodynamic and kinetic data. The stability of hydroxyphosphate compounds is greatest at pH 7.0, which corresponds with our experimental observations. These compounds possess high reactivity and show little tendency to form undesirable by-products.

Monosodium phosphate, due to its amphoteric properties and its ability to effectively accept and donate protons, becomes more negatively charged. This contributes to a more pronounced shift of pH toward the alkaline range as protons participate in hydrolysis reactions, thereby enhancing its inhibitive effect.

Thus, the findings confirm that hydroxyphosphate compounds formed with aluminum-modifying ions provide the highest level of protection among all orthophosphate-based systems. These results are consistent with the literature and confirm the reliability and effectiveness of these compounds in oxidation and corrosion prevention.

For iron-containing systems, the highest corrosion rate was observed at a 1:1 ratio. At other ratios, the corrosion rate remained approximately the same. In systems with lanthanum ions, the corrosion rate varied depending on concentration. The study revealed that the inhibitive performance of phosphate compounds is also strongly dependent on the pH of the corrosive environment: with increasing pH, the anticorrosive activity of phosphates toward iron and its alloys increases [23].

It is also noteworthy that a comprehensive quantitative assessment of the corrosion process parameters was carried out, including kinetic, chemical, physicochemical, thermodynamic characteristics, and anticorrosion efficiency.

To study the composition of the corrosion deposits, analysis was performed using an IR spectrometer (Figure 3). For this analysis, only those corrosion deposits exhibiting the highest protective efficiency were selected.

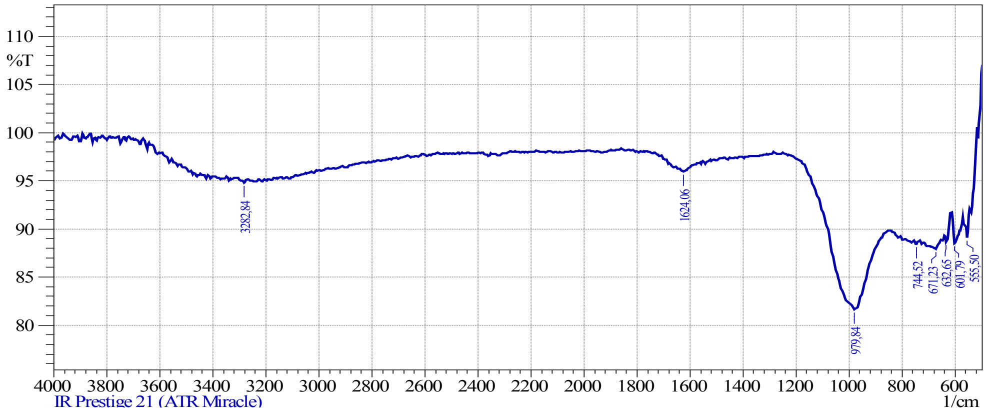

**Figure 3** – IR spectrum of corrosion products formed in the system of sodium hydrophosphate with aluminum (ratio 3:1)

Researchers [24] have shown that disodium hydrogen phosphate is characterized by absorption bands in the 1235-1215 cm⁻¹ range, which are attributed to the asymmetric stretching vibrations of phosphorus–oxygen bonds ν(P=O). In the same spectral region, a band corresponding to the symmetric stretching vibrations of the phosphorus–oxygen bonds ν(P=O) is observed, with a maximum absorption at 1130 cm⁻¹.

The bands in the range of 955-940 cm⁻¹ indicate the presence of phosphate residues. These are phosphorus-oxygen-phosphorus bonds ν(P–O–P). In addition, the symmetric vibrations of the phosphate residues are visible at 1130 cm⁻¹.

Analysis of the IR spectra showed that the corrosion spectrum was significantly different from that of sodium hydrogen phosphate. This suggests that new chemical compounds may be formed during the corrosion process.

According to the results, it can be seen that the corrosion process differs depending on the composition of the initial disodium hydrogen phosphate. This can be explained by the complexity of the chemical interactions, and further studies are needed to accurately determine the composition.

The analysis of the corrosion deposits was also conducted using a JOOL JSM-6490 LV low-vacuum scanning electron microscope (manufactured in Japan). The results of this analysis are presented in Figure 4.

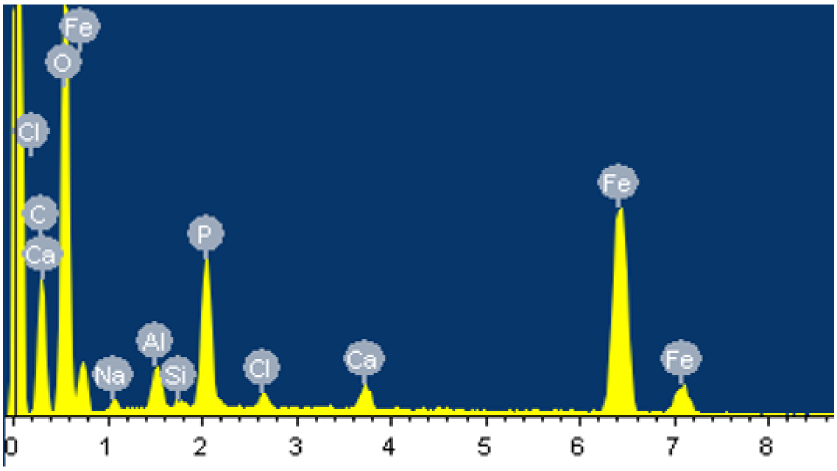

**Figure 4** – Elemental composition of corrosion products formed in the system o f sodium hydrophosphate with aluminum (ratio 3:1)

The primary elemental composition of the corrosion deposits formed in the sodium hydrogen phosphate–aluminum system at a 3:1 ratio (Figure 4) is as follows: oxygen (O): 36.17%, iron (Fe): 26.79%, phosphorus (P): 4.72%, sodium (Na): 0.78%, and aluminum (Al): 1.39%. The composition of the corrosion deposits indicates the formation of iron oxides and hydroxides, as well as phosphate compounds, which confirms the effectiveness of this system in corrosion protection.

From these results, it can be seen that phosphate-based inhibitors are more effective.

*The Study of the inhibitory ability of diphosphate systems*

A multicomponent system study was conducted for 18 systems. Figure 5 presents their results.

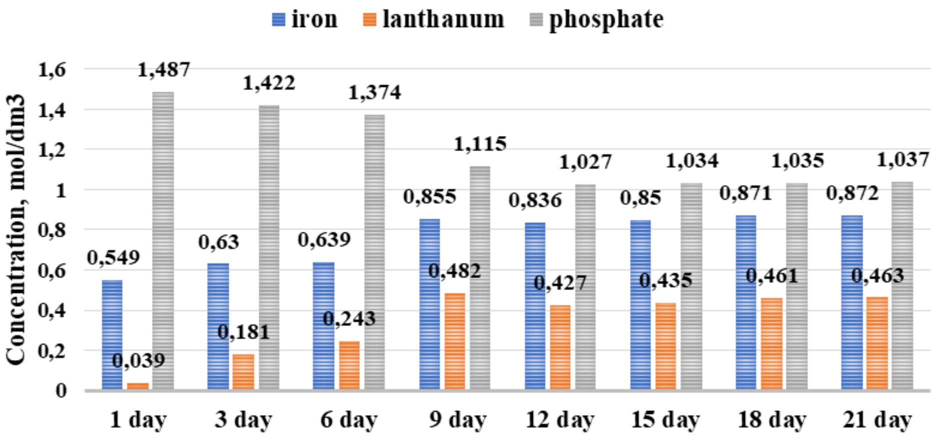

**Figure 5 –** Dependence of the change in the concentration of the lanthanum, iron, and phosphate modifier ion on time for disodium dihydrogen diphosphate

Nevertheless, the inhibition efficiency of the system reached 8.43%, the highest value among the 18 diphosphate systems studied.

The variation in corrosion rate depending on the component ratios in the disodium dihydrogen diphosphate system with modifier ions is presented in Figure 6. The effect of iron ions on the corrosion rate revealed a complex dependence on phosphate concentration.

A decrease in the corrosion rate is observed with an increase in phosphate concentration at a phosphate ratio of 2:1. This is due to the formation of protective phosphate layers. However, the opposite effect was observed at a ratio of 3:1. This is due to a change in the composition and properties of the resulting compounds.

For the system containing aluminum and lanthanum ions, an increase in corrosion rate was observed with rising phosphate concentrations. This may indicate the formation of soluble complexes or a disruption of the passivating effect of oxide films.

According to the literature [25], a distinctive feature of diphosphate ions in aqueous solutions is their lower stability compared to orthophosphates, which may explain their less pronounced protective effect.

Studies indicate that diphosphates tend to form soluble complex compounds such as Me $[Me_2(P_2O_7)_2]$, which remain stable in mildly acidic environments with pH values ranging from 3 to 5, thereby influencing the corrosion equilibrium. Overall, the presence of diphosphates promotes the formation of stable compounds, which contributes to a decrease in the corrosion rate.

Figure 7 shows a spectrogram of corrosion deposits revealing the presence of bands corresponding to different vibrational modes of the phosphate groups. This is a disodium dihydrogen diphosphate system with a lanthanum ion modifier in a 1:1 ratio.

According to the literature, bands in the region of 1270 $cm^{-1}$ correspond to asymmetric vibrations ν(P=O), while bands in the region of 1092–990 $cm^{-1}$ correspond to symmetric vibrations ν(P=O). Peaks at 884 $cm^{-1}$ and 792–595 $cm^{-1}$ are indicative of asymmetric and symmetric ν(P–O–P) vibrations, respectively. The presence of peaks in the ranges of 1030–980 $cm^{-1}$ and 1620 $cm^{-1}$ on the spectrogram of the corrosion precipitate confirms the formation of unstable compounds.

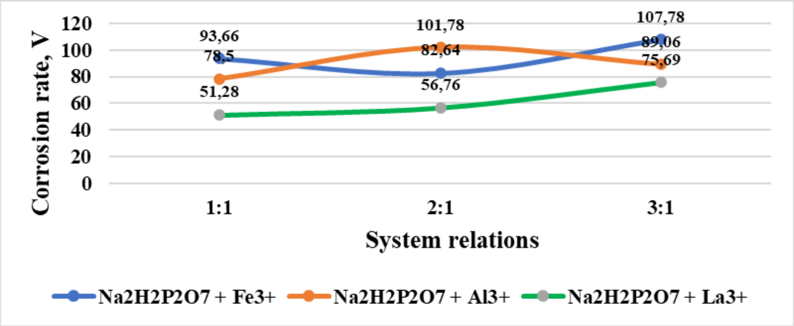

**Figure 6 –** Dependence of disodium dihydrogen phosphate in different ratios on the nature of the modifier ion

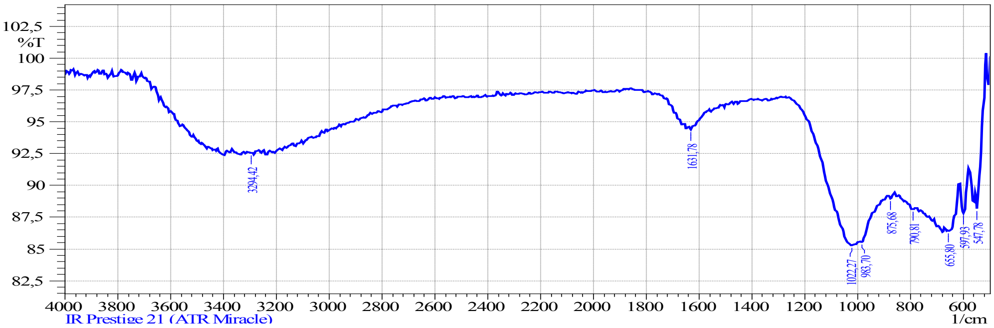

**Figure 7 –** Spectrogram of corrosion deposition of a composition of disodium dihydrogen diphosphate with lanthanum in a 1:1 ratio

Elemental analysis of the corrosion deposits performed using a scanning electron microscope (Figure 8) revealed that the deposits in this system contain 46.58% oxygen, 13.36% iron, and 7.92% phosphorus, along with trace amounts of sodium (0.44%).

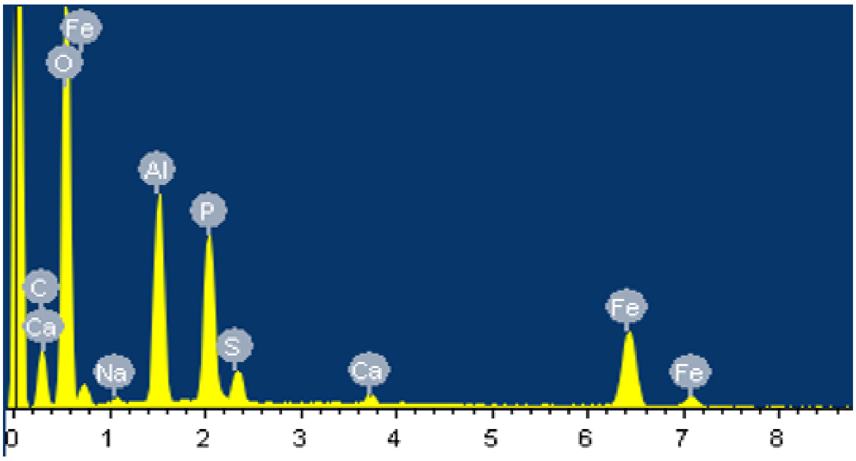

**Figure 8** – Elemental composition of corrosion products formed in the disodium hydrophosphate-lanthanum system (1:1 ratio), according to spectroscopy data

The obtained results indicate a complex mechanism of the inhibitory action of diphosphate systems on iron corrosion. Despite the limited stability of the resulting compounds, further research is required to optimize the composition and structure of diphosphate systems in order to enhance their protective properties and stabilize the resulting corrosion deposits.

*Studies of the inhibitory ability of cyclophosphate multicomponent systems*

In addition to orthophosphate and diphosphate compositions, 18 cyclophosphate systems exhibiting inhibitory activity were also investigated. The most pronounced inhibitory effect was demonstrated by the sodium trimetaphosphate system with the lanthanum ion modifier at a 3:1 ratio (Figure 9). The inhibition efficiency was 45.86%.

The dynamics of ion concentrations (Figure 9) revealed an increase in iron concentration and decrease in the concentration of lanthanum and phosphate ions.

On the ninth day, the concentration of iron and the concentration of lanthanum and phosphate ions continued to decrease. This indicates the formation of complex compounds that slow down the corrosion process.

As in the case of diphosphates, for cyclophosphate systems in the presence of iron ions, an increase in phosphate concentration at a 2:1 ratio leads to a reduction in the corrosion rate. However, at a 3:1 ratio, an increase in the corrosion rate is observed.

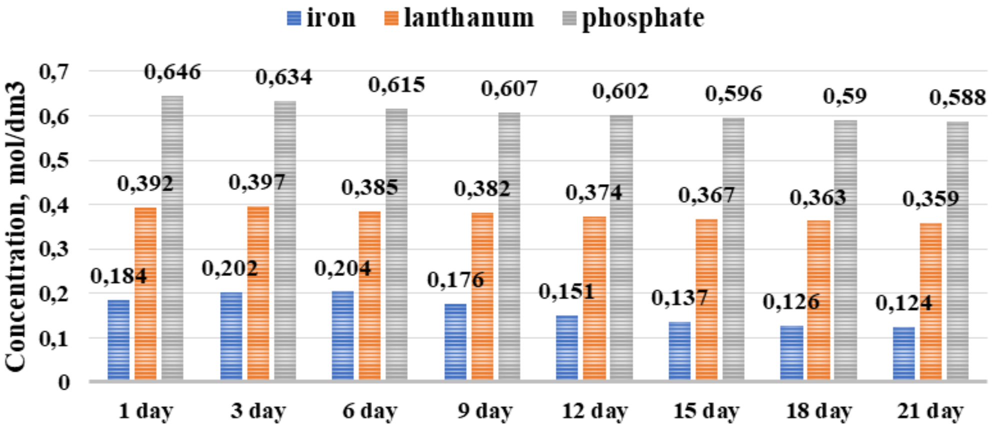

**Figure 9 –** Dynamics of the concentration of lanthanum, iron, and phosphate ions in the sodium trimetaphosphate system

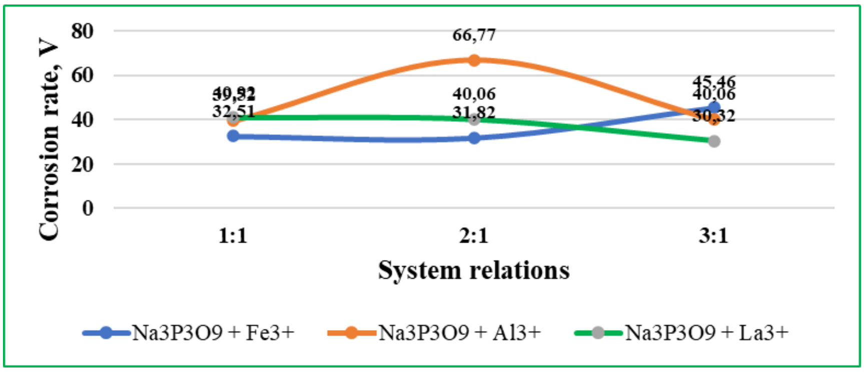

**Figure 10 –** Dependence of the corrosion rate on the nature of the modifier ion at different ratios for sodium trimetahosphate

For the system containing aluminum ions, an inverse dependence is observed, while for the system with lanthanum, a gradual decrease in the corrosion rate is recorded with an increase in phosphate concentration.

The analysis of the IR spectrum of corrosion products for the sodium trimetaphosphate system with lanthanum does not correspond to the previously described spectra, suggesting the formation of a new compound responsible for creating a protective film.

Figure 12 shows the analysis of corrosion deposits using a scanning electron microscope. The results revealed $O_2$ (36.97%), Fe (28.68%), and P (5.24%), as well as small amounts of Na and C.

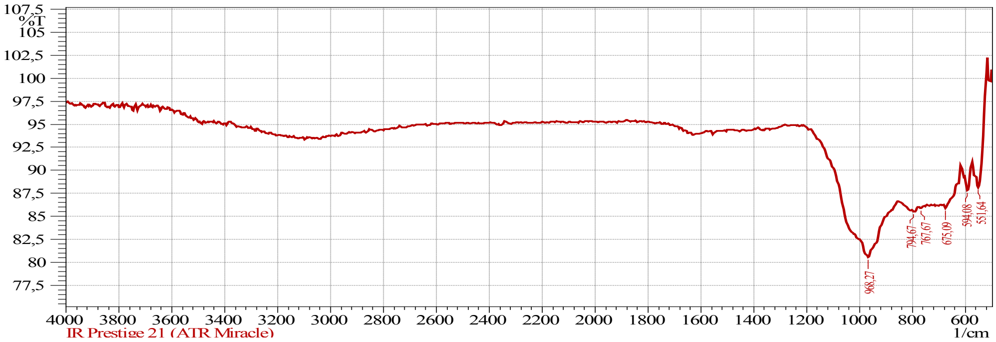

**Figure 11** – IR spectrum of corrosion products formed in the system of sodium trimetaphosphate with lanthanum (ratio 3:1)

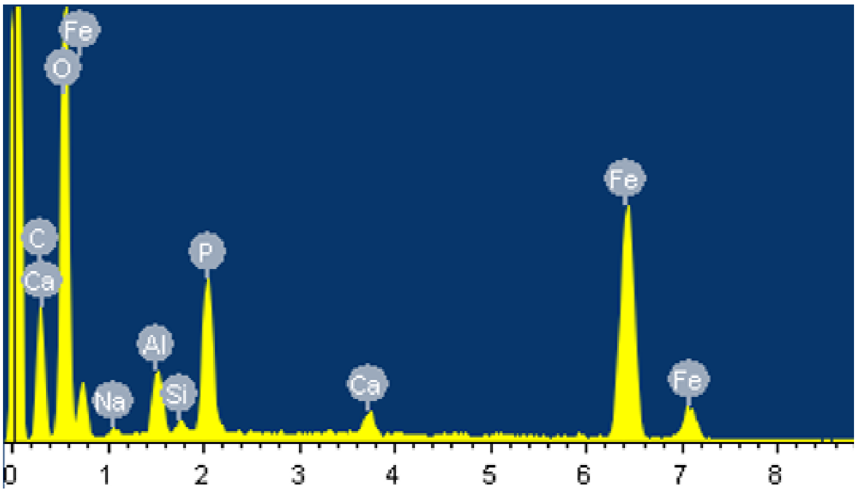

**Figure 12** – Elemental composition of corrosion products formed in the system of sodium trimetaphosphate with lanthanum (ratio 3:1), according to spectroscopy data

It should be noted that the inhibitory capacity of phosphates is observed only up to a certain concentration, beyond which their activity begins to decline. Specifically, for $Na_2HPO_4$, the maximum protective effect is achieved at a concentration of 0.05 mol/dm³.

Diphosphate systems are characterized by weaker protective activity, which is attributed to their lower stability in aqueous solutions and their tendency to form soluble protonated complexes that promote metal dissolution.

Diphosphates and cyclophosphates, unlike orthophosphates, have a stimulating effect on the corrosion process. Among cyclophosphate systems, trimetaphosphates have the highest protective properties. These systems reduce the corrosion rate. They are able to form polyphosphate compounds that inhibit the diffusion of oxygen to the metal surface. Aluminum, lanthanum, and iron ions also significantly enhance the protective functions of phosphate systems. The difference in the protective activity of lanthanum, iron, and aluminum ions is explained by the peculiarities of their structure and electronic configuration. The effect of these ions on the pH increases the thermodynamic stability of the system. Prevents the diffusion of corrosive agents. Promotes the formation of protective hydroxyphosphate compounds. Modification with aluminum ions has protective properties in phosphate systems. Aluminum ions react quickly and form stable complexes with hydroxyphosphates. This contributes to the formation of a strong protective film on the metal surface. The results obtained indicate that multicomponent phosphate systems are effective in the production of corrosion inhibitors. Phosphate systems are effective inhibitors of metal corrosion. They are environmentally friendly and affordable. However, they have limitations in certain situations. By modifying phosphate systems, their protective properties can be increased.

## Conclusion

Regularities based on experimental research. Analysis of the obtained data allows the formulation of the following conclusions:

1. Influence of the nature of phosphate anions on the pH of the medium and the kinetics of corrosion processes. The investigation of the effect of various phosphate anions on the corrosion behavior of metals revealed the following descending order of inhibitory activity, as determined by the degree of pH shift and the reduction in corrosion rate:

$$Na_2HPO_4 > Na_3P_3O_9 > Na_6P_6O_{18} > \\ > NaH_2PO_4 > Na_4P_2O_7 > Na_3PO_4$$

Results from potentiometric, photocolorimetric, and kinetic studies demonstrate that hydroorthophosphate anions, which exhibit amphoteric properties, are the most effective in shifting the pH of the medium toward the alkaline range. This effect is attributed to the ability of these anions to undergo protonation and deprotonation. In the mildly alkaline medium (pH 7.46-9.23) created by hydroorthophosphate, intensified interaction with the metal surface is observed, which in turn contributes to the deceleration of the corrosion process.

2. Influence of phosphate concentration on corrosion rate. A correlation between the inhibitory efficiency of phosphates and their concentration in solution has been established. The highest protective efficiency is exhibited by systems containing $Na_2HPO_4$. Phosphate anions of higher order (e.g., diphosphates and hexaphosphates) demonstrate weaker inhibitory properties. It is assumed that this is due to the formation of excessive phosphate deposits on the metal surface, leading to the development of a non-uniform and brittle protective film. Increasing phosphate concentration may promote decomposition of system components and disturb the acid-base equilibrium, thereby negatively impacting corrosion processes.

3. Influence of the nature of modifier ions on the corrosion rate. Studies have shown that systems modified with aluminum ions exhibit the greatest inhibitory effect. The descending order of inhibitory activity of the modifier ions is as follows:

$$Al^{3+}>Fe^{3+}>La^{3+}$$

The best protective performance was demonstrated by multicomponent systems modified with aluminum ions. This is attributed to the high reactivity of $Al^{3+}$ ions and their ability to form stable complexes that stabilize the protective films.

4. Advantages of hydroxyphosphate systems modified with aluminum ions.Systems modified with aluminum ions are characterized by several advantages, including the absence of undesirable side reactions, which increases their safety and effectiveness as corrosion inhibitors. The shift of the pH into the mildly alkaline range (approximately 7.5-9.0) enhances the corrosion resistance of metals and alloys, thereby reinforcing the inhibitory properties of phosphate systems. The obtained data indicate a high degree of material protection, as confirmed by low corrosion depth indicators (level 4), and underscore the effectiveness of these systems in preventing corrosion processes.

Systems modified with aluminum ions are characterized by the absence of adverse side reactions. They increase the corrosion resistance of metals and alloys in alkaline pH environments (approximately 7.5-9.0). At the same time, the inhibitory properties of phosphate systems are enhanced. The results obtained indicate a high level of material protection.

## Acknowledgments

The authors express their sincere gratitude to Galina Seitmagzimova, a head of the Department of Technology of Inorganic and Petrochemical Substances at South Kazakhstan State University, and colleagues of the Department for their assistance in conducting physico-chemical research in particular when performing corrosion tests, as well as for the opportunity to use SEM and ICS equipment. Their professional support and valuable advice have made a significant contribution to obtaining and interpreting the experimental data presented in this paper.

## Conflict of interest

The authors declare that they have no conflicts of interest.

## References

1. Rozenfield I.L. (1977) Ingibitory corrozi metallov [Metal corrosion inhibitors]. Moscow: Himia, 352 p.
2. Klinov I.Y. (1967) Corrozya himicheskoy apparatury I corrozinostiykie materiali [Corrosion of chemical equipment and corrosion-resistant materials]. Moscow: Mashinastroyenie, 468 p.
3. Vinogradova S.S., Tasieva R.F., Haydrikov R.A. (2014) Vzaimosvyazi kharakteristiki pittingivoy corrozii pri imitasionnom modelirovanii [Relationships between pitting corrosion characteristics in simulation modeling]. *Almanah sovremennoi nauki i obrazovaniya* [*Almanac of Modern Science and Education*], Tambov, vol. 5-6, no. 84, pp. 39-41.
4. Bebikh G.F. (2006) Nekotorie aspecti deystvia ingibitorov corrosii metallov v mnogofasnykh systemakh. *Corrosia. Materialy, Zashita* [Some aspects of the action of metal corrosion inhibitors in multi-faceted systems. *Corrosion. Materials, Protection*], pp.29-35.
5. Makasheva G.R. (1998) Nauchnye osnovyi prognozirovaniya uslovii synreza, gidroliticheskoy ustoychivosti I modifisirovania lineynyh phosphatov s-elementov. [Scientific principles for predicting the conditions of synthesis, hydrolytic stability and modification of linear s-element phosphates]. Abstract of the dissertation of a Doctor of Technical Sciences. 02.00.01 – Inorganic Chemistry. Almaty, 226 p.
6. Kuanisheva G.S., Makasheva G.R. (1996) Syntez mnogokomponentnykh phosphatnykh polymerov I ikh physico-khimicheskie svoistva [Synthesis of multicomponent phosphate polymers and their physical-chemical properties]. Almaty: Dayir, 224 p.
7. Khaydarova G.R., Tyisenkov A.S., Bugai D.E., et al. (2018) Rasrabotka I ispytanya svoistva ingibitorov corrozii na osnove chetvertichnykh ammonievych soedinenii. *Isvestiya vusov. Himia I himicheskaya technologia* [Development and testing of corrosion inhibitors based on quaternary ammonium compounds. *HEO News. Chemistry and Chemical Technology*], vol.61, no 7, pp. 130-136. https://doi.org/10.6060/ivkkt.20186107.5710.
8. Sheryazov S.K., Sarkulova Zh.S., Balgynova A.M., Shukirova S.S., Turispekova A.Zh. (2024) Metody anticorroziniy zashity oborudovaniya I trudoprovodov v neftegazovoi promyshlennosti. *Vestnik AGU imeni K. Zhubanova* [Methods of Anti-Corrosion Protection of Equipment and Pipelines in the Oil and Gas Industry. *Bulletin of K. Zhubanov ASU*], vol.76, no 76, pp.35-42. https://doi.org/10.70239/arsu.2024.t76.n2.05.
9. Sodikova M.R. (2020) Razrabotka I razshirenie assortimenta ingibitorov corrozii I ikh electrokhimicheskye issledovanya [Development and expansion of the range of corrosion inhibitors and their electrochemical studies]. Minsk, pp.509-511, https://elib.belstu.by/handle/123456789/36608.
10. Solop G.R. (2016) Razrabotka I primeneie ingibitorov corrozii na osnove productov neftechimii. [Development and application of corrosion inhibitors based on petrochemical products]. Dissertations for candidate of technical sciences. UFA.https://rusneb.ru/catalog/000199_000009_008823627/.
11. Rikhsikhodjayeva G.R., Rizaev A.N., Kudaibergenova N.T. (2024) Effectivnost raboty ingibitorov ot soleotlozheniya I corrozii dlya vodoobotnykh system neftepererabatyvayushikh promashlennosti [Efficiency of scale and corrosion inhibitors for oil refinery water systems]. *Multidisciplinary Journal of Science and Technology*, vol. 4, no 4, pp. 245-249. https://mjstjournal.com/index.php/mjst/article/view/1195.
12. Ma I.A.W., Ammar S., Kumar S.S.A., et al. (2022) A concise review on corrosion inhibitors: types, mechanisms and electrochemical evaluation studies. *J Coat Technol Res*., 19, pp. 241–268. https://doi.org/10.1007/s11998-021-00547-0.
13. Fouda A.S., El-Etre A.Y. (2021) Eco-friendly corrosion inhibitors for steel in acidic media: A review. *Journal of Molecular Liquids*, 323, 114688. https://doi.org/10.1016/j.molliq.2020.114688.
14. Jain P., Patidar B., Bhawsar J. (2020) Potential of Nanoparticles as a Corrosion Inhibitor: A Review. *J. Bio. Tribo. Corros*., 6, pp. 43. https://doi.org/10.1007/s40735-020-00335-0.
15. Bahremand F., Shahrabi T., Ramezanzadeh B., et al. (2023) Sustainable development of an effective anti-corrosion film over the St12-steel surface against seawater attacks using Ce(III) ions/tri-sodium phosphate anions. *Sci. Rep*., 13, pp. 12169. https://doi.org/10.1038/s41598-023-38540-9.
16. GOST 9.502 -82. (1986) Ingibitory corrosii metallov dlya vodnykh system metoda corrosiinykh ispytanii. [Corrosion inhibitors for water-based systems using the corrosion test method]. M., pp.25.
17. GOST 26449.1-85, 16. (1989) Opredelenie soderzhanya consentrasii zhelesa v rastvore fotometricheskim metodom [Determination of iron concentration in solution by photometric method]. M., pp.3
18. GOST 26449.1-85, 4. (1988) Opredelenie vodorodnogo pokasatelya vody [Determination of the hydrogen index of water]. M., pp. 14.

19. GOST 34100.3-2017. (1985) Staticheskaya obrabotka resultatov. Metodika otsenki neopredelennocti [Statistical processing of results. Uncertainty assessment methodology]. M., pp. 10.

20. GOST 18309-2014. (1983) Opredelenie phosphorsoderzhashih veshestv v vode [Determination of phosphorus-containing substances in water]. M., pp. 9.

21. Kura Genichiro. (1987) Hydrolysis reaction of inorganic cyclophosphates at various acid strengths. *Polyhedron*, 6(3), pp.531–533.

22. Kwolek P., Dychton K., Pytel M. (2020) Orthophosphoric acid solutions of sodium orthovanadate, sodium tungstate, and sodium molybdate as potential corrosion inhibitors of the $Al_2Cu$ intermetallic phase. *Journal of Solid-State Electrochemistry*, vol. 23, no 11, pp.3019-3029.

23. Tygankova L.E. (2010) Ingibidirovanie corrosii I pronoknovenie vodoroda v uglerodistuy stal copmositii IK-3H2 v sredash, soderzhashih $H_2S$ i $CO_2$. *Corrosiya: materyaly, zashity, materialy* [Inhibition of corrosion and hydrogen penetration into carbon steel in combination with IK-3H2 in environments containing $H_2S$ and $CO_2$. *Corrosion: materials, protections, materials*], no 5, pp.18-21.

24. Pechkovski V.V. (1981) Atlas IK-spectrov. Ortoposphaty [Album of IR-spectra. Orthophosphates]. M.: Nauka, pp. 248.

25. Niazbekova A., Akatyev N., Mukasheva M., Rakhova A. (2012) Quantum- chemical calculations of electronic structure of polyphosphate complexes of manganese, cobalt, copper and zinc. *Materials of the international research and practice Conference «European Science and Technology»*, Wiesbaden, Germany, pp. 82-85.

***Information about authors:***

*Aktoty Niyazbekova – Candidate of Technical Sciences, Associate Professor, West Kazakhstan Innovation and Technological University (Uralsk, Kazakhstan, e-mail: abnyazbekova@mail.ru).*

*Almagul Niyazbayeva – Candidate of Chemical Sciences, Associate Professor, Faculty of Chemistry and Chemical Technology, Al-Farabi Kazakh National University (Almaty, Kazakhstan, e-mail: almagulni63@mail.ru).*

*Nazgul Dalabayeva – Candidate of Chemical Sciences, Senior Lecturer, Faculty of Chemistry and Chemical Technology, Al-Farabi Kazakh National University (Almaty, Kazakhstan, e-mail: nazgulds81@gmail.com).*

*Laura Baytlesova – Candidate of Technical Sciences, Associate Professor, West Kazakhstan Innovation and Technological University (Uralsk, Kazakhstan, e-mail: beu64@mail.ru).*

*Timur Shakirov – Master of Engineering and Technology, Senior Lecturer, West Kazakhstan Innovation and Technological University (Uralsk, Kazakhstan, e-mail: shakirov_1985@mail.ru).*

*Maira Almagambetova – Candidate of Technical Sciences, Associate Professor, Zhangir Khan West Kazakhstan Agrarian Technical University (Uralsk, Kazakhstan, e-mail: maira0815@mail.ru).*

*Gulkhan Gubaidullina – Candidate of Technical Sciences, Associate Professor, L.N. Gumilyov Eurasian National University (Astana, Kazakhstan, e-mail: ggulkhan@mail.ru).*

*Zarina Kanapiya – Master of Chemical Sciences, Faculty of Chemistry and Chemical Technology, Al-Farabi Kazakh National University (Almaty, Kazakhstan, e-mail: kanapiazarina@gmail.com).*

International Journal of Biology and Chemistry 18, № 2 (2025)

IRSTI 31.25.01 https://doi.org/10.26577/IJBCh202518213

M.P. Azizova* , M.M. Aghahuseynova ,
S.A. Mammadkhanova

Azerbaijan State Oil and Industry University, Baku, Azerbaijan
*e-mail: azizova.maleyka@asoiu.edu.az

*(Received 15 December 2025; received in revised form 23 December 2025; accepted 25 December 2025)*

# Acid- and amide-controlled sol–gel synthesis of $SiO_2$-based polymer composites

**Abstract.** The sol–gel method is a versatile approach for synthesizing advanced inorganic and organic–inorganic hybrid materials with controlled structure, high purity, and tunable functionality. This study systematically investigated the hydrolytic polycondensation of tetramethoxysilane under acidic conditions to develop an optimized route for high-quality $SiO_2$-based polymer–inorganic composites. The effects of medium acidity, catalyst type, solvent, and amide-based drying-control chemical additives (DCCA) on hydrolysis and condensation kinetics were evaluated. Strong acids accelerated hydrolysis, while weak acids promoted gradual condensation, yielding highly porous but mechanically weaker gels. Acetic acid facilitated homogeneous gel formation and improved transparency and pore uniformity by removing volatile ester by-products. Among the amides, dimethylacetamide and diethylformamide were found to be effective pH regulators in gelation, yielding dense, crack-free gels with lower microporosity and improved mechanical strength. SEM investigations have confirmed the more homogeneous, more compact structures of dimethylacetamide-containting gels, as compared with amide-free gels. Use of acetic acid as the solvent played an important role in controlling the micro-pores, carbon content, density, and stability of gels. In general, this work presents a comprehensive methodological approach for designing sol–gel $SiO_2$-based hybrid nanomaterials with designed structural and physicochemical properties, with their potential use in advanced optical, catalysis, coatings, and other functional applications.

**Keywords:** sol-gel process, tetrametoxysilane, hydrolysis, polycondensation, acidic environment.

## Introduction

The term "sol-gel synthesis" covers a broad group of liquid-phase synthesis techniques characterized by the transition from sol to gel, typically yielding non-crystalline products with fractal-like structures. The overall process is controlled by temperature and, importantly, by catalytic conditions, particularly the acidic or basic environment in which the reactions occur. Due to its unique properties, the sol-gel method enables the fabrication of uniform, high-quality nanoparticles on an industrial scale [1]. Another significant advantage is the ability to obtain highly pure (up to 99.99%) and homogeneous composites [2].

During the sol-gel process, chemical precursors undergo hydrolysis and polycondensation, initially forming a nanodispersed sol [3]. The composition of the reaction medium, its pH, and the temperature determine the size of the particles and the degree of aggregation at this stage. In the final step, the construction of the gel network and the intensity of interparticle interactions define the mechanical and functional properties of the material [4]. The technique is commonly applied in the synthesis of metal oxides. These advantages make the sol-gel method a powerful route for producing materials with unique properties that are otherwise difficult or impossible to achieve by conventional techniques [5].

Despite its advantages, the sol-gel process also presents certain limitations. Precursors are highly sensitive to moisture, which restricts large-scale production–particularly in the field of optical coatings [6, 7]. Additionally, the process is time-consuming, since stabilization and careful drying steps are required to obtain monoliths or bulk materials (with the exception of thin coatings). Other technological challenges include substantial shrinkage of the gel and crack formation during drying.

The sol-gel process typically takes place at relatively low temperatures (usually below 100°C) in a

© 2025 al-Farabi Kazakh National University

liquid medium, yielding a solid material [8]. These solids are formed through polymerization reactions involving the creation of M–OH–M or M–O–M linkages (where M denotes a metal atom). Several parameters influence the hydrolysis and condensation reactions, including precursor reactivity, the water-to-alkoxide ratio, pH of the medium, temperature, solvent nature, and the presence of additives [9]. Catalysts are frequently employed to regulate the rate and extent of hydrolysis and condensation. By adjusting these processing conditions, materials with diverse microstructures and surface chemistries can be obtained [10, 11].

The structural characteristics of materials derived from the sol-gel method can thus be easily tailored by varying synthesis parameters and conditions. The resulting materials typically exhibit nanoscale porosity, making them highly suitable for applications in catalysis, sensors, optoelectronic devices, and functional coatings. Their high surface area also enables use as chemical sorbents and catalyst support [12]. Furthermore, optically transparent layers and nonlinear optical materials prepared via this approach are of great significance for solar cells and optical fibers.

The versatility of the sol-gel technique has also been exploited in sensor fabrication, where porous and chemically modified surfaces enhance sensitivity and selectivity [13]. In addition, sol-gel chemistry enables the synthesis of bioactive glasses and ceramics, drug delivery systems, and implant coatings, whose importance in biomedical applications continues to grow. Other industrial applications include antibacterial coatings and corrosion-resistant layers. In the energy sector, the method is used for the preparation of high-performance components for supercapacitors, lithium-ion batteries, and solar panels, where porous structures with stable ion conductivity and tunable functionality are especially critical [14].

The objective of this study is to synthesize $SiO_2$-based nanoparticles under acidic conditions using the sol-gel method and to investigate the relationship between their structure and properties [15]. For this purpose, the effects of amides, solvent, and catalysts on the hydrolysis and polycondensation reactions of tetramethoxysilane were systematically studied [16].

## Materials and methods

The synthesis of the silica matrix was carried out using the sol-gel method. This process enables the formation of inorganic networks under mild conditions and thus allows the stable incorporation of organic components.

In acidic medium, tetramethoxysilane (TMOS) was used as the main precursor. Since acid catalysis is essential for the hydrolysis and polycondensation of TMOS, hydrochloric acid was initially employed as the catalyst. The molar ratio of TMOS:water:ethanol was adjusted to 1:4:4. Owing to its strong acidity, HCl significantly accelerated the hydrolysis of TMOS, leading to the formation of silanol (Si–OH) groups. In practice, TMOS was first mixed with ethanol, followed by the addition of distilled water. The primary reaction at this stage proceeds as follows:

$$Si(OCH_3)_4 + 4H_2O \rightarrow Si(OH)_4 + 4CH_3OH \quad (1)$$

Subsequently, HCl was added as a catalyst, and the reaction mixture was stirred on an IKA C-MAG HS 7 magnetic stirrer with heating at 25-40°C for 2 h.

The silanol groups formed during hydrolysis underwent condensation reactions, producing a three-dimensional siloxane network:

$$Si(OH)_4 + Si(OH)_4 \rightarrow HO\text{–}Si\text{–}O\text{–}Si\text{–}OH + H_2O \quad (2)$$

or

$$Si(OH)_4 + Si(OCH_3)_4 \rightarrow HO\text{–}Si\text{–}O\text{–}\\ \text{–}\,Si\text{–}\,OCH_3 + CH_3OH \quad (3)$$

To further improve the efficiency of the process and enhance the structural properties of the product, acetic acid ($CH_3COOH$) was used instead of HCl. The advantage of $CH_3COOH$ lies in its ability to form volatile methyl esters ($CH_3COOCH_3$), which leave the reaction system, gradually changing the pH and thus optimizing the condensation stage. This leads to homogeneous, transparent, and crack-free monolithic gels:

$$CH_3COOH + CH_3OH \rightarrow CH_3COOCH_3 + H_2O \quad (4)$$

When $CH_3COOH$ was employed as the catalyst, acetic acid was used as the solvent. To stabilize the system and improve gel formation, a series of amides were added:

1. Formamide [$H\text{–}C(NH_2)\text{=}O$]
2. Dimethylformamide [$H\text{–}C(N(CH_3)_2)\text{=}O$]
3. Diethylformamide [$H\text{–}C(N(C_2H_5)_2)\text{=}O$]
4. Diisopropylformamide [$H\text{–}C(N(i\text{-}C_3H_7)_2)\text{=}O$]
5. Acetamide [$CH_3\text{–}C(NH_2)\text{=}O$]
6. Dimethylacetamide [$CH_3\text{–}C(N(CH_3)_2)\text{=}O$]

These amides absorbed protons, gradually increasing the pH and creating favorable conditions for condensation. Upon protonation, they also formed ammonium salts as by-products:

$$R–CONH_2 + H^+ \rightarrow R–CONH_3^+ \quad (5)$$

After the addition of amides, the homogeneous sol was left to gel at room temperature for 8-12 h. The resulting gels were first dried at room temperature and subsequently subjected to gradual heating up to 50-90°C to ensure the complete removal of volatile by-products (water, methanol, and others), ultimately yielding crack-free monolithic gels.

To investigate the structure, phase composition, and morphology of the synthesized hybrid composites, scanning electron microscopy (SEM) was employed. These analyses provided information on the microstructural organization and structural integrity of the gels obtained under different synthesis conditions.

## Results and discussion

The main stages of the sol-gel technology illustrate not only the general theoretical approach but also reflect the stepwise course of the synthesis processes carried out in the present study (Figure 1).

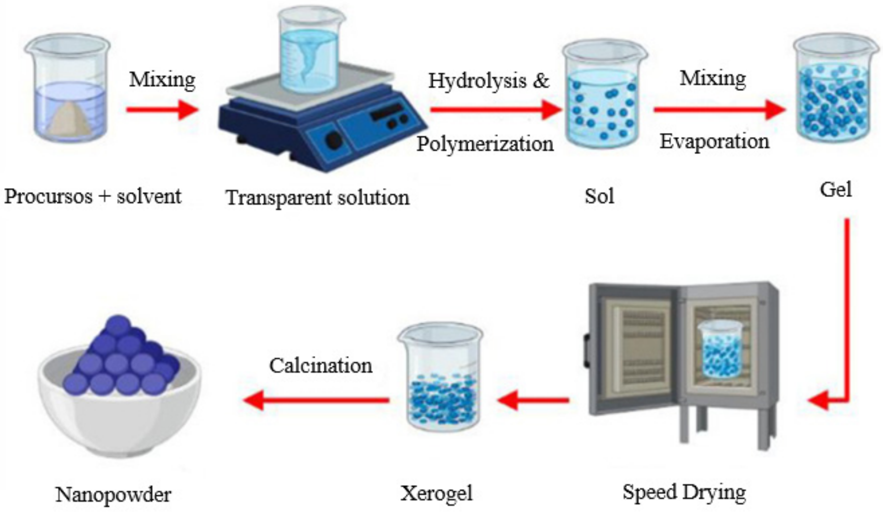

**Figure 1** – Schematic representation of the main stages of the sol-gel process from precursors to gel [6]

The hydrolysis and polycondensation of the initial precursors first lead to the formation of a sol system, followed by the gradual transition of the structure into the gel phase. Consequently, the morphological and physicochemical properties of the obtained material are directly determined by the specific features of this mechanism.

Experimental observations demonstrated that the pH of the medium had a significant effect on the rates of hydrolysis and condensation during the sol-gel synthesis. At lower pH values, the hydrolysis reaction proceeded more rapidly, whereas condensation occurred relatively weakly. As the numerical value of pH increased, the rate of hydrolysis initially decreased gradually but began to increase again when the pH exceeded 7. At the same time, the rate of condensation decreased inversely with increasing pH.

Figure 2 illustrates the changes in the relative rates of hydrolysis and condensation reactions as a function of pH. Based on the obtained results, it was determined that the hydrolysis reaction proceeded rapidly at low pH values, but its rate gradually decreased as the pH approached 7. When the pH exceeded 7, a renewed increase in the hydrolysis rate was observed. In contrast, the condensation reaction was relatively weak under acidic conditions and became even weaker as the pH increased. According to the conducted experiments, pH = 4 and pH = 9.5 were evaluated as optimal media, where hydrolysis and condensation reactions occurred in a balanced manner.

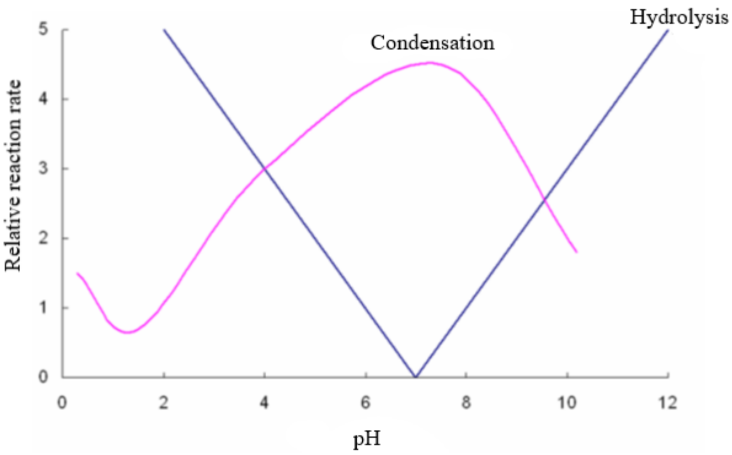

**Figure 2** – Variation of the relative rates of hydrolysis and condensation reactions under different pH conditions

The acidity of the medium plays a crucial role in the sol-gel synthesis of monolithic (crack-free after drying) silica gels. Strongly acidic conditions ($pH < 1$) are optimal for hydrolysis, whereas near-neutral conditions (pH 4–5) favor condensation. Thus, the effect of pH variation on the physicochemical parameters of the resulting gels was investigated.

To modify the structure of sol-gel materials and obtain crack-free gel bodies, a series of organic amides (DCCA) were introduced into the system:

1. $H\text{-}C(NH_2)\text{=}O$ (Formamide)
2. $H\text{-}C(N(CH_3)_2)\text{=}O$ (Dimethylformamide)
3. $H\text{-}C(N(C_2H_5)_2)\text{=}O$ (Diethylformamide)
4. $H\text{-}C(N(i\text{-}C_3H_7)_2)\text{=}O$ (Diisopropylformamide)
5. $CH_3\text{-}C(NH_2)\text{=}O$ (Acetamide)
6. $CH_3\text{-}C(N(CH_3)_2)\text{=}O$ (Dimethylacetamide)

The DCCA-type additives (1–6), which regulate the drying process, facilitated the formation of larger and more uniformly sized pores within the gel network. In such pores, capillary forces are weaker, which reduces internal stress during drying and prevents crack formation in the material. Moreover, due to the higher vapor pressure in larger pores, solvent evaporation occurs more rapidly. In addition, the amides interact with hydrogen ions, and depending on their structure, these reactions proceed at different rates. The introduction of these compounds into the system enabled a gradual and controlled variation of acidity during the sol-gel process, with the rate of change differing according to the specific amide employed (Figure 3).

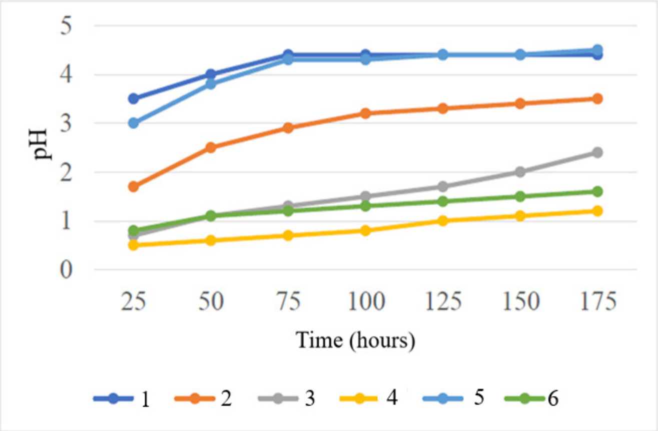

**Figure 3** – Time-dependent pH variation in solutions of amides 1-6

Among all synthesized gels, only the samples obtained in the presence of amides $3^{/}$,$4^{/}$,$5^{/}$ were monolithic and transparent. The comparison of the physicochemical properties of the synthesized gels, including gelation time, density, and hardness, is presented in Table 1. It shows that gels prepared in the presence of diethylformamide (3) and dimethylacetamide (6) exhibited the highest density, mechanical strength, and the lowest microporosity. $7^{/}$ – gel obtained without any amide addition.

Physical-chemical characteristics of the obtained gels (Comparison of gelation times, density, and hardness of synthesized gels) are shown in table 1. Hydrolytic polycondensation of TMOS proceeds most effectively when the hydrolysis rate of the amides adapts to the medium's acidity. During gelation, an optimal gradual pH shift from 0.7–0.9 to 1.8–2.5 ensures efficient hydrolysis and polycondensation. Among the studied amides, diethylformamide (3) and dimethylacetamide (6) were found to be more effective as DCCA reagents (drying-controlling additives) compared to formamide (1) and dimethylformamide (2). Moreover, it was demonstrated that the commonly applied amounts of DCCA (1–3 equivalents per 1 mol of tetrametoxysilane) are excessive; the optimal dosage should not exceed 0.1–0.2 equivalents to achieve controlled gelation and uniform pore structure.

**Table 1** – Physical-chemical characteristics of the obtained gels

| Samples | Gelation time | $SiO_2$, % | Density, g/cm³ | Hardness, kg/mm² |
|---|---|---|---|---|
| $1^{/}$ | 2.23 | 2.23 | 2.23 | - |
| $2^{/}$ | 9.78 | 9.78 | 9.78 | 56 |
| $3^{/}$ | 8.40 | 8.40 | 8.40 | 70 |
| $4^{/}$ | 7.83 | 7.83 | 7.83 | 35 |
| $5^{/}$ | 12.03 | 12.03 | 12.03 | - |
| $6^{/}$ | 8.45 | 8.45 | 8.45 | 112 |
| $7^{/}$ | 6.58 | 6.58 | 6.58 | 54 |

According to the scanning electron microscopy (SEM) results of the synthesized gels, specifically samples $6^{/}$ and $7^{/}$ as shown in Figure 4, significant differences in the microstructural organization can be observed.

The gel sample $6^{/}$, which was prepared by introducing dimethylacetamide (1) into the reaction system, exhibits a markedly more ordered and homogeneous network compared to gel $7^{/}$, which was synthesized without the addition of any amide. The reason why $6^{/}$ has greater structural unity and less porosity can be found in the molecular control exercised by dimethylacetamide in the sol-gel transition. Thus, dimethylacetamide acts as a molecular control agent that affects the silanol groups in the sol-gel transition. Since the presence of silanol groups triggers the hydrolysis step in a sol-gel transition, dimethylacetamide slows down the rate of the sol-gel transition. Therefore, there is more careful nucleation of a silica framework in $6^{/}$. Hence, the result is a more evenly distributed silica framework with fewer defects in $6^{/}$. Consequently, $6^{/}$ becomes more denser on the inside; therefore, the structural integrity of 6/ increases.

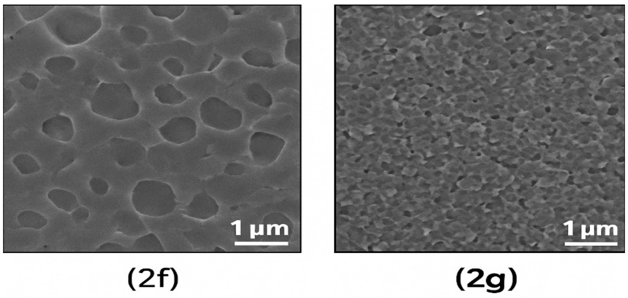

Sample $6^{/}$ Sample $7^{/}$

**Figure 4** – SEM images of samples obtained with dimethylacetamide and without any amide

In addition, a more compact micromorphology of the gel would be expected to positively affect the performance results when uniformness of structure, mechanical strength, and non-porosity are desired, as in optical films, supports of catalysts, or carrier matrices for biomedical purposes. In this way, the tests carried out above show the primary effect of amide additives on the control and development of morphology and functionality of sol-gel-based $SiO_2$ polymer composites.

## Conclusion

This work includes an examination of sol–gel processing of silicon dioxide-based materials synthesized with an acidic medium with attention to both kinetics of hydrolytic polycondensation of tetrametoxysilane and application of amide-based additives for drying control.

The results showed that the acidity of the reaction environment exerts a great influence on the hydrolysis of silicon-alkoxy groups and their further condensation into silicon-oxygen-silicon (Si-O-Si) bonds that control the properties of the gel network, transparency, and mechanical properties. Weakly acidic media favor slower gelation processes with the formation of porous gels of low mechanical strength in contrast to the use of strong acids, especially acetic, which provide a more homogeneous, transparent, and rigid gel with a well-distributed pore structure. Moreover, the work has shown that the influence of amide additive composition and content exerts a great influence on the gelation processes. The best agents regulating drying are diethylformamide and dimethyl-acetamide used in comparison with other amides.

The application of common higher concentrations proved unnecessary, whereas a lower quantity corresponding to 0.1–0.2 of reactive species was adequate for the controlled gelation and formation of nanostructure. The results offer a sound scientific basis for the preparation of silica-based gels with specific structural features and properties. Based on the control over acidity in the medium along with the addition of proper amide agents, monolithic gels with improved mechanical properties can be prepared. Overall, this work enhances the understanding of reaction kinetics and mechanisms in sol–gel processes and offers practical guidance for developing highly functional hybrid materials applicable in optical, catalytic, and biomedical technologies.

## Conflict of interest

The authors declare that they have no conflicts of interest.

## References

1. Kandiel T. A., Robben L., Alkaim A., Bahnemann D. (2013) Brookite versus Anatase $TiO_2$ Photocatalysts: Phase Transformations and Photocatalytic Activities. *Photochem. Photobiol. Sci*., vol.12, no. 4, pp. 602–609. https://doi.org/10.1039/C2PP25152F.

2. García-Martínez J.-M., Collar E. P. (2024) Current and future insights in organic–inorganic hybrid materials. *Polymers, vol. 16*, pp. 3043. https://doi.org/10.3390/polym160203043.

3. Silva A.G., Pereira M.F.R., et al. (2020) Sol–Gel synthesis of hybrid materials. *Journal of Sol-Gel Science and Technology, vol. 96*, pp. 1–23. https://doi.org/10.1007/s10971-020-05341-0.

4. Tan T.Y., Singh M.P., et al. (2022) Advanced Sol–Gel Synthesis of Nanohybrid Materials for Technological Applications. *Adv. Funct. Mater*., vol. 29, no. 10. https://doi.org/10.1002/adfm.202108541.

5. Salimian S., Zadhoush A., Naeimirad M., Kotek R., Ramakrishna S. (2018) A review on aerogel: 3D nanoporous structured fillers in polymer-based nanocomposites. *Polymer Composites, vol. 39, no.* 10, pp. 3383–3408. https://doi.org/10.1002/pc.24387.

6. Feinle A., Elsaesser M.S., Hüsing N. (2016) Sol–Gel synthesis of monolithic materials with hierarchical porosity. *Chemical Society Reviews, vol. 45, no.* 12, pp. 3377–3399. https://doi.org/10.1039/C5CS00710K.

7. Nasr L., Solhy A. (2021) Sol–Gel derived hybrid materials for catalysis: A review of synthesis and applications. *Journal of Sol-Gel Science and Technology, vol. 98, no.* 1, pp. 1–25. https://doi.org/10.1007/s10971-020-05399-1.

8. Escobar C.D.C., Dos Santos J.H.Z. (2014) Effect of the Sol–Gel Route on the Textural Characteristics of Silica Imprinted with Rhodamine B. *J. Sep. Sci*., vol. 37, no. 7, pp. 868–875. https://doi.org/10.1002/jssc.201300940.

9. Khan M.D., Ahn J.W., Nam G. (2018) Environmentally Benign Synthesis, Characterization and Mechanism Studies of Green Calcium Hydroxide Nanoplates Derived from Waste Oyster Shells. *J. Environ. Manage*., vol. 223, pp.947–951. https://doi.org/10.1016/j.jenvman.2018.07.080.

10. Faraji M., Mansouri F., Karimi B., Vali, H. (2025) A magnetic hybrid sol–gel ionic network catalyst for direct alcohol esterification under solvent-free conditions. *Nanoscale*, vol. 17, no. 31, pp. 18161–18172. https://doi.org/10.1039/D5NR02432C.

11. Shinde S.S., Patil P.S., Gaikwad R.S., Mane R.S., Pawar B.N., Rajpure K.Y. (2010) Influences in High Quality Zinc Oxide Films and Their Photoelectrochemical Performance. *J. Alloys Compd*., vol. 503, no. 2, pp. 416–421. https://doi.org/10.1016/j.jallcom.2010.05.080.

12. Lee R., Cho A.H., et al. (2020) Antibacterial and antifungal activity of $TiO_2$ and ZnO-based nanohybrids. *Journal of Biomedical Nanotechnology, vol. 15, no.* 3, pp. 249–263. https://doi.org/10.1166/jbn.2020.2924.

13. Catauro M., Tranquillo E., Di Poggetto G., Pasquali M., Dell'Era A., Vecchio S.C. (2018) Influence of the heat treatment on the particle size and on the crystalline phase of $TiO_2$ synthesized by the Sol–Gel method. *Materials, vol.11, no.* 12, pp. 2366. https://doi.org/10.3390/ma11122366.

14. Lamy A.M., Silva R.F., Durães L. (2018) Advances in carbon nanostructure–silica aerogel composites: A review. *Journal of Materials Chemistry A, vol. 6, no.* 4, pp. 1340–1369. https://doi.org/10.1039/C7TA08916A.

15. Sanchez C., Belleville P., Popall M., Nicole L. (2011) Applications of Advanced Hybrid Organic–Inorganic Nanomaterials: From Laboratory to Market. *Chem. Soc. Rev*., vol. 40, no. 2, 696–753. https://doi.org/10.1039/B909613A.

16. Verma R., Mantri B., Srivastava A.K. (2015) Shape-Control Synthesis, Characterizations, Mechanisms and Optical Properties of Large-Scaled Metal Oxide Nanostructures of ZnO and $TiO_2$. *Adv. Mater. Lett.*, vol. 6, no. 4, pp. 324–333. https://doi.org/10.5185/amlett.2015.5731.

***Information about authors:***

*Maleyka Azizova – Researcher, Faculty of Chemical Technology, Azerbaijan State Oil and Industry University (Baku, Azerbaijan, e-mail: azizova.maleyka@asoiu.edu.az).*

*Minira Aghahuseynova – Professor, Doctor of Chemical Sciences, Department of Technology of Chemical and Inorganic Substances Azerbaijan State Oil and Industry University (Baku, Azerbaijan, e-mail: minira.agahuseynova@asoiu.edu.az).*

*Sevinc Mammadkhanova – Professor, Doctor of Chemical Sciences, Dean of the Faculty of Chemical Technology, Azerbaijan State Oil and Industry University (Baku, Azerbaijan, e-mail: sevinc.mammadxanova@asoiu.edu.az).*

IRSTI 31.25.01 https://doi.org/10.26577/IJBCh202518214

N. Zhumasheva , E. Nurgaziyeva*

National Laboratory Astana, Nazarbayev University, Astana, Kazakhstan
*e-mail: elmira.nurgaziyeva@nu.edu.kz

*(Received 15 November 2025; received in revised form 20 December 2025; accepted 25 December 2025)*

# Solid polymer electrolytes and their role in the development of next generation Li-ion batteries

**Abstract.** Over the past ten years, lithium-ion batteries (LIBs) have become indispensable for powering wearable technology, smart electronics, and electric cars. However, the use of extremely flammable and volatile liquid electrolytes in typical Li-ion rechargeable batteries raises serious safety issues and prevents future advancements in energy density and dependability. Solid electrolytes have been suggested as viable solutions to these problems. In particular, polymer-based solid electrolytes combine high ionic conductivity with advantages such as low flammability, mechanical flexibility, thermal stability, and improved safety. This review highlights recent advances in solid polymer electrolytes for LIBs, with a focus on their fabrication strategies, structural designs, ionic conductivities, and electrochemical/mechanical stabilities.

**Keywords:** lithium-ion batteries, solid polymer electrolytes, ionic conductivity, safety, electrochemical stability, fabrication strategies.

## Introduction

The development of lithium-ion batteries (LIBs) began in the 1970s with early investigations on Li/$TiS_2$ systems [1]. In 1991, Sony Corporation and Asahi Kasei commercialized LIBs, which have since become dominant in diverse applications, including mobile electronics, wearable devices, and electric vehicles [2, 3]. LIBs offer high energy density and long cycle life; however, safety concerns remain a critical barrier to their broader deployment.

Lithium hexafluorophosphate ($LiPF_4$) dissolved in organic carbonate liquids is used as a liquid electrolyte in conventional LIBs. Further improvements in energy density and dependability are hampered by these electrolytes' extreme volatility, flammability, and thermal instability. Solid polymer electrolytes (SPEs) have been suggested as viable substitutes to address these issues [4, 5]. However, at room temperature, their comparatively low ionic conductivity and lithium-ion transference numbers have impeded their practical deployment.

Numerous techniques, such as the design of new polymer hosts and the addition of functional additives, have been the subject of extensive research efforts to solve these constraints [6-8]. Crucially, the safety profile of LIBs would be much improved by completely substituting SPEs for liquid electrolytes [9-11]. The development of flexible polymer hosts, such as poly(propylene carbonate), poly(ethylene oxide), and poly(tetrahydrofuran), has been the focus of recent advancements. These hosts exhibit improved ionic conductivity, higher lithium-ion transference numbers, better thermal stability, mechanical robustness, and enhanced interfacial adhesion [12-14]. Although ion conduction mechanisms and lithium-ion transport properties have been examined in a number of papers [8, 15, 16], a thorough summary of recent developments in SPE design is still required.

The goal of this review is to provide an overview of the most recent developments in solid polymer electrolytes, with a focus on synthesis techniques, ionic conductivity enhancement techniques, and assessments of their chemical and thermal durability. Lastly, prospects for the advancement of sophisticated SPEs are examined.

## 1. Polymer-based solid polymer electrolytes

Among solid polymer electrolytes (SPEs), polyethylene oxide (PEO)- and polyacrylonitrile (PAN)-based systems have been extensively studied [17, 18]. Enhancing $Li^+$ conductivity in SPEs requires a fundamental understanding of ion transport mechanisms. Polymers containing polar functional groups (–O–, –B–, –N–, C=O, C≡N, C–S–, and C–(O=S=O)–) can effectively dissolve lithium salts through polymer–

© 2025 al-Farabi Kazakh National University

salt complexation. Accordingly, polymers such as PEO, PAN, polyethyleneimine (PEI), and polypropylene carbonate (PPC) exhibit good lithium-salt solvation ability [16].

Electrolytes based on PPC are highly transparent due to their predominantly amorphous phase (Figure 1). Unlike many other polymers, PPC exhibits a glass transition temperature ($T_g$) close to room temperature, which facilitates ionic motion. Its good compatibility with lithium salts and high transparency make PPC a promising candidate for SPE applications. Furthermore, the carbonyl groups in PPC exhibit weaker coordination with lithium ions compared to the stronger coordination of $Li^+$ with the ether oxygen atoms in polyethers such as PEO [12]. This weaker binding contributes to enhanced ion mobility, and consequently, carbonyl-based PPC exhibits one of the highest room-temperature ionic conductivities among polymer hosts. However, its conductivity ($10^{-4}$–$10^{-5}$ S·cm$^{-1}$) remains below the practical requirements for solid polymer electrolytes in lithium-ion batteries.

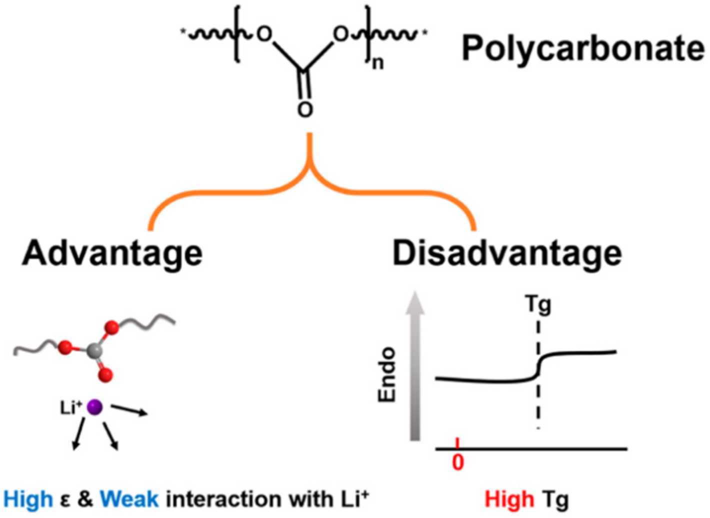

**Figure 1** – Schematic diagram illustrating the advantages and disadvantages of polycarbonates [12]

## 2. Fundamental Characteristics of Solid Polymer Electrolytes (SPEs)

*a) Ionic Conductivity*

It is well established that electronic conductivity in polymers is higher in spatially ordered systems, while greater ionic conductivity can be achieved in disordered or amorphous polymer domains. Complexes formed between lithium salts and solvating polymers exhibit varying degrees of ionic conductivity [19]. Polymers can be fully amorphous or semi-crystalline, depending on chain regularity. In amorphous polymers, segmental motion of the chains occurs above the glass transition temperature ($T_g$), while crystalline regions melt at the melting point ($T_f$). A key feature of polymer electrolytes is that ionic transport is confined to the amorphous phase above $T_g$, where $Li^+$ mobility is strongly coupled with the segmental motion of polymer chains [20].

Extensive research has focused on enhancing the ionic conductivity of polymer–Li salt systems over the past decades [21-23]. Nevertheless, the ionic conductivity of state-of-the-art SPEs ($10^{-4}$–$10^{-5}$ S·cm$^{-1}$) still falls short of liquid electrolytes ($10^{-2}$ S·cm$^{-1}$), highlighting the need for further development to enable practical replacement of flammable organic electrolytes.

*b) Electrochemical, Chemical, and Thermal Stability*

The practical applicability of SPEs is largely determined by their electrochemical stability window. The charge–discharge potentials of electrode materials must lie within this window; otherwise, side reactions may occur, leading to capacity fading and reduced safety. Current lithium-ion battery technology relies on intercalation-type cathodes and anodes with operating voltages close to $Li/Li^+$. Most commercial cathodes operate below 4.3 V [24], therefore, an ideal SPE should maintain stability within 0–5 V versus Li/Li$^+$.

Chemical stability is equally critical, particularly at the interface with the lithium-metal anode. Unstable interactions can result in dendrite formation, grain boundary opening, and the development of isolated "islands" at the interface, all of which compromise battery safety and performance [25].

Thermal stability is another essential parameter, as polymer electrolytes must withstand elevated operating temperatures without degradation. To replace conventional liquid electrolytes and separators, SPEs must resist shrinkage or dimensional changes at temperatures around 150–165°C [26]. Such thermal robustness is a prerequisite for improving the intrinsic safety of LIBs.

### *c) Mechanical Properties*

In addition to high ionic conductivity and chemical/thermal stability, SPEs must possess adequate mechanical strength to ensure reliable battery operation. Electrolytes that are too brittle or excessively rigid exhibit poor interfacial contact with electrodes, impeding charge transfer and increasing internal resistance [27, 28]. Thus, intimate electrode–electrolyte interactions and steady long-term cycling performance depend on striking a balance between mechanical integrity and flexibility.

## 3. Innovative Methods for Solid Polymer Electrolyte Synthesis

### *a) Techniques to Boost SPEs' Ionic Conductivity*

Polymer-based solid electrolytes have been thoroughly studied in recent years due to their potential to replace liquid electrolytes in lithium-ion batteries as well as their inherent safety. Improving SPEs' ionic conductivity has been the subject of extensive research.

The creation of ultrathin polymer electrolyte sheets is one successful tactic. Improved conductivity is achieved by decreasing the electrolyte thickness, which also shortens the ion migration path and lowers the ionic resistance. It is still difficult to prepare ultrathin solid polymer electrolytes without sacrificing their mechanical integrity. Excessive thinning can increase the risk of internal short circuits, particularly in electrolytes with low mechanical strength and toughness [29].

Recently, ultrathin solid polymer electrolytes (UTPEs) based on grafted agarose with polyethylene oxide (PEO) were reported, demonstrating an ionic conductivity of $1.2 \times 10^{-4}$ S·cm$^{-1}$ at room temperature [30]. In this work, UTPEs were synthesized via a reaction between single-helical agarose and PEO in the presence of isophorone diisocyanate (IPDI). Electrochemical impedance spectroscopy (EIS) of UTPEs with varying thicknesses was conducted using LiFePO$_4$ (LFP) || Li cells to assess interfacial stability. The cell employing a 32 μm UTPE exhibited lower interfacial impedance during cycling, while the one with a 72 μm UTPE showed progressively increasing impedance. Moreover, the solid-state LFP||Li cell with UTPE demonstrated superior cycling and rate performance compared to cells using an electrolyte mixture of agarose/PEO/LiTFSI (Figure 2).

The unique helical structure of ultrathin polymer electrolytes (UTPEs) not only enhances their mechanical properties but also increases free volume and facilitates segmental motion, both of which are crucial for lithium-ion hopping. As a result, the UTPE demonstrated an ionic conductivity of $1.2 \times 10^{-4}$ S·cm$^{-1}$ at room temperature.

In another approach, a polymer–polymer solid-state electrolyte was designed using an 8.6 μm-thick nanoporous polyimide (PI) film filled with polyethylene oxide/lithium bis(trifluoromethanesulfonyl) imide (PEO/LiTFSI) [31]. This composite electrolyte combines a nonflammable PI host containing vertically aligned nanochannels with Li-ion conducting PEO/LiTFSI fillers. The high modulus of the PI framework effectively suppresses lithium dendrite penetration, while the vertical nanochannels promote uniform infiltration of the polymer electrolyte and improve ionic transport. The resulting ultrathin polymer–polymer composite electrolyte exhibits excellent flexibility, low resistance, and high energy density in full-cell configurations.

Electrochemical performance and morphological studies (Figure 3) revealed that approximately 11% of the PI surface area was occupied by PEO/LiTFSI fillers. Cross-sectional SEM images confirmed that the fillers fully infiltrated the vertical nanochannels of the PI framework. Interestingly, the PEO/LiTFSI confined within aligned PI pores exhibited a higher ionic conductivity ($2.3 \times 10^{-4}$ S·cm$^{-1}$) compared to a conventional PEO/LiTFSI thin film ($5.4 \times 10^{-5}$ S·cm$^{-1}$), highlighting the beneficial effect of nanoscale confinement.

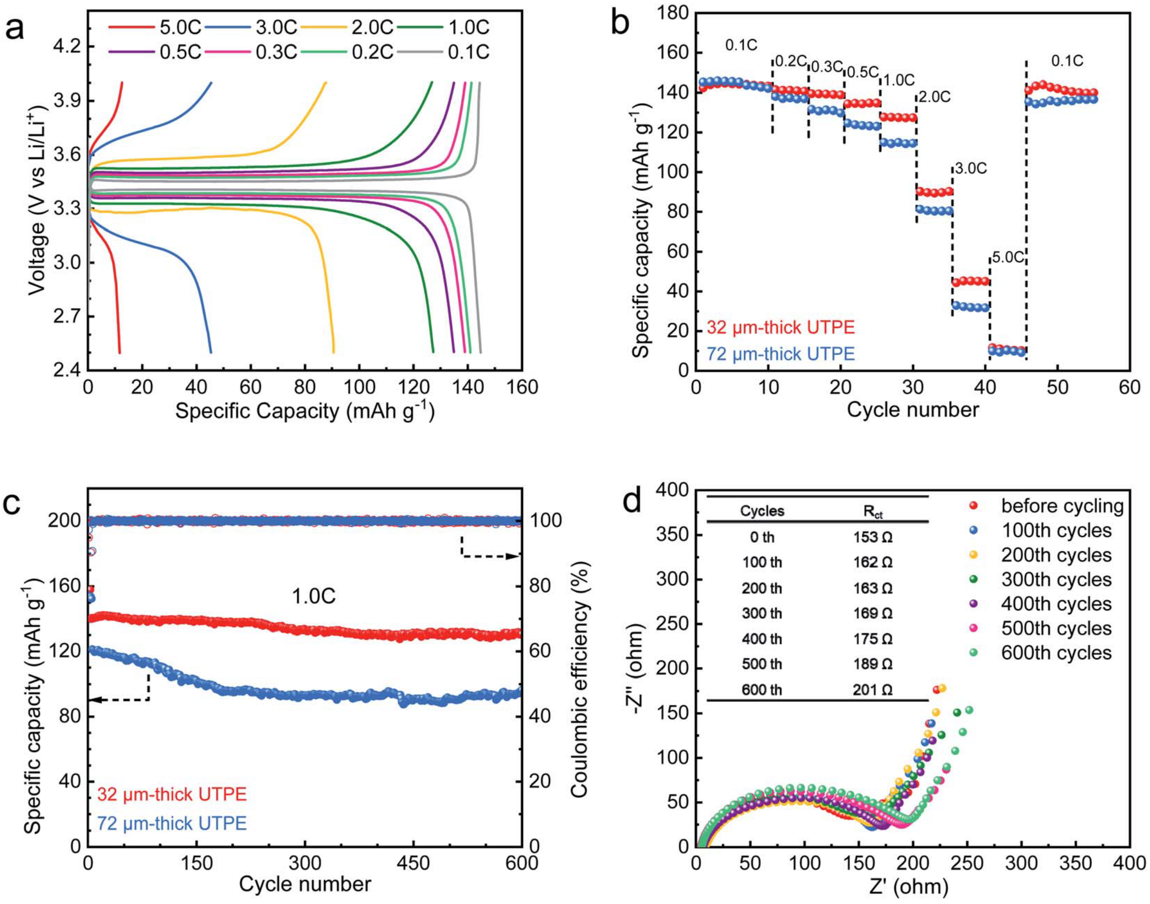

| Cycles | $R_{ct}$ |
|---|---|
| 0 th | 153 Ω |
| 100 th | 162 Ω |
| 200 th | 163 Ω |
| 300 th | 169 Ω |
| 400 th | 175 Ω |
| 500 th | 189 Ω |
| 600 th | 201 Ω |

**Figure 2** – (a) Voltage profiles of Li|LFP cells with a 32 μm UTPE at various C-rates at room temperature; (b) rate performance of Li|LFP cells with UTPEs of different thicknesses; (c) discharge capacity and coulombic efficiency at 1.0C; (d) EIS of Li|LFP cells with a 32 μm UTPE after different cycles [30]

Sun et al. [32] proposed another strategy to enhance ionic conductivity by employing an *in situ* solidification method based on the ring-opening polymerization of ε-caprolactone (ε-CL). This approach enabled the fabrication of ultrathin (~11 μm) poly(ε-caprolactone) (PCL)-based polymer electrolytes. The *in situ* polymerization not only simplified electrolyte preparation but also yielded mechanically stable films with improved interfacial compatibility and ionic transport, making them promising candidates for next-generation solid-state batteries.

Promising solid polymer electrolytes have been described from the polymerization of ε-caprolactone (ε-CL) monomers catalyzed by $Sn(Oct)_2$. According to the authors, when $Sn(Oct)_2$ is utilized as a catalyst during synthesis, it not only successfully stimulates the ring-opening polymerization of ε-CL but also changes into a layer of Li–Sn alloy when it comes into contact with the lithium metal anode. This alloy layer is essential for inhibiting the formation of dendrites. The study found that the in situ produced poly(ε-caprolactone) (PCL)-based polymer electrolyte (in situ PCL SPE) operated for up to 900 hours with a low polarization potential of 45 mV, exhibiting excellent stability in symmetric Li|Li cells. A tiny quantity of propylene carbonate (PC) was added to further enhance ionic conductivity and cell performance. The addition of the commercial liquid electrolyte mainly served to enhance ionic conductivity at room temperature, reaching $2.1 \times 10^{-5}$ S·cm$^{-1}$ at 27°C – approximately 30 times higher than that of the pristine in situ PCL SPE ($6.7 \times 10^{-7}$ S·cm$^{-1}$). Moreover, the polymer electrolyte exhibited favorable electrochemical properties, including a suitable lithium-ion transference number and broad electrochemical stability (–0.5 to 4.3 V), making it a viable candidate for high-performance solid-state lithium metal batteries (LMBs).

In general, the ionic conductivity of solid polymer electrolytes can also be improved by reducing the electrolyte thickness to the ultrathin scale. To address conductivity and interfacial issues, Jian-Fang Wu and Xin Guo investigated the incorporation of nanostructured metal–organic frameworks (MOFs) [33]. Due to their multifunctional properties, MOFs were found to enhance ionic conductivity, suppress polymer crystallinity, and improve interfacial stability with the lithium electrode. Specifically, the PEO-n-UIO composite polymer electrolytes, prepared by dispersing nanoporous UIO/Li-IL fillers in PEO, exhibited an increased lithium-ion conductivity of 1.3 × 10$^{-4}$ S·cm$^{-1}$ at 30°C. This improvement was attributed to the inherently high ionic conductivity of UIO/Li-IL and the suppression of PEO crystallinity.

Other researchers optimized the balance between crystallinity and ionic conductivity by incorporating well-established functional units into polymer electrolytes, such as ethylene oxide, carbonate, and lithium sulfonamide groups [17]. By tailoring the monomer stoichiometry, the resulting copolymer achieved an ionic conductivity of 1.2 × 10$^{-4}$ S·cm$^{-1}$ at 70°C. In this study, the polymers were synthesized via a two-step melt polycondensation process using poly(ethylene glycol) ($M_n$ = 1500), dimethyl carbonate, and a functional diol containing sulfonimide groups (Figure 3).

Using this synthetic route, three different copolymer compositions were targeted to optimize performance: PEO$_{34}$:bis-MPTFSI (lithium ((3-((3-hydroxy-2-(hydroxymethyl)-2-methylpropanoyl)oxy)propyl)sulfonyl)(trifluoromethyl)sulfonyl)amide) at 75:25 mol% (SIPC-1), 50:50 mol% (SIPC-2), and 25:75 mol% (SIPC-3). The ionic conductivity at room temperature was as follows: SIPC-3 > SIPC-2 > SIPC-1.

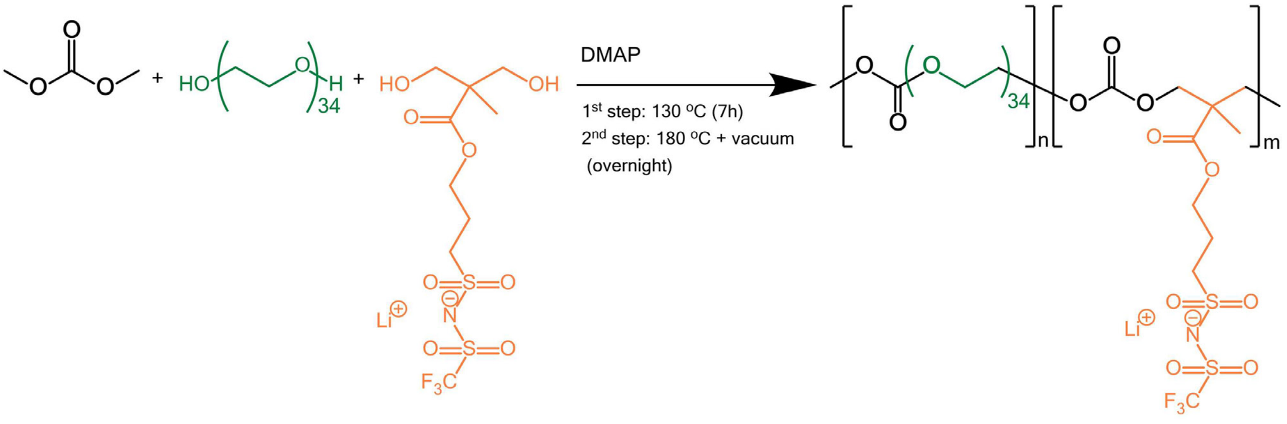

**Figure 3** – Polycondensation route of poly(ethylene oxide carbonate) polymer electrolytes [17]

When both carbonate and ether oxygens were taken into account, the O/Li molar ratio had a significant impact on Li$^+$ conduction above the melting temperature of the crystalline EO phase (T > 50°C). SIPC-2 showed the best balance between coordinating oxygen atoms and lithium ions, with O/Li = 35. On the other hand, SIPC-3 (O/Li = 6) showed decreased conductivity because there were not enough carbonate/EO units to properly coordinate and dissociate lithium ions, whereas SIPC-1 (O/Li = 110) had too little lithium to support effective ionic conduction. SIPC-2 attained an ionic conductivity of 1.2 × 10$^{-1}$ S·cm$^{-1}$ at 70°C.

Despite their promising conductivity, SIPC-based electrolytes exhibited low glass transition temperatures (~ –40°C) and linear chain structures, leading to poor mechanical stability above the melting point of the EO crystalline phase. To address this, PEG diacrylate (PEGDA, $M_n$ = 575) was incorporated as a cross-linker, with SIPC-2 selected for optimization due to its superior ionic conductivity above room temperature. Upon ultraviolet irradiation, freestanding films of single-ion conducting poly(ethylene oxide carbonate) were obtained with small amounts of networked PEGDA. The addition of 5 wt% PEGDA did not significantly affect ionic conductivity: at 70°C, SIPC-2 with 5 wt% PEGDA reached 3.2 × 10$^{-5}$ S·cm$^{-1}$, compared to 1.2 × 10$^{-4}$ S·cm$^{-1}$ for the uncrosslinked SIPC-2. However, increasing the PEGDA content to 10 wt% caused a sharp decline in conductivity (9.6 × 10$^{-7}$ S·cm$^{-1}$). Because this decrease was observed even above the EO crystalline melting point, it was attributed more to altered crystallinity and reduced chain mobility than to the semi-interpenetrated PEGDA network itself.

In a related approach, Meabe et al. [34] synthesized various aliphatic polycarbonates for use as solid polymer electrolytes via traditional polycondensation of diols with dimethyl carbonate. Recently, aliphatic polycarbonates have been proposed as promising alternatives to PEO-based matrices, offering excellent room-temperature ionic conductivity, broad electrochemical stability, and high lithium-ion transference numbers [35]. In this study, the authors fabricated a series of aliphatic polycarbonates containing between 4 and 12 methylene groups between carbonate units. The ionic conductivity of these polycarbonate-based SPEs was slightly improved by optimizing the $Li^+$/polymer ratio, reaching ~1 × $10^{-4}$ S·cm$^{-1}$. Interestingly, polymers with longer methylene spacers showed higher conductivities. Furthermore, the P10C and P12C samples, which exhibited the lowest molecular weights, delivered the highest conductivities due to reduced chain entanglement and improved segmental mobility.

Other authors have synthesized aliphatic carbonate-based solid polymer electrolytes through ring-opening polymerization of cyclic carbonates as well as copolymerization of $CO_2$ with epoxides [35, 36]. Mindemark and co-workers suppressed the crystallinity of poly(ε-caprolactone) (PCL) by copolymerizing it with trimethylene carbonate (TMC), which enhanced the ionic conductivity to 4.1 × $10^{-5}$ S·cm$^{-1}$ at 25°C. In this work, carbonate repeating units were incorporated into the PCL backbone, enabling the material to act as a more effective solid polymer electrolyte host. The authors demonstrated that introducing carbonate units not only reduced the crystallinity of the polyester but also broadened the temperature range over which higher ionic conductivity was maintained. They proposed that the improved $Li^+$ transport originated either from the weaker coordination of carbonate groups with $Li^+$ compared to ester groups, or from the disruption of the regular sequence of the PCL backbone, which enhanced chain mobility.

Morioka et al. [37] reported an alternative strategy by fabricating polycarbonates with oxyethylene (OE) end groups via alternating copolymerization of $CO_2$ and glycidyl ether monomers. In this study, three types of polycarbonates derived from $CO_2$ and glycidyl ether monomers were synthesized. These polymers combined the benefits of polycarbonates (low $T_g$, amorphous structure, wide electrochemical window) with the $Li^+$ coordination ability of oxyethylene segments, offering a promising design pathway for advanced solid polymer electrolytes.

They subsequently employed lithium bis(fluorosulfonyl)imide (LiFSI) to investigate the influence of oxyethylene (OE) chain length on the ion-conductive properties of the polycarbonate-based electrolytes. According to their findings, polycarbonates with ether end groups exhibited relatively high $Li^+$ transference numbers, often exceeding 0.4. The authors suggested that such elevated values indicate weaker interactions between the polymer main chains and cations compared to conventional polyethers. At a salt concentration of 188 mol%, most $Li^+$ ions were found to interact with carbonate groups, yet the polycarbonate electrolytes still maintained high $Li^+$ transference values. Notably, the polycarbonate with ethoxy side groups combined with LiTFSI achieved a $Li^+$ transference number above 0.7, comparable to those of single-ion conducting polymers [17].

Morioka and co-workers attributed this behavior to the fact that polycarbonates with ethoxy side groups contain only a single ether oxygen atom in the terminal group, making it difficult to form stable coordination structures as typically observed in the PEO system. Instead, the short ether side chains likely promote faster $Li^+$ migration, thereby contributing to both the enhanced ionic conductivity and the high transference values.

Yi Cui and co-workers reported the in-situ preparation method of polymer electrolytes containing ceramic $SiO_2$ particles (composite polymer electrolytes) (Figure 4) [38].

According to the research, the *in situ* CPE shows a dissociation ratio of 98.1%, which is significantly higher than those of the ceramic-free SPE (85.0%), PEO–fumed $SiO_2$ CPE (87.4%), and *ex situ* CPE (92.8%). This demonstrates that the *in situ* hydrolysis method markedly enhances the ability of the PEO matrix to dissociate $LiClO_4$. The high dissociation is mainly attributed to the small, highly monodisperse $SiO_2$ particles that provide a large surface area. Consequently, the *in situ* PEO–MU$SiO_2$ CPE exhibits ionic conductivity in the range of $10^{-4}$–$10^{-5}$ S cm$^{-1}$ at room temperature and reaches 1.2 × $10^{-3}$ S cm$^{-1}$ at 60°C, approaching that of liquid electrolytes. Its ionic conductivity at 30 and 60°C was also compared with literature values for similar systems prepared by mechanical mixing.

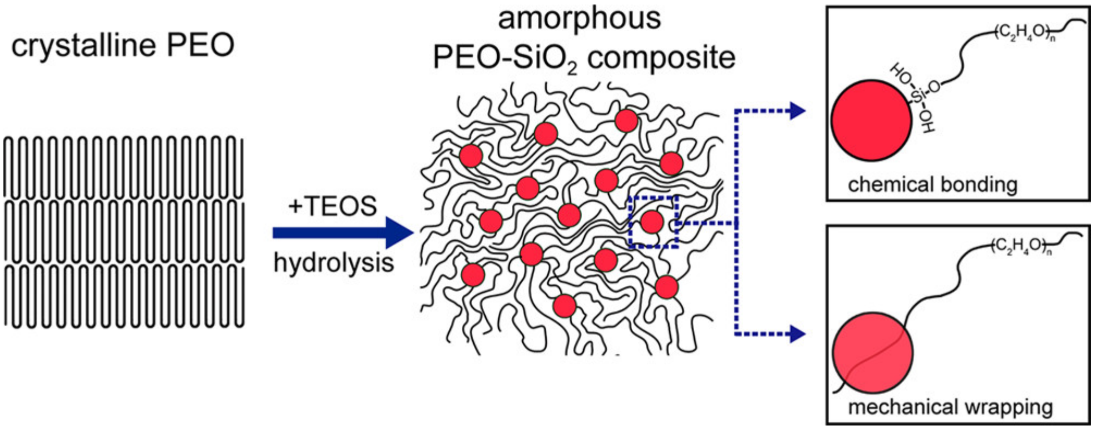

**Figure 4** – Schematic illustration of in-situ preparation of PEO-based composite polymer electrolyte

Lin et al. developed a homogeneous solid composite polymer electrolyte based on $LiClO_4$-doped PEO plasticized with meso-tetra(carboxyphenyl) porphyrin (TCPP), a porphyrin-based COF, using a simple and scalable solution-casting method [39]. The TCPP incorporation significantly enhances the thermal stability of PEO electrolytes to above 330°C and improves $Li^+$ ionic conductivity to $2.34 \times 10^{-5}$ S $cm^{-1}$ at room temperature, enabling safer and more stable lithium-ion battery operation. The authors also explained the interactions between the TCPP filler and the $LiClO_4$-doped PEO polymer electrolyte. They reported that complexation among PEO, $LiClO_4$, and TCPP disrupts the crystallinity of PEO, which in turn enhances the ionic conductivity of the PEO-based electrolyte (Figure 5).

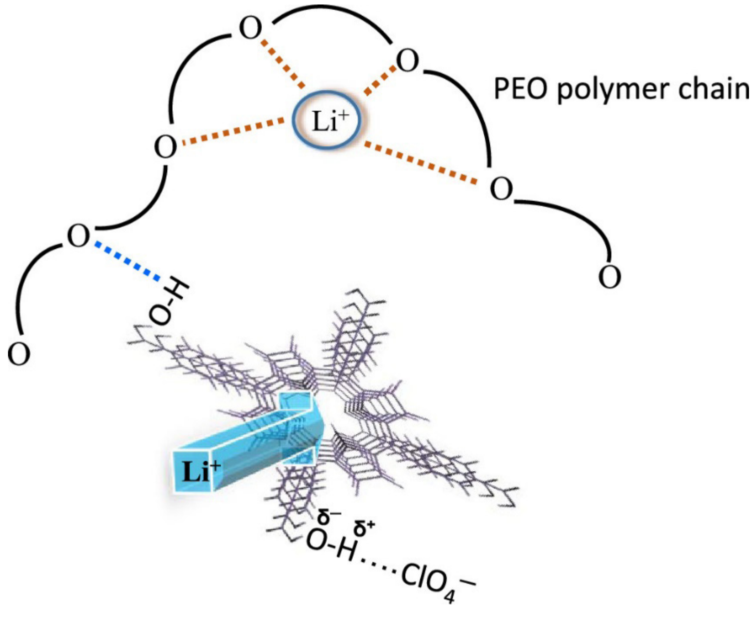

**Figure 5** – Schematic illustration of the interaction between filler, Li salt and PEO [39]

Another strategy to improve the ionic conductivity of solid polymer electrolytes involves the incorporation of ionic liquids (ILs). For instance, Anji Reddy Polu and Hee-Woo Rhee studied the effect of adding the ionic liquid 1-ethyl-3-methylimidazolium bis(trifluoromethylsulfonyl)imide (EMImTFSI) into a PEO–lithium difluoro(oxalato)borate (LiDFOB) polymer matrix. In this work, solid polymer electrolytes were prepared using a solution-casting technique [40].

The ionic conductivity of PEO-based solid polymer electrolytes can also be enhanced through phase modification induced by the incorporation of ionic liquids. To examine the influence of lithium salt and the ionic liquid EMImTFSI on the semi-crystalline nature of PEO, the authors performed X-ray diffraction (XRD) analysis.

According to the study, the intensity and crystallinity of the XRD peaks of pure PEO were noticeably reduced after incorporating LiDFOB into the PEO matrix. The complete dissolution of the lithium salt in the PEO matrix was demonstrated by the absence of LiDFOB diffraction peaks in any of the polymer electrolyte membranes. The peak intensities further dropped as the IL concentration increased when the ionic liquid was added to the PEO20–LiDFOB polymer electrolyte. This indicates that the polymer electrolytes' crystallinity was significantly reduced as a result of coordination contacts between $Li^+$ and EMIm cations with the ether oxygen atoms of PEO. Consequently, the energy barrier for segmental motion of polymers was reduced. According to conductivity experiments, adding LiDFOB enhanced the ionic conductivity to $1.2 \times 10^{-1}$ $S \cdot cm^{-1}$, which is three orders of magnitude higher than that of pure PEO. The PEO20–LiDFOB polymer electrolyte's ionic conductivity was further improved by the addition of ionic liquid, reaching $9.44 \times 10^{-1}$ $S \cdot cm^{-1}$ at ambient temperature and $1.85 \times 10^{-1}$ $S \cdot cm^{-1}$ at 30°C.

Polu and co-authors achieved a maximum ionic conductivity of $1.85 \times 10^{-4}$ $S \cdot cm^{-1}$ at 30°C for a 40 wt% IL content, demonstrating that ionic-liquid-incorporated PEO–LiDFOB polymer electrolytes are among the most promising candidates for lithium-ion batteries.

Lu et al. constructed a free-standing and flexible polymer electrolyte film based on a lithium-containing zwitterionic poly(ionic liquid) (PIL), with and without propylene carbonate (PC), via in-situ photopolymerization [41]. In this work, a polymerizable ionic liquid, [VIPS][LiTFSI], was synthesized by equimolar neutralization of the imidazolium-type zwitterion 3-(1-vinyl-3-imidazolio)propanesulfonate (VIPS) with lithium bis(trifluoromethylsulfonyl)imide (LiTFSI), driven by intermolecular electrostatic interactions. Upon UV cross-linking, the lithium-containing IL was polymerized into a flexible, free-standing electrolyte film.

The ionic conductivities of the pure PIL film and gel polymer electrolyte films containing different PC contents were measured using the alternating current (AC) impedance method. As shown in Figure 6, all electrolyte films demonstrated a progressive increase in ionic conductivity with increasing temperature. Specifically, in the range of 30-150°C, the pure PIL film without PC exhibited an increase in ionic conductivity from $2.4 \times 10^{-5}$ to $2.9 \times 10^{-3}$ $S \cdot cm^{-1}$.

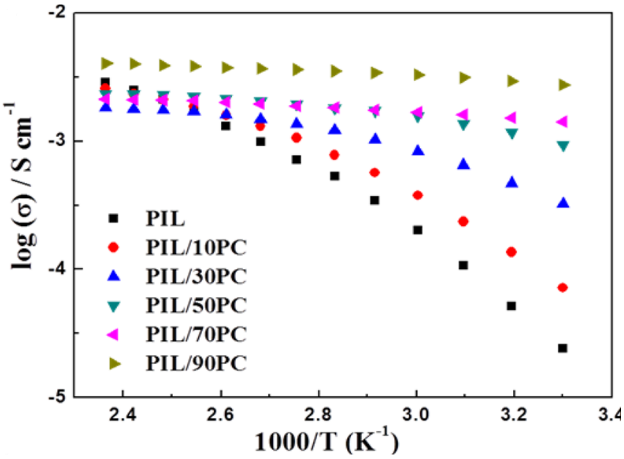

**Figure 6** – Temperature-dependent ionic conductivity of PIL/χPC polymer electrolytes (χ denotes the weight fraction of PC) [41]

The authors revealed that with the addition of PC, the ionic conductivities significantly increased to $\sim 10^{-3}$ at room temperature because of the further ion−dipole interaction between $Li^+$ and PC.

*b) Strategies to Improve the Thermal and Chemical Stability of SPEs*

Safety remains one of the major challenges limiting the widespread application of LIBs in the electric vehicle market. A critical strategy for enhancing thermal safety lies in tailoring the battery chemistry. Thermal failure of solid electrolytes and cathode–electrolyte interfaces (CEIs), as well as the underlying mechanisms, have been comprehensively discussed by Zu *et al.* [42]. The authors emphasized that the electrolyte composition, electrode type, and processing technique have a significant impact on the SEI/CEI's thermal stability.

Using chemicals to strengthen the SEI/CEI and improve its thermal robustness through precursor processes is one intriguing strategy. Tang *et al.* [43] demonstrated this by introducing two-dimensional (2D) additives, specifically few-layer vermiculite (VS) clay sheets, into PEO-based solid polymer electrolytes. With the incorporation of VS, the polymer electrolyte exhibited significant improvements in thermal stability, mechanical modulus, ionic conductivity, electrochemical stability, reduced flammability, and lower interfacial resistance.

The composite SPE was prepared by solution casting of a homogeneous mixture of PEO, LiTFSI, and VS in acetonitrile, and its thermal properties were compared with those of pristine PEO/LiTFSI SPE (Figure 7). As expected, the pristine SPE film underwent severe shrinkage at temperatures above 120°C, which could potentially lead to catastrophic short-circuiting between electrodes. In contrast, the VS-containing composite SPE maintained dimensional stability even above 200°C. The 2D VS effectively suppressed the melting-induced shrinkage of PEO and preserved the structural integrity of the composite, confirming its role in improving the high-temperature stability of SPEs.

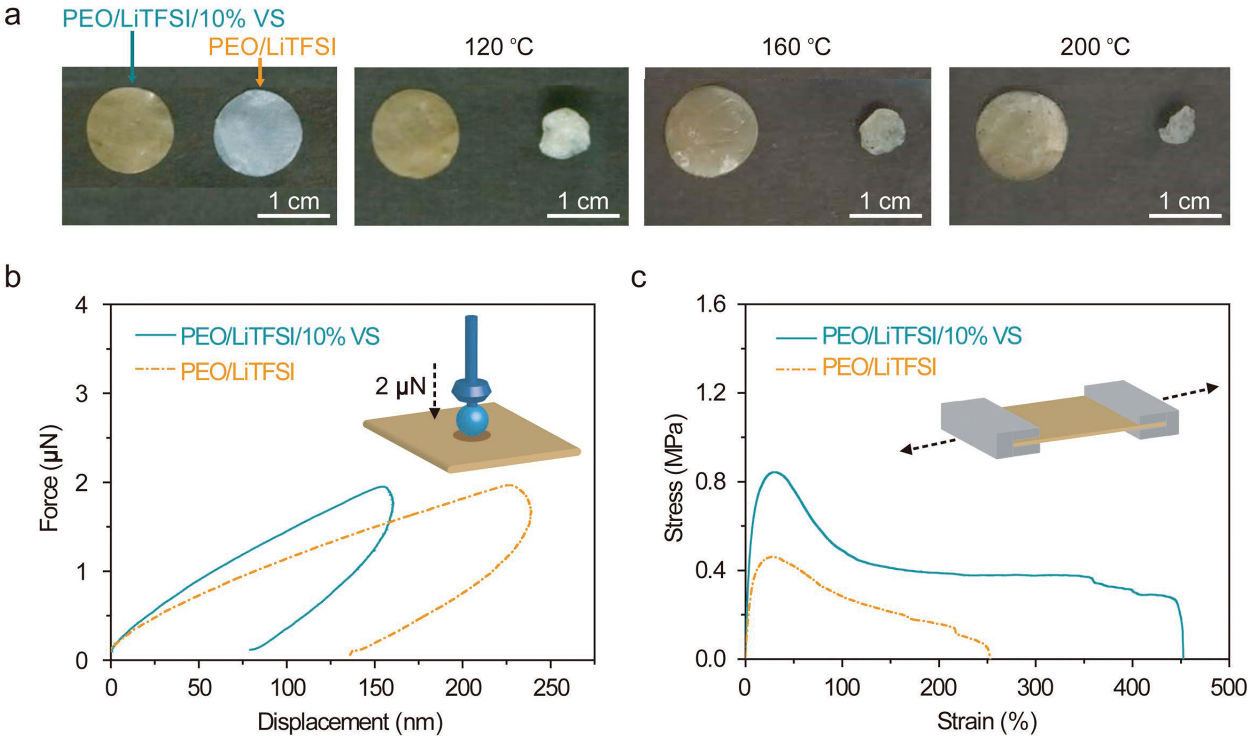

(a) photographs of VS composite and pristine SPEs before and after 30 min heat treatment at different temperatures;
(b) nanoindentation load–displacement curves; (c) tensile stress–strain curves of VS composite and pristine SPEs

**Figure 7** – Enhanced thermal and mechanical stability of SPEs with VS [43]

In addition to 2D filler approaches, certain functional components–including C=C, N≡C, halogen, phosphorus, sulfur, phenol, organic borates, boranes, and silanes–have been shown to promote the formation of thermally stable SEI/CEI layers [12, 44]. Another effective method is in situ polymerization/solidification, which can simultaneously enhance electrochemical, chemical, and thermal stability of polymer electrolytes [45]. Furthermore, a carefully designed fabrication procedure can help minimize interfacial resistance, a critical requirement for the ideal SEI/CEI.

Recent advances suggest that SPEs modified with inorganic fillers, vertically aligned channels, or layered sheet structures represent some of the most promising designs, offering a balance of thermal stability, high ionic conductivity, and long-term electrochemical stability [46-49].

## Conclusion

Solid polymer electrolytes have emerged as one of the most promising alternatives to liquid electrolytes for next-generation lithium-ion batteries due to their potential for enhanced safety, mechanical flexibility, and wide electrochemical stability windows. However, their practical deployment is still challenged by issues of relatively low ionic conductivity at room temperature, limited $Li^+$ transference numbers, and interfacial instability with electrodes.

Recent developments have shown that structural changes, including side-chain engineering, copolymerization, and the addition of aliphatic carbonate units, can successfully reduce polymer crystallinity and promote $Li^+$ transport. In the meantime, by weakening $Li^+$ coordination and improving ion dissociation, the development of ionic liquids, zwitterionic groups, and quaternary ammonium salts has opened up new ways to boost conductivity and transference numbers.

Strategies to deal with chemical and thermal stability are equally significant. The mechanical robustness, flame retardancy, and thermal endurance of polymer electrolytes have been greatly enhanced by the addition of 2D fillers (such as vermiculite sheets), inorganic nanoparticles, vertically oriented channels, and functional chemical groups. The simultaneous improvement of interfacial compatibility, electrochemical performance, and structural integrity is further made possible by in situ polymerization processes.

Overall, the ongoing development of SPEs necessitates a synergistic strategy that combines sophisticated processing techniques, functional additives, and polymer chemistry design. SPEs are anticipated to be crucial in enabling solid-state lithium-ion batteries with high energy density, safety, and durability for electric vehicles and large-scale energy storage as long as they continue to advance.

## Acknowledgements

This research was supported by the Scientific Committee of the Ministry of Science and Higher Education of the Republic of Kazakhstan within the framework of the project AP26196153 “Innovative composite polymer electrolytes for next-generation lithium-ion batteries”.

## Conflict of interest

No conflicts of interest are disclosed by the authors.

## References

1. Whittingham M.S. (1976) Electrical Energy Storage and Intercalation Chemistry.
2. Scrosati B., Garche J. (2010) Lithium batteries: Status, prospects and future. *J. Power Sources*, vol. 195, no. 9, pp. 2419–2430. https://doi.org/10.1016/j.jpowsour.2009.11.048.
3. Harper G., et al. (2019) Recycling lithium-ion batteries from electric vehicles. *Nature*, vol. 575, no. 7781, pp. 75–86. https://doi.org/10.1038/s41586-019-1682-5.
4. Liu J.б et al. (2019) Nonflammable and High-Voltage-Tolerated Polymer Electrolyte Achieving High Stability and Safety in 4.9 V-Class Lithium Metal Battery. *ACS Appl Mater Interfaces*, 11, 48, 45048–45056. https://doi.org/10.1021/acsami.9b14147.
5. Xu R., et al. (2021) Facile and Powerful in Situ Polymerization Strategy for Sulfur-Based All-Solid Polymer Electrolytes in Lithium Batteries. *ACS Appl Mater Interfaces*, vol. 13, no. 29, pp. 34274–34281, 2021, https://doi.org/10.1021/acsami.1c07805.
6. X. Wang et al. (2019) Rechargeable solid-state lithium metal batteries with vertically aligned ceramic nanoparticle/polymer composite electrolyte. *Nano Energy*, vol. 60, pp. 205–212. https://doi.org/10.1016/j.nanoen.2019.03.051.
7. Tian X., et al. (2020) Self-healing and high stretchable polymer electrolytes based on ionic bonds with high conductivity for lithium batteries. *J Power Sources*, vol. 450. https://doi.org/10.1016/j.jpowsour.2019.227629.
8. Yao P., et al. (2019) Review on Polymer-Based Composite Electrolytes for Lithium Batteries. *Front Chem*, vol. 7, no. August, pp. 1–17. https://doi.org/10.3389/fchem.2019.00522.
9. Kalhoff J., Eshetu G.G., Bresser D., Passerini S. (2015) Safer electrolytes for lithium-ion batteries: State of the art and perspectives. *ChemSusChem*, vol. 8, no. 13, pp. 2154–2175. https://doi.org/10.1002/cssc.201500284.
10. Huang Z., Pan Q., Smith D.M., Li C.Y. (2019) Plasticized Hybrid Network Solid Polymer Electrolytes for Lithium-Metal Batteries. *Adv Mater Interfaces*, vol. 6, no. 2, pp. 1–8. https://doi.org/10.1002/admi.201801445.
11. Orue A., et al. (2022) Enhancing the polymer electrolyte-Li metal interface on high-voltage solid-state batteries with Li-based additives inspired by the surface chemistry of $Li_7La_3Zr_2O_{12}$. *J Mater Chem A Mater*, vol. 10, no. 5, pp. 2352–2361. https://doi.org/10.1039/d1ta08362g.
12. Zhao Y., Bai Y., Li W., An M., Bai Y., Chen G. (2020) Design strategies for polymer electrolytes with ether and carbonate groups for solid-state lithium metal batteries. *Chemistry of Materials*, vol. 32, no. 16, pp. 6811–6830. https://doi.org/10.1021/acs.chemmater.9b04521.
13. Choudhury S., et al. (2019) Solid-state polymer electrolytes for high-performance lithium metal batteries. *Nat Commun*, vol. 10, no. 1. https://doi.org/10.1038/s41467-019-12423-y.
14. Yue H., et al. (2018) Sandwich-Like Poly(propylene carbonate)-Based Electrolyte for Ambient-Temperature Solid-State Lithium Ion Batteries. *ACS Sustain Chem Eng*, vol. 6, no. 1, pp. 268–274. https://doi.org/10.1021/acssuschemeng.7b02401.
15. Meyer W.H. (1998) Polymer Electrolytes for Lithium-Ion Batteries. *Adv. Mat.*, vol. 10, is. 6, pp. 439-448. https://doi.org/10.1002/(SICI)1521-4095(199804)10:6<439::AID-ADMA439>3.0.CO;2-I.

16. Zhao Y., et al. (2021) Solid Polymer Electrolytes with High Conductivity and Transference Number of Li Ions for Li-Based Rechargeable Batteries. *Advanced Science*, vol. 8, no. 7, pp. 1–22. https://doi.org/10.1002/advs.202003675.

17. Meabe L., Goujon N., Li C., Armand M., Forsyth M., Mecerreyes D. (2020) Single-Ion Conducting Poly(Ethylene Oxide Carbonate) as Solid Polymer Electrolyte for Lithium Batteries. *Batter Supercaps*, vol. 3, no. 1, pp. 68–75. https://doi.org/10.1002/batt.201900119.

18. Suk J., et al. (2016) Semi-interpenetrating solid polymer electrolyte based on thiol-ene cross-linker for all-solid-state lithium batteries. *J Power Sources*, vol. 334, pp. 154–161. https://doi.org/10.1016/j.jpowsour.2016.10.008.

19. Armand Michel (1990) Polymers with Ionic Conductivity. *Advanced Materials*, vol. 2, no. 617, pp. 278–286.

20. Kilue A., Lenest J., Gandini A., I H.C. (1982) Conductivity of Polyether-polyurethane Networks. vol. 358, pp. 351–358.

21. Wang J., Yang J., Shen L., Guo Q., He H., Yao X. (2021) Synergistic Effects of Plasticizer and 3D Framework toward High-Performance Solid Polymer Electrolyte for Room-Temperature Solid-State Lithium Batteries. *ACS Appl Energy Mater*, vol. 4, no. 4, pp. 4129–4137. https://doi.org/10.1021/acsaem.1c00468.

22. Karuppasamy K., Vijil Vani C., Antony R., Balakumar S., Sahaya Shajan X. (2013) Effect of succinonitrile and nano-hydroxyapatite on ionic conductivity and interfacial stability of polyether-based plasticized nanocomposite polymer electrolytes (PNC-SPE). *Polymer Bulletin*, vol. 70, no. 9, pp. 2531–2545. https://doi.org/10.1007/s00289-013-0970-8.

23. Toshiyuki Momma, Hiroaki Ito, Hiroki Nara, Hitomi Mukaibo, Stefano Passerini, Tetsuya Osaka (2003) Characteristics of Interpenetrated Polymer Network System made of Polyethylene Oxide-LiBF4 Complex and Polystyrene as the Electrolyte for Lithium Secondary Battery. *Electrochemistry*, 71(12), pp. 1182-1186. https://doi.org/10.5796/electrochemistry.71.1182.

24. Manthiram A. (2017) An Outlook on Lithium Ion Battery Technology. *ACS Cent Sci*, vol. 3, no. 10, pp. 1063–1069. https://doi.org/10.1021/acscentsci.7b00288.

25. Golozar M., et al. (2019) In situ observation of solid electrolyte interphase evolution in a lithium metal battery. *Commun Chem*, vol. 2, no. 1, pp. 1–9. https://doi.org/10.1038/s42004-019-0234-0.

26. Wu X., et al. (2019) Safety issues in lithium ion batteries: Materials and cell design. *Front Energy Res*, vol. 7, no. JUL, pp. 1–17. https://doi.org/10.3389/fenrg.2019.00065.

27. Möhl G.E., Metwalli E., Müller-Buschbaum P. (2018) In Operando Small-Angle X-ray Scattering Investigation of Nano-structured Polymer Electrolyte for Lithium-Ion Batteries. *ACS Energy Lett*, vol. 3, no. 7, pp. 1525–1530. https://doi.org/10.1021/acsenergylett.8b00763.

28. Aldalur I., Martinez-Ibañez M., Krztoń-Maziopa A., Piszcz M., Armand M., Zhang H. (2019) Flowable polymer electrolytes for lithium metal batteries. *J Power Sources*, vol. 423, no. March, pp. 218–226. https://doi.org/10.1016/j.jpowsour.2019.03.057.

29. Wu J., Yuan L., Zhang W., Li Z., Xie X., Huang Y. (2021) Reducing the thickness of solid-state electrolyte membranes for high-energy lithium batteries. *Energy Environ Sci*, vol. 14, no. 1, pp. 12–36. https://doi.org/10.1039/d0ee02241a.

30. Zhang X., Chu Y., Cui X., Li Y., Pan Q. (2021) An ultra-thin polymer electrolyte based on single-helical-structured agarose for high performance solid-state lithium batteries. *J Mater Chem A Mater*, vol. 9, no. 47, pp. 26939–26948. https://doi.org/10.1039/d1ta08195k.

31. Wan J., et al. (2019) Ultrathin, flexible, solid polymer composite electrolyte enabled with aligned nanoporous host for lithium batteries. *Nat Nanotechnol*, vol. 14, no. 7, pp. 705–711. https://doi.org/10.1038/s41565-019-0465-3.

32. Sun M., et al. (2021) Ultrathin polymer electrolyte film prepared by in situ polymerization for lithium metal batteries. *Mater Today Energy*, vol. 21, p. 100785. https://doi.org/10.1016/j.mtener.2021.100785.

33. Wu J.F., Guo X. (2019) MOF-derived nanoporous multifunctional fillers enhancing the performances of polymer electrolytes for solid-state lithium batteries. *J Mater Chem A Mater*, vol. 7, no. 6, pp. 2653–2659. https://doi.org/10.1039/c8ta10124h.

34. Meabe L., et al. (2017) Polycondensation as a Versatile Synthetic Route to Aliphatic Polycarbonates for Solid Polymer Electrolytes. *Electrochim Acta*, vol. 237, pp. 259–266. https://doi.org/10.1016/j.electacta.2017.03.217.

35. Mindemark J., Sun B., Törmä E., Brandell D. (2015) High-performance solid polymer electrolytes for lithium batteries operational at ambient temperature. *J Power Sources*, vol. 298, pp. 166–170. https://doi.org/10.1016/j.jpowsour.2015.08.035.

36. Morioka T., Ota K., Tominaga Y. (2016) Effect of oxyethylene side chains on ion-conductive properties of polycarbonate-based electrolytes. *Polymer* (Guildf), vol. 84, pp. 21–26. https://doi.org/10.1016/j.polymer.2015.12.036.

37. Tan J., et al. (2020) Polycation ionic liquid tailored PEO-based solid polymer electrolytes for high temperature lithium metal batteries. *Energy Storage Mater*, vol. 33, no. July, pp. 173–180. https://doi.org/10.1016/j.ensm.2020.08.009.

38. Dingchang Lin, Wei Liu, Yayuan Liu, Hye Ryoung Lee, Po-Chun Hsu, Kai Liu, Yi Cui (2016) High Ionic Conductivity of Composite Solid Polymer Electrolyte via In Situ Synthesis of Monodispersed $SiO_2$ Nanospheres in Poly(ethylene oxide). *Nano Lett.*, 16, 1, pp. 459–465. https://doi.org/10.1021/acs.nanolett.5b04117.

39. Wen-Yin Ko, Meng-Shan Lee, Han-Chung Hsu, and Kuan-Jiuh Lin (2021) One-Pot Green Synthesis of a PEO/TCPP/LiClO4 Solid Polymer Electrolyte with Improvement of Ion Transport. *J. Phys. Chem. C*, 125, pp. 22960−22969. https://doi.org/10.1021/acs.jpcc.1c05376.

40. Polu A.R., Rhee H.W. (2017) Ionic liquid doped PEO-based solid polymer electrolytes for lithium-ion polymer batteries. *Int J Hydrogen Energy*, vol. 42, no. 10, pp. 7212–7219. https://doi.org/10.1016/j.ijhydene.2016.04.160.

41. Lu F., Gao X., Wu A., Sun N., Shi L., Zheng L. (2017) Lithium-Containing Zwitterionic Poly(Ionic Liquid)s as Polymer Electrolytes for Lithium-Ion Batteries. *Journal of Physical Chemistry C*, vol. 121, no. 33, pp. 17756–17763. https://doi.org/10.1021/acs.jpcc.7b06242.

42. Zu C., Yu H., Li H. (2021) Enabling the thermal stability of solid electrolyte interphase in Li-ion battery. *InfoMat*, vol. 3, no. 6, pp. 648–661. https://doi.org/10.1002/inf2.12190.

43. Tang W., et al. (2018) Simultaneously Enhancing the Thermal Stability, Mechanical Modulus, and Electrochemical Performance of Solid Polymer Electrolytes by Incorporating 2D Sheets. *Adv Energy Mater*, vol. 8, no. 24. https://doi.org/10.1002/aenm.201800866.

44. Mackanic D.G., et al. (2018) Crosslinked Poly(tetrahydrofuran) as a Loosely Coordinating Polymer Electrolyte. *Adv Energy Mater*, vol. 8, no. 25. https://doi.org/10.1002/aenm.201800703.

45. Wu H., et al. (2020) LiDFOB Initiated In Situ Polymerization of Novel Eutectic Solution Enables Room-Temperature Solid Lithium Metal Batteries. *Advanced Science*, vol. 7, no. 23, pp. 1–9. https://doi.org/10.1002/advs.202003370.

46. Zhang S., et al. (2020) Room-temperature, high-voltage solid-state lithium battery with composite solid polymer electrolyte with in-situ thermal safety study. *Chemical Engineering Journal*, vol. 400, p. 125996. https://doi.org/10.1016/j.cej.2020.125996.

47. Nurgaziyeva E., Turlybay G., Tugelbayeva A., Mentbayeva A., Kalybekkyzy S. (2024) PTHF/LATP Composite Polymer Electrolyte for Solid State Batteries. *Polymers*, 16(22), pp. 3176. https://doi.org/10.3390/polym16223176.

48. Nurgaziyeva E., Mentbayeva A., Bakenov Z., Kalybekkyzy S. (2024) Crosslinked polytetrahydrofuran-based solid-state electrolytes with improved mechanical stability and electrochemical performance. *Appl Mater Today*, vol. 40. https://doi.org/10.1016/j.apmt.2024.102417.

49. Turlybay G., Nurgaziyeva E., Issayeva D., Mentbayeva A., Bakenov Z., Kalybekkyzy S. (2023) Synthesis and Characterization of LATP Solid Electrolyte by Solution Method. *International Journal of Biology and Chemistry,* 16 (2), pp. 123-28. https://doi.org/10.26577/IJBCh2023v16i2a13.

***Information about authors:***

*Nazerke Zhumasheva – PhD in Chemical Technology of Inorganic Substances, Researcher, National Laboratory Astana, Nazarbayev University (Astana, Kazakhstan, e-mail: nazerke.zhumasheva@nu.edu.kz).*

*Elmira Nurgaziyeva – PhD in Chemistry, Senior Researcher, National Laboratory Astana, Nazarbayev University (Astana, Kazakhstan, e-mail: elmira.nurgaziyeva@nu.edu.kz).*

IRSTI 31.27.21 https://doi.org/10.26577/IJBCh202518215

S. Kherouf[1], Y. Driouche[2], N. Bouarra[3, 4*]

[1]Organic Synthesis Laboratory Modeling and Optimization of Chemical Processes (LOMOP),
Badji Mokhtar University, Annaba, Algeria
[2]Environmental Research Center (CRE), Annaba, Algeria
[3]Center of Scientific and Technical Research in Physico-Chemical Analysis, Bou-Ismail, Tipaza, Algeria
[4]Laboratory of Environmental Engineering, Badji Mokhtar University, Annaba, Algeria
*e-mail: bouarranabil@yahoo.com/bouarra.nabil@crapc.dz

*(Received 11 November 2025; received in revised form 19 December 2025; accepted 25 December 2025)*

# Linking molecular structure to chromatographic behavior: a quantitative structure-retention relationship study of *Olea europaea* L. essential oil components

**Abstract.** A robust quantitative structure-retention relationship (QSRR) model was developed to accurately predict the linear retention indices (LRI) of 51 essential oil compounds. Molecular descriptors were calculated using alvaDesc software, and model construction was achieved through a multiple linear regression (MLR) approach. A rigorous variable selection process identified relevant descriptors, resulting in a statistically significant model with strong predictive performance ($R^2 = 0.9533$, $Q^2_{LOO} = 0.9339$, $Q^2_{LMO} = 0.9293$, $RMSE_{tr} = 55.0581$, $s = 50.0169$). External validation further confirmed the model's reliability, demonstrating excellent predictive capability ($R^2_{ext} = 0.9381$, $Q^2_{F1} = 0.9361$, $Q^2_{F2} = 0.9354$, $Q^2_{F3} = 0.9646$, $CCC_{ext} = 0.9663$, $RMSE_{ext} = 40.3308$). The findings highlight the efficiency of the QSRR-MLR model in predicting retention indices, providing valuable insights into molecular properties influencing compound retention. Additionally, the applicability domain assessment ensured reliable predictions within the studied chemical space. This methodology offers a deeper understanding of chromatographic behavior and presents potential for application to other chemical classes for predictive modeling.

**Keywords:** QSRR, essential oil, volatile chemicals, prediction set, validation.

## Introduction

The essential oils are aromatic and volatile chemicals extracted from plants by distillation under steam [1]. They smell like the original plant they were taken from. Essential oils have been used for therapeutic purposes for thousands of years; they are also fascinating and potent plant-based substances. They have been quite significant up till the current day. Essential oils also have various uses in the fields of flavoring, food, perfume, and the cosmetics industry [2, 3]. The olive tree (*Olea europaea* L.), a member of the *Oleaceae* family, is a regional specialty [4, 5]. Antioxidant, antibacterial, antiviral, hypoglycemic, anti-inflammatory, and anticancer bioactivities are only some of the many attributed to olive bioactive components. Because of its potential health advantages, olive bioactive components have attracted much attention [6].

The primary techniques for identifying these plant oils are gas chromatography (GC) and liquid chromatography (LC). In GC analysis, volatile chemicals or molecules with low volatility which may be chemically transformed to more appropriate molecules are often separated and analyzed using this approach [7]. When utilized under controlled analytical circumstances, the GC's single output parameter (retention index) allows for the identification of any volatile chemical [6]. Several intermolecular interactions, including dipole-diploe forces, dipole-induced forces, hydrogen bonds, etc., affect whether a compound elutes or is retained [8]. Looking for a quantitative link between molecular structure and GC retention indices is a fundamental task in chemistry. More theoretical depth may be gained by understanding the relationships between mobile and stationary phases by correlating retention time values and molecular structure. In addition, they may provide crucial details on how chemical structure influences retention behavior and potential absorption and elution processes [9].

One of the aims of this scientific endeavor is to allow accurate prediction of physicochemical properties of compounds based only on their

© 2025 al-Farabi Kazakh National University

molecular structure [10]. Many different approaches can be employed in establishing a relationship between the molecular structure of a compound and the physicochemical characteristics; quantitative structure-property relationship (QSPR) is one of the successful methods that has been used for this purpose. Each QSPR study has as its foundation the pursuit of optimal quantitative relationships for use in property prediction from molecular structures [11]. Once a solid relationship has been established, it may be used to predict similar characteristics in other buildings that are still without any kind of measurement or even design. QSRRs are statistical models that allow for the prediction of retention indices of new compounds by quantifying the relationship between a molecule's structure and its chromatographic retention index [12]. These relationships may provide theoretical light on the complex interplay that occurs between chemicals, mobile phases, and stationary phases during chromatographic analyses. They are also able to give useful information on the influence of the structure of the chemicals on the behavior of retention as well as the probable mechanisms behind adsorption and elution processes [13]. Studies using QSRR to estimate retention indices (RI) for a variety of organic compounds have been published in recent years. Choosing the right set of variables is essential for these methods to provide accurate predictions [14, 15].

Recent studies have focused on enhancing QSRR models by incorporating advanced feature selection techniques and expanding datasets to improve prediction accuracy and robustness. Some used multiple linear regression (MLR) and partial least squares (PLS) models with descriptors chosen by a genetic algorithm to predict retention for 80 oils including 20 test compounds [16, 17]. The support vector machine (SVM) nonlinear models were used in other studies employing the same dataset as a means of enhancing prediction performance [16]. In other work, QSRR models have also been published for retention indices of essential oils using GA with MLR or PLS, kernel PLS and Levenberg-Marquardt artificial neural networks [18-20]. Driouche and Messadi [21] developed a QSRR model for the prediction of retention indices of essential oil constituents from *Thymus vulgaris Lamiaceae* and demonstrated its efficiency and reliability through external validation. Navabi et al. [22] developed a GA-MLR and GA-BPANN model for predicting retention indices of essential oil components in Polygonum minus essential oil.

The objective of this study is to develop a robust QSRR model for predicting the retention indices of 51 essential oil components derived from *Olea europaea* L. grown in Mediterranean and arid regions of Algeria. By employing advanced statistical methods and validation techniques, this work aims to provide accurate and reliable predictions of LRIs, contributing to a deeper understanding of the chromatographic behavior of essential oils and their molecular properties.

## Materials and methods

### *Dataset collection*

This study used experimental linear retention index (LRI) data sourced from the work of Tlili et al. [23]. The LRI values, presented in Table 2, were determined through GC-MS analysis were performed with a Varian CP-3800 gas-chromatograph equipped with a DB-5 capillary column and a Varian Saturn 2000 ion trap mass detector. The dataset includes 51 volatile compounds identified in *Olea europaea* L. cultivars, providing detailed insight into their chromatographic retention characteristics.

### *Descriptors generation*

The structures of the compounds are produced using MarvinSketch V24.3.0 [24]. Thereafter, PM7 semi-empirical method has been used in MOPAC software (version 2016, Stewart Computational chemistry) [25] to improve the finale geometry. The resulting minimum-energy conformations were used to calculate three-dimensional geometrical descriptors with alvaDesc (version 3.0.4) [26]. These descriptors, derived from the 3D arrangement of atoms, capture molecular shape, size, and spatial orientation. They help distinguish between structurally similar compounds and reflect conformational variability across molecules.

### *Dataset Division*

The current challenge in QSRR model development is building a model that can accurately predict the behavior of new chemical compounds. When external experimental data are not available for validation, a common approach is to divide the available dataset into two parts: a training set used to construct the model, and a prediction set used to assess its predictive performance. The prediction set typically represents 15 to 40% of the total dataset [27].

In this study, the Kennard and Stone algorithm (CADEX) [28], was used to divide the 51 compounds based on their molecular descriptors. This deterministic method ensures an even and representative distribution of samples across the descriptor space. The algorithm starts by selecting the two most dissimilar samples using Euclidean distance, then iteratively adds the next most distant compound from those already selected. This process continues until all compounds are ranked.

The dataset was split into a training set of 35 compounds and a prediction set of 16 compounds. The training set was used to establish the relationship between the descriptors and the linear retention index (LRI), while the prediction set was used to evaluate the model's robustness, goodness-of-fit, and external predictive power.

*Model development and validation*

The quantitative structure-retention relationship (QSRR) model was developed using the Multiple Linear Regression (MLR) technique, based on the ordinary least squares (OLS) method as implemented in the QSARINS software (version 2.2.4) [29]. This modeling approach was selected for its simplicity, reproducibility, and interpretability. After preparing and splitting the dataset, molecular descriptor selection was performed on the training set by evaluating all possible combinations of up to four descriptors. This step ensured exhaustive coverage of low-dimensional models before considering more complex ones. The optimal model was chosen based on its leave-one-out cross-validation coefficient ($Q^2_{LOO}$), ensuring a balance between predictive performance and model simplicity.

The final regression equation takes the general form of:

$$\hat{y} = b_0 + b_1x_1 + b_2x_2 + \ldots + b_nx_n \quad (1)$$

where $\hat{y}$ is the predicted linear retention index (LRI); $x_i$ are the selected molecular descriptors, and $b_i$ are their respective regression coefficient. Only descriptor with p-values ≤ 0.05 were retained to ensure statistical significance and reduce overfitting.

To assess internal model performance and robustness, two cross-validation techniques were applied: Leave-One-Out (LOO) and Leave-Many-Out (LMO). The $Q^2_{LOO}$ value, indicating how well the model predicts compounds not included during training, was calculated using the following equation:

$$Q^2_{LOO} = 1 - \frac{\sum_{i=1}^{n}\left(\hat{y}_{i/i} - y_i\right)^2}{\sum_{i=1}^{n}(y_i - \bar{y})^2} \quad (2)$$

where $y_i$ is the experimental value, $\hat{y}_{i/i}$ is the predicted value for compound $i$ when it is omitted from the training set, and $\bar{y}$ is the mean of the experimental values in the training set.

For external validation, the dataset of 51 compounds was divided using the Kennard and Stone (CADEX) algorithm into training set of 35 compounds and a prediction set of 16 compounds. This deterministic method ensures a representative and uniform distribution across the descriptor space. The model's predictive performance was assessed using several statistical indicators, such as $Q^2_{F1}$, $Q^2_{F2}$, $Q^2_{F3}$ and $CCC_{ext}$ (Eq. 3-8), which have been previously described and discussed in our earlier publications [30-32].

$$Q^2_{F1} = 1 - \frac{PRESS_{EXT}}{SS_{EXT}(\bar{y}_{TR})} \quad (3)$$

$$PRESS_{EXT} = \sum(y_i - \hat{y}_i)^2 \quad (4)$$

$$Q^2_{F2} = 1 - \frac{PRESS_{EXT}}{SS_{EXT}(\bar{y}_{EXT})} \quad (5)$$

$$SS_{EXT}(\bar{y}_{EXT}) = \sum(y_i - \bar{y}_{EXT})^2 \quad (6)$$

$$Q^2_{F3} = 1 - \frac{\left(\frac{PRESS_{EXT}}{n_{EXT}}\right)}{\left(\frac{TSS}{n_{TR}}\right)} \quad (7)$$

$$CCC_{ext} = \frac{2\sum_{i=1}^{n}(y_i - \bar{y})(\hat{y}_i - \bar{\hat{y}})}{\sum_{i=1}^{n}(y_i - \bar{y})^2 + \sum_{i=1}^{n}\left(\hat{y}_i - \bar{\hat{y}}\right)^2 + n\left(\bar{y} - \bar{\hat{y}}\right)^2} \quad (8)$$

where $n_{ext}$ and $n_{tr}$ are the number of compounds in the prediction and training sets, and $\bar{y}_{tr}$ and $\bar{y}_{ext}$ are the means of the training and prediction experimental values.

To verify the statistical robustness and eliminate the possibility of chance correlation, a Y-randomization test (Y-scrambling) was conducted. The dependent variable (LRI) was randomly permuted, and models were rebuilt. A sharp drop in $Q^2$ values after scrambling confirmed the model's validity.

*Applicability domain*

The model's applicability domain was assessed using the Williams plot, which shows standardized residuals alongside leverage values. Williams plots are used to identify outliers and establish a confidence interval for the model's predictions [33]. It guarantees that the investigation adheres to the third principal of the OECD [34]. Leverage is calculated as:

$$h_i = x_i^T (X^T X)^{-1} x_i \qquad (9)$$

where $x_i$ is the descriptor row vector of the query compound, and X is the n*k matrix containing k model descriptor values for n training set compounds. Transpose of matrix/vector denoted by the superscript ’’T’’ the control leverage h* is fixed at (3k+1)/n, where k is the number of model parameters and n is the number of observations used to compute the model. Compounds with $h_i > h^*$ or residuals outside ±3 standard deviations were considered influential or outlier compounds, respectively.

The QSRR-MLR model developed in this study met all these conditions, demonstrating excellent fit, predictive power, and structural interpretability. These results confirm the model’s reliability for predicting LRI values of essential oil constituents and its applicability in chromatographic behavior modeling.

## Results and discussion

*Modeling of the linear retention index (LRI)*

In this study, the linear retention indices (LRI) of essential oil compounds were modeled using a quantitative structure-retention relationship (QSRR) approach based on multiple linear regression (MLR). The modeling was performed using the QSARINS software [29] a robust platform for building, validating, and interpreting QSAR/QSPR models using a genetic algorithm-based variable selection approach and extensive internal and external validation techniques. The regression model is expressed as:

$$\mathbf{LRI}=373.90+1.83\ \mathbf{BertzCT}+116.71\ \mathbf{Hy}+284.87\ \mathbf{Chi1\_EA(ed)}-262.53\ \mathbf{Mor25v} \qquad (10)$$

where: **BertzCT:** Bertz complexity index; **Hy:** Hydrophilic factor; **Chi1_EA(ed)**: Connectivity-like index of order 1 from edge adjacency mat. Weighted by edge degree; **Mor25v**: 3D-MoRSE.signal 25 / weighted by van der Waals volume.

The model’s accuracy and predictive performance were evaluated using key statistical metrics summarized in Table 1.

**Table 1** – Statistical performance indicators for the training and prediction sets

| Statistical Parameters | | | |
|---|---|---|---|
| Training Set | | Prediction Set | |
| $R^2$ | 0.954 | $R^2_{ext}$ | 0.915 |
| $Q^2_{LOO}$ | 0.946 | $Q^2_{F1}$ | 0.909 |
| $RMSE_{tr}$ | 25.70 | $Q^2_{F2}$ | 0.904 |
| s | 23.40 | $Q^2_{F3}$ | 0.910 |

The QSRR model shows strong statistical performance in both training and prediction sets. In the training phase, the model achieved an $R^2$ of 0.954, indicating that 95.4% of the variation in experimental LRI values is captured by the selected descriptors. The $Q^2_{LOO}$ value of 0.946, close to $R^2$, confirms model robustness and lack of overfitting. Low RMSE (25.70) and standard error (s=23.40) indicate accurate predictions within the training data. The high Fisher statistic (F=208.50) supports the significance of the regression.

External validation further confirms model reliability. The prediction set yielded $R^2_{ext} = 0.915$, with $Q^2_{F1}$, $Q^2_{F2}$, and $Q^2_{F3}$ all above 0.90, exceeding the OECD’s threshold (>0.5) for valid QSAR models. The external concordance correlation coefficient ($CCC_{ext} = 0.957$) and $RMSE_{ext} = 20.57$ affirm high predictive power and low prediction error. Together, these metrics demonstrate that the model is both statistically sound and externally predictive.

Table 2 illustrates the prediction results and the values of the descriptors used in the model developed.

The coefficients and associated statistical parameters are summarized (Table 3).

**Table 2** – List of names, experimental, predicted LRI, and descriptors values involved in the model

| ID | Name | Status | Exp.LRI | Pred. LRI | BertzCT | Hy | Chi1_EA (ed) | Mor25v |
|---|---|---|---|---|---|---|---|---|
| 1 | hexanal | Tr | 802 | 831.064 | 41.445 | -0.802 | 1.644 | -0.025 |
| 2 | (E)-2-hexenal | Tr | 856 | 875.783 | 64.58 | -0.802 | 1.644 | -0.034 |
| 3 | (Z)-3-hexen-1-ol | Tr | 857 | 914.321 | 48.142 | -0.088 | 1.644 | 0.022 |
| 4 | 1-hexanol | Tr | 869 | 872.599 | 27.361 | -0.088 | 1.644 | 0.036 |
| 5 | n-nonane | Tr | 900 | 907.511 | 33.303 | -0.954 | 2.144 | 0.102 |
| 6 | heptanal | Tr | 903 | 899.535 | 50.349 | -0.828 | 1.894 | 0.036 |
| 7 | (Z)-2-heptenal | Tr | 958 | 955.484 | 74.456 | -0.828 | 1.894 | -0.009 |
| 8 | 6-methyl-5-hepten-2-one | Tr | 987 | 985.815 | 118.529 | -0.848 | 1.695 | -0.042 |
| 9 | (E,E)-2,4-heptadienal | Tr | 1011 | 980.633 | 100.954 | -0.828 | 1.894 | 0.08 |
| 10 | limonene | Tr | 1032 | 1064.477 | 162.877 | -0.96 | 1.779 | 0.009 |
| 11 | phenylacetaldehyde | Tr | 1045 | 1074.079 | 170.744 | -0.848 | 1.919 | 0.229 |
| 12 | n-undecane | Tr | 1100 | 1099.823 | 49.059 | -0.965 | 2.644 | 0.017 |
| 13 | linalool | Tr | 1101 | 1110.171 | 154.256 | -0.294 | 1.733 | 0.021 |
| 14 | phenylethyl alcohol | Tr | 1111 | 1111.710 | 155.406 | -0.213 | 1.919 | 0.261 |
| 15 | (E,E)-2,6-nonadienal | Tr | 1153 | 1194.102 | 122.69 | -0.864 | 2.394 | -0.055 |
| 16 | menthone | Tr | 1154 | 1102.784 | 148.952 | -0.877 | 1.851 | -0.119 |
| 17 | methyl chavicol | Tr | 1197 | 1191.035 | 209.257 | -0.877 | 2.093 | 0.228 |
| 18 | safranal | Tr | 1198 | 1174.535 | 231.257 | -0.877 | 1.655 | -0.031 |
| 19 | -cyclocitral | Tr | 1222 | 1146.305 | 198.918 | -0.877 | 1.655 | -0.149 |
| 20 | 1,2-benzisothiazole | Tr | 1223 | 1205.518 | 245.642 | -0.742 | 1.851 | 0.224 |
| 21 | carvone | Tr | 1244 | 1233.890 | 223.027 | -0.877 | 1.837 | -0.117 |
| 22 | (E)-2-decenal | Tr | 1262 | 1232.220 | 105.44 | -0.877 | 2.644 | -0.055 |
| 23 | bornyl acetate | Tr | 1287 | 1283.986 | 269.495 | -0.835 | 2.12 | 0.342 |
| 24 | (E,Z)-2,4-decadienal | Tr | 1293 | 1253.442 | 133.808 | -0.877 | 2.644 | 0.062 |
| 25 | theaspirane I | Tr | 1298 | 1341.364 | 264.409 | -0.905 | 2.157 | 0.097 |
| 26 | p-vinylguaiacol | Tr | 1314 | 1251.880 | 256.736 | -0.206 | 1.862 | 0.375 |
| 27 | theaspirane II | Tr | 1315 | 1392.556 | 264.409 | -0.905 | 2.157 | -0.098 |
| 28 | phenylethyl propionate | Tr | 1351 | 1381.369 | 245.264 | -0.822 | 2.627 | 0.358 |
| 29 | (E)- -damascenone | Tr | 1382 | 1527.077 | 327.145 | -0.905 | 2.285 | -0.034 |
| 30 | n-tetradecane | Tr | 1400 | 1371.431 | 74.039 | -0.975 | 3.394 | -0.034 |
| 31 | dihydrodehydro- -ionone | Tr | 1422 | 1457.342 | 292.357 | -0.905 | 2.32 | 0.027 |
| 32 | (E)-geranylacetone | Tr | 1454 | 1449.609 | 229.62 | -0.905 | 2.685 | 0.015 |
| 33 | dihydroactinidiolide | Tr | 1536 | 1404.142 | 288.465 | -0.822 | 1.998 | -0.11 |
| 34 | caryophyllene oxide | Tr | 1581 | 1557.778 | 330.327 | -0.917 | 2.521 | 0.122 |
| 35 | benzophenone | Tr | 1627 | 1609.632 | 352.152 | -0.905 | 2.885 | 0.477 |
| 36 | benzaldehyde | Pr | 963 | 951.392 | 158.826 | -0.828 | 1.624 | 0.302 |
| 37 | 3-ethenyl pyridine | Pr | 969 | 998.288 | 172.826 | -0.828 | 1.624 | 0.221 |
| 38 | (E,Z)-2,4-heptadienal | Pr | 997 | 980.896 | 100.954 | -0.828 | 1.894 | 0.079 |
| 39 | octanal | Pr | 1002 | 1011.323 | 59.588 | -0.848 | 2.144 | -0.063 |
| 40 | p-cymene | Pr | 1028 | 1059.216 | 180.078 | -0.96 | 1.779 | 0.149 |
| 41 | 1-octanol | Pr | 1071 | 1030.862 | 43.832 | -0.213 | 2.144 | 0.035 |
| 42 | nonanal | Pr | 1103 | 1082.127 | 69.129 | -0.864 | 2.394 | -0.002 |

*Continuation of the table*

| ID | Name | Status | Exp.LRI | Pred. LRI | BertzCT | Hy | Chi1_EA (ed) | Mor25v |
|---|---|---|---|---|---|---|---|---|
| 43 | 1,4-Dimethyl-DELTA.-3-tetrahydroacetophenone | Pr | 1150 | 1156.890 | 202.918 | -0.877 | 1.707 | -0.105 |
| 44 | (E)-2-nonenal | Pr | 1163 | 1136.662 | 94.901 | -0.864 | 2.394 | -0.03 |
| 45 | 2-phenylethyl formate | Pr | 1177 | 1277.730 | 197.603 | -0.79 | 2.467 | 0.261 |
| 46 | n-dodecane | Pr | 1200 | 1156.257 | 56.439 | -0.969 | 2.894 | 0.123 |
| 47 | n-tridecane | Pr | 1300 | 1279.479 | 66.107 | -0.972 | 3.144 | -0.009 |
| 48 | (E,E)-2,4-decadienal | Pr | 1317 | 1245.304 | 133.808 | -0.877 | 2.644 | 0.093 |
| 49 | eugenol | Pr | 1358 | 1369.930 | 269.563 | -0.244 | 2.157 | 0.318 |
| 50 | (Z)-jasmone | Pr | 1395 | 1340.027 | 233.389 | -0.888 | 2.306 | 0.055 |
| 51 | (E)- -ionone | Pr | 1488 | 1476.244 | 292.357 | -0.905 | 2.32 | -0.045 |

**Table 3** – Characteristic of the descriptors in the optimal MLR model

| Descriptor | Coefficient | Std. Coefficient | Std. Error | (+/-) Co. int. 95% | p-value |
|---|---|---|---|---|---|
| Intercept | 373.90 | – | 44.53 | 90.9323 | 0.000 |
| BertzCT | 1.83 | 0.812 | 0.10 | 0.204 | 0.000 |
| Hy | 116.71 | 0.136 | 41.57 | 84.8926 | 0.0083 |
| Chi1_EA(ed) | 284.87 | 0.561 | 23.57 | 48.1442 | 0.000 |
| Mor25v | -262.53 | -0.189 | 64.93 | 132.6146 | 0.0003 |

The statistical quality of the model is high, as indicated by the very low p-values (< 0.01) for all descriptors, confirming their significant contribution to the prediction of the linear retention index.

Assessing the model's applicability domain is a key part of the validation process. The Williams plot (Fig. 1) shows standardized residuals versus leverage values, which reflect how similar each compound is to those in the training set. All residuals fall within the ±3s range, except for one training compound ((E)- - damascnone), identified as a Y outlier due to a likely error in its experimental value.

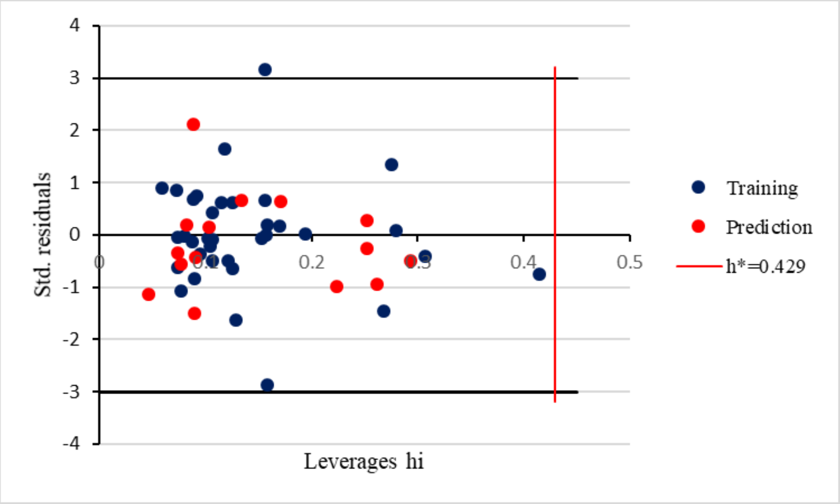

**Figure 1** – Williams plot of the developed MLR model showing standardized residuals versus leverage values

All leverage values ($h_i$) remain below the threshold ($h^* = 0.429$), indicating that no compound exerts excessive influence on the model. This confirms that the MLR model provides reliable linear retention index (LRI) predictions. The model can be applied to screen chemical databases or virtual compounds, using the applicability domain to exclude structurally dissimilar molecules.

Figure 2 shows the correlation between the predicted and experimental linear retention index (LRI) values obtained using the QSRR-MLR model. Red dots represent the training set, while blue dots correspond to the external prediction set. Most points are closely aligned along the diagonal line, indicating a strong agreement between observed and predicted values.

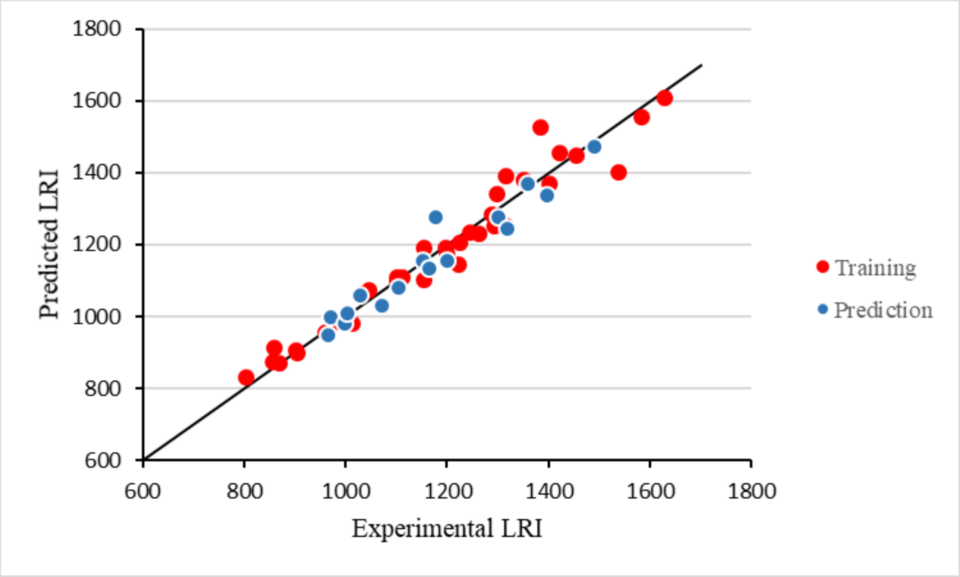

**Figure 2 –** Plot of predicted vs Experimental LRI values

The determination coefficients ($R^2$ = 0954 for the training set and $R^2_{ext}$ = 0.915 for the prediction set) confirm that the model performs well both in fitting the training data and in predicting unseen data. The absence of major outliers supports the robustness and reliability of the regression model in capturing retention behavior based on molecular descriptors.

Figure 3 illustrates the results of the Y-randomization (or Y-scrambling) test used to assess the statistical reliability of the QSRR model. Red and yellow dots represent the $R^2$ and $Q^2$ values, respectively, for models developed from randomly shuffled response data. The blue dots in the upper right corner correspond to the original model's $R^2$ and $Q^2$ values.

The randomized models yield significantly lower $R^2$ and $Q^2$ values, mostly clustered near or below zero, clearly separated from the original model's performance. This confirms that the developed QSRR model is not a result of chance correlations. It demonstrates genuine predictive ability based on meaningful structural information encoded in the selected descriptors.

*Model descriptors interpretation*

The regression model obtained in equation 10, provides a coherent mechanistic view of the chromatographic retention of essential oil compounds on a DB-5 type nonpolar stationary phase. On such a column, the separation mechanisms are mainly governed by London dispersion forces, where retention increases with the size, molecular surface area, and boiling point of the analytes [35]. Analysis of the model coefficients allows us to decipher the quantitative influence of different molecular properties on the retention index.

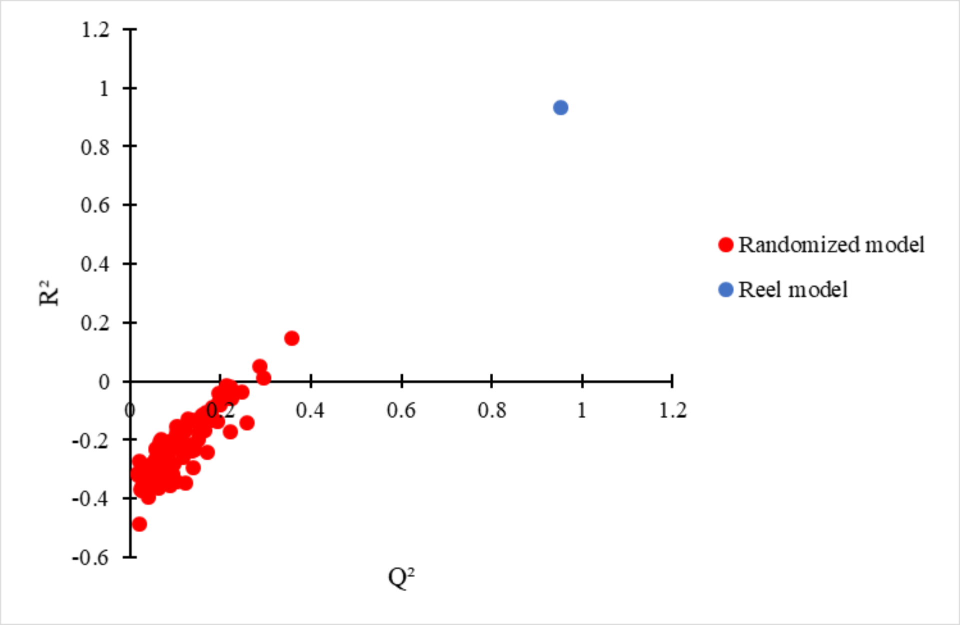

**Figure 3** – Y-Randomization test

The topological descriptor Chi1_EA(ed) (connectivity index) and Bertz complexity index (BertzCT) positively influence retention, with respective coefficients of +284.87 and +1.83. The high coefficient of the Chi1_EA(ed) index reflects the electronic and topological connectivity of a molecule: a high value reflects a more rigid, better connected, and often conjugated or aromatic structure [36]. These characteristics promote polarization and π–π or dispersion interactions with the stationary phase, which prolongs the elution time. Similarly, BertzCT quantifies overall structural complexity by taking into account ramifications, cycles, and types of atoms present [37]. More complex and ramified molecules have an increased contact surface area and interact more strongly with the nonpolar DB-5 phase, which delays their elution. This behavior is well documented in QSRR models based on topological descriptors [38].

The Mor25v descriptor, derived from 3D-MoRSE descriptors, has the most strongly negative coefficient (-262.53), acting as the main factor unfavorable to retention. The 3D-MoRSE descriptors encode precise information about the three-dimensional geometry of the molecule based on simulated electron diffraction [39]. The negative coefficient suggests that this descriptor is an indicator of molecular compactness or sphericity. A more compact molecule, for the same molar mass, has a smaller external contact surface, which significantly reduces the possible dispersion forces with the stationary phase [40]. The negative coefficient suggests that a molecular geometry leading to a more dispersed electron distribution (and therefore a smaller effective contact surface with the stationary phase) promotes faster elution.

The Hy (hydrophilic factor) descriptor has a positive coefficient (+116.71), indicating that polarity contributes modestly but significantly to retention. Although the DB-5 phase is essentially nonpolar, it contains about 5% phenyl groups, whose π electrons are polarizable. Thus, analytes with polar groups (hydroxyl, carbonyl, ester) can interact via induced dipole-dipole forces with the aromatic rings of the phase [40]. These interactions, although secondary to dispersion forces, slightly increase retention. In addition, more polar molecules generally have higher boiling points, which reduces their volatility and indirectly increases their retention. This behavior has already been observed in QSRR studies on polar compounds in essential oils [35]. The Hy (hydrophilic factor) descriptor has a positive coefficient (+116.71), indicating that polarity contributes modestly but significantly to retention. Although the DB-5 phase is essentially non-polar, it contains approximately 5% phenyl groups, whose π electrons are polarizable. Thus, analytes with polar groups (hydroxyl, carbonyl, ester) can interact via induced dipole-dipole forces with the aromatic rings of the phase [40]. These interactions, although secondary to dispersion forces, slightly increase retention. In addition, more polar molecules generally have higher boiling points, which reduces their volatility and indirectly increases their retention. This behaviour has already been observed in QSRR studies on polar compounds in essential oils [35].

## Conclusion

The QSRR-MLR model developed in this work provides an effective and interpretable approach for predicting the linear retention indices (LRI) of 51 essential oil components from *Olea europaea* L. The model, built using a rigorously selected set of molecular descriptors, demonstrates strong statistical performance with high internal ($R^2$ = 0.9533, $Q^2_{LOO}$ = 0.9339) and external validation metrics ($R^2_{ext}$ = 0.9381, $Q^2_{F1-F3} > 0.93$, $CCC_{ext}$ = 0.9663). The selected descriptors reflect key structural features-topological complexity, polarity, connectivity, and 3D molecular shape-that significantly influence chromatographic behavior. The model passed all recommended validation steps, including Y-randomization and applicability domain analysis, confirming its reliability and robustness. These results support the use of QSRR-MLR as a practical and accurate tool for retention time prediction in essential oil analysis. The methodology can be extended to other volatile compounds datasets, facilitating compound identification, optimization of chromatographic methods, and molecular-level understanding of retention mechanisms.

## Acknowledgments

We thank Prof. Paola Gramatica for the free license of QSARINS software. We are thankful to the Algerian Directorate-General for Scientific Research and Technological Development (DGRSDT) for providing financial assistance for this research.

## Conflict of interest

The authors declare that they have no conflicts of interest.

## References

1. Hyldgaard M., Mygind T., Meyer R.L. (2012) Essential oils in food preservation: mode of action, synergies, and interactions with food matrix components. *Front Microbiol*., vol. 3, p. 12. https://doi.org/10.3389/fmicb.2012.00012.
2. Baris O., Güllüce M., Sahin F., Ozer H., Kılıc H., Ozkan H., Sökmen M., Ozbek T. (2006) Biological activities of the essential oil and methanol extract of Achillea biebersteinii Afan (Asteraceae). *Turk J Biol*., vol. 30, pp. 65–73.
3. Wei A., Shibamoto T. (2010) Antioxidant/Lipoxygenase inhibitory activities and chemical compositions of selected essential oils. *J Agric Food Chem*., vol. 58, pp. 7218–7225. https://doi.org/10.1021/jf101077s.
4. Gilani A.H., Khan A.U. (2010) Medicinal value of combination of cholinergic and calcium antagonist constituents in olives. In: Preedy V.R., Watson R.R. (Eds.), Olives and Olive Oil in Health and Disease Prevention. Elsevier: Amsterdam, The Netherlands, pp. 835–843. https://doi.org/10.1016/B978-0-12-374420-3.00089-9.
5. Mannina L., Segre A.L. (2010) NMR and olive oils: A geographical characterization. In: Preedy V.R., Watson R.R. (Eds.), Olives and Olive Oil in Health and Disease Prevention. Elsevier: Amsterdam, The Netherlands, pp. 117–124. https://doi.org/10.1016/B978-0-12-374420-3.00014-0.
6. Jiang L., Lu J., Qin Y., Jiang W., Wang Y. (2020) Antitumor effect of guava leaves on lung cancer: A network pharmacology study. *Arab J Chem*., vol. 13, pp. 7773–7797. https://doi.org/10.1016/j.arabjc.2020.09.010.
7. Pavlić B., Teslić N., Kojić P., Pezo L. (2020) Prediction of the GC–MS retention time for terpenoids detected in sage (Salvia officinalis L.) essential oil using QSRR approach. *J Serb Chem Soc*., vol. 85, no. 1, pp. 9–23. https://doi.org/10.2298/JSC190416097P.
8. Azar A.P., Nekoei M., Riahi S., Ganjali M.R., Zare K. (2011) A quantitative structure–retention relationship for the prediction of retention indices of the essential oils of Ammoides atlantica. *J Serb Chem Soc*., vol. 76, no. 6, pp. 891–902. https://doi.org/10.2298/JSC100219076A.
9. Pourbasheer E., Riahi S., Ganjali M.R., Norouzi P. (2010) Quantitative structure–retention relationship (QSRR) models for predicting the GC retention times of essential oil components. *Acta Chromatogr*., vol. 22, no. 3, pp. 357–373. https://doi.org/10.1556/achrom.22.2010.3.2.
10. Rojas C., Duchowicz P., Tripaldi P., Diez R.P. (2015) QSPR analysis for the retention index of flavors and fragrances on a OV-101 column. *Chemom Intell Lab Syst*., vol. 140, pp. 126–132. https://doi.org/10.1016/j.chemolab.2014.09.020.
11. Hu R., Liu H., Zhang R., Xue C., Yao X., Liu M., et al. (2005) QSPR prediction of GC retention indices for nitrogen-containing polycyclic aromatic compounds from heuristically computed molecular descriptors. *Talanta*., vol. 68, no. 1, pp. 31–39. https://doi.org/10.1016/j.talanta.2005.04.034.

12. Luan F., Liu H.T., Wen Y., Zhang X. (2008) Quantitative structure–property relationship study for estimation of quantitative calibration factors of some organic compounds in gas chromatography. *Anal Chim Acta*., vol. 612, no. 2, pp. 126–135. https://doi.org/10.1016/j.aca.2008.02.037.

13. Polyakova Y., Jin L., Row K. (2006) Linear regression based QSPR models for the prediction of the retention mechanism of some nitrogen containing heterocycles. *J Liq Chromatogr Relat Technol*., vol. 29, pp. 533–552. https://doi.org/10.1080/10826070500479062.

14. Navabi A., Isfahani T., Ramazani M., Alimoradi M. (2021) QSPR models for predicting retention indices of Polygonum minus Huds. essential oil composition using GA–BWMLR and GA–BPANN methods. *J Essent Oil Bear Plants*., vol. 24, pp. 879–896. https://doi.org/10.1080/0972060X.2021.1976284.

15. Bayat Z., Yazdan Abad M.F. (2011) Quantitative structure–property relationship (QSPR) study of Kovats retention indices of some adamantane derivatives by the genetic algorithm and multiple linear regression (GA–MLR) method. *Pet Coal*., vol. 53, no.2.

16. Riahi S., Pourbasheer E., Ganjali M.R., Norouzi P. (2009) Investigation of different linear and nonlinear chemometric methods for modeling of retention index of essential oil components: Concerns to support vector machine. *J Hazard Mater*., vol. 166, no. 2–3, pp. 853–859. https://doi.org/10.1016/j.jhazmat.2008.11.097.

17. Noorizadeh H., Farmany A. (2010) QSRR models to predict retention indices of cyclic compounds of essential oils. *Chromatographia*., vol. 72, pp. 563–569. https://doi.org/10.1365/s10337-010-1660-4.

18. Noorizadeh H., Farmany A., Noorizadeh M. (2011) Quantitative structure–retention relationships analysis of retention index of essential oils. *Quim Nova*., vol. 34, pp. 242–249. https://doi.org/10.1590/S0100-40422011000200014.

19. Noorizadeh H., Farmany A. (2010) Exploration of linear and nonlinear modeling techniques to predict retention index of essential oils. *J Chin Chem Soc*., vol. 57, pp. 1268–1277. https://doi.org/10.1002/jccs.201000188.

20. Noorizadeh H., Farmany A., Khosravi A. (2013) Investigation of retention behaviors of essential oils by using QSRR. *J Chin Chem Soc*., vol. 57, pp. 982–991. https://doi.org/10.1002/jccs.201000137.

21. Driouche Y., Messadi D. (2019) Quantitative structure–retention relationship model for predicting retention indices of constituents of essential oils of Thymus vulgaris (Lamiaceae). *J Serb Chem Soc*., vol. 84, no. 4, pp. 405–416. https://doi.org/10.2298/JSC180817010D.

22. Navabi A., Isfahani T., Ramazani M., Alimoradi M. (2021) QSPR models for predicting retention indices of Polygonum minus Huds. essential oil composition using GA–BWMLR and GA–BPANN methods. *J Essent Oil Bear Plants*., vol. 24, pp. 879–896. https://doi.org/10.1080/0972060X.2021.1976284.

23. Tlili A., Bouziane M., Flamini G., Hadj-Mahammed M. (2022) Volatiles variation of two major cultivars of Olea europaea L. cultivated in Mediterranean and arid regions of Algeria. *Rec Nat Prod*., vol. 16, no. 1, pp. 34–45. http://doi.org/10.25135/rnp.249.21.02.1989.

24. ChemAxon Ltd. (2024) ChemAxon software suite. Available at: https://chemaxon.com

25. Stewart J.J.P. (2016) MOPAC2016, Stewart Computational Chemistry, Colorado Springs, CO, USA.

26. Alvascience. (2024) alvaDesc (software for molecular descriptors calculation), version 3.0.4. Available at: https://www.alvascience.com

27. Martin T., Harten P., Young D., Muratov E., Golbraikh A., Zhu H., Tropsha A. (2012) Does rational selection of training and test sets improve the outcome of QSAR modeling? *J Chem Inf Model*., vol. 52, no. 10, pp. 2570–2578. https://doi.org/10.1021/ci300338w.

28. Kennard R., Stone L.A. (1969) Computer aided design of experiments. *Technometrics*., vol. 11, pp. 137–148. https://doi.org/10.1080/00401706.1969.10490666.

29. Gramatica P., Chirico N., Papa E., Cassani S., Kovarich S. (2013) QSARINS: A new software for the development, analysis, and validation of QSAR MLR models. *J Comput Chem*., vol. 34, pp. 2121–2132. https://doi.org/10.1002/jcc.23361.

30. Kherouf S., Bouarra N., Messadi D. (2019). Quantitative modeling for prediction of boiling points of phenolic compounds. *Int J Chem Technol*., vol. 3, pp. 121–128. http://dx.doi.org/10.32571/ijct.636581.

31. Bouarra N., Nadji N., Nouri L., Boudjemaa A., Bachari K., Messadi D. (2021). Predicting retention indices of PAHs in reversed-phase liquid chromatography: A quantitative structure retention relationship approach. *J Serb Chem Soc*., vol. 86, pp. 63–75. https://doi.org/10.2298/JSC200219019B.

32. Bouarra N., Nadji N., Kherouf S., Nouri L., Boudjemaa A., Bachari K., Messadi D. (2022). QSER modeling of half-wave oxidation potential of indolizines by theoretical descriptors. *J Turk Chem Soc A: Chem*., vol. 9, pp. 709–720. https://doi.org/10.18596/jotcsa.1065043.

33. Golbraikh A., Tropsha A. (2002) Beware of $q^2$! . *J Mol Graph Model*., vol. 20, no. 4, pp. 269–276. https://doi.org/10.1016/s1093-3263(01)00123-1.

34. OECD. (2007) Principles for the validation, for regulatory purposes, of (quantitative) structure–activity relationship models. Paper presented at 37th Joint Meeting of the Chemicals Committee and Working Party on Chemicals, Pesticides and Biotechnology, Paris, France. ENV/JM/MONO(2007)2.

35. Poole C.F. (2012) Packed columns for gas–liquid and gas–solid chromatography. In: *Gas Chromatography*, pp. 97–121.ISBN 978-0-12-385540-4.

36. Bertz S.H. (1981) The first general index of molecular complexity. *J Am Chem Soc*., vol. 103, no. 12, pp. 3599–3601. https://doi.org/10.1021/ja00402a071.

37. Schuur J.H., Selzer P., Gasteiger J. (1996) The coding of the three-dimensional structure of molecules by molecular transforms and its application to structure–spectra correlations and studies of biological activity. *J Chem Inf Comput Sci*., vol. 36, no. 2, pp. 334–344. https://doi.org/10.1021/ci950164c.

38. Kier L.B., Hall L.H. (1986) Molecular Connectivity in Structure–Activity Analysis. Research Studies Press: Letchworth, Hertfordshire, England. ISBN 9780471909835

39. Randić M. (1975) Characterization of molecular branching. *J Am Chem Soc*., vol. 97, no. 23, pp. 6609–6615. https://doi.org/10.1021/ja00856a001.

40. Todeschini R., Consonni V. (2009) Molecular Descriptors for Chemoinformatics. Wiley–VCH: Weinheim. ISBN:9783527318520. https://doi.org/10.1002/9783527628766.

***Information about authors:***

*Soumaya Kherouf – Senior Researcher, Organic Synthesis Laboratory Modeling and Optimization of Chemical Processes (LOMOP), Department of Chemistry, Badji Mokhtar University (Annaba, Algeria, e-mail: soumaya.kherouf@univ-annaba.org).*

*Youssouf Driouche – Senior Researcher, Environmental Research Center (CRE) (Annaba, Algeria, e-mail: y.driouche@cre.dz).*

*Nabil Bouarra – Doctor of Science, Senior Researcher, Center of Scientific and Technical Research in Physico-Chemical Analysis, Bou-Ismail, (Tipaza, Algeria), Laboratory of Environmental Engineering, Faculty of Engineering Sciences, Department of Process Engineering, Badji Mokhtar University (Annaba, Algeria, e-mail: bouarranabil@yahoo.com, bouarra.nabil@crapc.dz).*

International Journal of Biology and Chemistry 18, № 2 (2025)

IRSTI 31.21.15 https://doi.org/10.26577/IJBCh202518216

**S. Bayazit**

Kazakh-British Technical University, Almaty, Kazakhstan
e-mail: *bayazitsarah@gmail.com*

*(Received 6 November 2025; received in revised form 20 December 2025; accepted 25 December 2025)*

# In silico docking and interaction analysis of KazMeI with α-glucosidase as a potential antidiabetic agent

**Abstract**. The present study focuses on the molecular docking and interaction analysis of the Kazcaine (1-(2-ethoxyethyl)-4-ethynyl-4-benzoyloxypiperidine) derivative KazMeI with the α-glucosidase enzyme (PDB ID: 5NN4), the principal therapeutic target in the treatment of type 2 diabetes mellitus. For crystal structure modeling of human lysosomal acid-alpha-glucosidase, GAA/N-acetyl-cysteine complex was utilized. The ligand structure was designed in ChemDraw, geometry-optimized using a Python-based MM2 molecular mechanics force field, and converted to PDBQT format in AutoDockTools v1.5.6. The protein structure was prepared by removing water molecules, adding polar hydrogens, and centering the docking grid at coordinates (–6.152, –33.636, 91.204 Å). Docking simulations performed in AutoDock4.2 using the Lamarckian Genetic Algorithm produced ten conformations with highly consistent binding orientations. The lowest binding free energy (ΔG) was –7.00 kcal/mol, corresponding to an inhibition constant (Ki) of 7.37 μM, indicating moderate yet biologically relevant affinit . Interaction analysis revealed that KazMeI forms hydrophobic and π–π stacking contacts with Leu286, Pro285, Leu291, and Trp613, and hydrogen bonding with Ser601 and Thr286, while the quaternary ammonium group interacts electrostatically with Arg600. These results confirm the predicted antidiabetic potential of the patented derivative KazMeI compound (Utility Model Patent No. 9796, Kazakhstan, 2024) and support its further development as a lead α-glucosidase inhibitor.

**Keywords:** Autodock, Pymol, ChemDraw, molecular docking, α-glucosidase, Kazcaine derivative, antidiabetic agents.

## Introduction

Type 2 diabetes mellitus (T2DM) is a tenacious metabolic disorder that incidence exceeds 400 million globally and is anticipated to rank among the top causes of morbidity in the year 2030. The disorder is typified by hyperglycemia due to defective insulin secretion, insulin resistance, or both. Chronic postprandial hyperglycemia is the reason for the gravest long-term complication, such as cardiovascular problems, nephropathy, as well as neuropathy. Targeting of α-glucosidase, an indispensable catalyst for the cleavage of complex carbs into assimilable monosaccharides, is among the chief therapeutic methods used in curbing these problems. Slowing down glucose uptake in the small intestine through inhibition of α-glucosidase, consequently lowers postprandial blood glucose peaks [1]. The crystallographic structure of human lysosomal acid α-glucosidase in a complex with N-acetyl-cysteine (PDB ID: 5NN4) is used as a high-resolution guide for the rationale design of α-glucosidase inhibitors [2].

Among the therapeutic targets of extreme biomedical significance, α-glucosidase has gained significant interest. It plays an indispensable role in carbohydrate digestion by catalysing the hydrolysis of α-glucosidic linkages, and its inhibition was identified as an efficient measure for the regulation of postprandial hyperglycemia in type 2 diabetes mellitus [1]. Access to an impressive set of high-resolution crystallographic structures of α-glucosidase, for example, human lysosomal acid-α-glucosidase in complex with N-acetyl-cysteine [1], enabled the process of structure-based drug discovery. Current computational as well as experimental investigations reaffirm the fact that α-glucosidase continues to emerge as an established and potential therapeutic target for the discovery of novel antidiabetic agents [3].

Of exceptional interest are the piperidine derivatives as being a structurally diverse but highly pharmacologically relevant heterocyclic nitrogen-containing system widely applicable in the field of medicinal chemistry [4].

© 2025 al-Farabi Kazakh National University

It has also been illustrated in the past the promise of nitrogen-containing heterocyclic scaffolds as biological entities. Specifically, Yu [5] announced the synthesis as well as biological profiling of 1,3,8-triazaspiro[4.5]decane-2,4-dione derivatives for the exhibition of potential myelostimulatory activity. These observations further underscore the pharmaceutical implication of heterocyclic entities, especially those possessing piperidine-like moieties, as multifaceted templates for lead scaffolds.

Among them, the Kazcaine (1-(2-ethoxyethyl)-4-ethynyl-4-benzoyloxypiperidine hydrochloride) and its analogues exhibited significant pharmacology as an anesthetic as well as for cardioprotection [6]. Utility Model Patent No. 9796 [7] reveals some of the newer analogues of the Kazcaine show unprecedented inhibitory activity where the reported values go up to 95% inhibition of α-glucosidase rendering the scaffold as an interesting lead for the development of antidiabetic agents.

To investigate this hypothesis, a rigorous in-silico docking and visualization analysis was carried out. The ligand was drafted in ChemDraw [8] and was optimized by applying a Python-coded MM2 type of molecular mechanics force field. The protein was taken from the RCSB Protein Data Bank, was cleaned from bad atoms by applying AutoDockTools v1.5.6, and was treated with AutoDock4.2 docking simulations using the Lamarckian Genetic Algorithm [9]. Structural analysis and electrostatic surface mapping were also conducted with MOE ([10] and PyMOL. It is an in-silico analysis that attempts to define the binding mode, interaction profile, and energetic parameters of the patented KazMeI (code name KaZMeI) derivative with α-glucosidase, as theoretical justification for it being a potential new antidiabetic lead compound.

*Object of the study.* The object of the study is the interaction between the enzyme α-glucosidase and a biologically active Kazcaine and methyl iodide derivative – KazMeI, investigated by the use of the AutoDock software package.

## Materials and methods

### *Ligand Preparation*

Molecular structures of quaternary ammonium derivative of Kazcaine and methyl iodide (Figure 1) as alkylating agent in quaternization reaction were first depicted in ChemDraw 20.0 (PerkinElmer Informatics). The 2D drawings were then converted into 3D structures using Chem3D module and saved in the form of .mol files. Geometry optimization of structural geometry was carried out through a Python-based interface utilizing MM2 molecular mechanics force field in order to reduce steric strain by assuming stable conformers for purpose of docking. The ligands thus optimized were then further converted to PDBQT format through ADT (AutoDockTools) v1.5.6 by imposition of Gasteiger partial charges, combination of non-polar hydrogens, and specification of rotatable bonds.

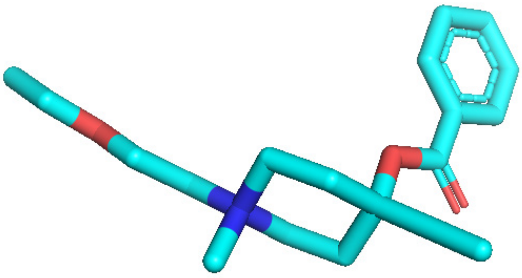

**Figure 1** – Optimized 3D structure of KazMeI

### *Protein Preparation*

The 3D structure of α-glucosidase (PDB ID: 5NN4) was downloaded from the RCSB Protein Data Bank (Figure 2).

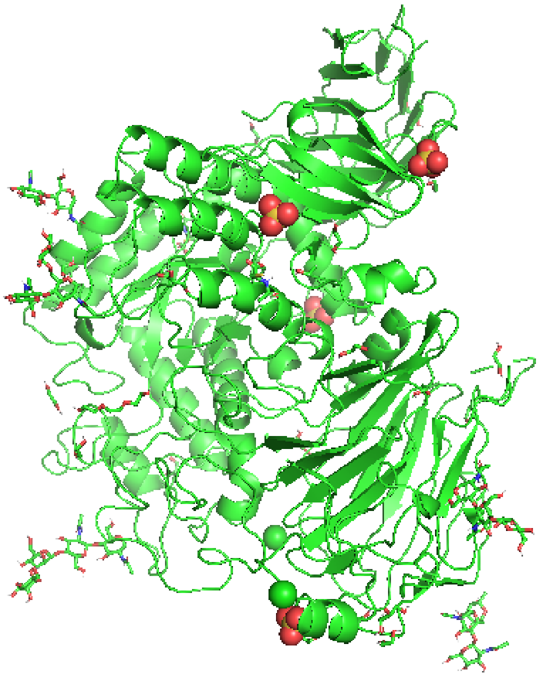

**Figure 2** – Crystal structure of human lysosomal acid-alpha-glucosidase, GAA, in complex with N-acetyl-cysteine

*Identification of the Binding Pocket and Electrostatic Surface*

The active binding site for α-glucosidase was observed through the electrostatic surface potential and polar as well as nonpolar residue polar distributions. The three-dimensional structure of the enzyme (PDB code: 5NN4) was visualized and processed with PyMOL v2.5 and AutoDockTools or ADT. The pocket was delineated around the catalytic residues (Asp214, Glu276, Asp349, His600, and Arg600), ascertained through the AutoGrid mapping step of docking preparation, with their centers at coordinates (–6.152, –33.636, 91.204) Å.

To display the electrostatic features, the receptor surface was displayed in PyMOL with the use of the "coulomb" potential color scheme, in which red is used to define negatively charged sites, blue is used for positive potential, and green/white is used for neutral/hydrophobic surfaces (Figure 3). The figure indicated that the active site of α-glucosidase constitutes a mostly hydrophobic cavity that is lined by some charged residues, creating an environment of high energy for binding of quaternary ammonium derivatives of Kazcaine. The surface mapping also validated that the region of ligand binding is that of maximum electrostatic complementarity of the positive ammonium group of KazMeI with the negatively polarized residues Asp and Glu, stabilizing the ligand by way of ionic and hydrogen bond interaction.

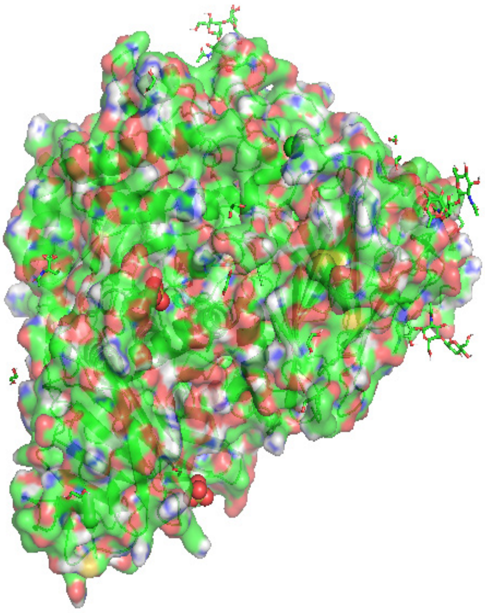

**Figure 3** – Electrostatic surface mapping of crystal structure of human lysosomal acid-alpha-glucosidase, GAA, in complex with N-acetyl-cysteine

All water molecules and co-crystallized ligands were removed, while polar hydrogens and Kollman charges were added using *ADT*. The prepared receptor was saved as a PDBQT file for grid map generation and docking Figure 4).

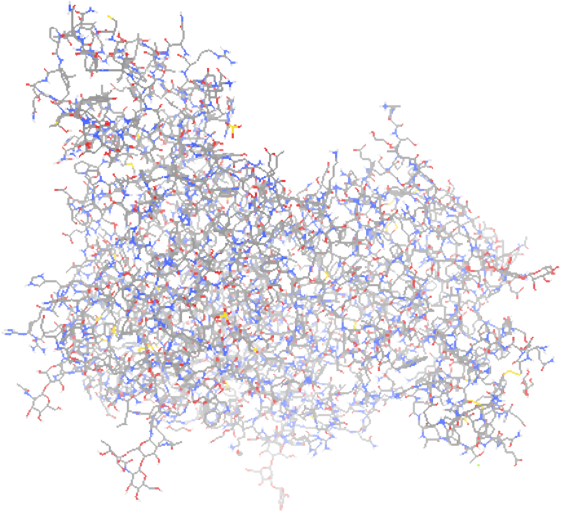

**Figure 4** – PDBQT file representation of Crystal structure of human lysosomal acid-alpha-glucosidase

*Grid Map Generation*

Grid parameters were defined in order to encompass the catalytic pocket of dimensions 98 × 126 × 122 points with a spacing of 0.375 Å. The search box of the grid was placed at coordinates (–6.152, –33.636, 91.204) Å, including important active site residues Trp613, Leu286, Pro285, and Ser601. Grid maps for atom type A, C, OA, and N were computed by AutoGrid4, as well as electrostatic (.e.map) and desolvation ((.d.map) potential maps.

*Docking Protocol*

Docking simulations were carried out with AutoDock4.2 utilizing the Lamarckian Genetic Algorithm (LGA). The search settings were population of 150, maximum energy evaluations of $2.5 \times 10^6$, and 10 independent dockings for every ligand. The maximum generations were adjusted to 27,000, with mutation and crossover rates of 0.02 and 0.8, respectively. The torsional degrees of freedom (TORSDOF) for the ligand were adjusted to 7. The dockings log files (.dlg) were processed with ADT for retrieval of binding energies and inhibition constants (Ki). The optimal docking pose of every ligand was determined by the most adverse binding energy (ΔG) and population of the most significant clusters.

*Visualization and Analysis*

Top-ranked complexes were visualized and explored by means of PyMOL v2.5 (Schrödinger LLC). The receptor was shown in cartoon mode (gray), and ligands were colored in stick model by magenta (Figure 5). Hydrogen bonds were shown as blue dashed lines in a radius of cut-off of 3.2 Å and angle limit of 20°. Hydrophobic interaction was detected by nearness (Ø4.0 Å) to residues of non-polar character. Binding sites and their neighborhood amino acid residues were labeled for publication-ready images. All renderings were carried out in white background at 600 dpi by using the ray-tracing facility of PyMOL.

## Results and Discussion

The quaternary ammonium derivative of KazMeI was successfully docked with α-glucosidase (PDB ID: 5NN4) by utilizing AutoDock4.2. Ten independent docking simulations were produced in all by utilizing the Lamarckian Genetic Algorithm, all of them converging into related binding orientations in the active pocket of the enzyme, implying an orderly and stable binding mode. Calculated binding free energies (ΔG) were in the range –5.94 to –7.00 kcal/mol, while estimated inhibition constants (Ki) ranged from 7.37 to 44.44 µM, in agreement with a moderate binding affinity characterizing non-covalent α

Of the ten conformations, the pose with the lowest energy (-ΔG = –7.00 kcal/mol, Ki = 7.37 µM) was chosen as the most likely bioactive shape. An analysis of docking indicated that KazMeI binds, in a compact, stable complex, in the hydrophobic cavity of the enzyme. The interaction energy of the pose was –9.09 kcal/mol, with contributions from van der Waals, hydrogen bonds, and desolvation energies (-7.45 kcal/mol), and electrostatics (-1.64 kcal/mol). The torsional energy penalty was much lower (\+2.09 kcal/mol), such that the ligand assumed its low-energy form with no appreciable structural strain (Table 1).

According to previously published AutoDock4.2 and MOE-based studies, the binding free energies (ΔG) of acarbose and miglitol toward α-glucosidase (PDB IDs: 3A4A, 5NN4) typically range from –6.2 to –8.0 kcal·mol$^{-1}$, corresponding to inhibition constants (Ki) between 2–20 µM [1,3]. In comparison, the Kazcaine-derived quaternary ammonium compound *KazMeI* exhibited a binding free energy of *–7.00 kcal·mol*$^{-1}$ and an estimated *Ki of 7.37 µM*, which places it within the same energetic range as these standard inhibitors.

Visualization of the best-ranked complex (Figure 5) in PyMOL v2.5 verified that the KazMeI molecule was trapped in the active-site cleft of the enzyme with the help of some important residues – Pro285, Thr286, Leu286, Leu291, Ser601, Arg600, His612, and Trp613. The aromatic phenyl ring of the ligand engaged in π–π stacking contacts with Trp613, whereas the aliphatic side chain was stabilized by hydrophobic contacts with Leu291 and Pro285. The amide and ether oxygens of KazMeI were directed towards Ser601 and Thr286, establishing hydrogen bonds, supporting the stability of the complex additionally. The quaternary ammonium donor was directed near Arg600, implying potential cation–π or dipole–dipole contacts, that in many cases, were significant for substrate recognition in glycosidase catalysis.

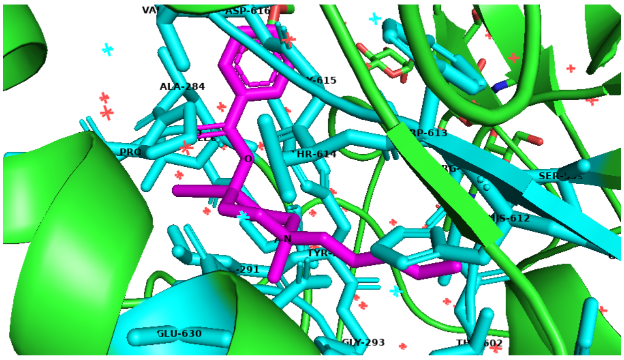

**Figure 5** – Visualization of the best docking pose of ligand obtained from AutoDock4.2

Electrostatic surface mapping of the α-glucosidase (Figure 3) revealed that the active site constitutes an almost exclusively hydrophobic pocket lined with negatively charged residues (Asp and Glu), in turn creating an electrostatically complementary site for the positively charged ammonium ammonium group of KazMeI. This complementariness most probably gives rise to the strongbinding energy and strengthens ligand. The binding orientation predicted for KazMeI is similar close to that of some known reported α-glucosidase inhibitors, further substantiating the correctness of the pose that was predicted (Table 1).

**Table 1** – Docking Results per GA Run

| Run | ΔG (kcal/mol) | Ki (μM) | Intermolecular | vdW+Hbond+desolv | Electrostatic |
|---|---|---|---|---|---|
| 1 | -6.41 | 19.89 | -8.5 | -7.0 | -1.51 |
| 2 | -5.94 | 44.44 | -8.03 | -6.87 | -1.15 |
| 3 | -7.0 | 7.37 | -9.09 | -7.45 | -1.64 |
| 4 | -6.34 | 22.36 | -8.43 | -6.84 | -1.6 |
| 5 | -6.19 | 29.22 | -8.27 | -7.64 | -0.63 |
| 6 | -6.32 | 23.14 | -8.41 | -7.19 | -1.22 |
| 7 | -6.51 | 16.91 | -8.6 | -7.32 | -1.27 |
| 8 | -6.36 | 21.61 | -8.45 | -7.7 | -0.75 |
| 9 | -6.41 | 19.99 | -8.5 | -7.03 | -1.47 |
| 10 | -6.0 | 40.02 | -8.09 | -6.95 | -1.14 |

The docking results show regular binding affinities in the 10 runs of GA, with estimated free energies between -5.94 to -7.00 kcal/mol. The lowest binding energy (–7.00 kcal/mol) was observed in conformation 3, corresponding to the highest affinity (Ki = 7.37 μM) and minimal RMS deviation (cRMS = 0.0). All conformations exhibited similar poses, suggesting stable ligand accommodation within the α-glucosidase binding pocket.

The cluster analysis identified six discernable conformational clusters, with the most populated and least energetic cluster exhibiting ΔG = -7.00 kcal/mol. The primary energetic contributions come from van der Waals and hydrogen bonding interaction, while electrostatic terms are moderate (-1.2 to -1.6 kcal/mol).

The quaternary KazMeI derivative iodide showed consistent and positive interaction profile in the molecular docking analysis against α-glucosidase, with binding free energies of –5.94 to –7.00 kcal/mol in ten independent runs of the Lamarckian Genetic Algorithm (LGA). The most prominent binding energy of –7.00 kcal/mol, corresponding to an estimated inhibition constant (Ki) of 7.37 μM, indicate moderate to good affinity of the KazMeI ligand for the active site of α-glucosidase. The value falls in the normal range of bioactive small molecules that display measurable inhibitory activities.

The interaction energy decomposition revealed that hydrogen bond and van der Waals, and contributions (-≈7.0 kcal/mol) predominate the ligand–receptor interaction, with modest contribution of electrostatic forces (-1.2 to –1.6 kcal/mol). The torsional free energy penalty of +2.09 kcal/mol, related to the ligand conformational flexibility, is rather low, signifying that the compound is capable of fitting well into the binding pocket of the enzyme with modest energetic penalty. These findings complement the amphiphilic character of the Kazcaine scaffold, whereby polar carbonyl and amide areas can form hydrogen bonds, and the area of the aromatics, as well as the alkyl regions, offers hydrophobic stabilization.

In general, the results of the docking indicate that the quaternary methylated Kazcaine derivative ((KazMeI) interacts effectively with α-glucosidase by associating with hydrophobic and hydrogen bonds contacts. The estimated binding affinity lends credence to the argument that structural alteration of Kazcaine with short alkyl side-chains would extend its interaction capacity with metabolic enzymes of potential involvement in the regulation of diabetes mellitus.

The docking parameters including the population size (150), the maximum energy evaluations ($2.5 \times 10^6$), and the settings for the Lamarckian Genetic Algorithm were selected based on already proven studies [9, 10], where similar protocols generated the native ligand poses within an RMSD of ≤ 2 Å. Thus, the credibility of the present grid configuration and scoring function are methodologically equivalent to proven validated methods.

## Conclusion

The molecular docking investigation of the quaternary ammonium Kazcaine derivative KazMeI (KazMeI ) with α-glucosidase (PDB ID: 5NN4) revealed a consistent and energetically favorable interaction pattern. The lowest binding free energy (ΔG = –7.00 kcal/mol) and inhibition constant (Ki = 7.37 μM) indicate a moderate yet biologically meaningful affinity, consistent with known α-glucosidase inhibitors in the low micromolar range. The complex was stabilized primarily by hydrophobic and π–π stacking interactions with Leu286, Pro285, Leu291, and Trp613, supplemented by hydrogen bonding with Ser601 and Thr286, and minor electrostatic stabilization involving Arg600.

These computational findings support the antidiabetic potential of the patented compound (Utility Model Patent No. 9796, Kazakhstan, 2024) and highlight KazMeI as a promising structural scaffold for the rational design of novel α-glucosidase inhibitors. Future studies involving analogues and in vitro enzymatic validation will further substantiate its pharmacological relevance.

## Conflict of interest

The authors declare that they have no conflicts of interest.

## References

1. Moustafa Younis, John Pham, Hussein Asad, Majdi S. Hamarshi (2020) Computer-Based versus Paper-Based Insulin Infusion Algorithms in Diabetic Ketoacidosis. *Current Diabetes Reviews*, vol. 16(6), pp. 628-634, https://doi.org/10.2174/1573399815666190712191932.
2. Roversi P., Xu Y. (2017) RCSB Protein Data Bank.
3. Babar Zainib Khan, Mazhar Zahra, Mubeen Anwar, Munazza Noor, Kashif Hashmi, Huma Suleman, Muhammad Khan, Muhammad Shah, Abdullah Ali, Shahid Syed, Ali Syed. (2020) Drug similarity and structure-based screening of medicinal compounds to target macrodomain- I from SARS-CoV-2 to rescue the host immune system: a molecular dynamics study. *Journal of biomolecular structure & dynamics*, 40 (6). https://doi.org/10.1080/07391102.2020.1815583.
4. Sandmeier T, Carreira EM (2020) Asymmetric allylic alkylation, allylation, and related reactions. John Wiley & Sons 249–271.
5. Yu V., Ten A., Baktybayeva L., Sagatbekova I., Praliyev K., Zolotareva D., Seilkhanov T., Zazybin A. (2018). Activation of Leukopoiesis in Rat Blood with Trimecaine-Based Ionic Compounds. *BioMed Research International*, 7346835.
6. Kemelbekov U.S., Hagenbach A., Lentz D. (2010) Pharmacology and structures of the free base of the anaesthetic kazcaine and its complex with β-cyclodextrin. *Journal of Inclusion Phenomena and Macrocyclic Chemistry*, 68(3), pp. 323–330.
7. Utility Model Patent of RK No. 9796. Zazybin A.G., Yu V.K., Dauletbakov A.A., Belyankova E.O., Zolotaryova D.S., Asylbekova S.E., Zhumakova S.S., Bayazit S., Basharimova A.A. (2024) The compound 4-(benzoyloxy)-1-(2-ethoxyethyl)-4-ethynyl-1-methylpiperidin-1-ium iodide, which has antidiabetic activity.
8. Clark A.M., Labute P. (2007) 2D Depiction of Protein−Ligand Complexes. *Journal of Chemical Information and Modeling*, 47(5), pp. 1933–1944.
9. Trott O., Olson A.J. (2010) AutoDock Vina: Improving the Speed and Accuracy of Docking with a New Scoring Function, Efficient Optimization and Multithreading. *Journal of Computational Chemistry*, 31(2) pp. 455–461.
10. Chemical Computing Group. (2022). Molecular Operating Environment (MOE), 2022.02. Montreal, QC, Canada.

***Information about author:***

*Sarah Bayazit – PhD student, Researcher of Kazakh-British Technical University (Almaty, Kazakhstan, e-mail: bayazitsarah@gmail.com)*.

# Content

IB №17004
Signed to publishing 28.12.2025. Format 60x84/8. Offset paper.
Digital printing. Volume 15,3 printer's sheet. Order №3080.
Publishing house «Kazakh University»
www.read.kz Telephone: +7 (727) 3773330, fax: +7 (727) 3773344
Al-Farabi Kazakh National University KazNU, 71 Al-Farabi, 050040, Almaty
Printed in the printing office of the Publishing house «Kazakh University»